1 of 3
AD
A101 675

LEVEL

AD A101675

ARO

AUBURN UNIVERSITY
ENGINEERING EXPERIMENT STATION

AEROSPACE ENGINEERING

AN AERODYNAMIC ANALYSIS OF DEFORMED WINGS

IN SUBSONIC AND SUPERSONIC FLOW

JUL 21 1981

FINAL REPORT

AN AERODYNAMIC ANALYSIS OF DEFORMED WINGS

IN SUBSONIC AND SUPERSONIC FLOW

by

John E. Burkhalter
John M. Abernathy
Milton E. Vaughn, Jr

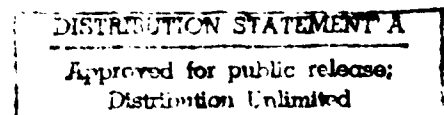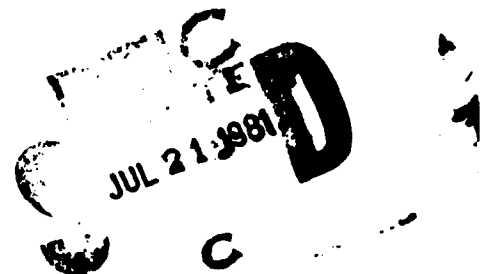FINAL REPORT

Contract No. DAAG29-78-G-0036
January 1980-April 1981

Department of Aerospace Engineering
Auburn University, Alabama   36849

for

U.S. Army Research Office
Research Triangle Park, N.C.   27709

REPORT DOCUMENTATION PAGE		READ INSTRUCTIONS BEFORE COMPLETING FORM
1. REPORT NUMBER	2. GOVT ACCESSION NO. AD-A101675	3. RECIPIENT'S CATALOG NUMBER
4. TITLE (and Subtitle) An Aerodynamic Analysis of Deformed Wings in Subsonic and Supersonic Flow		5. TYPE OF REPORT & PERIOD COVERED Final Report, Jan 1980 — April 1981
		6. PERFORMING ORG. REPORT NUMBER
7. AUTHOR(s) John E. Burkhalter John M. Abernathy Milton E. Vaughn, Jr.		8. CONTRACT OR GRANT NUMBER(s) DAAG29-78-G-0036
9. PERFORMING ORGANIZATION NAME AND ADDRESS Engineering Experiment Station Auburn University Auburn, Alabama 36849		10. PROGRAM ELEMENT, PROJECT, TASK AREA & WORK UNIT NUMBERS
11. CONTROLLING OFFICE NAME AND ADDRESS U. S. Army Research Office P. O. Box 12211 Research Triangle Park, NC 27709		12. REPORT DATE April 1981
		13. NUMBER OF PAGES 200
14. MONITORING AGENCY NAME & ADDRESS(if different from Controlling Office) Same		15. SECURITY CLASS. (of this report) unclassified
		15a. DECLASSIFICATION/DOWNGRADING SCHEDULE

16. DISTRIBUTION STATEMENT (of this Report)

Approved for public release; distribution unlimited.

17. DISTRIBUTION STATEMENT (of the abstract entered in Block 20, if different from Report)

Same

18. SUPPLEMENTARY NOTES

The findings in this report are not to be construed as an official Department of the Army position, unless so designated by other authorized documents.

19. KEY WORDS (Continue on reverse side if necessary and identify by block number)

Aerodynamic Wing Loading, Elevon Loading, Hinge Moments, Deformed Wings, Wing-Elevon Gap Effects, Subsonic and Supersonic Flow

20. ABSTRACT (Continue on reverse side if necessary and identify by block number)

The aerodynamic loading for deformed wings with elevons in both subsonic and supersonic flow is considered. The solution procedure falls into the potential flow category with appropriate restrictions. For subsonic flow, a lifting surface Kernel function formulation is used in which the local pressure loading for both wing and elevon is determined simultaneously in a semi-closed summation manner. Cases under study included gaps between wing and elevon in addition to arbitrary wing-elevon deformations. Results

20. ABSTRACT (CONT)

for all cases compared very well with experimental data. Experimental data
taken in a low speed wind tunnel is also presented for a cropped delta wing
and rectangular elevon in which the wing-elevon gap was the primary test
variable. For supersonic flow, 3-D supersonic theory forms the basis for
the solution procedure. Deformations are accounted for with the use of
doublet paneling added to the basic 3-D solution. Results agree very well
with existing experimental data. The gapped elevon and thick wing trailing
edge problem is also addressed with satisfactory results.

Accession For		
NTIS GRA&I	�	
DTIC TAB	☐	
Unannounced	☐	
Justification		
By		
Distribution/		
Availability Codes		
	Avail and/or	
Dist	Special	
A		

ABSTRACT

The aerodynamic loading for deformed wings with elevons in both subsonic and supersonic flow is considered. The solution procedure falls into the potential flow category with appropriate restrictions. For subsonic flow, a lifting surface Kernel function formulation is used in which the local pressure loading for both wing and elevon is determined simultaneously in a semi-closed summation manner. Cases under study included gaps between wing and elevon in addition to arbitrary wing-elevon deformations. Results for all cases compared very well with experimental data. Experimental data taken in a low speed wind tunnel is also presented for a cropped delta wing and rectangular elevon in which the wing-elevon gap was the primary test variable. For supersonic flow, 3-D supersonic theory forms the basis for the solution procedure. Deformations are accounted for with the use of doublet paneling added to the basic 3-D solution. Results agree very well with existing experimental data. The gapped elevon and thick wing trailing edge problem is also addressed with satisfactory results.

i

PREFACE

The work as reported in this document represents the completion of
the various tasks as prescribed in Contract No. DAAG29-78-G-0036, for
the Army Missile Command, Huntsville, Alabama. This research is
monitored through the U.S. Army Research Office, Research Triangle Park,
North Carolina, and is the result of the work done during the period
January 1980-April 1981. The program manager with the Army Missile
Command was Dr. Donald J. Spring.

Some of the experimental work presented in Chapter III and Chapter
IV was supported by Auburn University Engineering Experiment Station.

ii

ACKNOWLEDGMENTS

TABLE OF CONTENTS

TABLE OF CONTENTS (CONT)

LIST OF FIGURES

LIST OF FIGURES (CONT)

LIST OF FIGURES (CONT)

vii

LIST OF SYMBOLS

Symbol	Definition
a	Nondimensional body radius
AR	Aspect ratio
b	Wing span
B_L	Wing loading coefficients
B_{nm}	Wing loading coefficients
B_{pq}	Elevon loading coefficients
$\bar{c}$	Mean aerodynamic chord, reference length
c	Local wing chord*
c_{R_E}	Root chord of elevon*
c_{T_E}	Tip chord of elevon*
C	Local wing chord**
C_w	Local chord of wing**
C_E	Local chord of elevon**
C_R	Root chord**
C_T	Tip chord**
$c^2 c_m$	Section pitching moment coefficient
C_L	Lift coefficient
C_M, C_{M_y}	Pitching moment coefficient about wing root chord leading edge
C_H	Hinge moment coefficient
C_p	Pressure coefficient $(p-p_\infty)/q_\infty$
ΔC_p	Pressure loading coefficient (pressure difference between upper and lower surface)

---

*Subsonic flow
**Supersonic flow

viii

Symbol	Definition
HL	Hinge line of elevon
I	Integral of the chordwise term of the pressure loading function $$\int_{LE}^{TE} \xi^n \sqrt{\frac{1-\xi}{\xi}}\ d\xi$$
ΔK	Value of Kernel function integral over a subpanel
L	Lift force on the wing
M	Moment produced by the wing
M_∞	Freestream Mach number
ΔP	Pressure differential across the wing
$P(x_o, y_o)$	Pressure loading parameter from 3-D supersonic flow theory
q_∞	Freestream dynamic pressure
r_b	Dimensional body radius
S	Wing planform area, reference area
t_{TE}	Wing trailing edge thickness
V_∞	Freestream velocity
VLE	Leading edge vortex
w	Non-dimensional perturbation velocity W/V_∞, parallel to z-axis
x,y,z	Cartesian coordinates
x_H	Hinge line location along x-axis
x_{LE}	Distance from y-axis to leading edge of wing
x_o, y_o	Integration variables

LIST OF SYMBOLS (CONT)

Symbol	Definition

Greek Symbols

α	Angle of attack
β	Mach flow parameter, $\sqrt{1-M_\infty^2}$
ε	Gap width between wing trailing edge and elevon leading edge
γ	Non-dimensional vorticity Γ/V_∞
δ	Elevon angle relative to wing (trailing edge down is positive)
λ	Taper ratio, (tip chord)/(root chord)
Λ	Wing leading edge sweep angle
ϕ	Nondimensional perturbation velocity potential ϕ/V_∞
θ	Nondimensional spanwise variable
θ_c	Local deformed wing slope at a control point
θ_o	Local deformed wing slope relative to the chord line
θ_T	Positive surface slope of the aft portion of the wing
ξ,η	Non-dimensional chordwise and spanwise variables, respectively

Subscripts

E	Elevon
H	Hinge characteristics
HL	Hinge line
LE	Leading edge
nm	Points or constants associated with the wing
n	Normal
pq	Points or constants associated with the elevon
o	Denotes wing coordinate variables
T	Total

Symbol	Definition

Subscripts

TE	Trailing edge
∞	Freestream conditions
w	Wing
x,y,z	Coordinate axes
i,j,k	Unit vectors
FWD	Forward
AFT	Aft

I. INTRODUCTION

Subsonic Flow

It has been observed that failures associated with the control surfaces have occurred on certain missile configurations. It is believed that these failures have occurred because of adverse loading on the control surface due to large deformations in the wing surfaces. A preliminary study[1] was completed which attempted to identify the aerodynamic changes which occurred because of these deformations. The present study addresses the problem in more detail including various wing-elevon-gap planform configurations, subsonic and supersonic Mach numbers, moderate wing and elevon deformations of an arbitrary nature, and blunt trailing edges for the wing.

In recent years, major efforts have been made to model multi-element airfoil configurations (wing-elevon combinations) and to predict resulting loads and moments. Most of the research efforts concerning these multi-element lifting surfaces have been two-dimensional analyses as typified by the early work of Glauert[2,3] in 1924 and 1927 and more recently by the work of Halsey.[4,5] However, the case of the wing, air gap, control surface combination has generally been neglected as pointed out by Ashley[6] who also expressed the need for such an analysis.

Extension of analyses to include three-dimensional effects or finite wings has generally employed vortex lattice formulations or some form of constant pressure paneling such as that of Woodward[7] and Lan.[8] The Lan approach has received considerable attention of late since the leading

1

edge suction terms and Kutta condition at the trailing edge are properly accounted for in the analysis. DeJarnette[9] extended the "strip" approach of Lan to provide for a "continuous" loading in the spanwise direction. Aside from the Lan-DeJarnette formulation, general vortex lattice approaches suffer from traditional shortcomings such as large computer storage and long run times even on today's high-speed computers. Formulation of the problem using the Kernel function approach in its usual form as typified by Cunningham[10,11] has been generally neglected but offers the potential for increased accuracy, lower computer run times and less storage than does the vortex lattice approach. The Lan[8]-DeJarnette[9] analysis requires comparable run times and storage and offers a viable alternative to the solution of the problem at least for single element airfoils. Extension to multi-element airfoils, as far as is known, has not been completed.

For the most part, previous theoretical analyses have been restricted to planar lifting surfaces with no camber or twist. Wing-elevon configurations generally have been sealed-gap cases. However, White and Landahl[12,13] have developed a procedure requiring the method of matched asymptotic expansions which is used to determine the load distribution when a gap exists between the wing and elevon in two-dimensional flow.

Both the vortex lattice and Kernel function approaches have enjoyed certain successes but certainly the vortex lattice has been more extensively used. There are certain problems which, though amenable to vortex lattice solutions, are more easily handled by the present lifting surface techniques; namely, that of wing irregularities such as twist, camber, and arbitrary deformations. Certainly camber and twist have been

addressed in previous efforts, but analyses of moderate "arbitrary" deformations of a lifting surface have not been found in the literature.

The present work is concerned with the wing-elevon problem for configurations with moderate wing deformations such as camber, twist, and general deformations due to high wing loading or distortion of the surfaces due to aerodynamic heating. Lifting surface theory is employed with the solution following the procedure established by Purvis[14] and Burkhalter, et al.[15] The loading function over the multiple lifting surface is defined, and the Kernel function is then integrated over the surfaces. For this work, the gap distances are considered to be small enough that vortex rollup is assumed negligible.

Comparison is made with experimental data on several general configurations. For the gap case, data was obtained from low speed wind tunnel tests with gap distance as a primary test variable. Data for several elevon deflection angles and hinge line locations are shown for each configuration at numerous angles of attack. Experimental data is lacking for wing load deformations at subsonic speeds but comparisons are made with wings which have moderate camber and twist.

Supersonic Flow

For supersonic flow there are several approaches which address the problem of predicting loads on a planar wing. These methods range from two-dimensional shock expansion theory to three-dimensional wing theory to vortex lattice theory. Some approaches are useful for variably swept wings while others are only applicable to wings with straignt leading edges. The basic elements of the major supersonic flow theories will be summarized in the following paragraphs.

Shock-expansion theory is two-dimensionally restricted to attached shocks but it is general and can be used for thick and thin 2-D bodies alike. However, because the results are difficult to express in concise analytical form, shock-expansion theory is mainly used for obtaining numerical solutions for diamond shaped airfoils. If, however, one assumes a thin wing in steady flow at a small angle of attack; i.e., small perturbations; then the approximate relations for weak shocks and expansions may be used. This thin airfoil theory results in a simple analytical expression for calculating the pressure coefficient.

Although these two-dimensional theories are valuable, they are not sufficient to correctly model three-dimensional flow. Two of the first three-dimensional theories were point source theory and line source theory. These theories were adapted to thin supersonic airfoils with straight leading edges and various types of symmetrical crossections. In each theory the velocity potential for the wing is obtained by analytically integrating over the forecone from the point in question. Either subsonic or supersonic leading edges may be handled in this manner as well as delta wings with supersonic leading and trailing edges. These theories, however, do not allow for the interaction between the upper and lower surfaces of the wing which would result from subsonic leading edges as well as from subsonic wing tips.

Thin wings with straight subsonic leading edges may be handled by conical flow theory. As the flow properties are constant along rays emanating from the vertex of the wing the flow is two-dimensional. The Tschaplygin transformation is used to transform the small perturbation equation in polar coordinates into the two-dimensional Laplace equation.

Complex variable techniques developed for incompressible flow are then
used to obtain an analytical solution for the pressure coefficients.
This technique has also been extended to wings with straignt supersonic
leading edges and also to wings with straight subsonic and supersonic
leading edges combined.

All of these techniques are basically inadequate in predicting
loads for a deformed wing; a deformed wing in this case meaning moderate
arbitrary deformations which include camber and twist. Most are amenable
to general planform shapes but are usually restricted to straight leading
and trailing edges and do not include fuselage effects. A more recent
attempt to include curved leading edges was completed by Carlson[16] in
which a vortex lattice scheme was used to model the wing planform. Al-
though resulting computations were highly oscillatory, a "smoothing"
routine introduced by Carlson produced acceptable results for thin planar
wings. Another recent formulation[17] of the problem utilizing supersonic
line sources has also produced good results on curved planform shapes
and does not require any post data manipulation.

The solution technique used in the present research is fundamentally
based on three-dimensional supersonic flow theory as outlined in Refs. 18,
15 and 19, but is modified to account for wing deformations. Potential
flow is still assumed so that solutions to the potential equations may
be added. The deformed wing is "overlaid" with a doublet paneling sheet
whose strength everywhere is determined through matrix inversion tech-
niques and the doublet solution is then added to the basic three-dimensional
supersonic solution. This is accomplished by subdividing the wing planform
into very small panels over which the pressure is assumed constant.

, Integration is completed over each subpanel in closed form and results
may then be written in summation notation. The vorticity paneling
produces perturbation velocities which account for deformations in the wing
surface.

II. SUBSONIC FLOW-THEORY

Fundamental Equations

The appropriate equations and solution procedure for the Kernel function formulation used in the subsonic analysis are outlined in this section. The equations are well known (Refs. 20 and 21) and the solution procedure is developed in detail in Ref. 14.

Compressibility is included in the potential equation which is written as

$$\phi(x,y,z) = \frac{1}{4\pi} \iint_S \frac{\gamma(x_o,y_o)}{(y-y_o)^2+z^2} z \left[1 + \frac{(x-x_o)}{\sqrt{(x-x_o)^2+\beta^2(y-y_o)^2+\beta^2z^2}} \right] dx_o \, dy_o$$

The downwash at an arbitrary point (x,y) in the $z=0$ plane due to an infinitesimal area $(dx_o \, dy_o)$ of a lifting surface is

$$w(x,y,0) = \frac{1}{8\pi} \iint_S \frac{\Delta C_p(\xi,\eta)}{(y-y_o)^2} \left[1 + \frac{(x-x_o)}{\sqrt{(x-x_o)^2+\beta^2(y-y_o)^2}} \right] dx_o \, dy_o \qquad (1)$$

where ξ and η are dimensionless chordwise and spanwise variables, respectively. These variables are made non-dimensional by the definitions:

$$\xi = \frac{x-x_{LE}(y)}{c(y)} , \qquad\qquad \eta = \frac{y}{b/2} \qquad (2)$$

The functional form of the pressure loading coefficient is assumed as

$$\Delta C_p(\xi,\eta) = \sum_{n=0}^{N} \frac{1}{c(\eta)} \sum_{m=0}^{M} B_{nm} \sin(2m+1)\theta \sqrt{\frac{1-\xi}{\xi}} \, \xi^n \qquad (3)$$

7

where $\eta = \cos\theta$ and N and M represent an arbitrary number of chordwise and spanwise control points, respectively. It is readily seen that this form produces the required leading edge square root singularity, satisfies the Kutta condition at the trailing edge, and has slender wing behavior at the wing tips. A discussion of the logic behind this assumed form of the pressure loading is presented in Reference 14.

Over a sufficiently small subpanel of the wing planform, ΔC_p is essentially constant and may be taken outside the integral of eq. (1). The resulting expression may be evaluated in closed form to give

$$\Delta w(x,y) = \frac{\Delta C_p(\bar{\xi},\bar{\eta})}{8\pi} \; [K(x_2,y_2) -K(x_2,y_1) -K(x_1,y_2) +K(x_1,y_1)] \quad (4)$$

where, as an example, $K(x_1,y_1)$ is evaluated in the form

$$K(x_1,y_1) = - \frac{(x-x_1) + \sqrt{(x-x_1)^2 + \beta^2(y-y_1)^2}}{(y-y_1)}$$

$$+ \; \beta \, \log_e [\beta(y-y_1) + \sqrt{(x-x_1)^2 + \beta^2(y-y_1)^2} \;] \quad (5)$$

The other K's of eq. (4) are evaluated by making the appropriate substitution of the subscripted variables in eq. (5). Also in eq. (4), $\Delta C_p(\bar{\xi},\bar{\eta})$ is evaluated at the centroid of the subpanel. The wing and subpanel are illustrated in Fig. 1.

For small angles-of-attack, the boundary condition imposed is the requirement of no flow through the wing; i.e.,
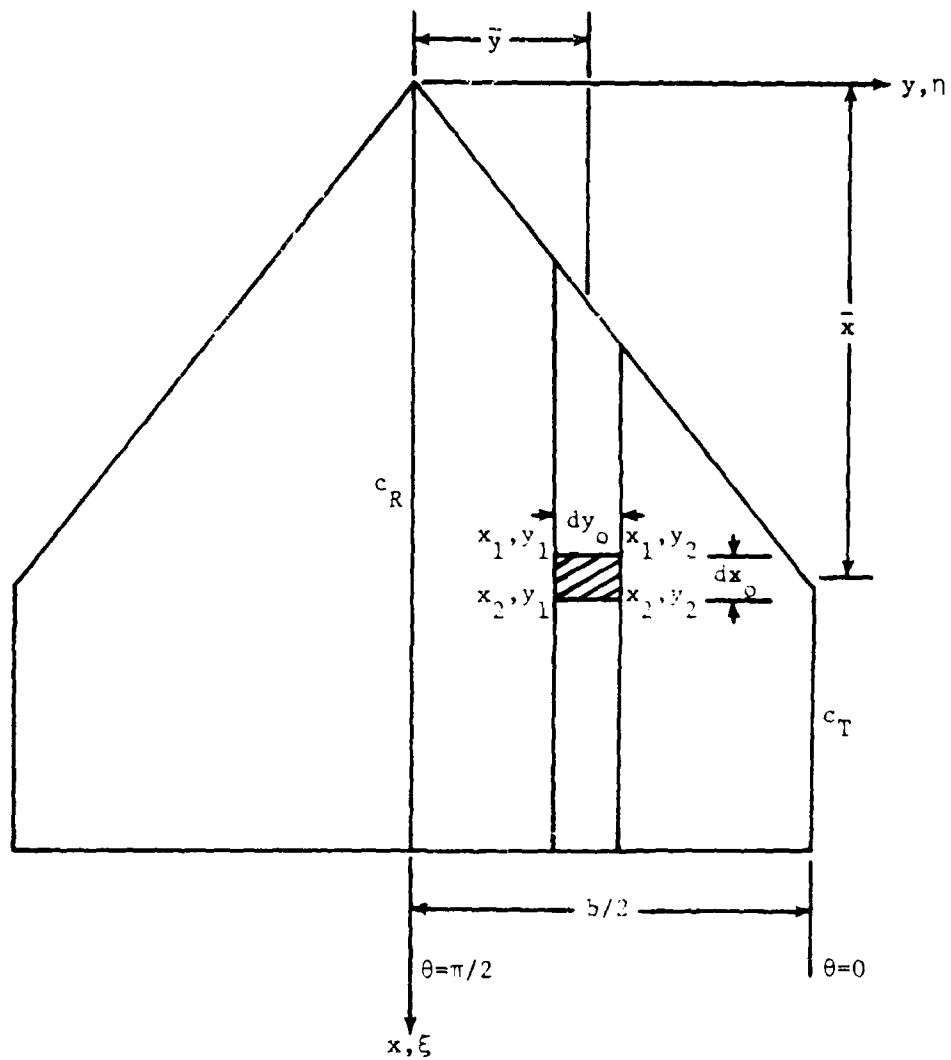
$$w(x,y) + \sin\alpha(x,y) = 0 \quad (6)$$

Figure 1. Wing and Subpanel Coordinates.

The total downwash at any control point due to the entire wing is found by summing the effect of each subpanel of the surface and Eq. (6) becomes

$$\sum_{S}\sum \Delta w(x_i, y_j) + \sin \alpha(x_i, y_j) = 0 \tag{7}$$

where (x_i, y_j) are the control points, and are located according to a cosine distribution[9]

$$x_i = x_{LE}(y_i) + \frac{c(y_i)}{2} (1 - \cos \frac{\pi i}{N+1}) \quad , \quad i = 1,2,\ldots N$$

$$y_j = \frac{b}{2} (1 - \cos \frac{\pi j}{M+1}) \quad , \quad j = 1,2,\ldots M \tag{8}$$

The set of simultaneous, linear equations for the NxM unknown loading coefficients, B_{nm}'s, defined by substituting eq. (3) into eq. (4) and the result into eq. (7), may now be solved, and the loading at any point on the wing is defined by Eq. (3)

Loading Function for Wing-Gap-Elevon Configuration

The above analysis is for a wing configuration only. When a control surface (elevon) is added to the wing, the load distribution will of course change. Further changes in this distribution occur when a gap is introduced between the wing and elevon. In the present work, it is assumed that the elevon span is equal to the wing span, and the elevon hinge line is perpendicular to the wing centerline. With these stipulations, the solution procedure for the basic wing is paralleled except for the loading function.

First, for the sealed-gap case with a deflected elevon, a two-function formulation using eq. (3) to describe the pressure distribution is used. The nondimensional chordwise variable, ξ, of eq. (3) is redefined and is

considered separately for the wing and elevon. For the wing and elevon, respectively, it becomes

$$\xi_W = \frac{x - x_{LE_W}(y)}{c_W(y) + c_E(y)} \quad , \quad \zeta_E = \frac{x - x_{LE_E}(y)}{c_E(y)} \tag{9}$$

This geometry is shown in Fig. 2. With these definitions, it is easily verified that the leading edge singularity is satisfied on both the wing and elevon, and the Kutta condition is met at the elevon trailing edge. These singularities agree with usual assumed loading function with control surfaces pointed out by Landahl in Reference 13. At the wing trailing edge, the Kutta condition is not satisfied, nor is the usual singularity obtained, but rather a finite value. This loading is used to allow a closed form solution to the sectional lift integral. Error due to this assumption is considered to be on the order of error due to the assumption of an infinite loading, while the advantages of a closed form solution are considerable. This (chordwise) distribution is shown schematically in Fig. 3a.

When a gap exists between the wing and elevon, the loading function over the wing and elevon is defined in order to create the effect of two wings. The leading edge singularity and Kutta condition must be satisfied on each surface. Equation (3) produces this distribution by redefining the chord-wise variables illustrated in Fig. 2 as

$$\xi_W = \frac{x - x_{LE_W}(y)}{c_W(y)} \quad , \quad \xi_E = \frac{x - x_{LE_E}(y)}{c_E(y)} \tag{10}$$

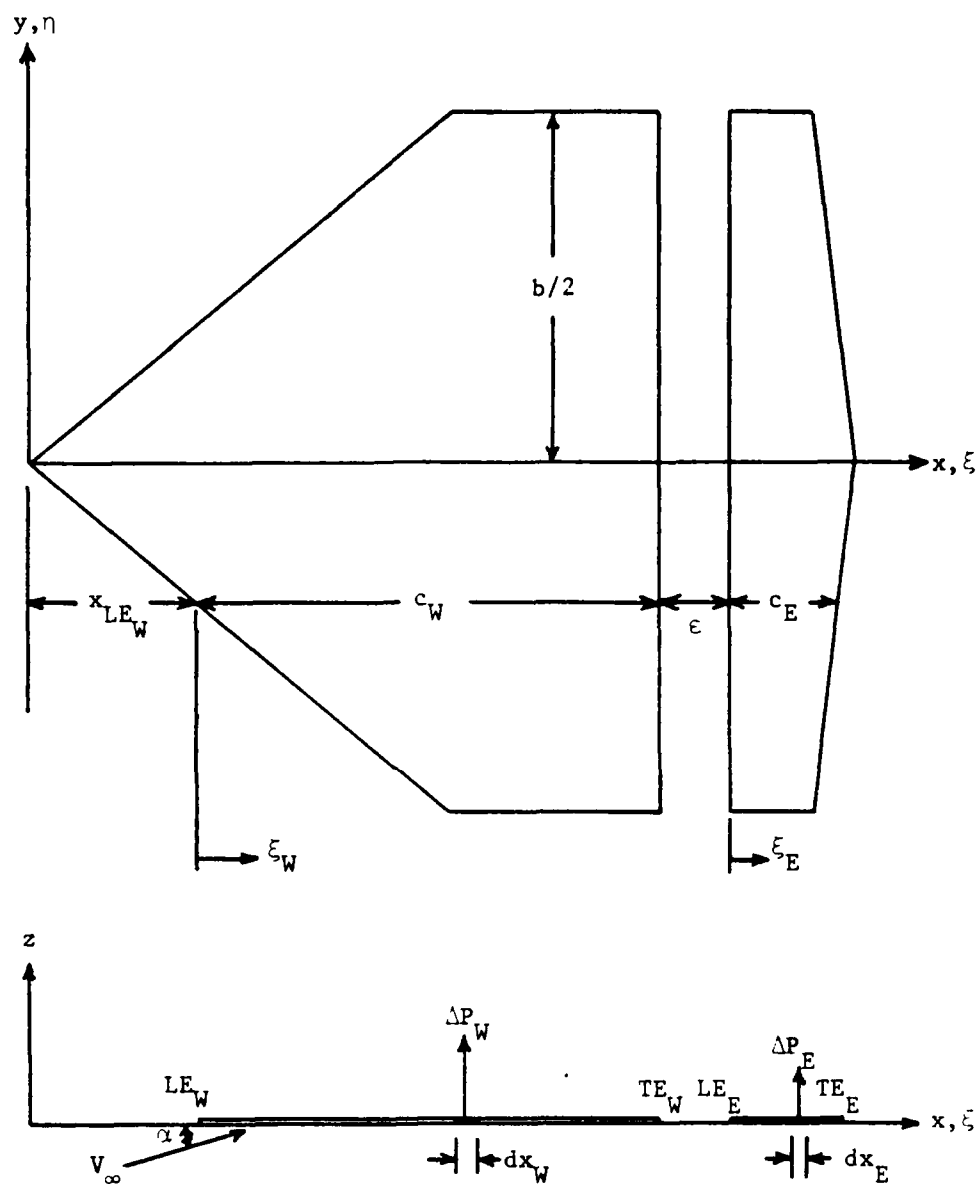for the wing and elevon, respectively. This loading is shown in Fig. 3b.

12

Figure 2.   Wing Geometry and Aerodynamic Forces.
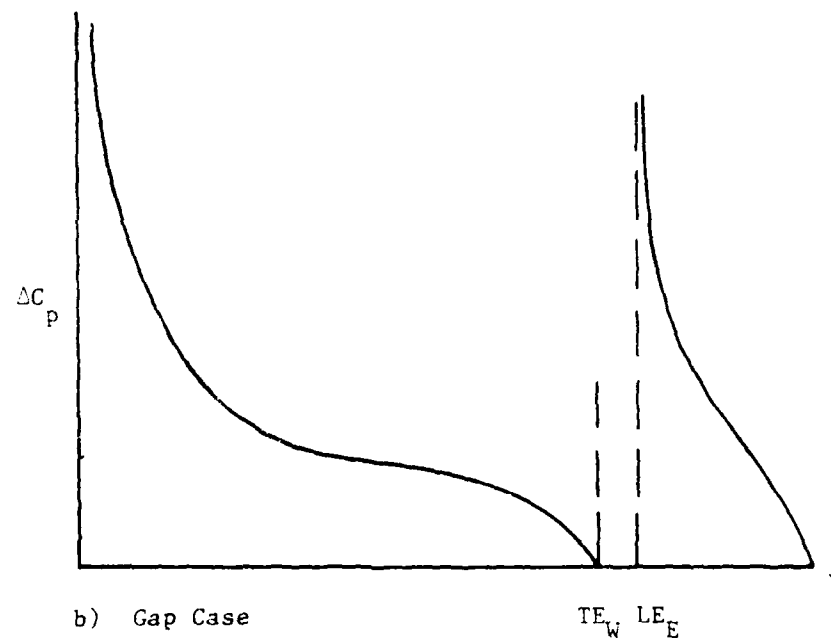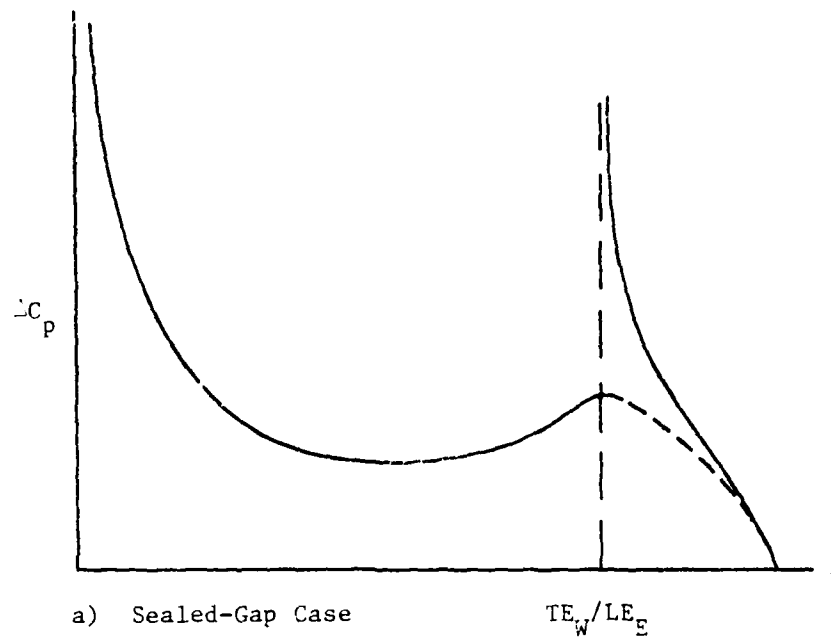
a) Sealed-Gap Case

b) Gap Case

Figure 3. Chordwise Loading Functions.

After the load distribution has been defined, eq. (7) with eqs. (3) and (4) is used to produce a set of simultaneous, linear equations for the unknown coefficients for both the wing and elevon. The typical control point location and corresponding matrix for the unknown coefficients are shown in Fig. 4. The control points are located using eq. (8) separately for both the wing and elevon. The summation is performed over the entire surface of the wing and elevon, and for the control points on the elevon, the boundary condition becomes

$$w(x_i, y_j) + \sin[\alpha(x_i, y_j)] = 0 \tag{11}$$

It should be noted that the loadings for the wing and elevon are solved simultaneously, therefore, iteration of the interference between the surfaces is eliminated. The pressure at any point on the wing or elevon is given by eq. (3), with the appropriate definition of ξ_W and ξ_E (eq. (9) or (10)), and the appropriate values of the B_{nm}'s (wing or elevon).

Total Aerodynamic Forces and Moments

From the wing-elevon configuration, shown in Fig. 1, the total lift is given by

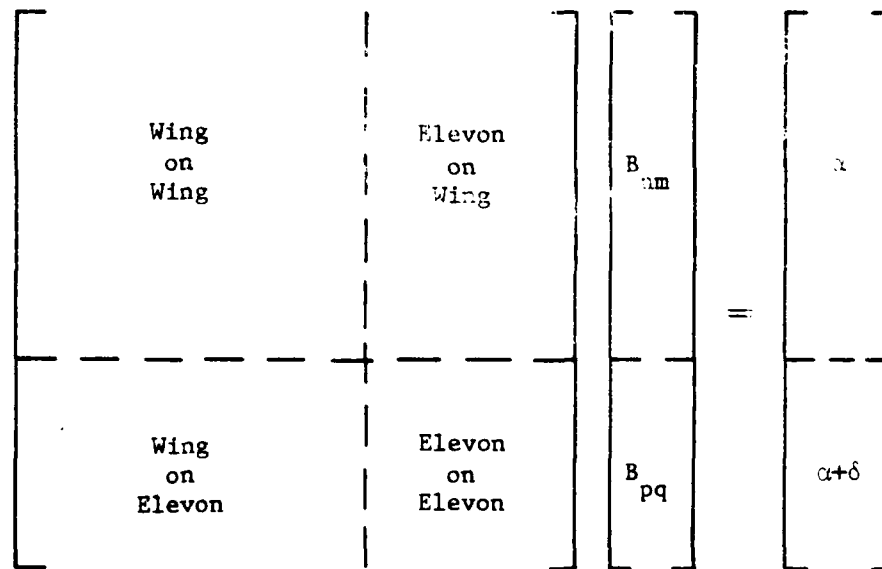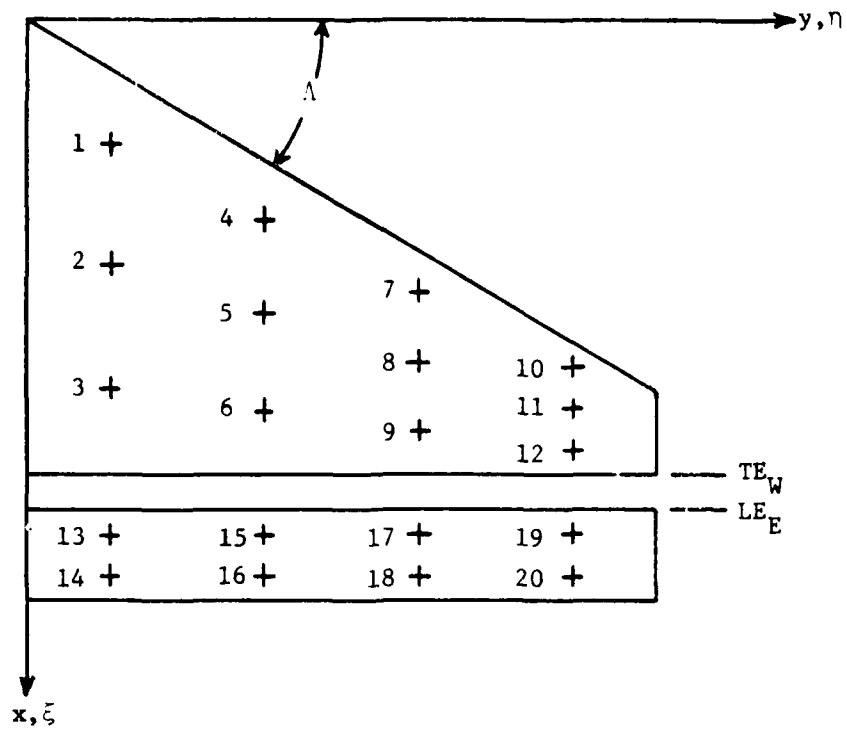$$L = \int_{y=-b/2}^{y=b/2} \int_{x=x_{LE}}^{x=x_{TE}} \Delta P \; dx \; dy \tag{12}$$

Figure 4. Control Point Location and Corresponding
Matrix for Wing-Gap-Elevon Configuration.

Separating eq. (12) into the contributions for the wing and elevon, and

using the definition for the pressure coefficient, the above equation

becomes

$$L = q \int_{-b/2}^{b/2} \left[\int_{x_{LE_W}}^{x_{TE_W}} \Delta C_{P_W} dx_W + \int_{x_{LE_E}}^{x_{TE_E}} \Delta C_{P_E} dx_E \right] dy \qquad (13)$$

It is convenient to define the sectional lift coefficient as

$$cc_\ell = \int_{LE}^{TE} \Delta C_P \, dx \qquad (14)$$

Considering the sectional lift for the entire configuration to be

$$cc_\ell(y_o) = cc_{\ell_W}(y_o) + cc_{\ell_E}(y_o) \qquad (15)$$

the lift becomes

$$L = q \int_{-b/2}^{b/2} cc_\ell(y_o) \, dy \qquad (16)$$

where

$$cc_\ell(y_o) = \int_{x_{LE_W}}^{x_{TE_W}} \Delta C_{P_W} dx_W + \int_{x_{LE_E}}^{x_{TE_E}} \Delta C_{P_E} dx_E \qquad (17)$$

Combining eqs. (9) and (10), the dimensionless chordwise variable can

be defined by

$$\xi_W = \frac{x - x_{LE_W}(y)}{c_{W_T}(y)} \quad , \quad \xi_E = \frac{x - x_{LE_E}(y)}{c_E(y)} \qquad (18)$$

where

$$c_{W_T} = \begin{cases} c_W & \text{, gap case} \\ c_W + c_E, & \text{gap-sealed case} \end{cases}$$

With these definitions, the sectional lift becomes

$$cc_\ell(y_o) = \int_0^{TE_W} \Delta C_{P_W}(\xi_W,\eta) c_{W_T}\, d\xi_W + \int_0^1 \Delta C_{P_E}(\xi_E,\eta) c_E\, d\xi_E \qquad (19)$$

Using eq. (3) for the pressure distribution, the integration of eq. (19) may be performed as in Reference 15 to give

$$cc_\ell(y_o) = \sum_{n=0}^{N_W} \sum_{m=0}^{M} I_n\, B_{nm}\, \sin(2m+1)\theta$$

$$+ \sum_{p=0}^{N_E} \sum_{q=0}^{M} I_p\, B_{pq}\, \sin(2q+1)\theta \qquad (20)$$

where B_{nm} represents the pressure loading coefficients obtained from eq. (11) corresponding to the wing loading, and B_{pq} represents the coefficients of the elevon loading. Also, in eq. (20) for the wing

$$I_0 = \frac{\pi}{4} + \sqrt{\xi_{TE_W} - \xi_{TE_W}^2} + \frac{1}{2}\sin^{-1}(2\xi_{TE_W} - 1) \qquad (21)$$

and

$$I_n = \frac{1}{n+1}\left[\frac{2n-1}{2} I_{n-1} - \xi_{TE_W}^{n-2}\left(\xi_{TE_W} - \xi_{TE_W}^2\right)^{3/2} \right], \quad n=1,2,\ldots N_W \qquad (22)$$

and for the elevon

$$I_0 = \frac{\pi}{2} \qquad (23)$$

and

$$I_p = \frac{2p-1}{2(p+1)} I_{p-1}, \qquad p = 1,2,\ldots N_E \qquad (24)$$

Note that for the gap case, $\xi_{TE_W} = 1$, and eqs. (21) and (22) reduce to eqs. (23) and (24) with n instead of p.

Returning to eq. (16) and using the dimensionless spanwise variable, η, of eq. (2), the total lift is

$$L = q \int_{-1}^{1} cc_\ell(\eta) \, d\eta \tag{25}$$

With the definition of the lift coefficient, and for a symmetric wing, eq. (25) becomes

$$C_L = \frac{2}{S} \int_{0}^{1} cc_\ell(\eta) \, d\eta \tag{26}$$

Similar manipulation of the force equations leads to the total moment about the root chord leading edge (of the wing) as

$$C_M = \frac{2}{S\bar{c}} \int_{0}^{1} c^2 c_m(\eta) \, d\eta \tag{27}$$

with the sectional pitching moment coefficient given by

$$c^2 c_m(\eta) = x_{LE_W} \sum_{n=0}^{N_W} \sum_{m=0}^{M} I_n B_{nm} \sin(2m+1)\theta$$

$$+ c_{W_T} \sum_{n=0}^{N_W} \sum_{m=0}^{M} I_{n+1} B_{nm} \sin(2m+1)\theta$$

$$+ x_{LE_E} \sum_{p=0}^{N_E} \sum_{q=0}^{M} I_p B_{pq} \sin(2q+1)\theta$$

$$+ c_E \sum_{p=0}^{N_E} \sum_{q=0}^{M} I_{p+1} B_{pq} \sin(2q+1)\theta \tag{28}$$

where the first two terms are seen to be the moment due to the wing, and the last two are the moment due to the elevon.

For the wing alone, the integration of the lift and moment equations is performed analytically in closed form. However, because of the discontinuity resulting from the addition of an elevon, eqs. (26) and (27) must be integrated numerically when a gap exists or the elevon is deflected.

In defining the lift and moment coefficients for the entire configuration, the reference area, S, is the total surface area of the wing and elevon combined, excluding the gap area. Similarly, the reference length in the moment coefficient equation is the mean aerodynamic chord, $\bar{c}$, of the wing and elevon, without considering gap distance.

Elevon Hinge Moments

When an elevon is included in the configuration, elevon hinge moments are important in determining control forces for the vehicle. For a straight elevon leading edge with the hinge line located at the leading edge, the total elevon hinge moment is

$$M_H = qb \int_{-1}^{1} c^2 c_{m_H}(\eta) d\eta \tag{29}$$

where the sectional hinge moment coefficient is defined as

$$c^2 c_{m_H}(\eta) = c_E^2 \int_0^1 \Delta C_{P_E}(\xi_E, \eta) \xi_E \, d\xi_E \tag{30}$$

Writing eq. (29) in terms of the moment coefficient and for a symmetric wing, it becomes

$$C_H = \frac{2}{S_E \bar{c}_E} \int_0^1 c^2 c_{m_H}(\eta) \, d\eta \tag{31}$$

Considering both the wing and elevon contributions of eq. (27) separately, it is noted that eq. (30) is the elevon moment about the elevon leading edge, the solution of which is given by the last term of eq. (28), or

$$c^2 c_{m_H} = c_E \sum_{p=0}^{N_E} \sum_{q=0}^{M} I_{p+1} B_{pq} \sin(2q+1)\theta \qquad (32)$$

Substituting eq. (32) into eq. (31), the integration may be evaluated in closed form (Reference 14) to obtain

$$C_H = -\frac{2c_{R_E}}{S_E \bar{c}_E} \frac{\pi}{4} \sum_{p=0}^{N_E} B_{p1} I_{p+1} + \frac{c_{R_E} - c_{T_E}}{c_E \bar{c}_E} \sum_{p=0}^{N_E} \sum_{q=0}^{M} B_{pq} I_{p+1} G_q \qquad (33)$$

where

$$G_q = \int_0^{\pi/2} \sin 2\theta \, \sin(2q+1)\theta \, d\theta \qquad (34)$$

For the elevon hinge moments, the reference area, S_E, is the total area of the elevon. Also, the reference length, $\bar{c}_E$, is the mean aerodynamic chord of the elevon.

Thus far, the analysis has been limited to a hinge line at the elevon leading edge. If the elevon lift is also known, the lift and moment produce a couple at the elevon leading edge. The moment about any chordwise station may be found by summing moments at that point. This gives

$$M_{HL} = M_{LE} + L_{LE} \, x_{HL} \qquad (35)$$

where x_{HL} is the chordwise location of the hinge line measured from the elevon leading edge. Dividing by $q\, S_E \bar{c}_E$ gives the equation in coefficient form

$$C_{H_{HL}} = C_H + C_{L_E}\, \frac{x_{HL}}{\bar{c}_F} \qquad (36)$$

where C_H is given by eqs. (33) and (34).

The total lift for the elevon is

$$C_{L_E} = \frac{2}{S_E} \int_0^1 c c_\ell(\eta)\, d\eta \qquad (37)$$

with the sectional lift of the elevon given by

$$c c_{\ell_E}(\eta) = c_E \int_0^1 \Delta C_{P_E}(\xi_E, \eta)\, d\xi_E \qquad (38)$$

It is readily seen that this is the second integral in eq. (19) and the solution is given by the last term of eq. (20); thus

$$c c_{\ell_E}(\eta) = \sum_{p=0}^{N_E} \sum_{q=0}^{M} I_p\, B_{pq}\, \sin(2q+1)\theta \qquad (39)$$

where I_p is given by eqs. (23) and (24).

For the elevon, the lift may be obtained in closed form. Substituting eq. (39) into eq. (37), and integrating gives

$$C_{L_E} = \frac{\pi}{2S_E} \sum_{p=0}^{N_E} B_{p0}\, I_p \qquad (40)$$

where, in the loading coefficients B_{pq}, only the $q=0$ term appears.

Thus, using eqs. (40) and (33) in eq. (36), the elevon hinge moment about the hinge line is obtained in closed form. The only requirement

for the analysis is that the hinge line be perpendicular to the wing root chord.

Non-Planar Wings

Lifting surfaces which do not lie entirely in the x-y plane present a different view to the flow field than the planar wing previously considered. To analyze non-planar wings, it is necessary to consider the angle that each control point and each grid element makes with the x-y plane. Non-planar effects of primary interest include wing twist, cambered airfoils, and arbitrary chordwise and spanwise deformations.

For the case of wing twist, at any given spanwise location on the wing, the chord line lies in a plane that differs from the initial x-y plane by the twist angle, α_{TW}, at that station. This angle may be included in the boundary condition such that eq. (6) becomes:

$$w(x_i,y_j) + \sin [\alpha(x_i,y_j) + \alpha_{TW} (x_i,y_j)] = 0 \tag{41}$$

The boundary condition for the elevon, eq. (11), may be rewritten in a similar manner.

For cambered or arbitrarily deformed airfoils, the chord line may be replaced by the mean camber line. The downwash produced by each grid element is proportional to the angle which that element makes with the x-axis, or

$$\Delta w(x_i,y_j) = \Delta w(x_i,y_j) \cos\alpha_i \tag{42}$$

where α_i is the angle relative to the x-axis and is given by

$$\alpha_i = \tan^{-1} (\frac{dz}{dx})\bigg|_{x_i} \tag{43}$$

This is the velocity component in the z-direction; however, each control

point also has a z-coordinate. The boundary condition is for no flow

through the wing, or that the normal component of velocity to the wing

be zero. The angle that the control point makes with the x-axis is

given by

$$\alpha_c = \tan^{-1}\left(\frac{dz}{dx}\right)\Bigg|_{x_c} \tag{44}$$

Thus the component of velocity normal to the wing is

$$\Delta w(x_i, y_j) = \Delta w(x_i, y_j)\cos\alpha_c \tag{45}$$

It should be noted that the boundary condition of the deformed wing is

satisfied on the x-axis, although the coordinate of the mean line lies

off the axis; however, this is equivalent to the planar wing approxi-

mation essential to thin airfoil theory. The actual normalwash is found

by combining equations (42) and (45)

$$\Delta w(x_i, y_j) = \Delta w(x_i, y_j)\cos(\alpha_i - \alpha_c) \tag{46}$$

By defining a function $z(x)$ many variations and amplitudes of camber

and wing deformation in the chordwise direction may be obtained. Com-

binations of twist and camber or deformation may also be analyzed. How-

ever, the condition of no flow separation still applies at all points.

Interference Effects

In the present analysis, interference effects, such as fuselage per-

turbations and leading edge suction, are also included. An infinite

line doublet is used to simulate fuselage interference effects on the

induced velocity over the wing. The potential equation for the line

doublet may be differentiated to determine the velocity component normal to the plane of the wing. To calculate the lift and moment of a fuselage in the presence of a wing, an image wing inside the fuselage is employed. The sectional characteristics of the actual wing are integrated over the image wing span to determine the lift and moment. Both of these principles are well known and the theoretical development can be found in Reference 22.

Leading edge suction, which makes a significant contribution to the lift of highly swept wings at large angles of attack, has also been incorporated into the present theory. Purvis (Ref. 23) has shown that, for an assumed pressure distribution in the form of eq. (3), and for an elliptic spanwise lift distribution, a general, closed form solution for the leading edge suction is

$$C_{L_{VLE}} = (C_{L_p} \sin\alpha - \frac{C_{L_p}^2}{\pi AR} \cos\alpha) \frac{\cos\alpha}{\cos\Lambda} \tag{47}$$

where C_{L_p} represents the potential flow lift coefficient, which is given by eq. (26). Also, from Reference 23, the moment may be written as

$$C_{M_{VLE}} = \frac{2.212072\ C_{L_p}}{c\ b\ \cos\lambda} \sin\alpha - \frac{C_{L_p}}{\pi AR} \cos\alpha \int_0^{b/2} x_{LE}[\eta\sqrt{1-\eta^2} + \sin^{-1}(\eta)]dy \tag{48}$$

Using the definition of η in eq. (2) gives

$$C_{M_{VLE}} = \frac{1.10603 C_{L_p}}{\bar{c}\ \cos\lambda} \sin\alpha - \frac{C_{L_p}}{\pi AR} \cos\alpha \int_0^1 x_{LE}[\eta\sqrt{1-\eta^2} + \sin^{-1}(\eta)]d\eta \tag{49}$$

For a constant leading edge sweep angle, this integral may be evaluated in closed form. The coordinate of the leading edge is given by

$$x_{LE} = \eta \cos\Lambda$$

therefore, eq. (49) becomes

$$C_{M_{VLE}} = \frac{1.106036 C_{L_p}}{\bar{c}} (\frac{\tan\Lambda}{\cos\Lambda})[\sin\alpha - \frac{C_{L_p}}{\pi AR} \cos\alpha] \int_0^1 [\eta^2\sqrt{1-\eta^2} + \eta \sin^{-1}(\eta)]dy \qquad (50)$$

Integration produces

$$C_{M_{VLE}} = \frac{0.65151}{\bar{c}} [C_{L_p} \sin\alpha - \frac{C_{L_p}}{\pi AR} \cos\alpha](\frac{\tan\Lambda}{\cos\Lambda}) \qquad (51)$$

Since the current gap analysis assumes small gaps such that there is no vortex rollup, interference effects will be confined to the fuselage and leading edge suction. These correction terms are necessary to allow a comparison between theory and experiment in many instances; therefore, by including them, a more versatile analysis is obtained.

Order of Polynomials

Before proceeding, comments on the effect of polynomial order on the solution is in order. The unknown constants, B_{nm} in eq. (3) are really coefficients for the various terms in the polynomial describing the pressure loading on the wing. It has been suggested that if the polynomial order is increased to a large number of terms (i.e., $>$ 50) that the sectional coefficients such as cc_ℓ will tend to "oscillate" in the spanwise direction. For the formulation used in the present analysis, no oscillations are observable at least up to 50 terms in the equation. However, oscillations do indeed occur if terms on the order of 80 or more are used in the pressure loading. It does not appear that this is due to "numerical" instability as would be the case if numerical integration were used, but rather due to overkill. That is, the pressure loading function is rather general and for most wings only a few terms ($<$ 20) are

required for a solution   If more terms are used, it is analogous to fitting a 50th degree polynomial to a linear curve; oscillations are the inevitable results.

III. EXPERIMENTAL MODEL AND TESTS - SUBSONIC

Model

To verify the gap effects and subsequent elevon loading, an experimental model shown in Fig. 5 was fabricated and tested in a low speed wind tunnel.[24] The baseline configuration consisted of a thin, low-aspect ratio, cropped delta wing with rectangular elevons. These surfaces were symmetrical about both the chord line and the fuselage centerline. The fuselage was included to facilitate mounting of the hinge moment balance mechanism. An ogive nosecone and tailcone were also included. The fuselage and wing tips were designed to allow for a two-inch translation in the elevon mounting position, which could be used to vary the gap distance and/or the elevon hinge line location. The model was floor-mounted to an external six-component pyramidal balance.

Test Procedures

The model was tested at a dynamic pressure of 3.5 inches of water corresponding to a speed of approximately 126 feet per second and a Reynolds number of 0.76 million per foot.

Data was obtained for an angle of attack range from -19 to +5 degrees in 2-degree increments. The negative range was used to minimize strut interference effects on the elevons. Several elevon deflection angles (0° to 20°), gap distances (0 to 75% c_E) and hinge line locations (0 to 50% c_E) were tested.

All linear dimensions are in inches.
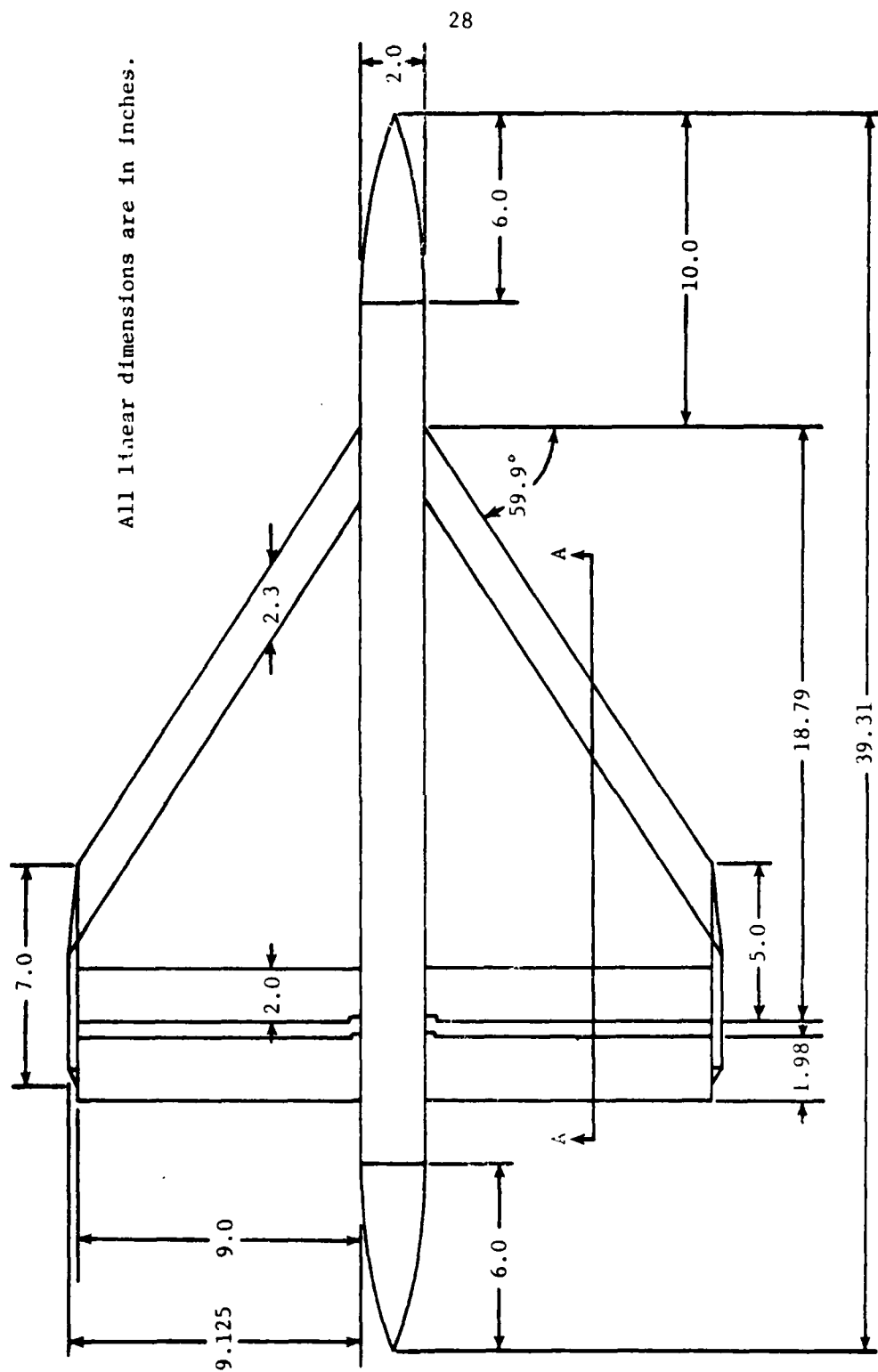
Figure 5. Experimental Model Details.

0.1875

20.25

9.0

2.0

9.0

Front View

1.95°

2.3

0.1875

1.8°

Wing

2.0

0.0625

1.98

0.0625

Elevon
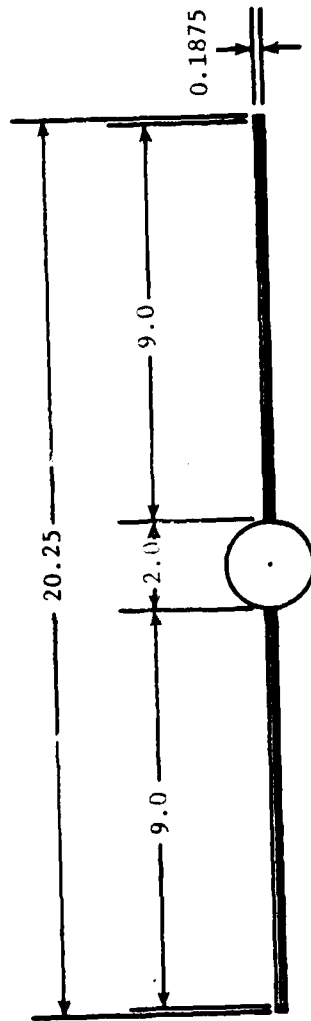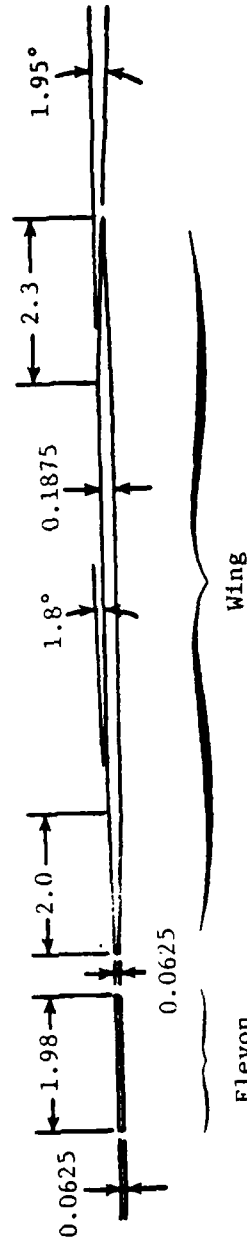
Section A-A

Figure 5.   concluded.

IV. RESULTS - SUBSONIC FLOW

Results for a wing configuration are compared to other well known theories in Figs. 6 and 7. Agreement is good for all cases considered. In obtaining results using the present theory, the wing subpanel mesh of constant loading was 45 by 45 (chordwise by spanwise), and the control point grid was 4 by 4. The total CPU time required was 45 seconds on an IBM 3031 compared to 1 minute for the method of Lan on the Honeywell 635.[8] Storage requirements for the present method are negligible on a large machine. This mesh size may be reduced such that total CPU time is reduced to 20 seconds, with a change in accuracy of approximately 5 percent.

A comparison of theory and experiment for the "base" configuration of the wing-fuselage model is presented in Fig. 8. Both linear theory and leading edge suction are included. The importance of the nonlinearity introduced by leading edge suction in the high angle of attack region is easily realized from this figure.

The theoretical pressure distribution for a deflected elevon is compared with experimental data (from Ref. 25) in Fig. 9. From this figure, it is seen that the assumed functional form for the chordwise pressure distribution for the sealed-gap case represents an adequate model of the actual flow. Total lift and hinge moments are presented in Fig. 10 where agreement is good, particularly in the low angle of attack regime.

The analysis developed for the general case of deformed wings, elevons, gap, and fuselage is used to predict the lift, pitching moment,
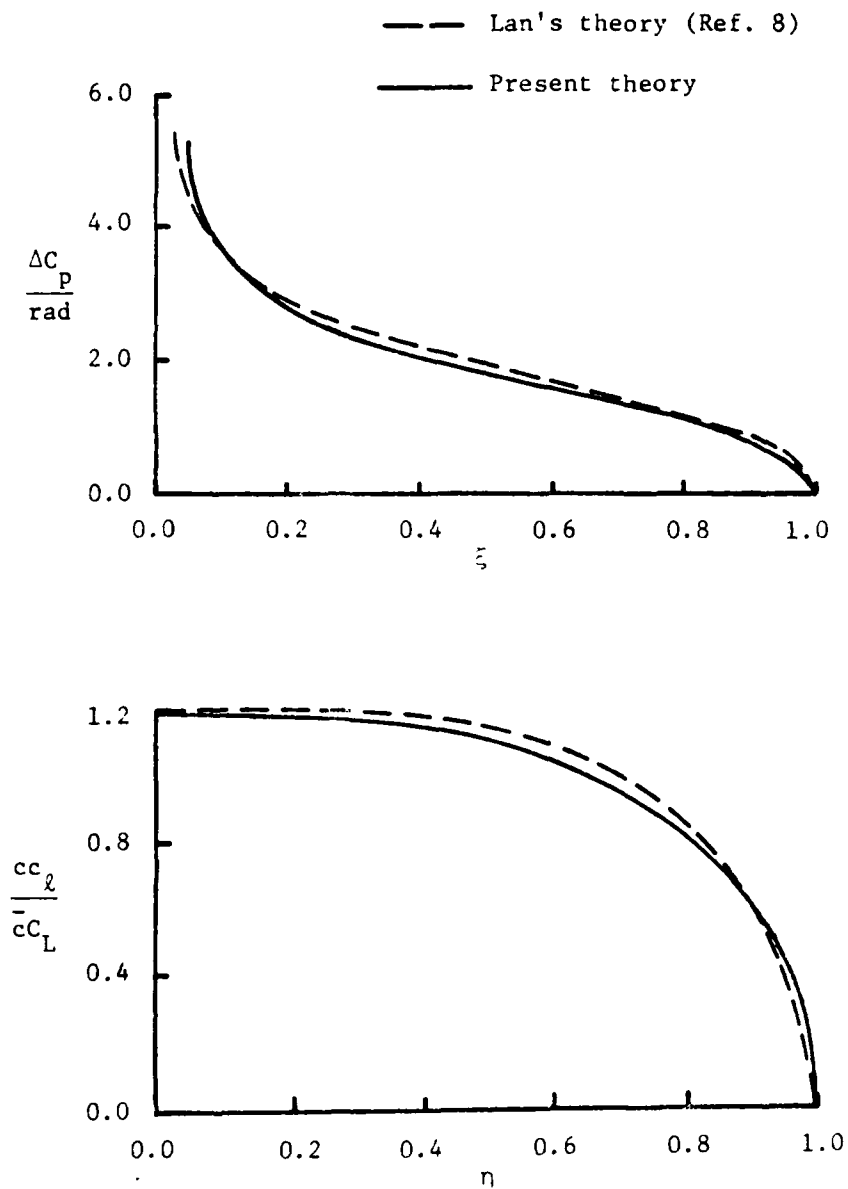
Figure 6. Comparison of Two Theories for a
Swept and Tapered Wing of Aspect
Ratio 2.828.
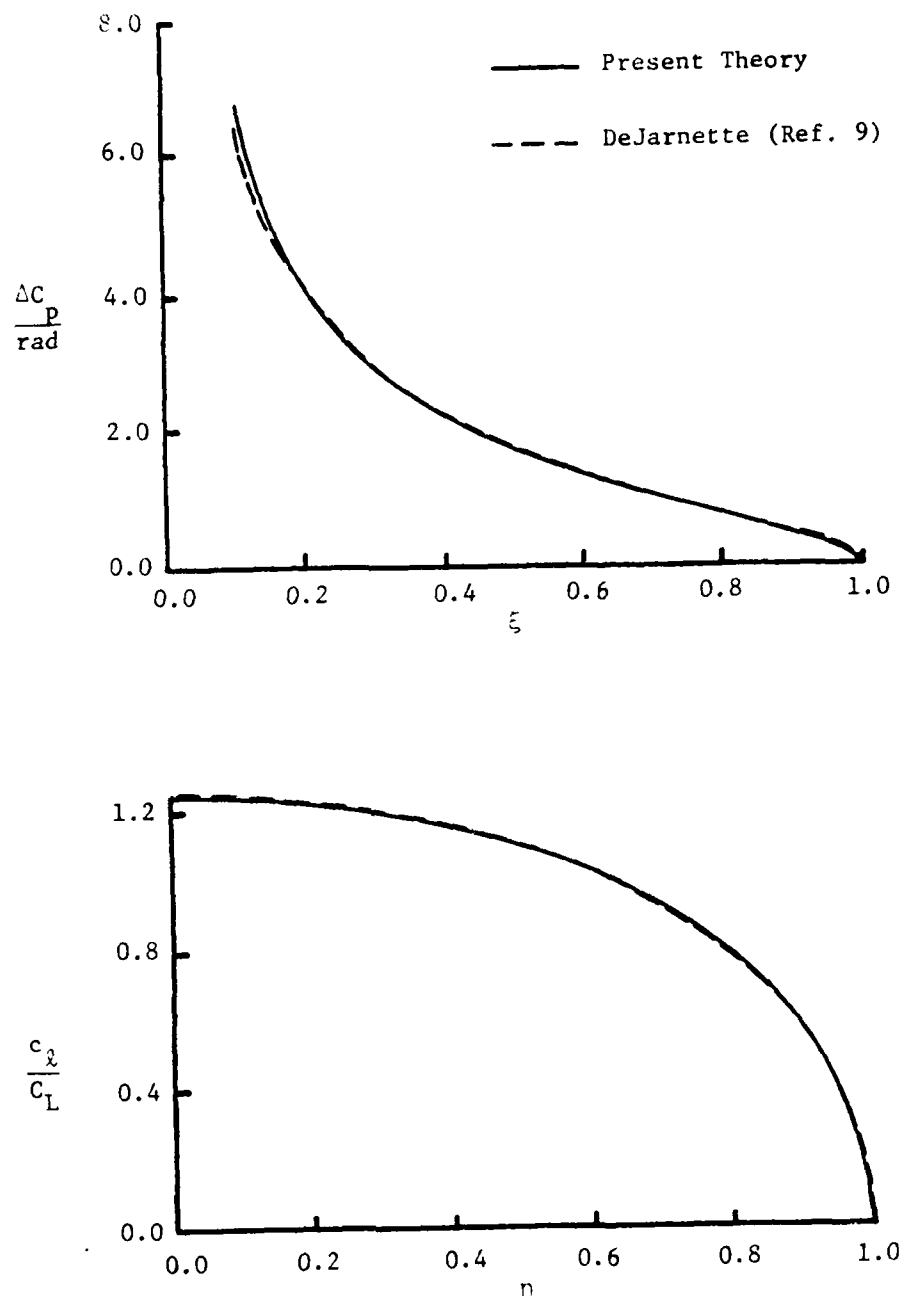
Figure 7. Comparison of Two Theories for a Rectangular
Wing of Aspect Ratio 2.
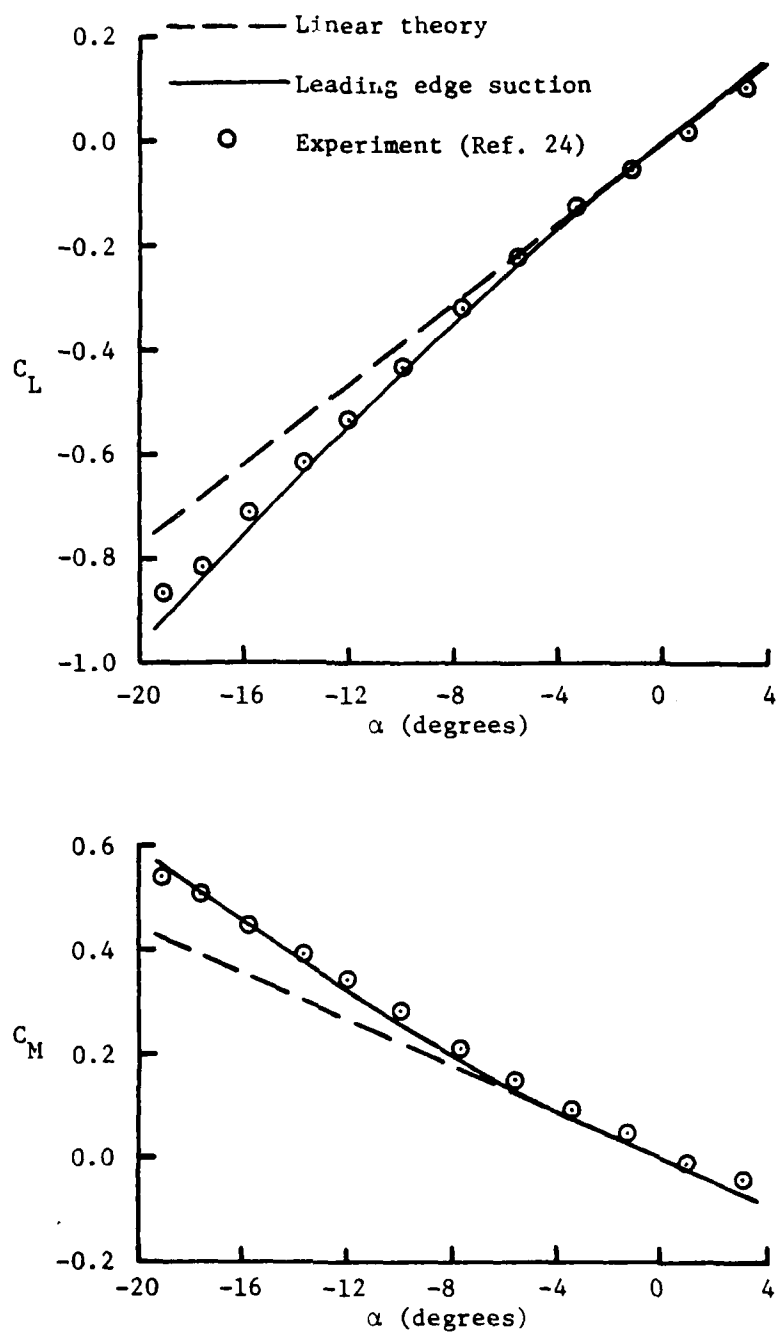
Figure 8. Leading Edge Suction on a Highly Swept
Cropped Delta Wing with a Fuselage.
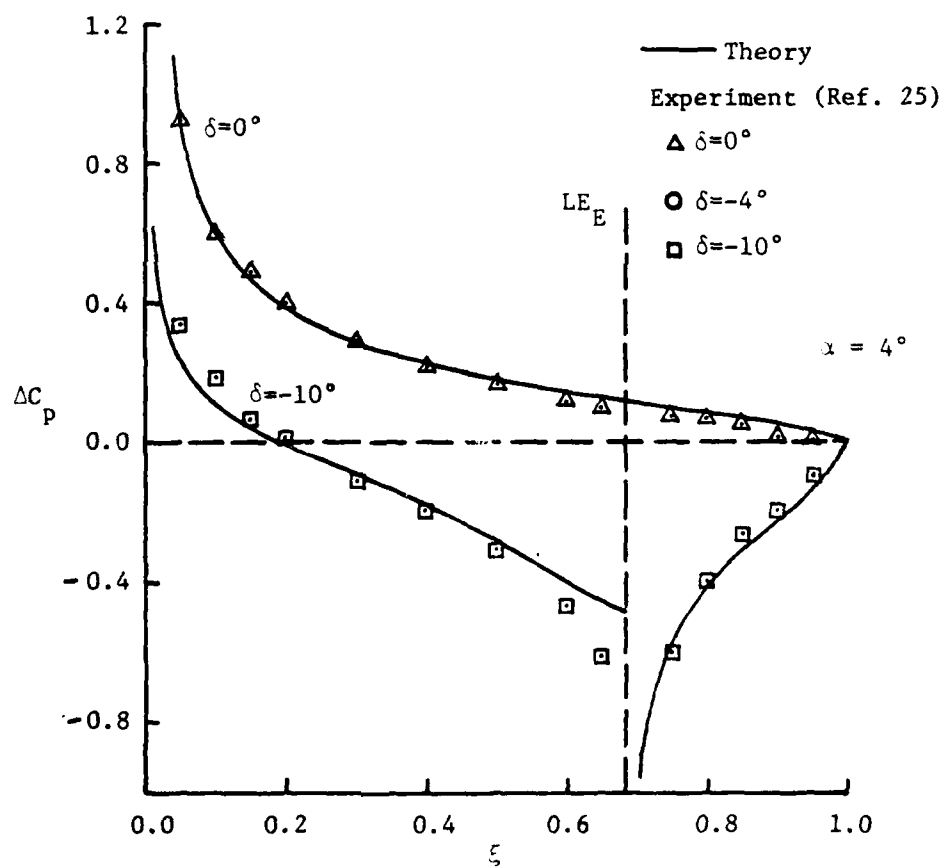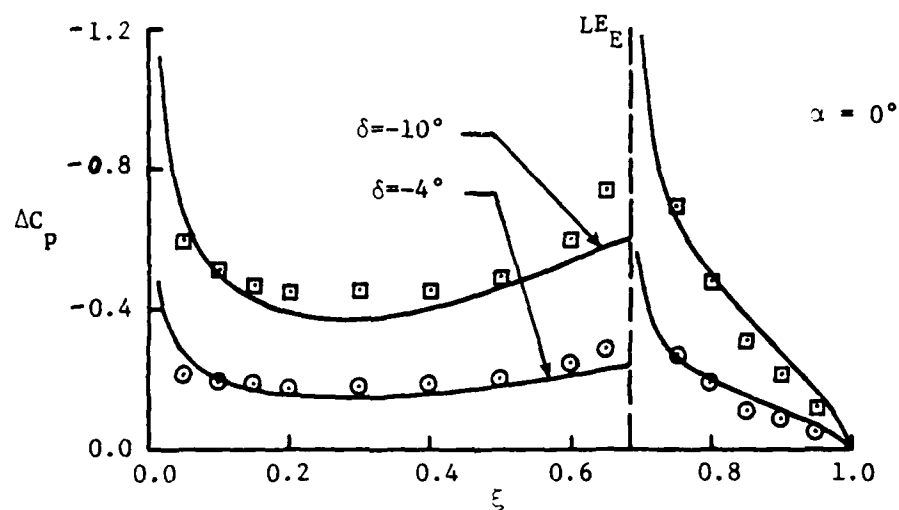
Figure 9. Chordwise Loading with a Deflected
Elevon at $\eta = 0.5$.
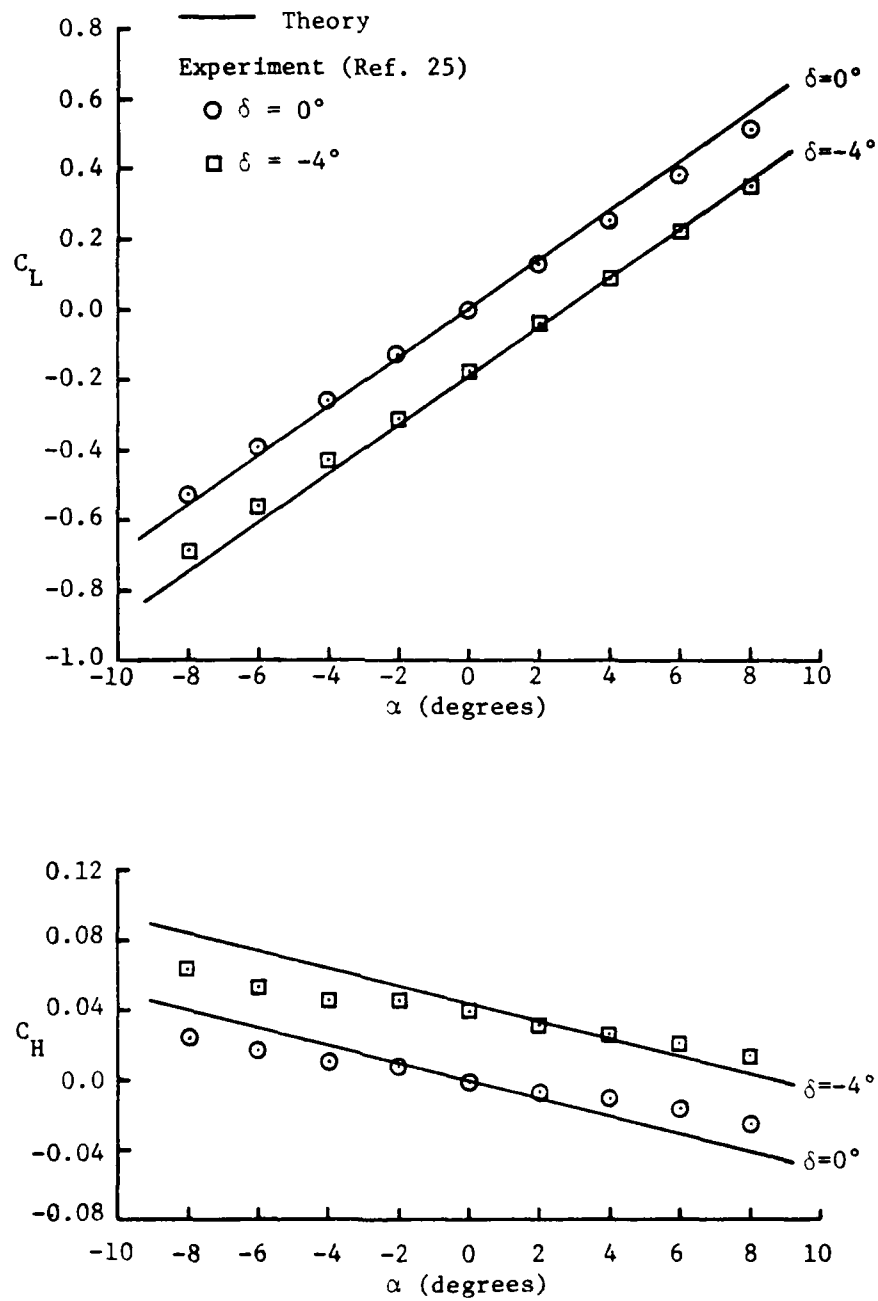
Figure 10. Lift and Hinge Moments for a
Wing-Elevon Configuration.

and hinge moment slopes for the model tested in the low speed tunnel and is shown as a function of gap distance in Fig. 11.

Certainly the most interesting trend with respect to the gap is that, for all cases, hinge moments increase slightly as gap distance increases. It is also noted from Fig. 11 that the coefficient slopes vary more noticeably with changes in elevon deflection while the changes with angle of attack are essentially negligible. Figure 12 illustrates the theoretical spanwise pressure distribution over the wing and elevon for the present cropped delta wing configuration. This figure confirms the predicted increase in the loading over the elevon, and shows the slight loading change with respect to angle of attack. This loading form is in agreement with the two-dimensional results obtained by White, et al,[12] as well as the present experimental data. In Fig. 13, the hinge moments are presented for several hinge line locations on the elevon. It is seen here that there is a chordwise point, in this case between 15 and 20 percent of the elevon mean aerodynamic chord, where the hinge moments are independent of gap distance. It is noted that this point does not coincide with $C_{H_\delta} = 0$, which gives the elevon aerodynamic center. This aspect could be significant in the design of variable geometry wings where gap distances are subject to change. Also the minimum value of the hinge moment, which corresponds to minimum control forces, occurs for the sealed-gap case.

The slopes of the pitching moments curves illustrated in Fig. 11 are seen to be essentially constant in nature. Since the moment is referenced to a fixed point on the wing, the increase in the moment arm with increasing gap coupled with increased elevon loading might tend to suggest an
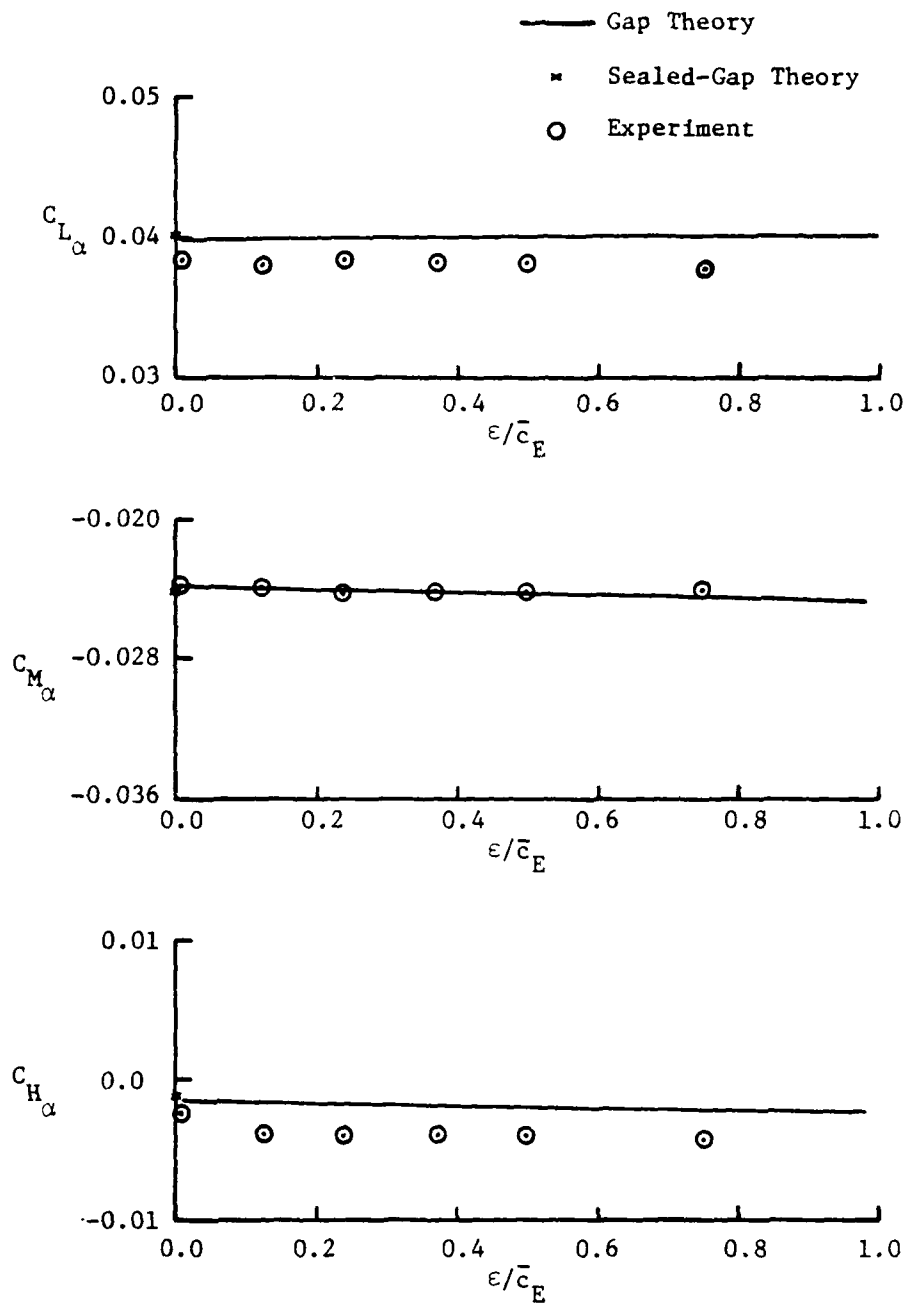
Figure 11. Aerodynamic Characteristics for a
Gapped Configuration.
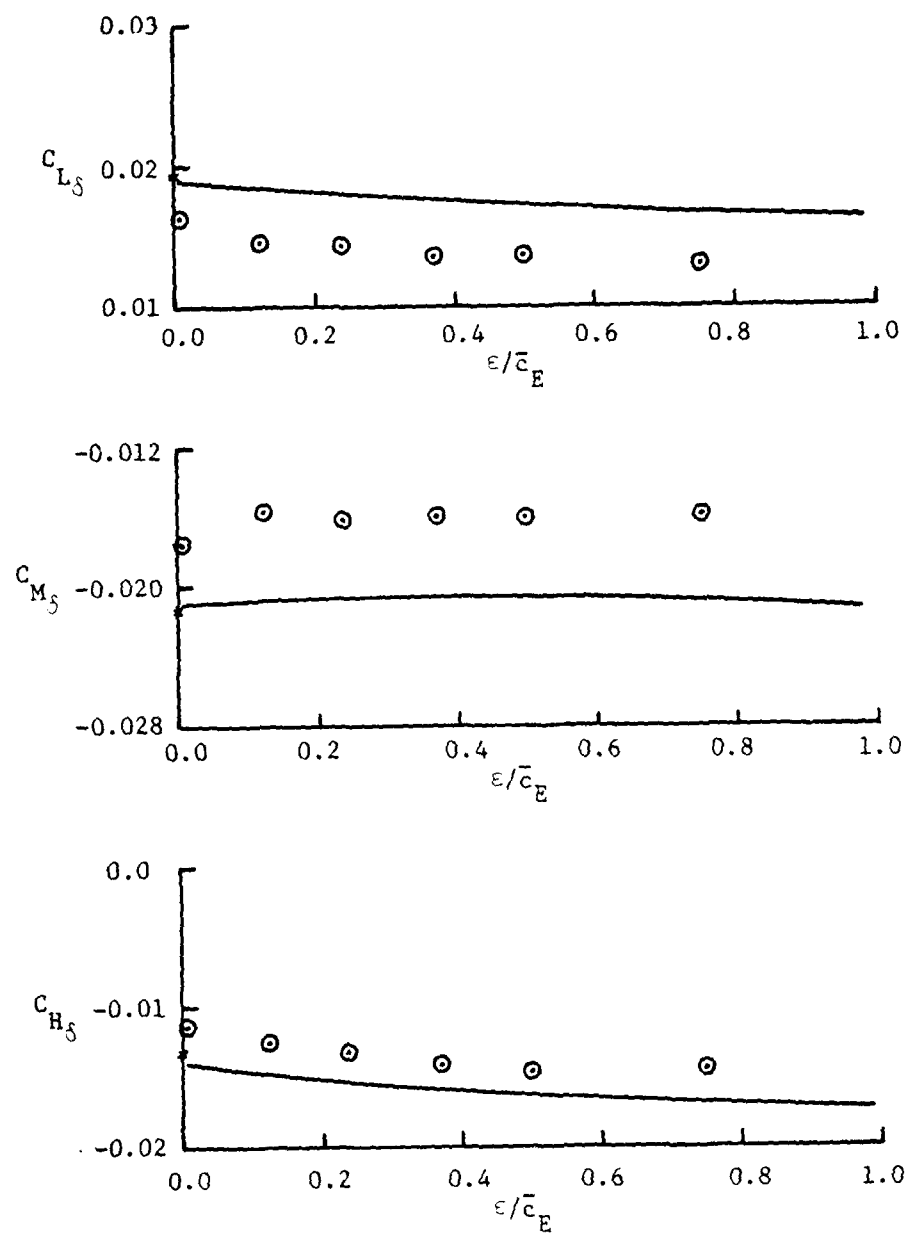
Figure 11. concluded
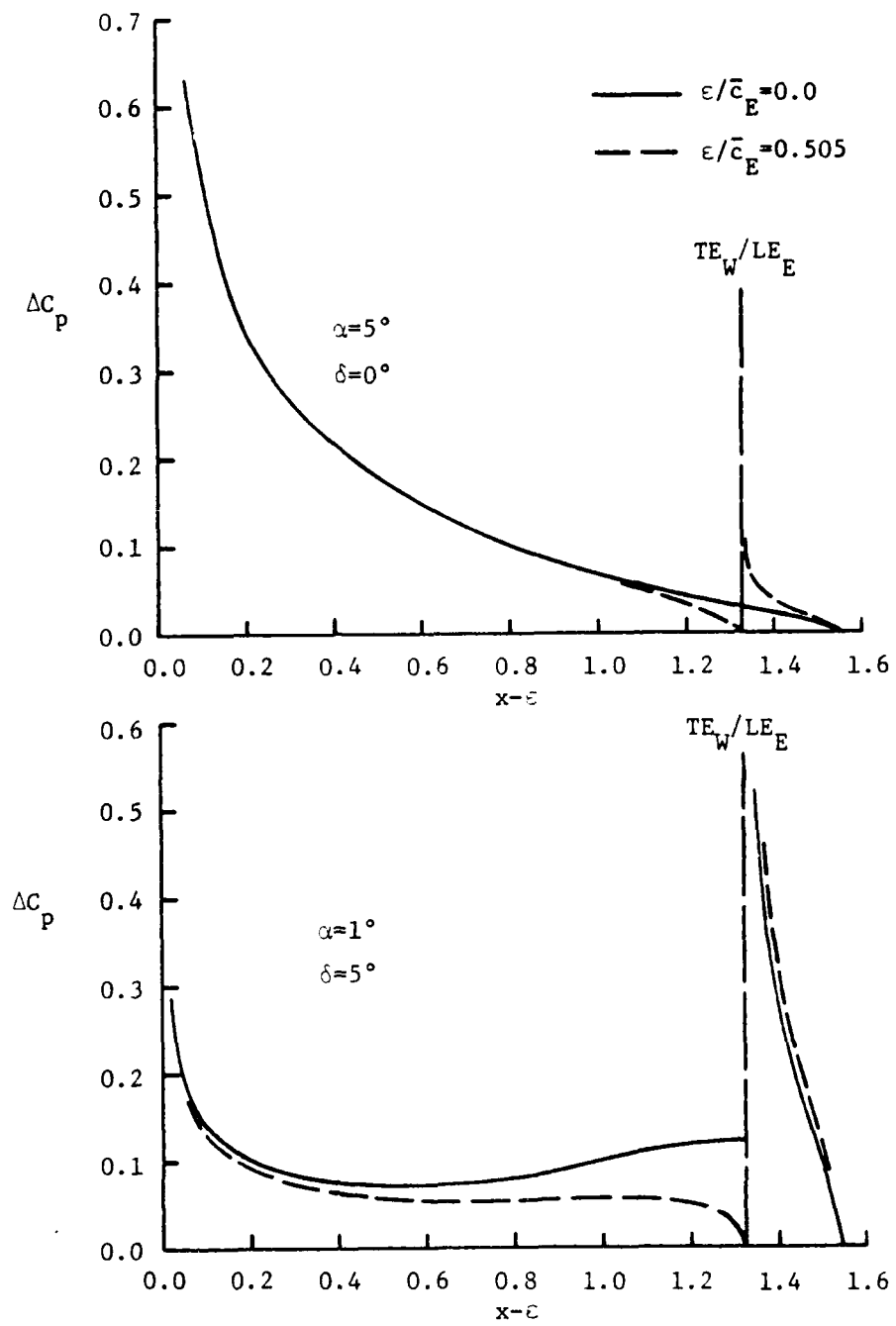
Figure 12. Gap Effects on Chordwise Load
Distribution.
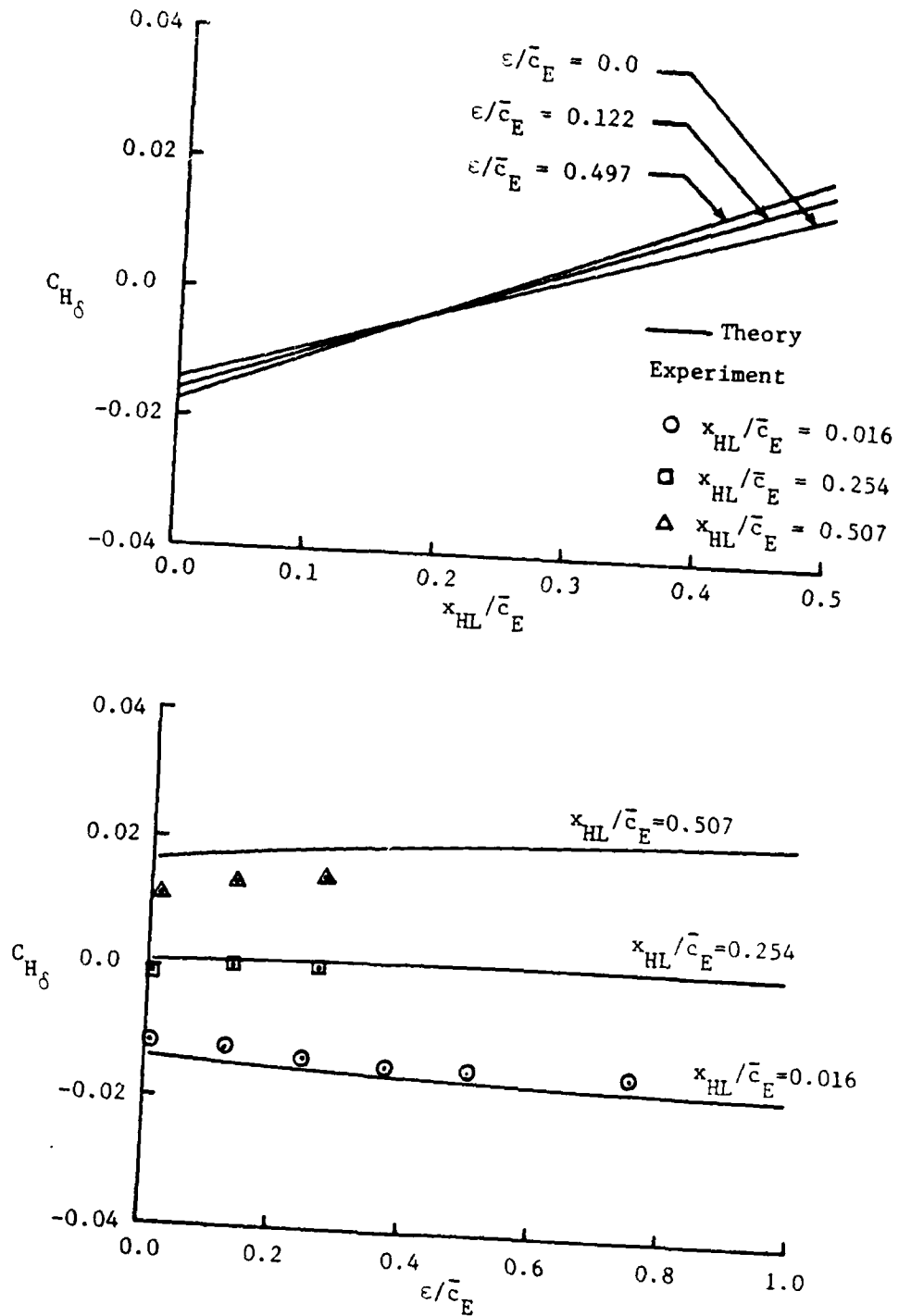
Figure 13. Elevon Hinge Moments for Several
Hinge Line Locations.

increase in the moment. However, from Fig. 12 it can be seen that the change in pressure distribution more than offsets these factors. Yet, as the gap becomes large, the theoretical pressure distribution must approach that of two separate wings, without interference. The moment referred to a fixed point on the wing must become infinitely large as the gap distance approaches infinity.

For large gaps, it was found experimentally (Figs. 14 and 15) that there is a considerable increase in the total lift and moment for an elevon deflection of -20°. The decrease in the forces becomes larger with increasing gap distance. However, elevon hinge moments did not reflect this trend, indicating that it is due more to the gap rather than to flow separation over the elevon. In any case, it is apparently a viscous phenomena and cannot be modeled properly using potential flow techniques.

The experimental data for different hinge lines is presented in Figs. 16 and 17. Theoretically, there are no changes in the total forces and moments with a change in the hinge line. This result also appeared in the experimental data despite the fact that, for a deflected elevon, the elevon leading edge no longer lies in the plane of the wing. From the data in Fig. 16, it is seen that the hinge moments at $x_{HL}/\bar{c}_E = .254$, or approximately the quarter chord of the elevon, are quite small and show little variation with angle-of-attack or elevon deflection. This in-dicates that this point is near the aerodynamic center for the elevon. However, the slopes change with a change in gap distance, thus the aero-dynamic center must also be gap dependent, as previously shown on Fig. 13.
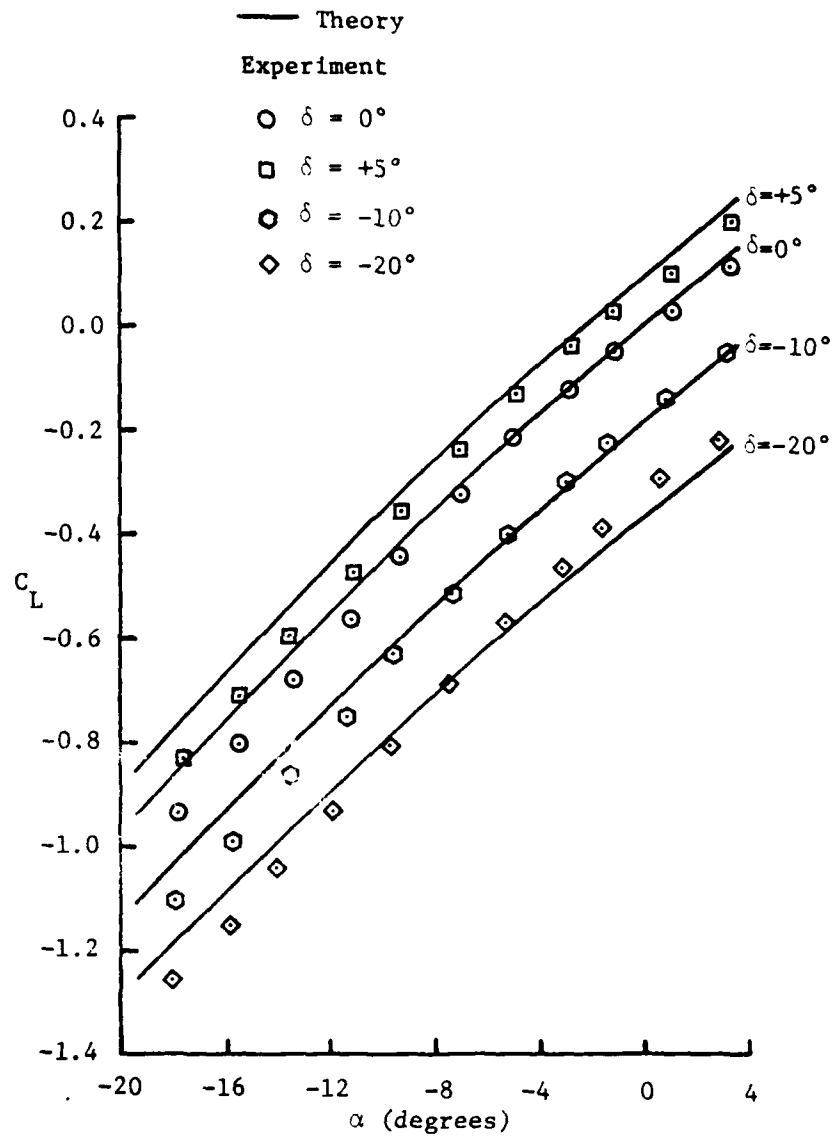
Figure 14. Characteristics of a Wing-Fuselage-Elevon Model for $x_{HL}/\bar{c}_E = 0.016$ and $\varepsilon/\bar{c}_E = 0.004$.
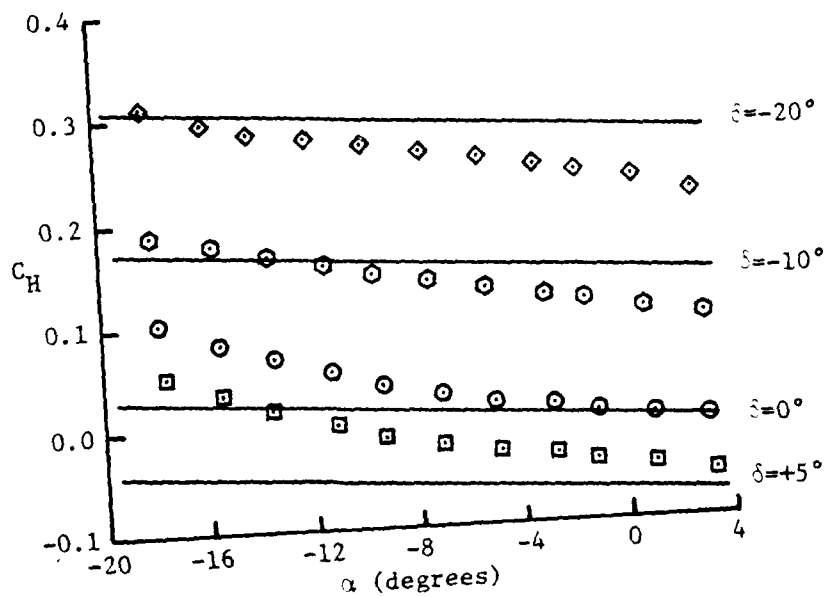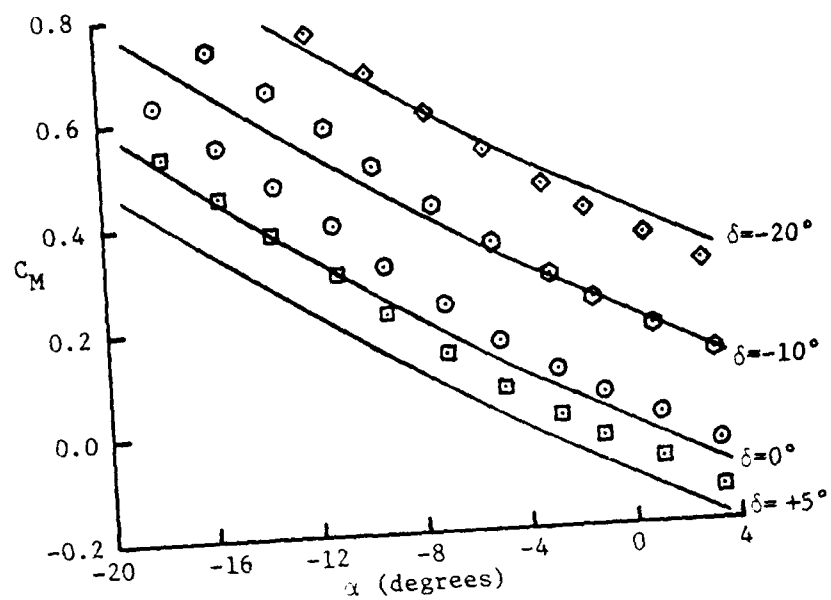
Figure 14. concluded

44
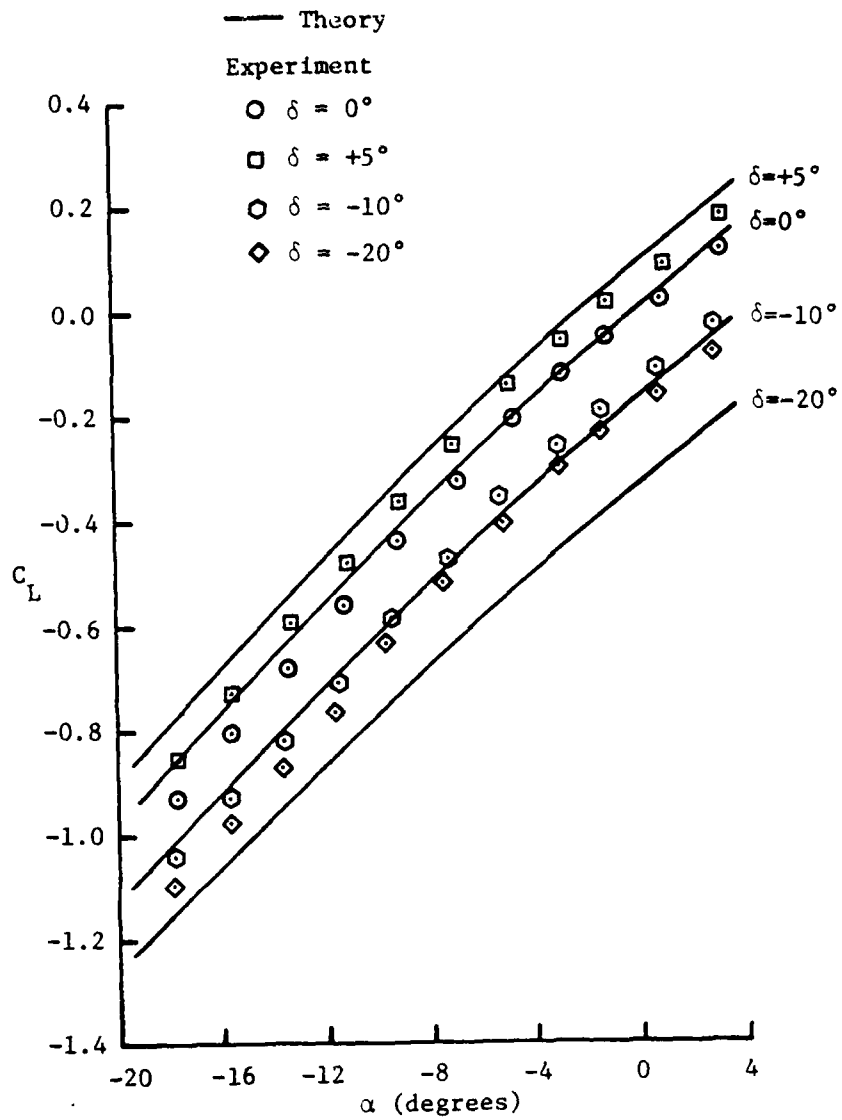
Figure 15.   Characteristics of a Wing-Fuselage-Elevon
Model for $x_{HL}/\bar{c}_E = 0.016$ and $\epsilon/\bar{c}_E = 0.497$.
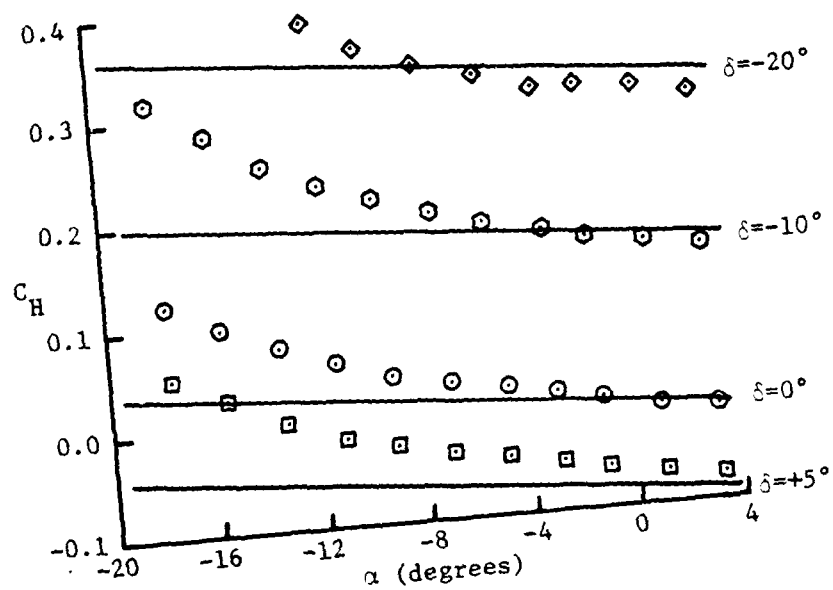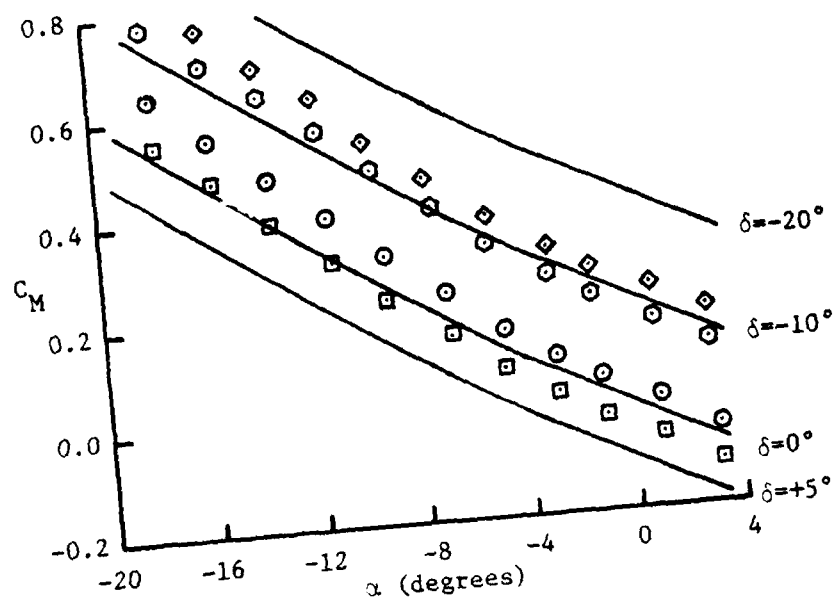
Figure 15. concluded
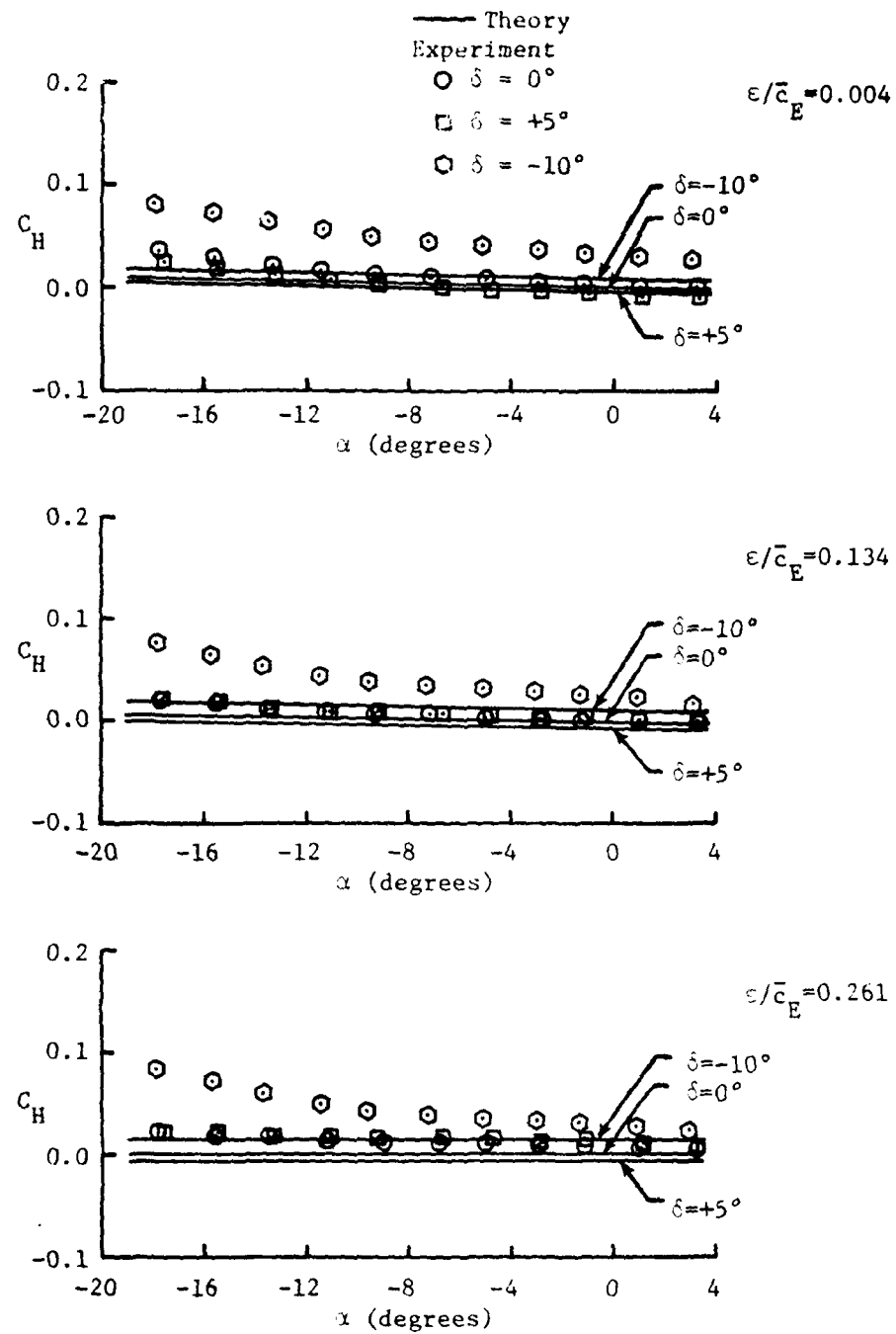
Figure 16. Hinge Moments on a Wing-Fuselage-Elevon Model for $x_{HL}/\bar{c}_E = 0.254$.
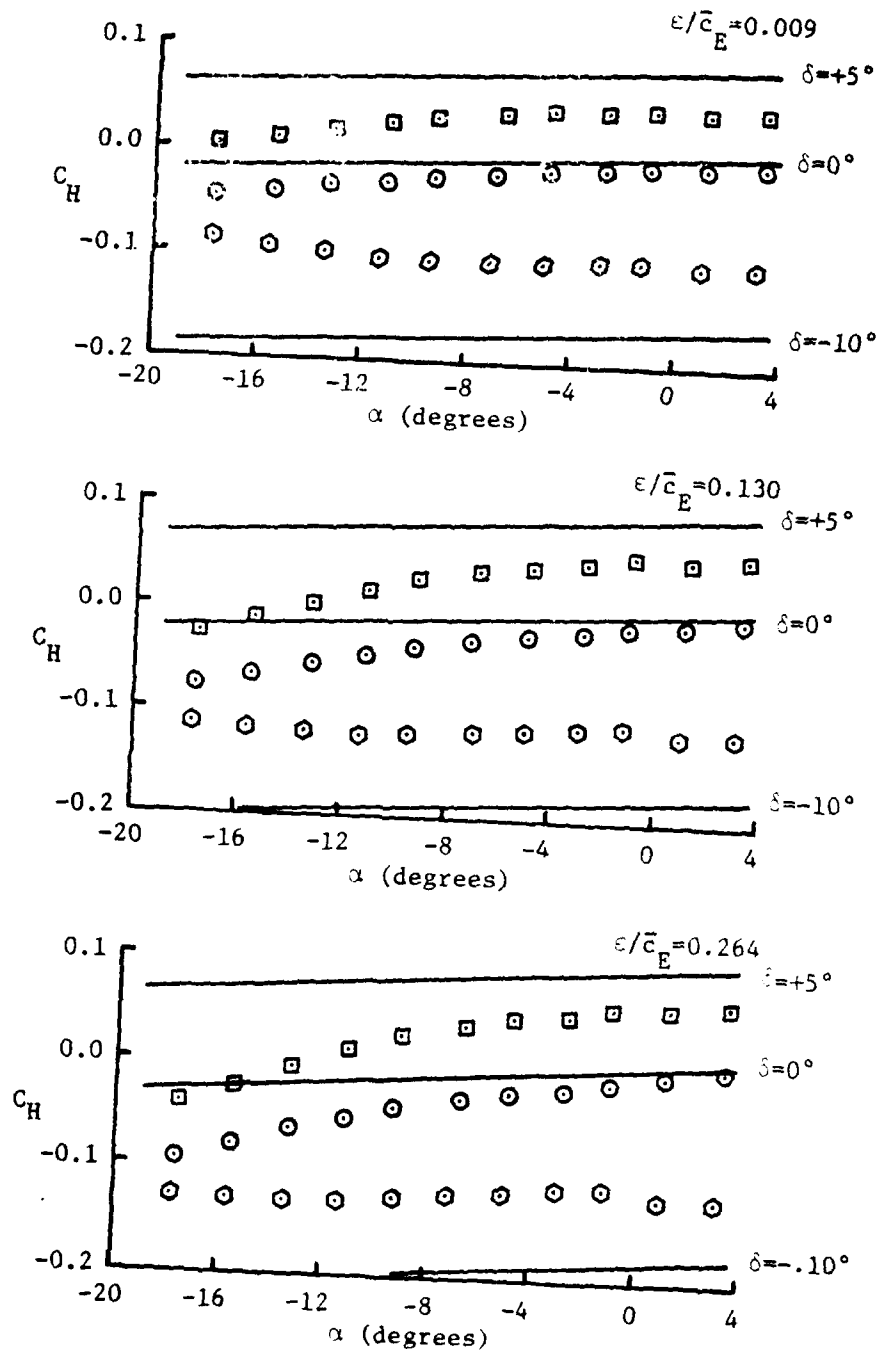
Figure 17.   Hinge Moments of a Wing-Fuselage-
Elevon Model for $x_{HL}/\bar{c}_E = 0.507$.

Results for arbitrarily deformed airfoils are difficult to find in the literature; therefore, perhaps the best basis for comparison is two-dimensional thin airfoil theory. Table 1 illustrates theoretical results for the two arbitrary mean lines shown. The present theory, extended to two-dimensional results and thin airfoil theory show good agreement.

For cambered airfoils, experimental data may be obtained from Ref. 26. Results are presented for the NACA 747A315 laminar flow airfoil in Fig. 18. The current theory predicts experimental data very well. Again, the thin airfoil and present theory are closely matched. This result should be expected since, for two-dimensional flow, the present theory would become thin airfoil theory as the limit of the wing subpanel areas with a constant ΔC_p approached zero.

For a finite wing, Fig. 19 compares theoretical predictions with experimental data (Ref. 27) at several Mach numbers for a wing that is both cambered (NACA 3-1.0 mean camber line) and twisted. It should be noted that the experimental model was tapered and the maximum camber varied with the spanwise coordinate. In the theoretical model the wing was replaced by the mean camber line at each 20 percent of the span and this distribution remained constant for that section. Also, a linear spanwise distribution of twist was assumed, while there was a slight variation from this experimentally. Nontheless, agreement of theory and experiment is very good over the entire experimental Mach number range..

— Present theory
— Thin wing analysis

$\dfrac{\Delta C_\ell}{\Delta x}\Big|\alpha_{OL}$

$\dfrac{\Delta C_\ell}{\Delta x}\Big|\alpha_{OL}$
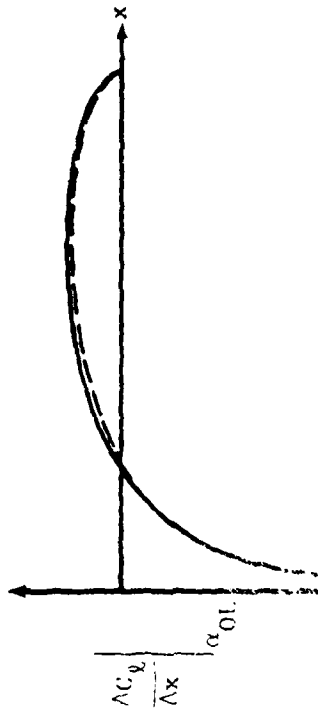
Present

$\alpha_{OL} = -2.244°$

$C_{L_\alpha} = .10702$

Thin Wing

$\alpha_{OL} = -2.292°$

$C_{L_\alpha} = .10966$
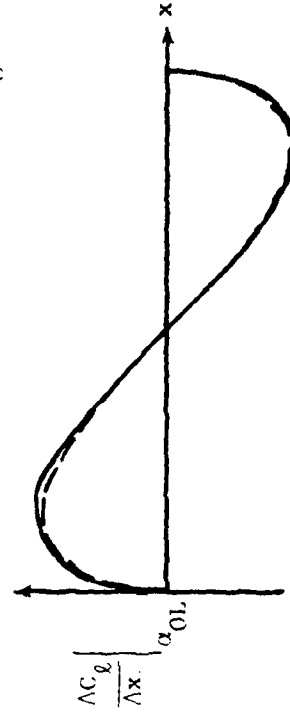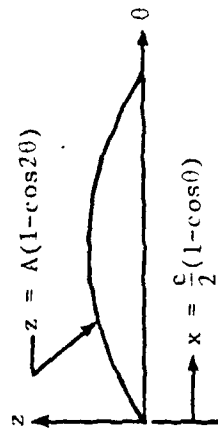
Present

$\alpha_{OL} = 2.30°$

$C_{L_\alpha} = .1079$

Thin Wing

$\alpha_{OL} = 2.292°$

$C_{L_\alpha} = .10966$

$z = A(1-\cos2\theta)$

$x = \dfrac{c}{2}(1-\cos\theta)$

$z = A(\cos\theta-\cos3\theta)$

Table 1. Results for Arbitrary Mean Lines.

——— Present theory

— — — Thin airfoil theory

○ Experiment
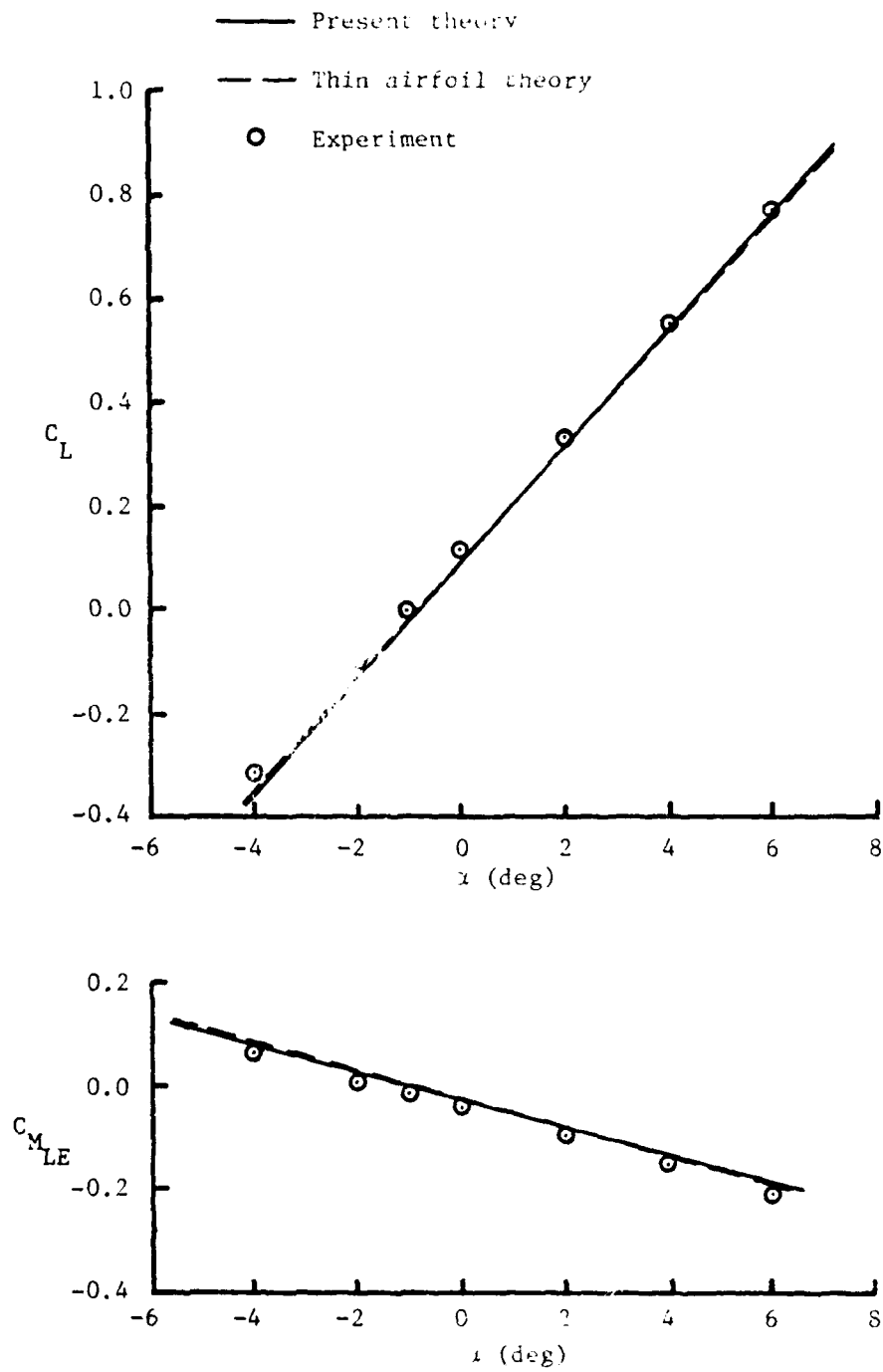
Figure 18. Characteristics of the NACA 747A315
Airfoil Section.
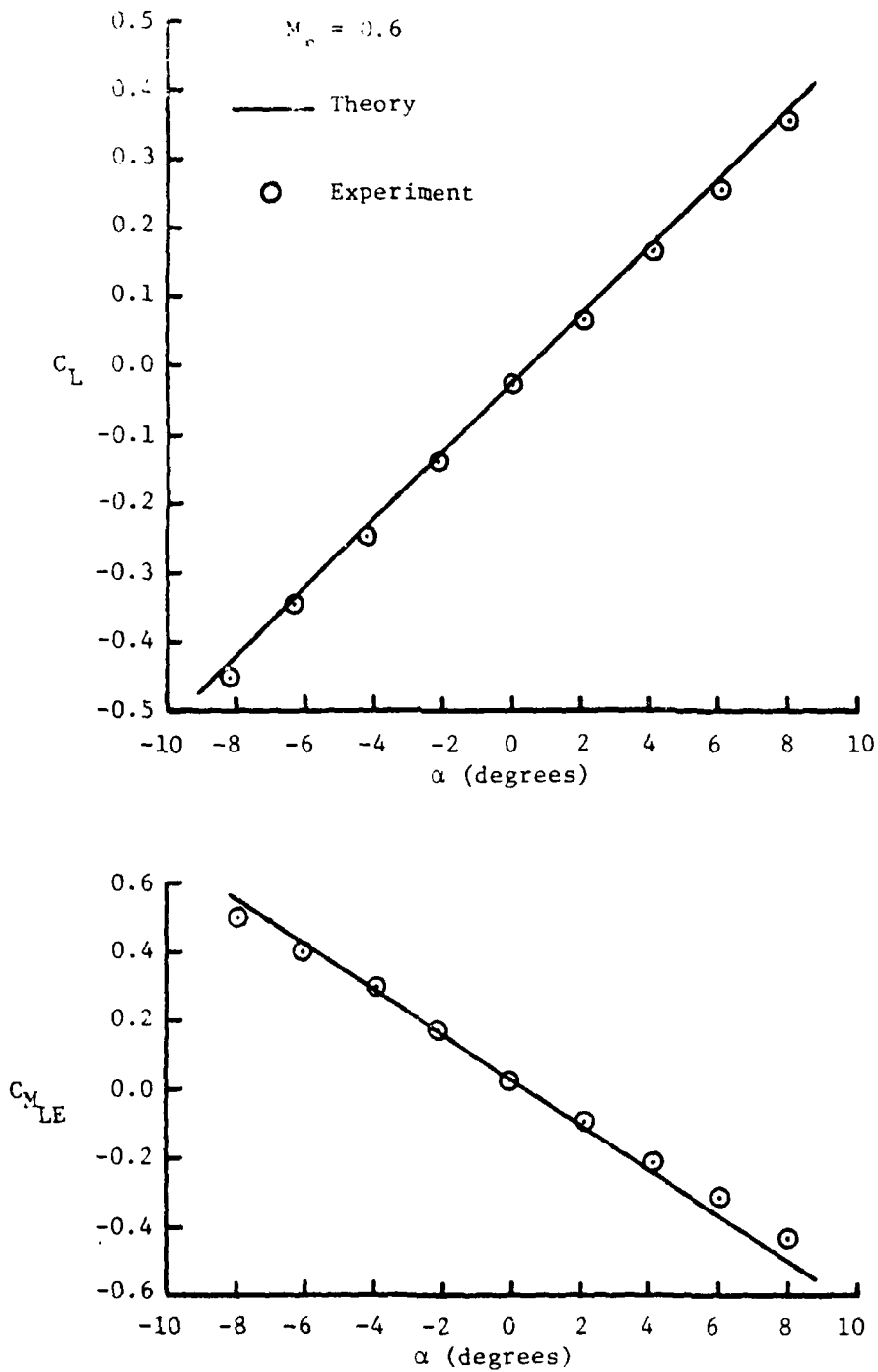
Figure 19. Characteristics of a Finite Wing that is Both Cambered and Twisted.
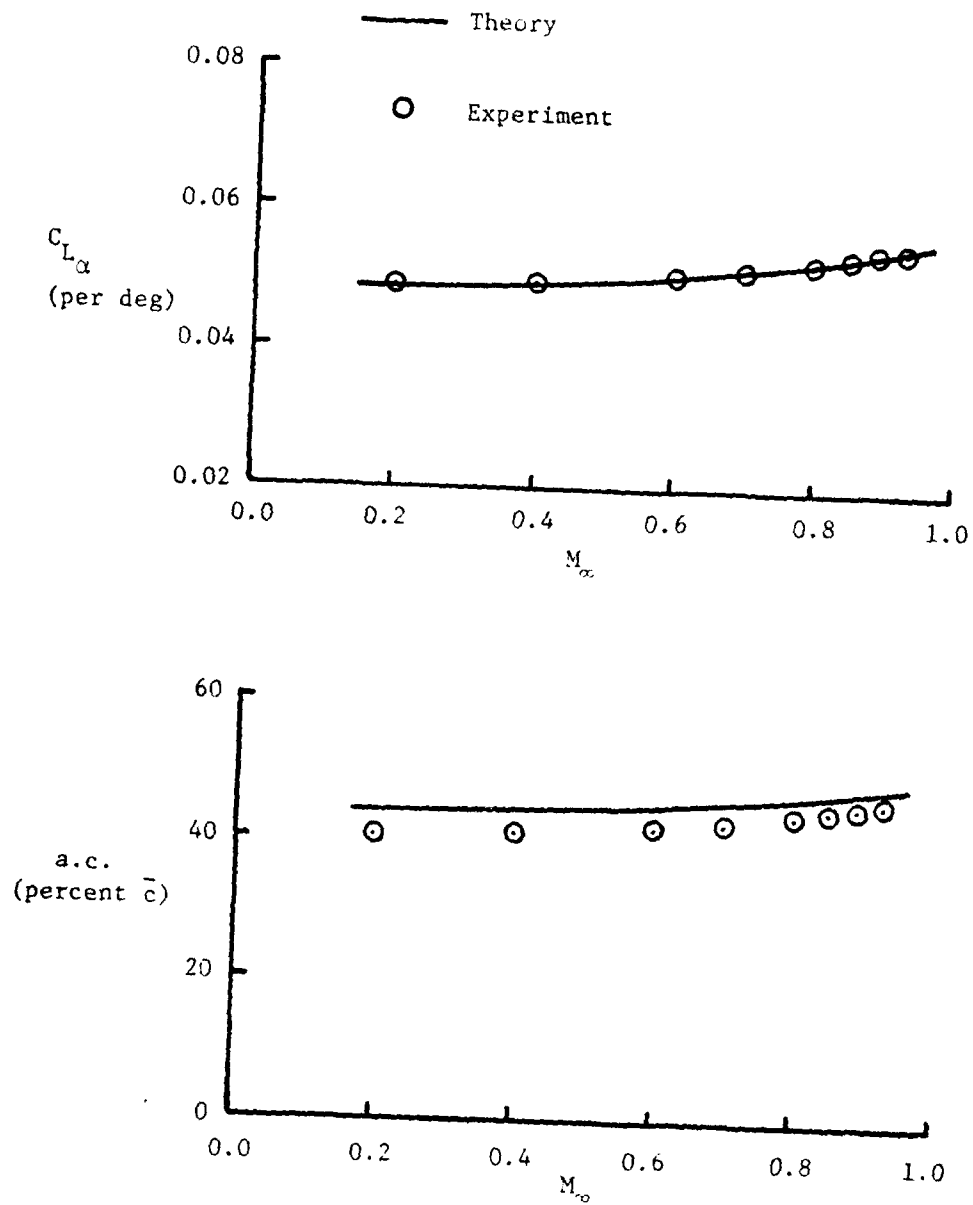
Figure 19. concluded

V. CONCLUSIONS - SUBSONIC FLOW

From the preceeding results, it is seen that the present theory produces good results in the inviscid flow regime. Configurations ranging from a basic wing to varying combinations of wings, elevons, gap, and fuselage may be modeled as well as moderate wing and/or elevon deformations. Since compressibility effects are included, reasonable results up to large (subsonic) Mach numbers are generally obtained.

For the finite gap case, the theory provides an excellent means for obtaining early design characteristics in a short time for small angles-of-attack and elevon deflections. However, it is shown that for large elevon deflections there was a considerable decrease in total lift and moment characteristics when a large gap was present. This appears to be a viscous phenomena and therefore cannot be modeled with potential flow techniques. Vortex rollup, which must be included for very large gaps, has also been neglected in the present theory. Results for cambered, twisted, and arbitrarily deformed wings may also be obtained easily with the present theory. Results are good as long as the requirements of potential flow are met on the surface.

Several advantages of the current method occur as a consequence of the assumption of a constant ΔC_p over a sufficiently small subpanel of the wing. The wing can be divided into many subsections, yet only a relatively small matrix must be inverted to obtain the load distribution. This assumption also allows ΔC_p to be taken outside the downwash integral and yields a closed form solution to the equation. As a result, this method

requires considerably smaller computational times and storage space than many methods, such as vortex lattice, since they usually require a matrix equivalent in size to the number of wing subpanels.

VI. SUPERSONIC FLOW - THEORY

Fundamental Equations

The theoretical approach for the supersonic Mach number regime is a potential flow formulation in which solutions are superimposed. The source solution introduced by Evvard[28] forms the basis of 3-D supersonic theory used in the present analysis and vorticity paneling is added to account for wing deformations. The vorticity paneling, as previously introduced, is actually a continuously distributed doublet panel which satisfies the supersonic potential equation

$$\phi(x,y,z) = \frac{1}{2\pi} \iint_{S_o} \frac{\gamma(x_o,y_o)}{(y-y_o)^2+z^2} \, z \left[\frac{(x-x_o)}{\sqrt{(x-x_o)^2-\beta^2(y-y_o)^2-\beta^2z^2}} \right] dx_o dy_o \qquad (52)$$

As for subsonic flow, the vorticity distribution $\gamma(x_o,y_o)$ may be replaced by the pressure loading coefficient $\frac{1}{2}\Delta C_p(x_o,y_o)$. The downwash equation is obtained by differentiation in the standard manner and when evaluated in the $z=0$ plane (planar flow) becomes

$$w(x,y) = \frac{1}{4\pi} \iint_{S_o} \frac{\Delta C_p(x_o,y_o)}{(y-y_o)^2} \left[\frac{(x-x_o)}{\sqrt{(x-x_o)^2-\beta^2(y-y_o)^2}} \right] dx_o dy_o \qquad (53)$$

where the area S_o is that contained on the wing surface in the upstream running Mach cone emanating from the field point (x,y). Although the vorticity paneling is formulated for planar flow, it may be used to account for non-planar velocity components if the slope of the nonplanar surface is properly taken into account. A more detailed discussion of how this is done is explained later.

55

The assumed pressure loading consists of the basic three-dimensional supersonic flow term plus the perturbation term from the vorticity paneling and is then written as

$$\Delta C_p(x_o, y_o) = P(x_o, y_o)\sin(\alpha+\theta_o) + P(x_o, y_o) \sum_{n=0}^{N} \sum_{m=0}^{M} B_L \ \eta^m \ \cos\frac{n\pi\xi}{2} \qquad (54)$$

The first expression on the right-hand side is the 3-D loading term modified to account for <u>local</u> wing deformations and is valid for both subsonic and supersonic leading edges. The second term uses the 3-D pressure functions $P(x_o, y_o)$[15] as a weighting function which, when multiplied by the unknown coefficient B_L, and the series $\eta^m \cos\frac{n\pi\xi}{2}$ accounts for small deformations in the wing surface in the upstream Mach cone from the point (x,y). The order of the terms in the second expression seldom exceeds 3 or 4 and for planar wings, the entire second term is unnecessary. Increasing the polynomial order for larger wing deformations or higher angles of attack does not seem to provide better agreement with experimental data.

The form of the assumed pressure loading term to account for perturbation velocities was chosen as a polynomial in the spanwise direction and a trigometric or Fourier series type function in the chordwise direction. No <u>strong</u> justification for these assumptions can be given except that in the spanwise direction the 3-D loading term should produce acceptable results, even for deformed wings, and corrections, which the polynomial provides, should be small. Subsequent good agreement with experimental data seem to justify this assumption. In the chordwise direction where more severe changes occur in the pressure loading, a trigometric correction, which is somewhat more general than the

polynomial, was chosen with subsequent good agreement with experimental data.

As in subsonic flow, the ΔC_p term is removed from the integral in eq. (53) and the resultant expression is integrated in closed form over a small subpanel. Results of this integration over various shaped subelements is presented in Ref. 15.

It is convenient to define the value of this integral as $\beta \Delta K$ so that the total downwash at a point (x,y) becomes

$$w(x,y) = \sum_{i=1}^{I} (\Delta K)_i [\Delta C_p(\bar{x}_o, \bar{y}_o)]_i \left(\frac{\beta}{4\pi}\right) \tag{55}$$

where I is the total number of subpanels in the region (cone) of integration. The boundary condition is

$$w(x,y) + \sin(\alpha+\theta_c) = 0 \tag{56}$$

where θ_c is the local deformation angle at a control point. Rearranging and combining equations (54), (55) and (56) yields

$$\sum_{i=1}^{I} (\Delta K)_i [P(\bar{x}_o, \bar{y}_o) \sin(\alpha+\theta_o)]_i +$$

$$\sum_{i=1}^{I} (\Delta K)_i [P(\bar{x}_o, \bar{y}_o) \sum_{n=0}^{N} \sum_{m=0}^{M} B_L n^m \cos \frac{n\pi\xi}{2}]_i$$

$$= -\frac{4\pi}{\beta} \sin(\alpha+\theta_c) \tag{57}$$

where $L = n + mN$.

Body perturbation effects on the wing loading are accounted for by assuming that the body is cylindrically shaped. The cylinder is generated with an infinite line doublet whose axis is in the z-direction perpendicular to the wing planform. The results of adding the body to the

analysis simply adds another term to the right-hand side of eq. (57) which, after a little manipulation, becomes

$$- \frac{4\pi a^2 \sin\alpha}{\beta(a+\eta)^2} \tag{58}$$

where a is the nondimensional body radius defined by $a = r_b/(b/2)$.

Equations (57) and (58) are combined and rearranged as

$$\sum_{i=1}^{I} (\Delta K)_i [P(\bar{x}_o, \bar{y}_o) \sum_{n=0}^{N} \sum_{m=0}^{M} B_L \eta^m \cos \frac{n\pi\xi}{2}]_i =$$

$$- \frac{4\pi}{\beta} \sin (\alpha+\theta_c) + \frac{4\pi a^2 \sin\alpha}{\beta(a+\eta)^2}$$

$$+ \sum_{i=1}^{I} (\Delta K)_i [P(\bar{x}_o, \bar{y}_o) \sin(\alpha+\theta_o)]_i \tag{59}$$

The above equation represents a set of N simultaneous linear algebraic equations and is conveniently arranged in matrix form for a Gaussian reduction solution for the unknown coefficients B_L. Once the unknown coefficients are determined, the localized loading is obtained from equation (54).

Lift and Pitching Moment for Wing Elevon Combinations

In the preceding section, the basic equations were presented for finding the resulting pressure distribution on a wing or elevon in supersonic flow. For the wing alone, these equations may be applied directly since there is no upstream influence due to the elevon. After the pressure loading coefficients in eq. (54) are determined, the pressure coefficient may be computed at any point on the wing surface and appropriate subsequent integration produces the lift.

For the elevon, a similar procedure is followed with the exception that the elevon is flying in the wake of the wing and therefore the downwash produced by the wing and the elevon must be considered. The mechanism used to compute this downwash is discussed in another section.

The lift for the wing-elevon configuration is the sum of that produced by the wing and that produced by the elevon. It is convenient to define nondimensional chordwise and spanwise variables for the wing as

$$\xi_w = (x-x_{LE})/C_w \tag{60}$$

and

$$\eta_w = y/(b/2) \tag{61}$$

For the elevon, using the same coordinate system, these definitions become

$$\xi_E = (x-C_R-\epsilon)/C_E \tag{62}$$

and

$$\eta_E = y/(b/2) \tag{63}$$

With these definitions, integration of the pressure distribution over the wing for the lift becomes

$$C_{L_w} = \frac{b}{2S} \int_{\eta=-1}^{\eta=1} \int_{\xi_w=0}^{\xi_w=1} (\Delta C_{P_w} C_w \, d\xi_w) d\eta_w \tag{64}$$

and for the elevon

$$C_{L_E} = \frac{b}{2S} \int_{\eta=-1}^{\eta=1} \int_{\xi_E=0}^{\xi_E=1} (\Delta C_{P_E} C_E \, d\xi_E) d\eta_E \tag{65}$$

It is convenient to define sectional properties as

$$(cc_\ell)_w = C_w \int_{\xi_w=0}^{\xi_w=1} \Delta C_{P_w} \, d\xi_w \tag{66}$$

and

$$(cc_\ell)_E = C_E \int_{\xi_E=0}^{\xi_E=1} \Delta C_{P_E} \, d\xi_E \tag{67}$$

from which we get the total lift coefficient

$$C_L = \frac{b}{S} \int_{\eta=0}^{\eta=1} [(cc_\ell)_w + (cc_\ell)_E] d\eta \tag{68}$$

Because of the nature of the pressure loading function, equation (54), equations (66), (67) and (68) must be integrated numerically.

A similar analysis leads to the moment equation about the y axis (see Figs. 1 and 2) as

$$M_y = \int_{A_w} \Delta P_w \, x \, dA_w + \int_{A_E} \Delta P_E \, x \, dA_E \tag{69}$$

For the first integral in eq. (69), we note that

$$x = x_{LE} + \xi C_w \tag{70}$$

and

$$dA_w = dxdy = (C_w d\xi)(\frac{b}{2} \, d\eta) \tag{71}$$

and

$$x_{LE} = y \tan \Lambda = \frac{b}{2} \eta \tan\Lambda \tag{72}$$

Using these definitions, the first of these integrals over the wing can be written as

$$I_1 = qb \int_{\eta=0}^{\eta=1} \{ \frac{b}{2} \eta \tan\Lambda [C_w \int_0^1 \Delta C_{P_w} d\xi_w] + C_w^2 \int_0^1 \Delta C_{P_w} \xi_w d\xi_w \} d\eta \tag{73}$$

In a similar manner, the second of these integrals become

$$I_2 = qb \int_{\eta=0}^{\eta=1} \{ (C_{R_w} + \varepsilon) [C_E \int_0^1 \Delta C_{P_E} d\xi_E] + C_E^2 \int_0^1 \Delta C_{P_E} \xi_E d\xi_E \} d\eta \tag{74}$$

The moment coefficient about the y axis is defined as

$$C_{M_y} = M_y / (qS\bar{c})$$

so that

$$C_{M_y} = \frac{b}{S\bar{c}} \int_{\eta=0}^{\eta=1} \{ [\frac{b}{2} \eta \tan\Lambda (cc_\ell)_w + C_w^2 \int_0^1 \Delta C_{P_w} \xi_w d\xi_w]$$

$$+ [(C_R + \varepsilon)(cc_\ell)_E + C_E^2 \int_0^1 \Delta C_{P_E} \xi_E d\xi_E] \} d\eta \tag{75}$$

In order to evaluate eqs. (66), (67), (68), and (75), we must first determine the constants, B_L in eq. (54) for both the wing and elevon. Since the elevon solution cannot affect the wing solution (zone of silence), then the wing loading is solved independently of any elevon considerations through a Gaussian reduction of eq. (59).

For the elevon solution, we must consider the downwash produced by that portion of the wing in the forecone of some arbitrary point on the

elevon. This downwash from the wing on the elevon will enter the elevon solution through an additional term in the boundary conditions. That is, for the elevon

$$\sum_{i=1}^{I} (\Delta K)_i [\Delta C_{P_E} ((\bar{x}_o, \bar{y}_o)]_i = - \frac{4\pi}{\beta} [w_w + \sin(\alpha + \delta)] \tag{76}$$

where w_w is the downwash produced by the wing at a particular control point on the elevon. Evaluation of w_w is considered in the next section.

Wing Downwash on Elevon

To evaluate the downwash from the wing on the elevon, a direct approach was first considered. That is, integration was to be carried out over the forecone from a point on the elevon surface. However, because of the gap between wing and elevon, this did not seem to be a feasible approach, especially in light of its complexity. Thus another approach was considered and used.

Since the wing solution is completed first, sectional properties on the wing may be computed at any spanwise location. Thus the wing is divided into equally spaced "strips" along the span and the sectional lift is computed for each strip. It is assumed that a horseshoe vortex is attached to each strip in a lattice manner whose strength is determined by the sectional lift coefficient. That is, from the Kutta-Joukowski theorem, the lift per unit span for some ith section is

$$(\Delta L / \Delta \eta)_i = \rho V \Gamma'_i = 2q \Gamma_i \tag{77}$$

where

$$\Gamma'_i = V \Gamma_i$$

Placement of these vortices are shown in Fig. 20. Note that in the figure, the bound portions are shown attached to the quarter chord and the trailing legs trail behind the wing to infinity.

If the wing is symmetrically loaded, the lift may be written as

$$L = qb \int_0^1 (cc_\ell)_w \, d\eta_w \tag{78}$$

so that for a strip

$$\Delta L = qb \int_{\eta_1}^{\eta_2} (cc_\ell)_w \, d\eta_w$$

Dividing by $\Delta\eta$ and equating to eq. (77) yields

$$\Gamma_i = [\frac{1}{\Delta\eta} \int_{\eta_1}^{\eta_2} (cc_\ell)_w d\eta_w]_i$$

If it is assumed that over the strip the term cc_ℓ is constant, then the integration may be completed in closed form.

At the junction between any two strips, the resulting trailing filament strength is the difference between adjacent filaments and may be written as

$$\Gamma_{R_i} = \Gamma_i - \Gamma_{i+1} = (\overline{cc_\ell})_i - (\overline{cc_\ell})_{i+1} \tag{79}$$

The starting point of these filaments is assumed to be the wing trailing edge (for lack of a better assumption). Fortunately, the down-wash induced from all trailing filaments is small in comparison to the
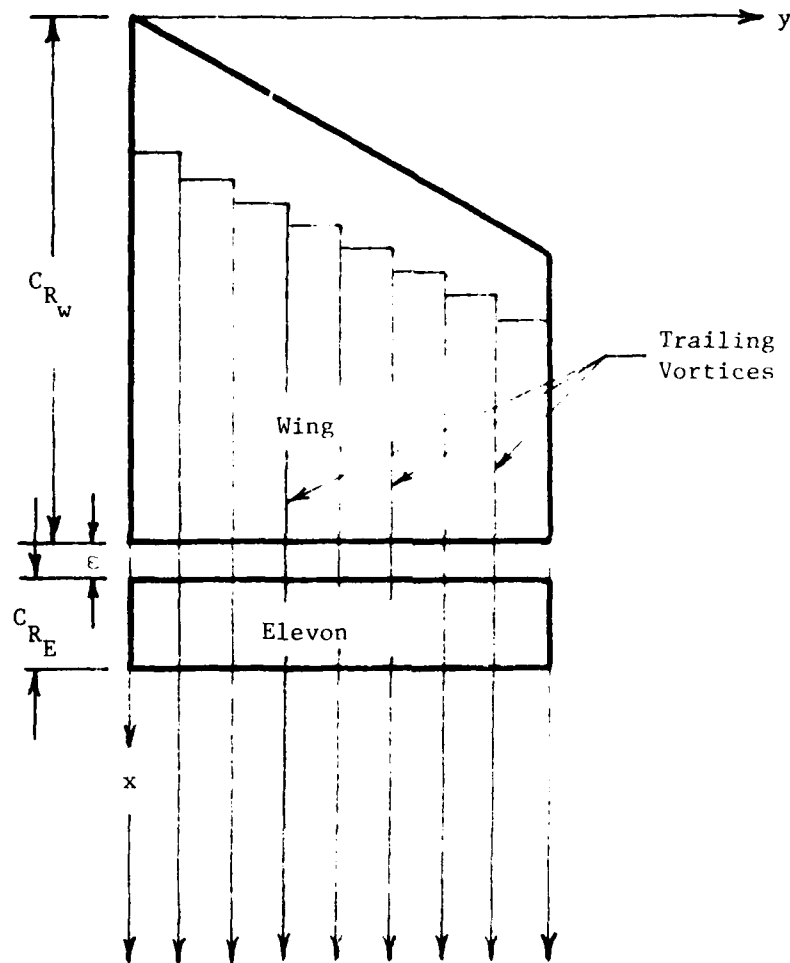
Figure 20. Schematic of Wing-Elevon Coordinate
System and Wing Trailing Vortices.

free stream components and thus an error in the starting point of the
filament does not significantly influence the final elevon loading.
Obviously, though, the filaments must start somewhere on the wing. From
From a planform view of the wing-elevon trailing filament configuration,
it may be shown that if a particular field point (x,y,z) is in the region
of influence of a particular filament starting at (x_Γ, y_Γ), then

$$x > (x_\Gamma + \beta |y_\Gamma - r|) \tag{80}$$

where $r^2 = y^2 + z^2$. That is, if eq. (80) is satisfied, then the field
point (x,y,z) "feels" the downwash from the trailing filament (x_Γ, y_Γ).

To compute the velocity induced at some field point (x,y,z), the
Biot-Savart Law is used as an approximation. Although this theorem is
actually only valid for subsonic incompressible flow, it will be suf-
ficient for the present analysis if proper account is taken for the
region of influence (zone of silence).

In vector form, the Biot-Savart relation governing the velocity
induced at some point by a vortex filament is

$$\bar{V}(x,y,z) = -\frac{\Gamma}{4\pi} \int \frac{\bar{r} \times d\bar{\ell}}{r^3} \tag{81}$$

In this expression, $\bar{r}$ is the vector from the field point to an
arbitrary point on the filament, $\overline{d\ell}$ is a vectored differential length
along the filament, r is the magnitude of the vector $\bar{r}$, and Γ is the
filament strength. Referring to Fig. 21, these quantities may be
written as

$$\overline{d\ell} = (i \cos\theta_\Gamma + k \sin\theta_\Gamma)d\ell \tag{82}$$
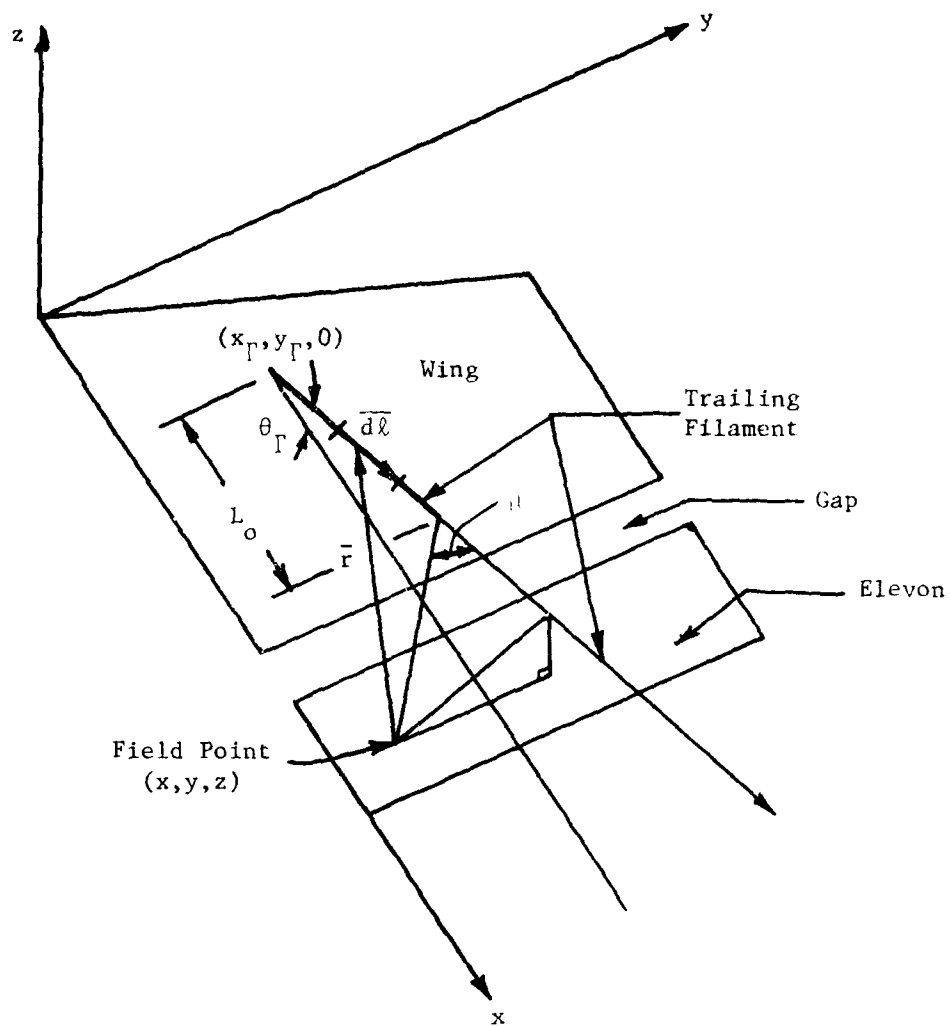
Figure 21. Schematic of the Wing-Elevon-Trailing
Vortex Filament Configuration.

and

$$\bar{r} = (x_\Gamma - x + L\cos\theta_\Gamma)i + (y_1 - y)j + (L_o\sin\theta_\Gamma - z)k \tag{83}$$

Equations (82) and (83) are introduced into eq. (81) so that the integrals for the three velocity components are

$$V_x = -\frac{\Gamma}{4\pi}\int_{\ell=0}^{\ell=L_o}(y_1\sin\theta_\Gamma/D_m)d\ell \tag{84}$$

$$V_y = \frac{\Gamma}{4\pi}\int_{\ell=0}^{\ell=L_o}((x_1\sin\theta_\Gamma + z\cos\theta_\Gamma)/D_m)d\ell \tag{85}$$

and

$$V_z = \frac{\Gamma}{4\pi}\int_{\ell=0}^{\ell=L_o}(y_1\cos\theta_\Gamma/D_m)d\ell \tag{86}$$

where

$$x_1 = x_\Gamma - x, \qquad y_1 = y_\Gamma - y, \tag{87}$$

$$A = 2x_1\cos\theta_\Gamma - 2z\sin\theta_\Gamma \tag{88}$$

$$B = (x_1^2 + y_1^2 + z^2) \tag{89}$$

$$D_m = (L_o^2 + \Lambda L_o + B)^{3/2} \tag{90}$$

and

$$I = \frac{2}{(4B-A^2)}\quad\frac{2L_o+A}{{}_o^2+AL_o+B} - \frac{A}{\sqrt{B}} \tag{91}$$

These integrals may be evaluated in closed form with the results

$$V_x = -\Gamma(y_1 \sin\theta_\Gamma) I/(4\pi) \tag{92}$$

$$V_y = \Gamma(x_1 \sin\theta_\Gamma + z \cos\theta_\Gamma) I/(4\pi) \tag{93}$$

and

$$V_z = \Gamma(y_1 \cos\theta_\Gamma) I/(4\pi) \tag{94}$$

The induced velocity from these filaments <u>on the elevon</u> is of primary concern and more specifically the velocity induced normal to the elevon. In vector form, a unit normal to the elevon is

$$\bar{n} = -i \sin\delta + k \cos\delta \tag{95}$$

so that

$$V_n = \bar{V} \cdot \bar{n} = - V_x \sin\delta - V_z \cos\delta \tag{96}$$

or

$$V_n = -\Gamma y_1 I [\cos(\theta_\Gamma + \delta)]/(4\pi) \tag{97}$$

Wing Trailing Edge Blocking of Elevon

To complete the theoretical analysis, the wing thickness and blunt wing trailing edge and the subsequent effect on the elevon loading must be considered in addition to the gap between the wing trailing edge and the elevon leading edge. The configuration being used in this analysis is shown in Figure 22. The flow just aft of the blunt wing trailing edge is highly turbulent as expected and details describing the subsequent flow field is fundamentally grounded in solutions of the Navier Stokes equations. The implication then is that viscous effects dominate the solution as was suggested in Ref.[1] However, this conclusion is not necessarily true. It is clearly recognized that viscous effects

a) Planform View

b) Sectional View

Figure 22. Dimensional Planform and Sectional Sketch of an
Experimental Wing-Elevon Configuration, Ref. 1.

immediately behind the wing trailing edge are very important, but it is believed that the dominant effects over most of the elevon can be predicted by potential flow methods. Justification of this conclusion is presented in a later section.

As depicted in Fig. 22, the flow is assumed to be tangent to the surface of the aft portion of the wing for all angles of attack. The streamlines thus emanating from the upper and lower aft wing surface impinge on the elevon surface as shown in Fig. 22, forming a "blanked out" region bounded by the blunt wing trailing edge, the upper and lower streamlines and a section of the elevon chord line. In this blanked region, details of the flow field are not well known. Thus for purposes of this analysis, it is assumed that this wake pressure coefficient is zero such that essentially free stream conditions exist.

From Fig. 22 the location of the aft impingement point is

$$
x_{AFT} = C_R + \frac{(x_H - C_R)\tan - t_{TE}/2}{\tan - \tan_i} +
$$

(98)

and the forward location is

$$
x_{FWD} = C_R + \frac{(x_H - C_R)\tan + t_{TE}/2}{\tan + \tan_T} +
$$

(99)

where θ_T is the positive surface slope of the aft portion of the wing. That is, for the schematic in Fig. 22, $_T$ is about $2.0°$ and ^{6} is about $-10°$.

Equations (98) and (99) are valid for ^{6} 0.0. If the elevon deflection angle is positive, then the forward location is determined from eq. (98) and the aft location from eq. (99). It is obvious from Fig. 22

that there are elevon angles where the leading edge of the elevon lies
entirely within the wake region with some portion of the aft section out-
side the wake. Also, for very small elevon deflection angles, the entire
elevon is immersed in the wing wake and thus is completely unloaded.

In order to justify the use of eqs. (98) and (99) to form a blanked-
out region (Newtonian approach) a wind tunnel experiment was designed to
study this flow field. A two-dimensional model consisting of a wing with
a blunt trailing edge and a diamond shaped elevon was constructed (see
Fig. 22) and tested at a Mach number of 1.94 in a 4" by 4" test section.
The total pressure was about 30 psia with a freestream unit Reynolds
number of 1.6 x 10^6. Selected schlieren photographs of the results of
these tests are shown in Fig. 23. In the upper left where $\alpha = 0.0°$ and
$\delta = 0.0°$, the elevon lies entirely within the wake of the wing as is
clearly seen. The important thing to note here, though, is the well de-
fined streamline emanating from the top surface of the wing and impinging
on the elevon boundary layer near the apex of the elevon midchord. In
the upper right where $\iota = 0.0°$ and $\delta = -9.0°$, the leading edge of the
elevon is about 4° outside the wing wake region but apparently still
inside the wing boundary layer. The aft impingement point on the upper
elevon surface is still clearly visible but the forward point cannot be
clearly located.

In the lower left, where $\iota = -4.14$ and $\delta = -9.0°$, the aft impingement
point is located easily while the elevon leading edge remains submerged in
the wing wake. In the lower right where $\iota = -4.14°$ and $\delta = -10.0°$, the
results are inconclusive. The overall results of these tests indicate
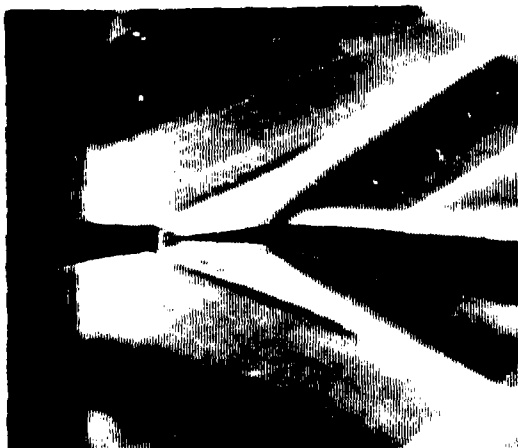
$\alpha=0.0°$, $\delta=0.0°$

$\alpha=0.0°$, $\delta=-9.0°$

$\alpha=-4.14°$, $\delta=-4.0°$

$\alpha=-4.14°$, $\delta=-10.0°$

Fig. 23. Schlieren Photographs of the Blunt Wing Trailing Edge and
Elevon Leading Edge, M=1.94.

that some sort of blanking region is formed which is not totally independent of angle of attack and is more strongly dependent on the elevon deflection angle than that predicted by eqs. (98) and (99). Nevertheless, these equations do provide "bounds" for the mathematical analysis and, as will be shown later, provide good agreement with experimental data.

VII. SUPERSONIC FLOW - RESULTS

Comparison with experimental data of the theoretical analysis as previously presented is divided into two major categories: (1) planar wings and (2) deformed wings. In many cases, the planform shapes chosen were dictated by available experimental data. In some cases, experimental data was available for both deformed and undeformed wings with the same planform shape. Four of the planform shapes analyzed are shown in Fig. 24.

Planar Wings

Results of the pressure loading and sectional lift and pitching moment for three of these configurations are shown in Figs. 25-30 for selected Mach numbers and low angles of attack. More complete data summary results for these configurations are presented in Appendix A. In these figures the theoretical solution for the pressure loading is basic three-dimensional supersonic theory as presented in Refs. 15 and 18. No vorticity paneling is required. The double summation terms in eq. (54) are omitted and only the $P(x_o, y_o) \sin (\alpha)$ term is used to compute the pressure.

In most cases, the sectional normal forces agree well with the experimental data especially on the inboard sections of the wings. It is observed that the worst agreement is near the wing tips as one would expect. This deviation at the tips is not as detrimental as might first appear since most of the configuration loading is concentrated on the inboard sections.

74
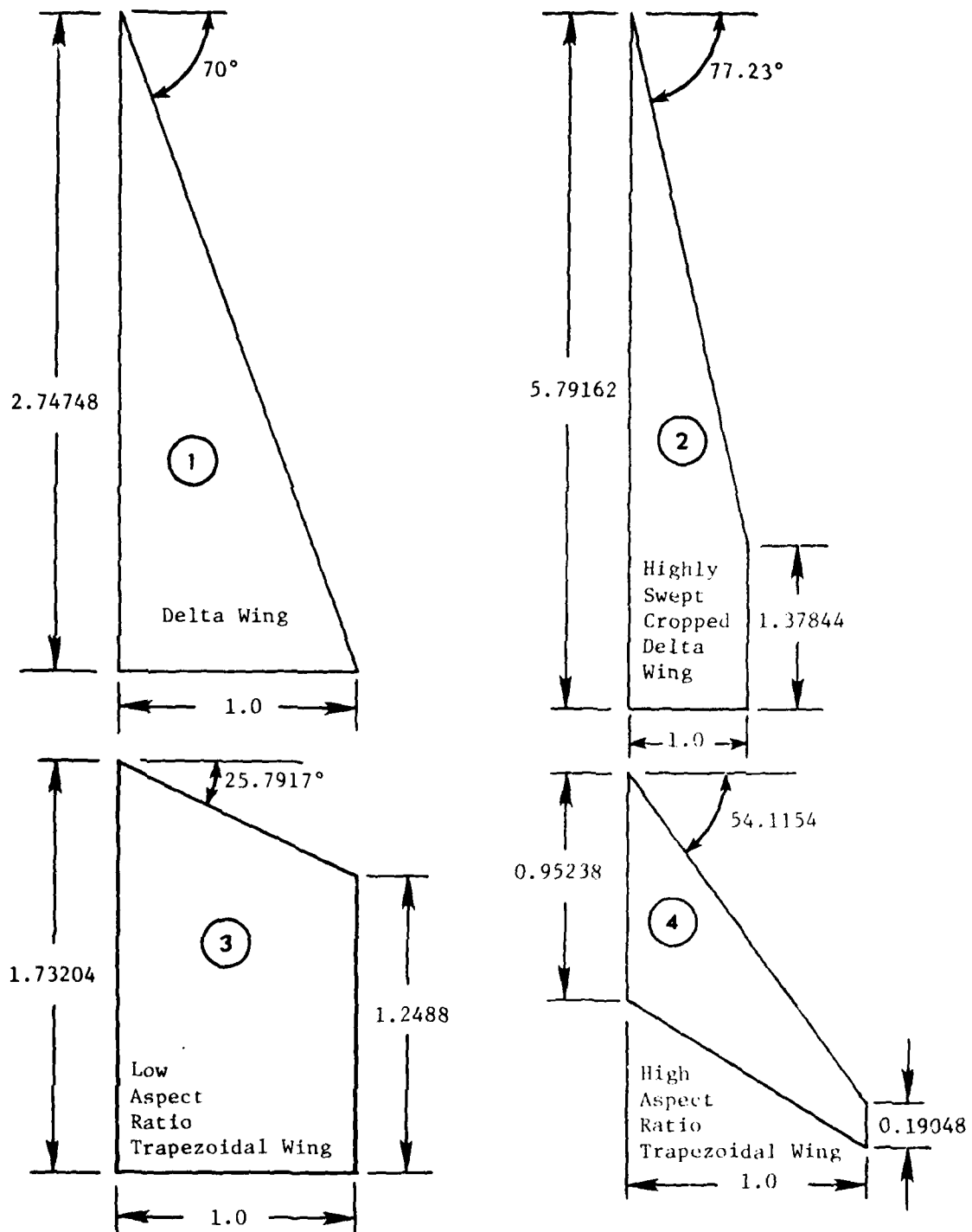
Fig. 24. Dimensional Sketch of Four Wing Planform Shapes Under Study.

The sectional moment coefficients about the y-axis shows the same kind of agreement as does the normal forces. In each case the discrepancies are not severe and the location of the sectional aerodynamic center is predicted quite well.

The experimental data for these plots (including those in Appendix A) were obtained from Refs. 29 and 30 and was integrated numerically to obtain the sectional normal forces and pitching moments. Integration to produce the normal forces agreed quite well with that tabulated in the original reports; however, the sectional pitching moment data as published in Refs. 29 and 30 was not reproducible by numerical means. Consequently, these experimental data as presented in Figs. 25-30 (and Appendix A) for the sectional coefficients was obtained by numerical integration of the pressures and is not that which is "tabulated" in Refs. 29 and 30.

For these planar configurations, the theory is a linear theory and thus tabulation of the total forces and moments is sufficient to illustrate overall agreement. Table 2 is a comparison of the lift curve slope and moment curve slope for the three planar configurations under study, as found by numerical integration of the curves in Figs. 26, 28 and 30.

From Figs. 25-30 and those in Appendix A, it is difficult to picture exactly how the sectional loading profiles are spread over the wing. Consequently, Figs. 31-34 were produced showing the isobars and the large influence produced by the wing tips. Note also the supersonic leading edge behavior for the low aspect ratio trapezoidal wing and rectangular wing.

It is apparent from Figs. 25-30 and from Table 2 that the linear theory is excellent for most cases considered. The disagreement near the
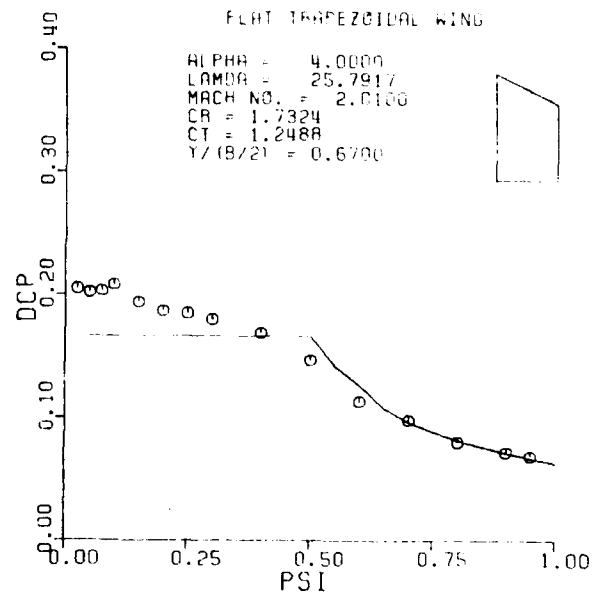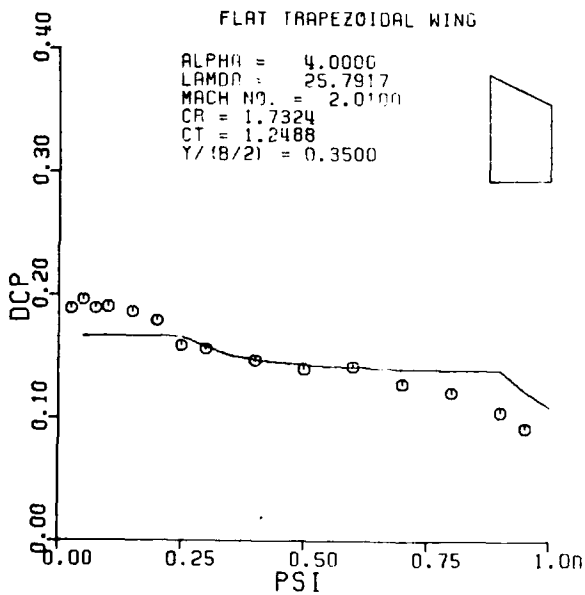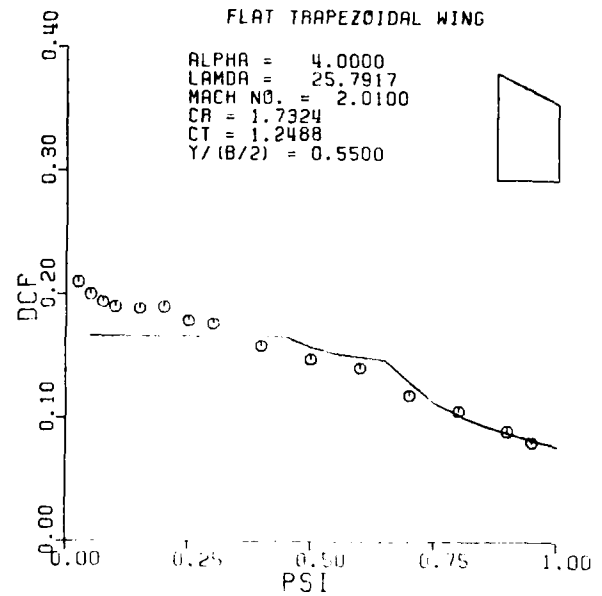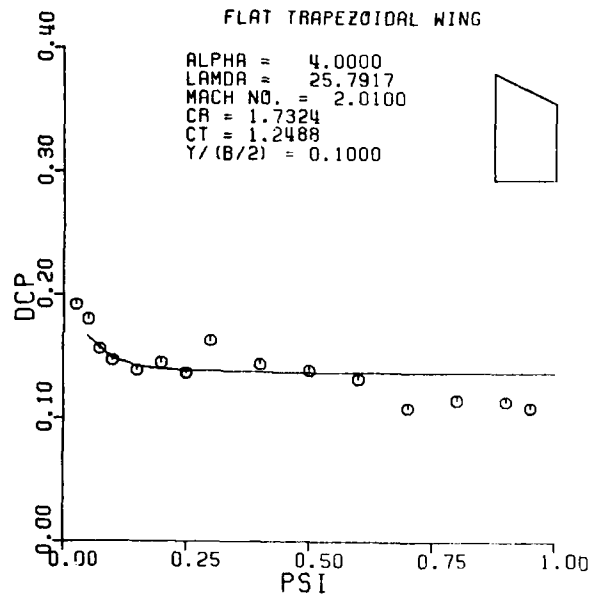
Figure 25. Pressure Distribution on a Flat Trapezoidal Wing; M = 2.01,
α = 4.0.

FLAT TRAPEZOIDAL WING

ALPHA   =   4.0000
LAMDA   =   25.7917
MACH NO. =   2.0100
CR = 1.7324
CT = 1.2488
Y/(B/2) = 0.7700

FLAT TRAPEZOIDAL WING

ALPHA   =   4.0000
LAMDA   =   25.7917
MACH NO. =   2.0100
CR = 1.7324
CT = 1.2488
Y/(B/2) = 0.9700

FLAT TRAPEZOIDAL WING

ALPHA   =   4.0000
LAMDA   =   25.7917
MACH NO. =   2.0100
CR = 1.7324
CT = 1.2488
Y/(B/2) = 0.8700

Figure 25.   Continued

FLAT TRAPEZOIDAL WING

ALPHA = 4.0000
LAMDA = 25.7917
MACH NO. = 2.0100
CR = 1.7324
CT = 1.2488

FLAT TRAPEZOIDAL WING

ALPHA = 4.0000
LAMDA = 25.7917
MACH NO. = 2.0100
CR = 1.7324
CT = 1.2488
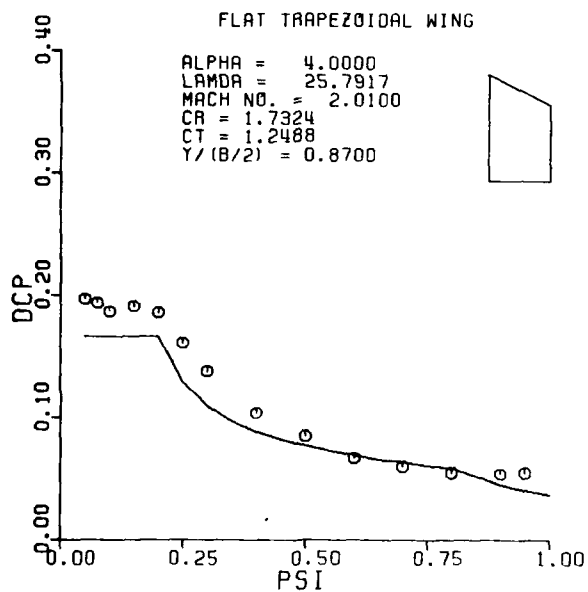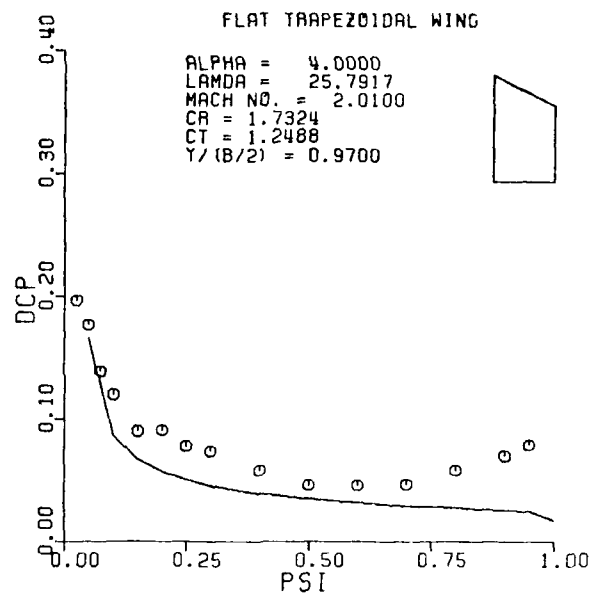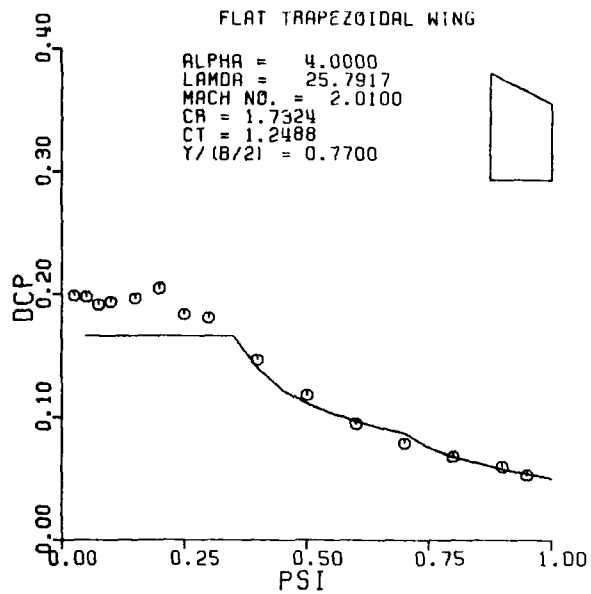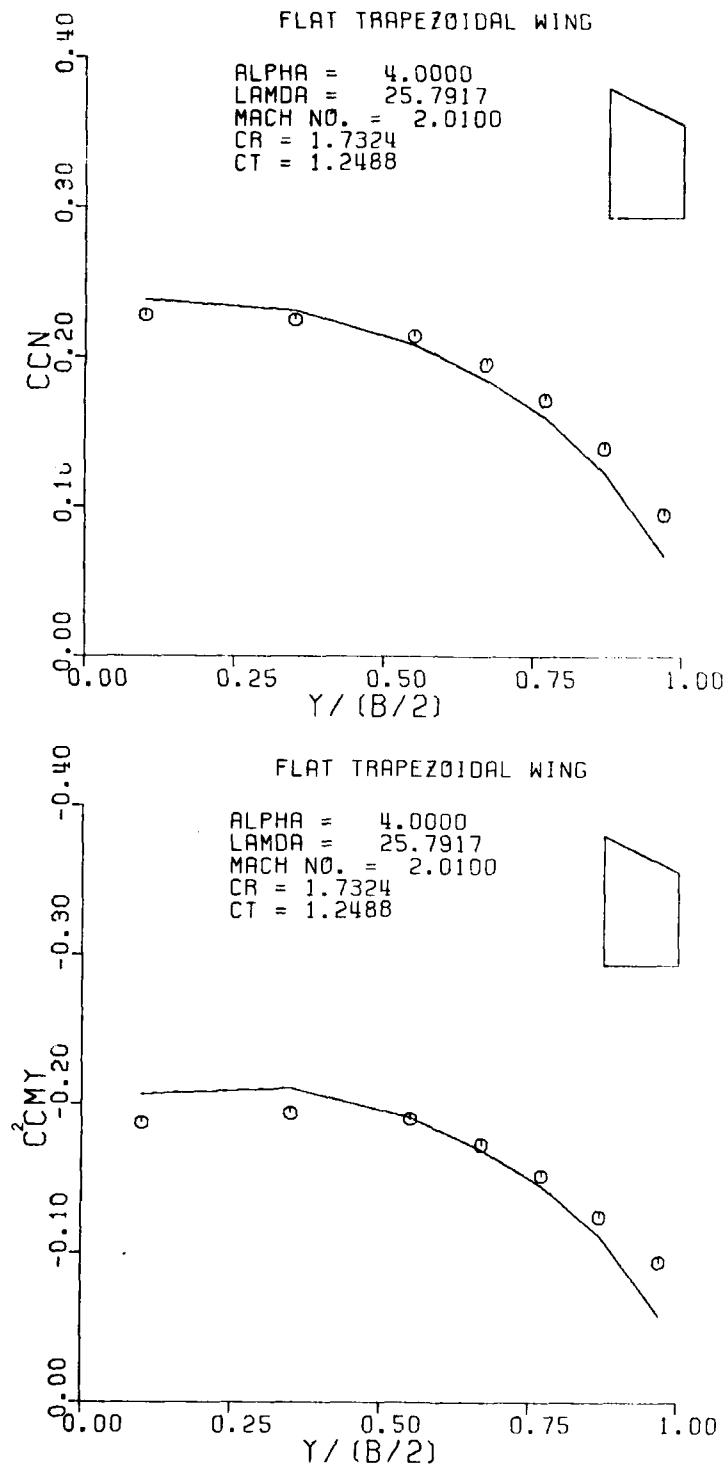
Figure 26.   Sectional Normal Force and Pitching Moment for a Flat
Trapezoidal Wing; M = 2.01, α = 4.0.
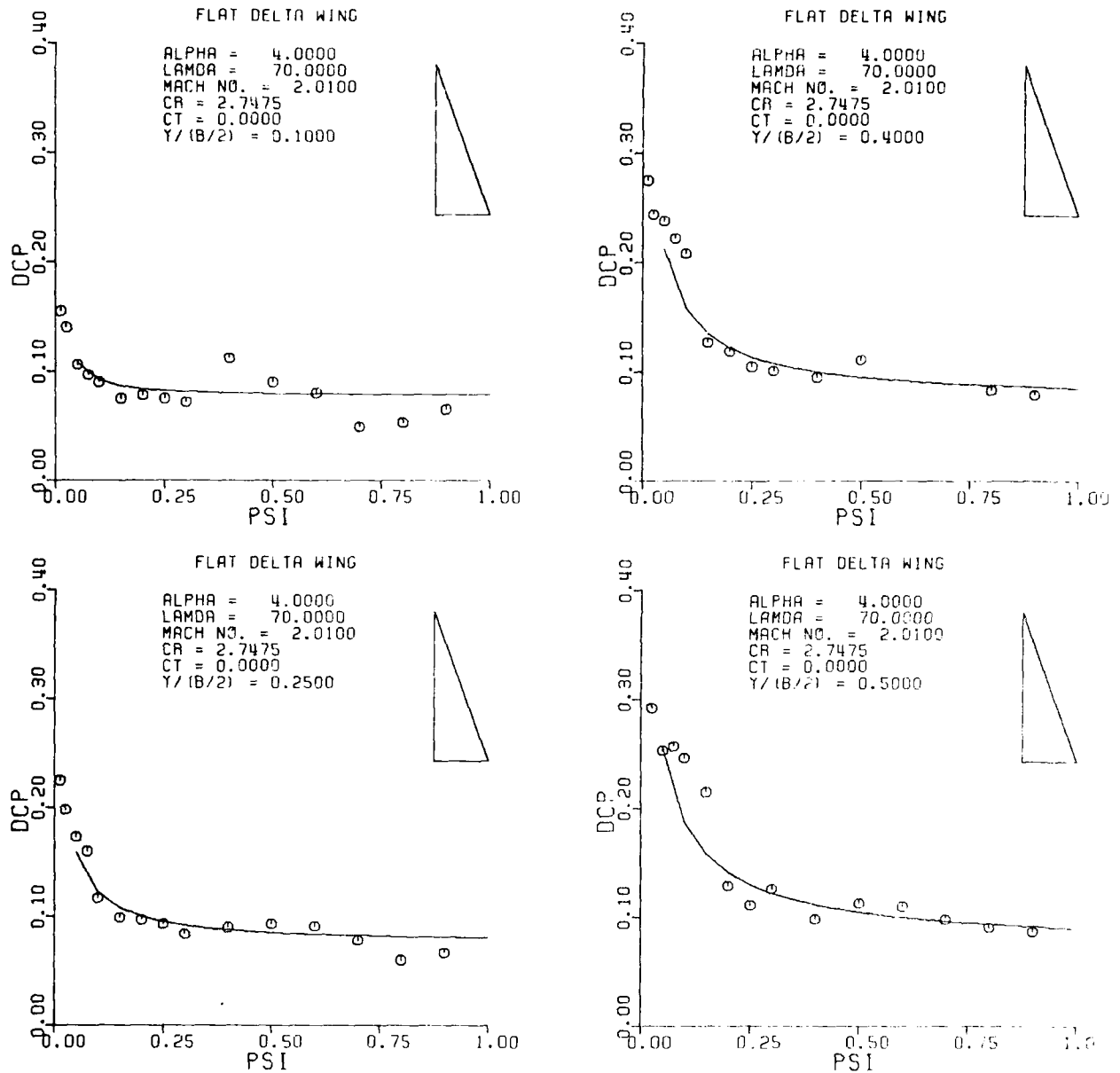
Figure 27. Pressure Distribution on a Flat Delta Wing; M = 2.01, α = 4.0.

Figure 27.   Continued

FLAT DELTA WING

ALPHA = 4.0000
LAMDA = 70.0000
MACH NO. = 2.0100
CR = 2.7475
CT = 0.0000

FLAT DELTA WING

ALPHA = 4.0000
LAMDA = 70.0000
MACH NO. = 2.0100
CR = 2.7475
CT = 0.0000
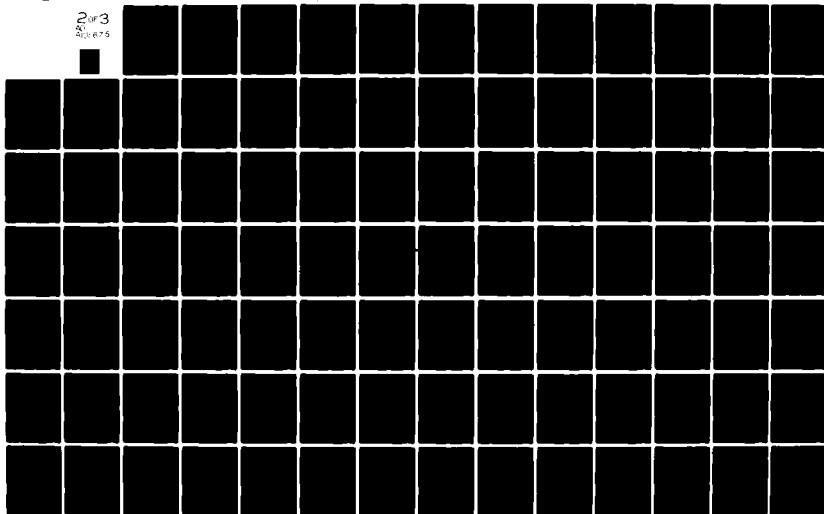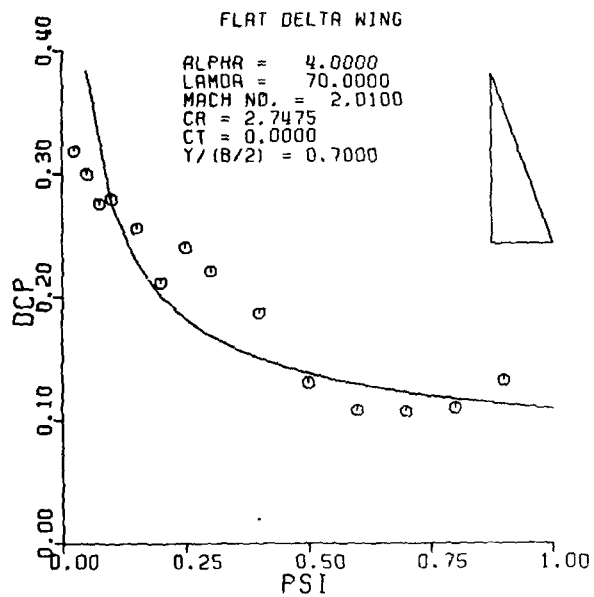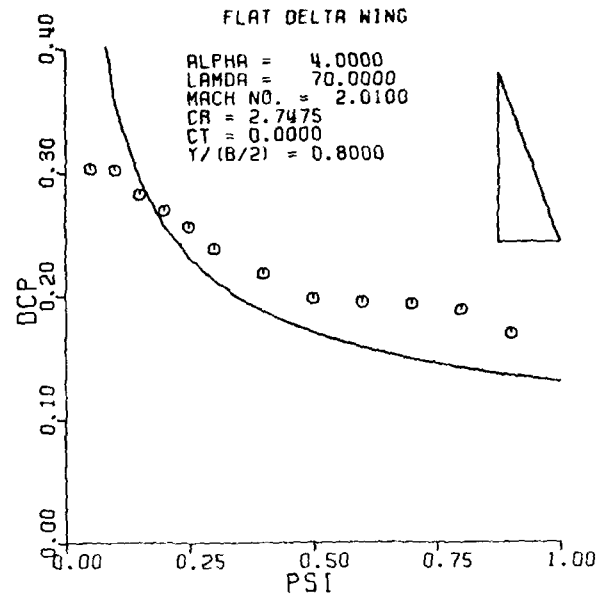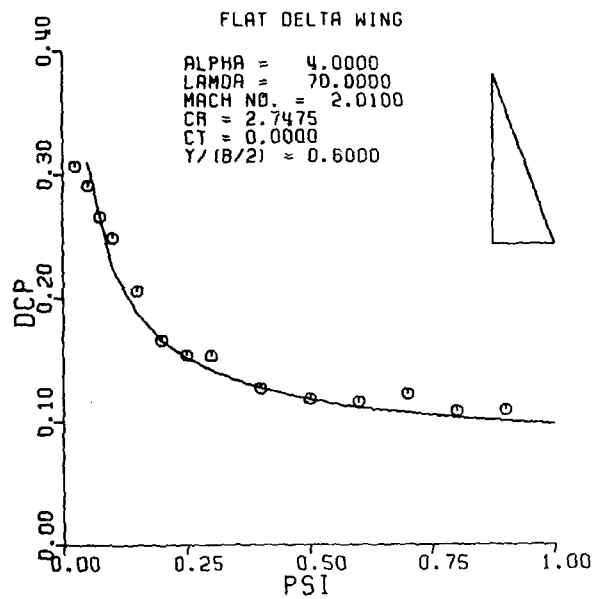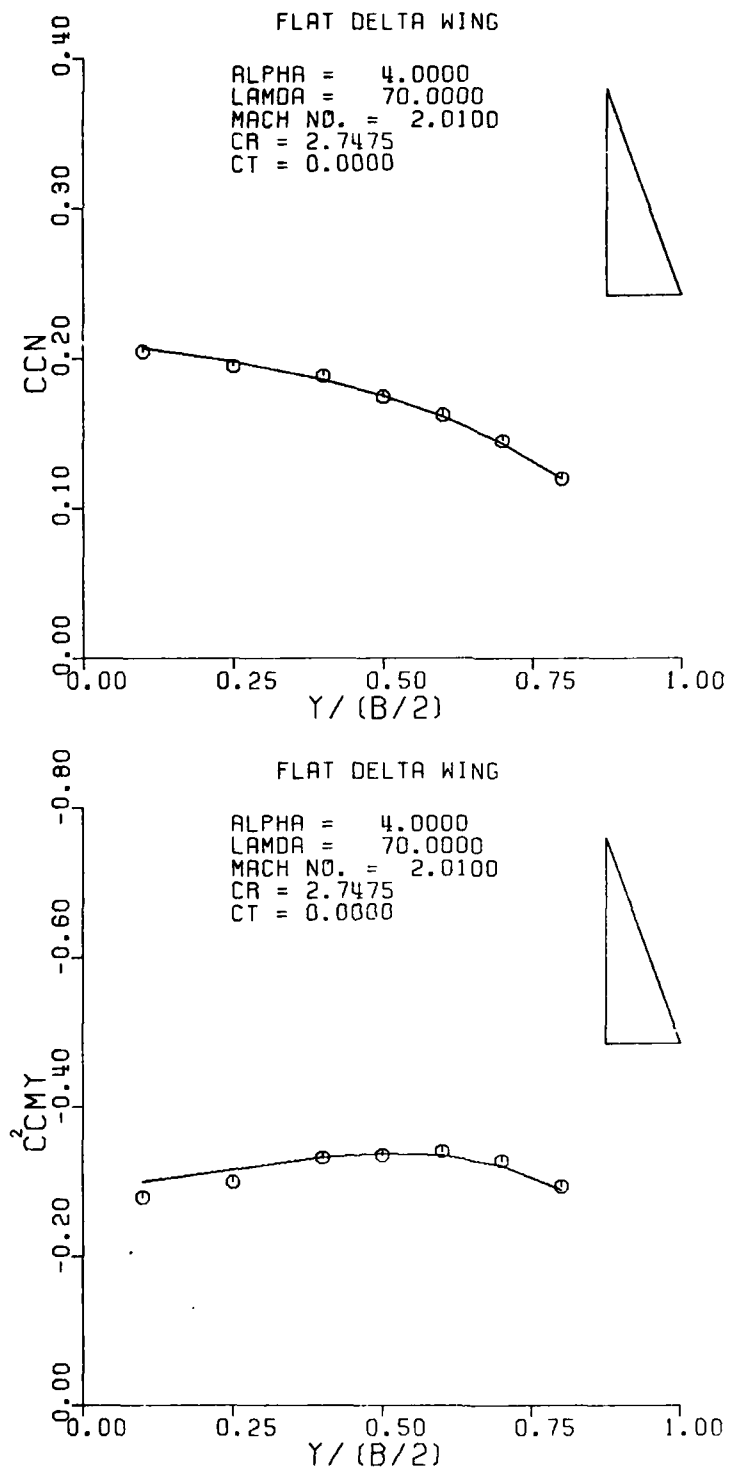
Figure 28.   Sectional Normal Force and Pitching Moment for a
Flat Delta Wing; M = 2.01, α = 4.0.
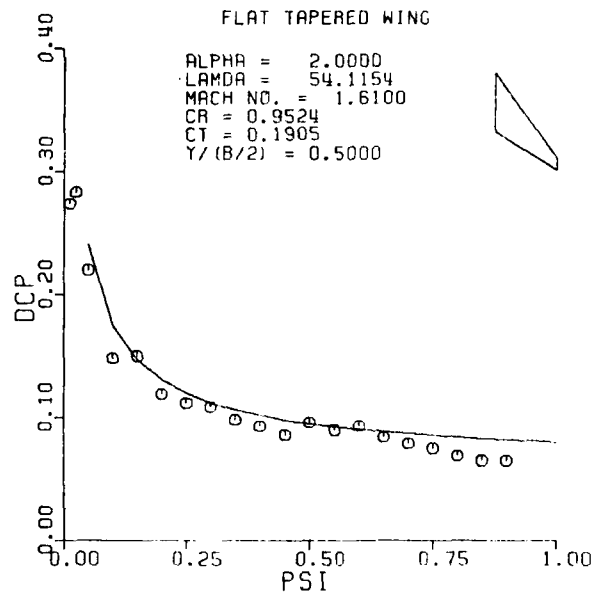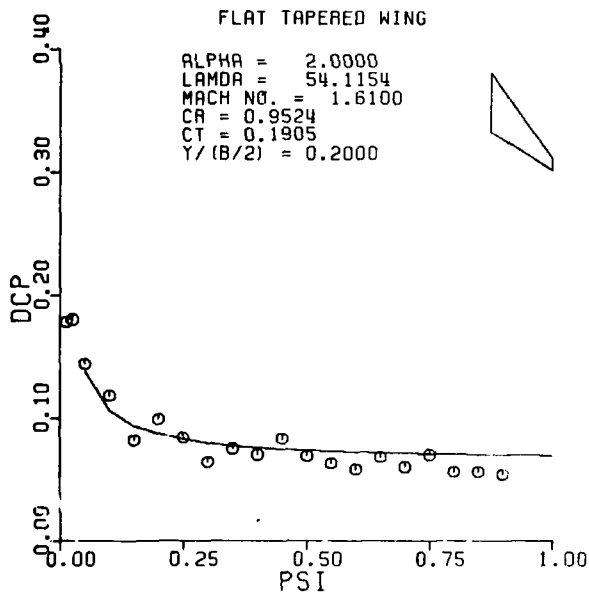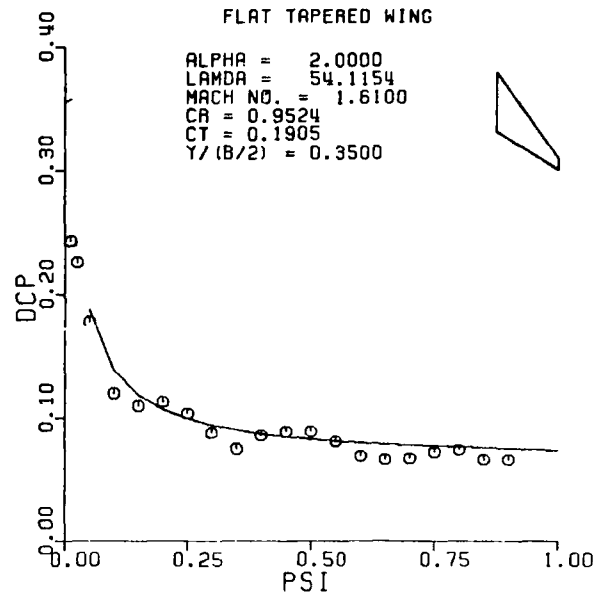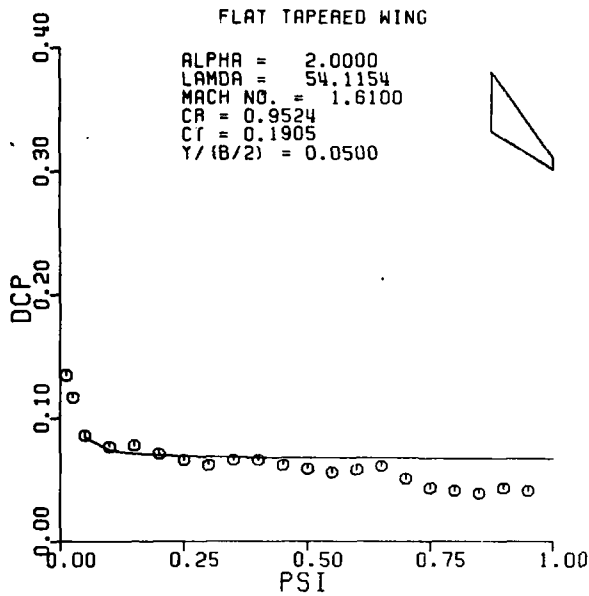
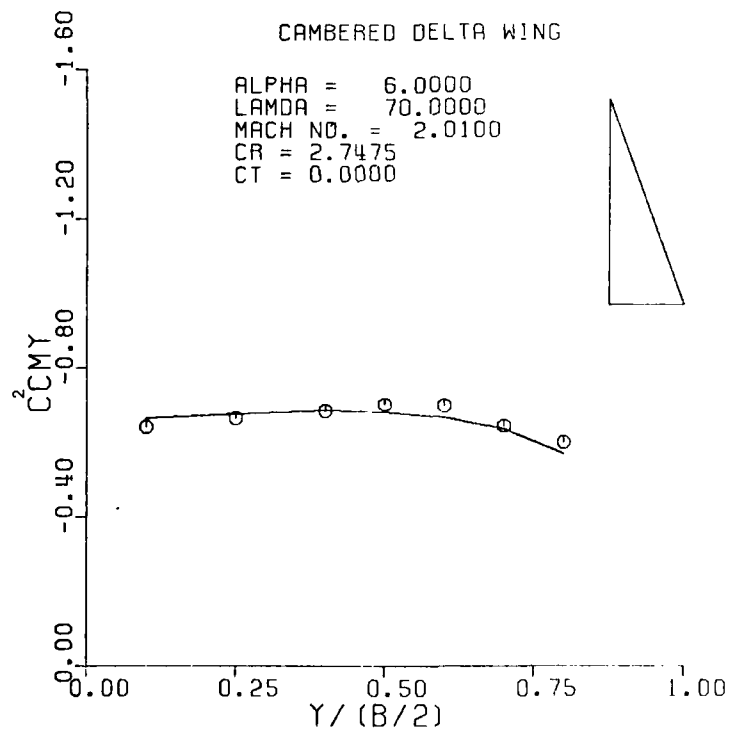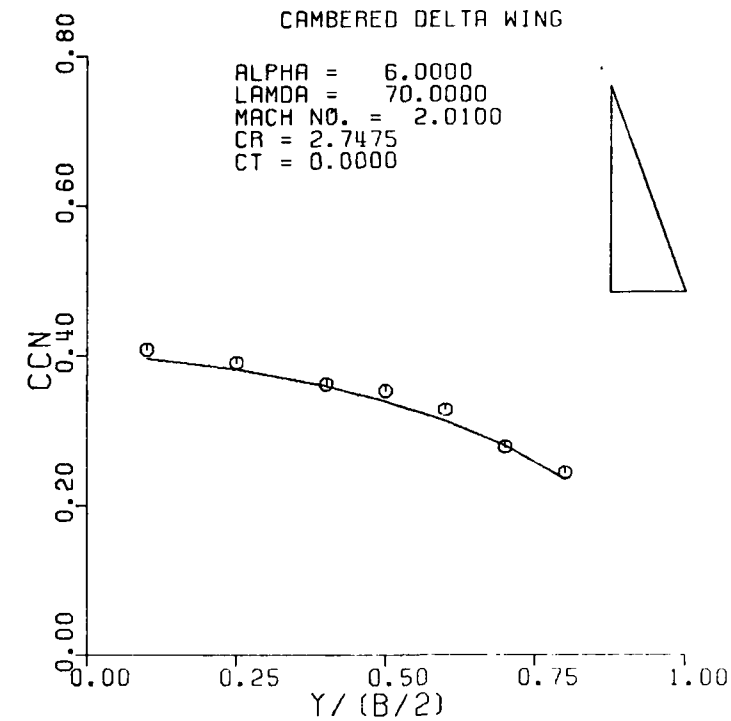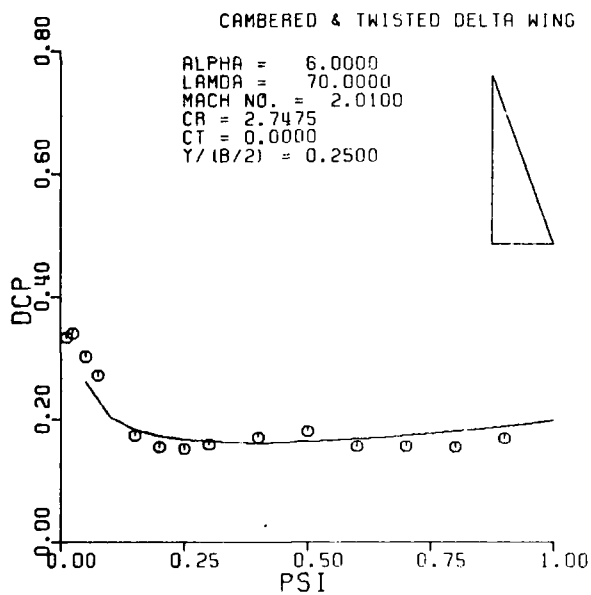Figure 29.   Pressure Distribution on a Flat Tapered Wing; $M = 1.61$, $\alpha = 2.0$.

FLAT TAPERED WING

ALPHA   =   2.0000
LAMDA   =   54.1154
MACH NO. =   1.6100
CR = 0.9524
CT = 0.1905
Y/(B/2) = 0.7000

FLAT TAPERED WING

ALPHA   =   2.0000
LAMDA   =   54.1154
MACH NO. =   1.6100
CR = 0.9524
CT = 0.1905
Y/(B/2) = 0.9000
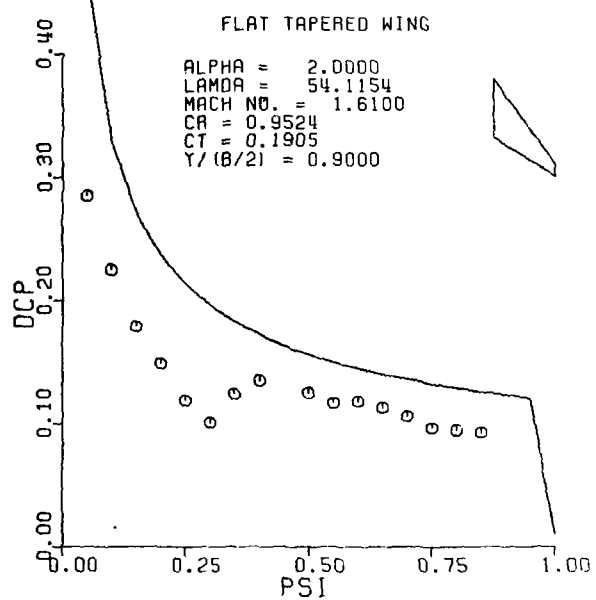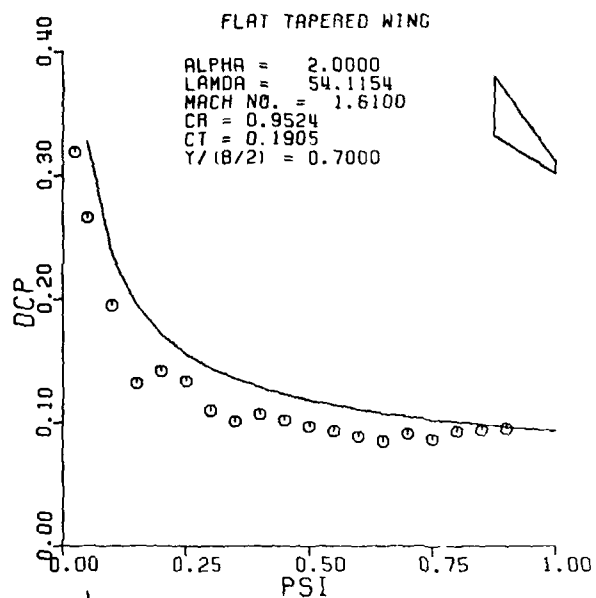
Figure 29.   Continued
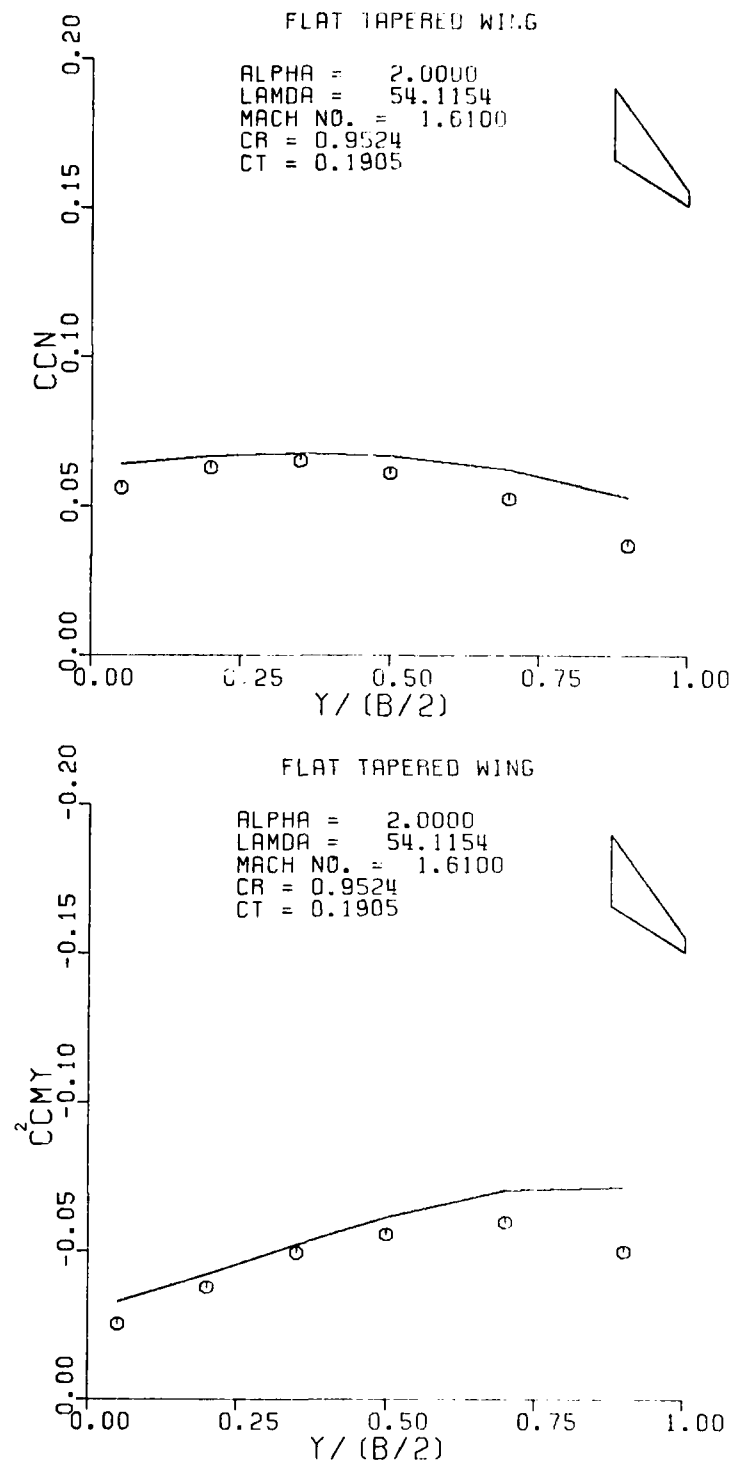
Figure 30.   Sectional Normal Force and Pitching Moment
for a Flat Tapered Wing; M = 1.61, α = 2.0.
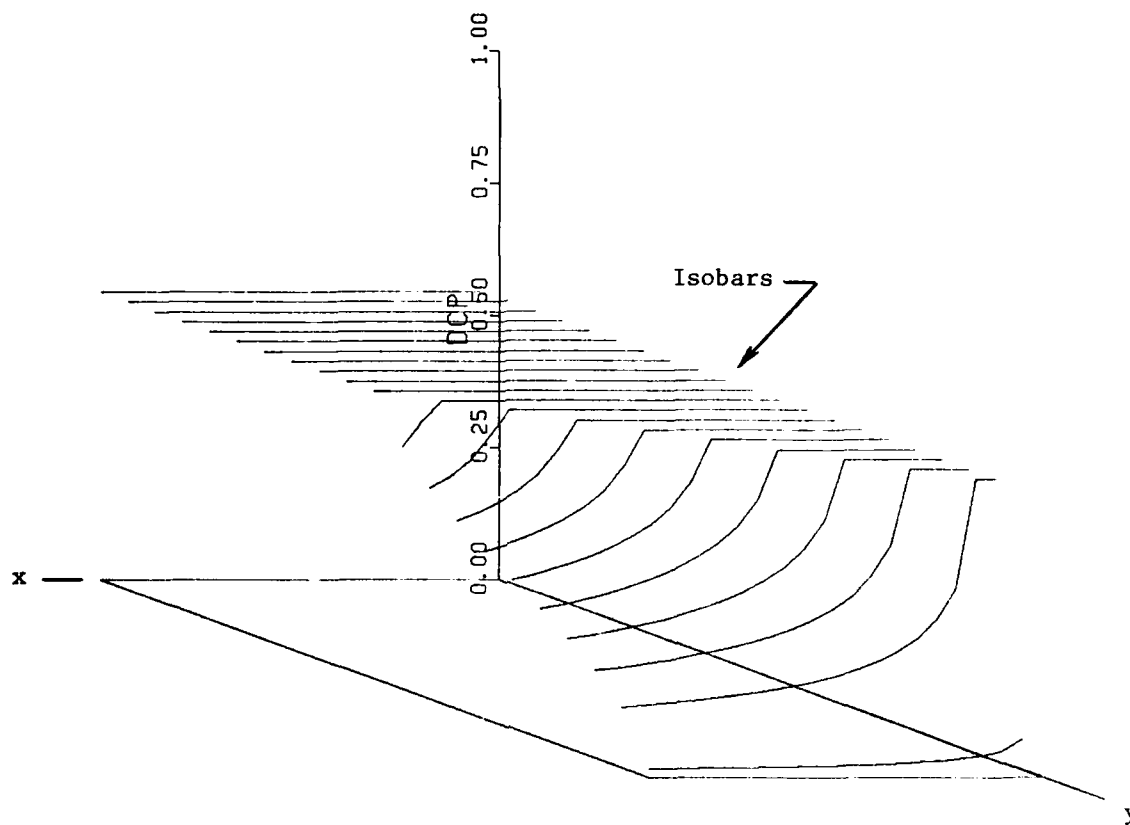
WING PRESS. LOADING

ALPHA = 10.00
LAMDA = 0.00
CR = 0.61
CT = 0.61
M = 1.62

Fig. 31. Typical Multiple Isobars on a Rectangular Wing Planform.

Isobars

DCP

0.00   0.25   0.50   0.75   1.00

x

WING PRESS. LOADING

ALPHA =   10.00

LAMDA =   70.00

CR =   1.79

CT =   0.00

M =   1.61

y
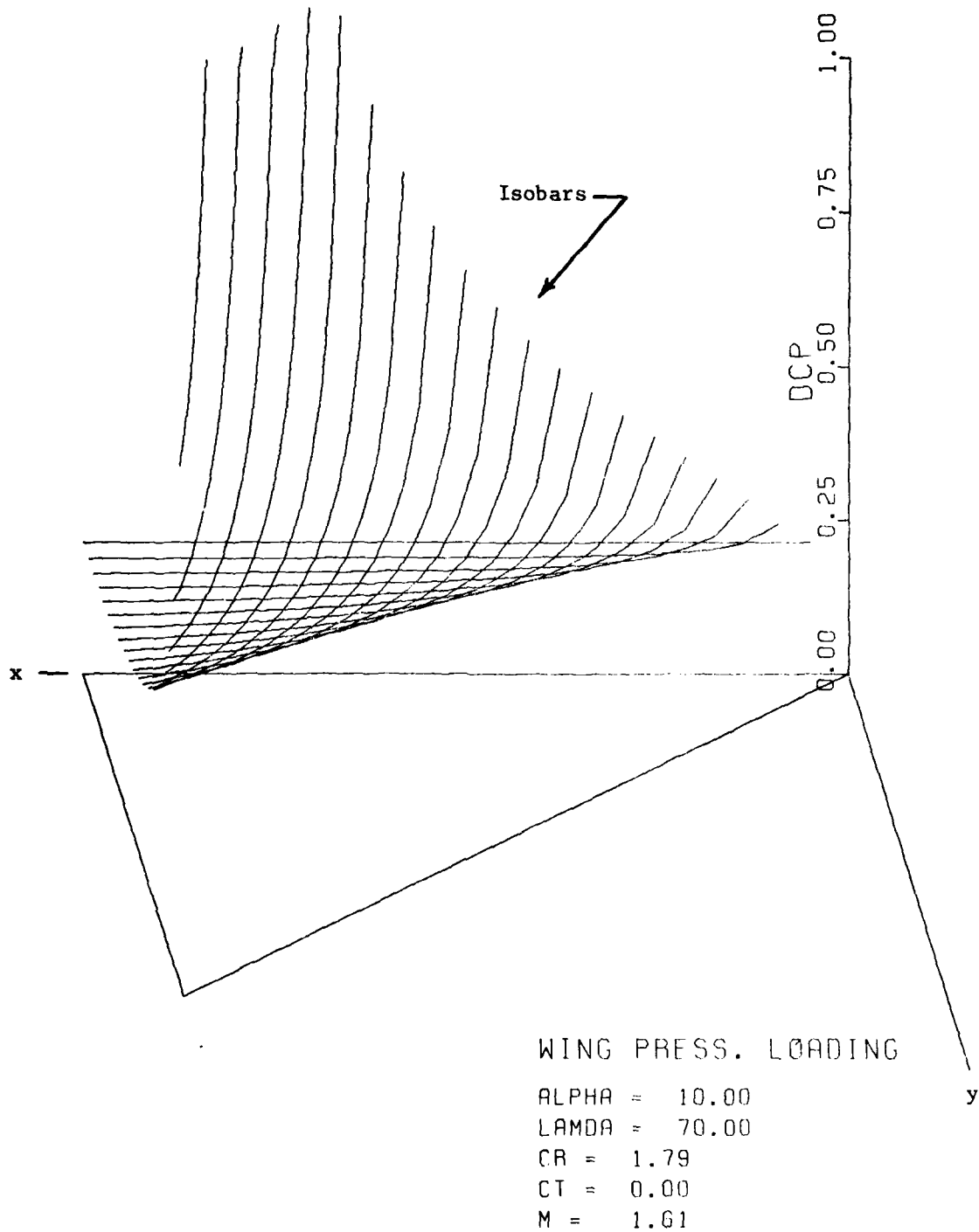
Fig. 32.   Typical Multiple Isobars on a Delta Wing Planform.

Isobars

DCP

1.00

0.75

0.50

0.25

0.00

x

y
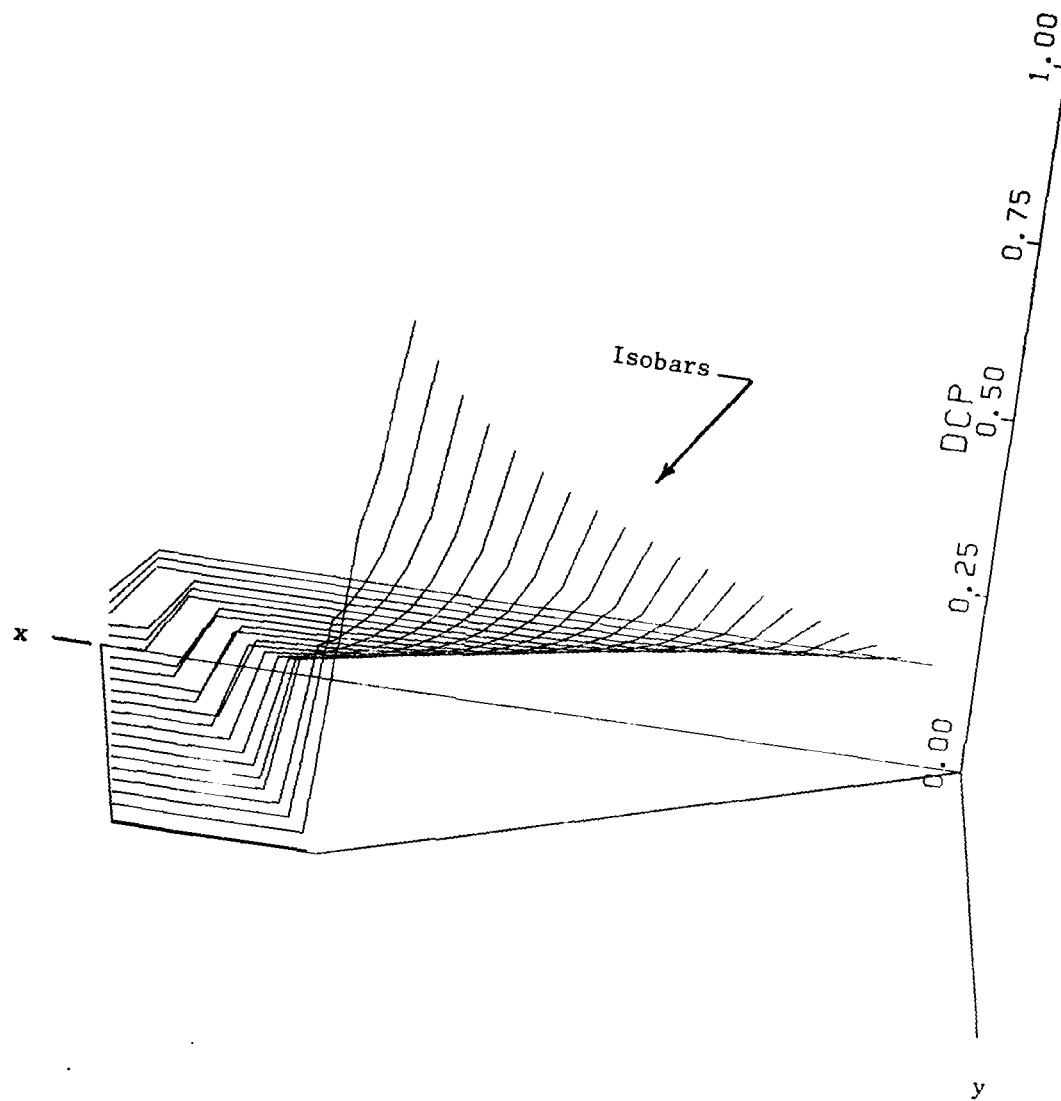
WING PRESS. LOADING

ALPHA =   10.00
LAMDA =   77.23
CR =   5.79
CT =   1.38
M =   1.62

Fig. 33. Typical Multiple Isobars on a Cropped Delta Wing Planform.

Isobars

x

y
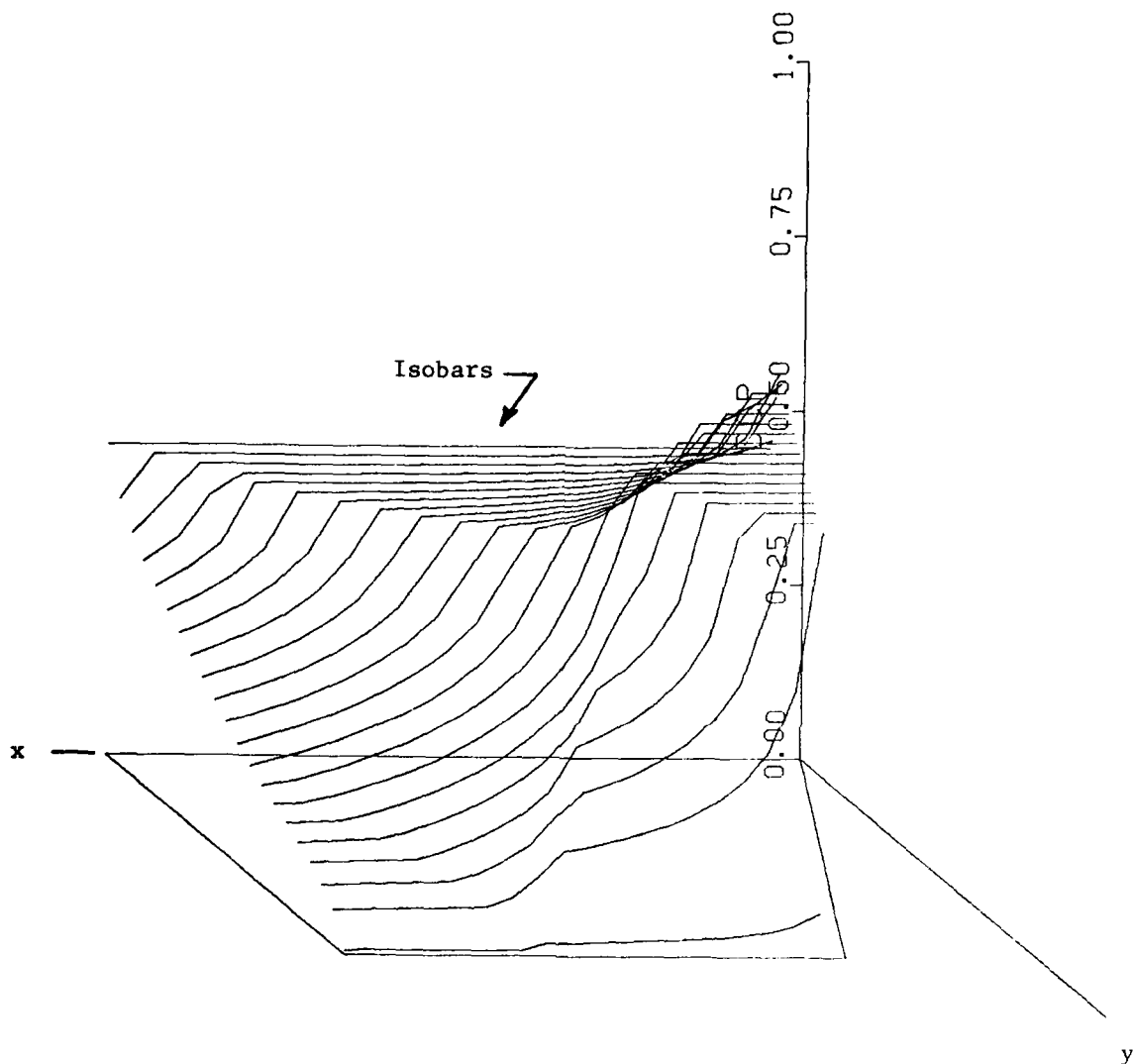
WING PRESS. LOADING

ALPHA = 10.00
LAMDA = 25.79
CR = 1.73
CT = 1.25
M = 1.61

Fig. 34. Typical Multiple Isobars on a Trapexoidal Wing Planform.

Table 2

		Delta Wing	Low AR Trapezoidal Wing	High AR Trapezoidal Wing
C_{L_α}	Experiment	.029	.033	.048
$\alpha = 0$	Theory	.029	.032	.053
$(C_{M_\alpha})_y$	Experiment	-.029	-.019	-.064
$\alpha = 0$	Theory	-.029	-.019	-.073

leading edge and wing tip is to be expected and is due to wing thickness, shocks, and wing twist; the latter, of course, is not significant for the low aspect ratio wings.

Deformed Wings

These same wings under various kinds of deformation were also analyzed by including vorticity paneling as well as the 3-D theoretical loading terms in the ΔC_p distribution. Deformation shapes of three of these wings are shown in Fig. 35. The delta wing (No. 1) in Fig. 35 was cambered and the slope relative to the chord line of the mean camber line was determined to be

$$\theta = -3.00825 + \tan^{-1}[\tan 6°(\xi - \xi\eta + \eta)] \tag{100}$$

where $\eta = y/(b/2)$ and $\xi = (x - x_{LE})/c$. The camber (see Fig. 35) is uniform in the spanwise direction and produces a maximum deflection angle of three degrees relative to the chord line. Although this seems like a small task, this is actually a severe test of the theory and its agreement with experimental data. In Figs. 36 through 41, results are presented for three

(a) Cambered Delta Wing

$$\theta_{i,j} = -3.00825 + \tan^{-1}[\tan 6°(\xi-\xi\eta+\eta)]$$

(b) Cambered and Twisted Delta Wing

$$\theta_{i,j} = \tan^{-1}[0.140541(\xi-\xi\eta+\eta)\eta]$$

(c) Warped Trapezoidal Wing
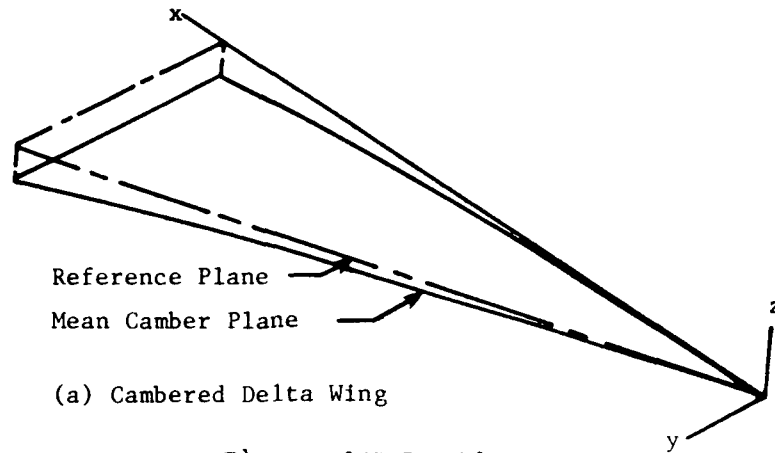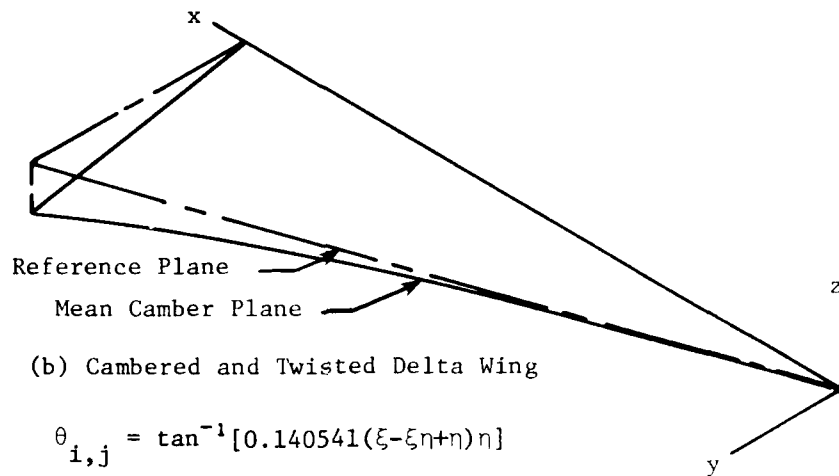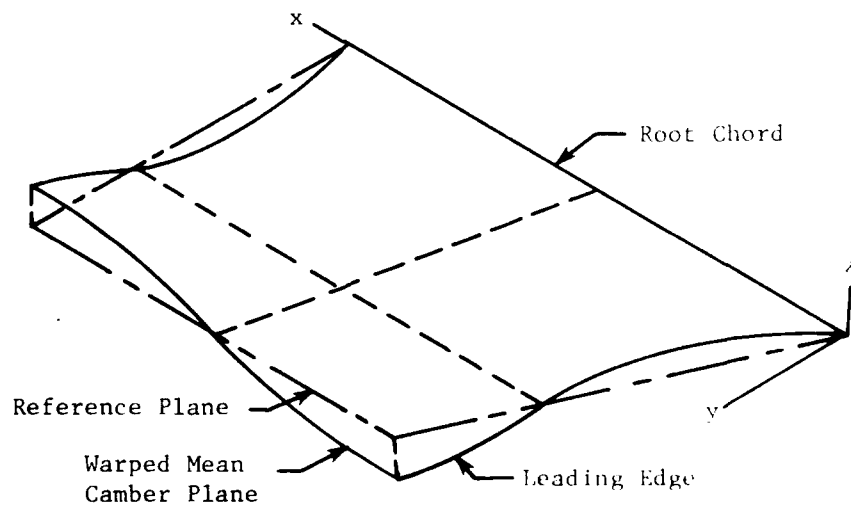
$$\theta_{i,j} = -\tan^{-1}[-0.033454\pi \sin(\frac{3\pi\eta}{2})\sin(\pi\xi)]$$

Fig. 35.   Schematic of Three Deformed Wing Shapes.
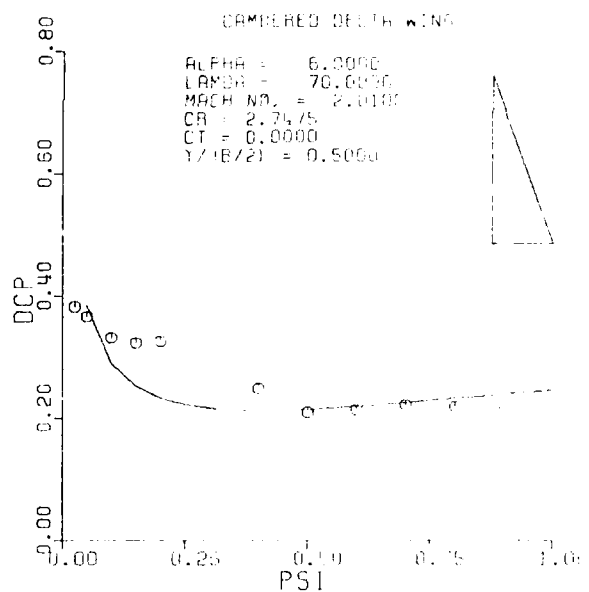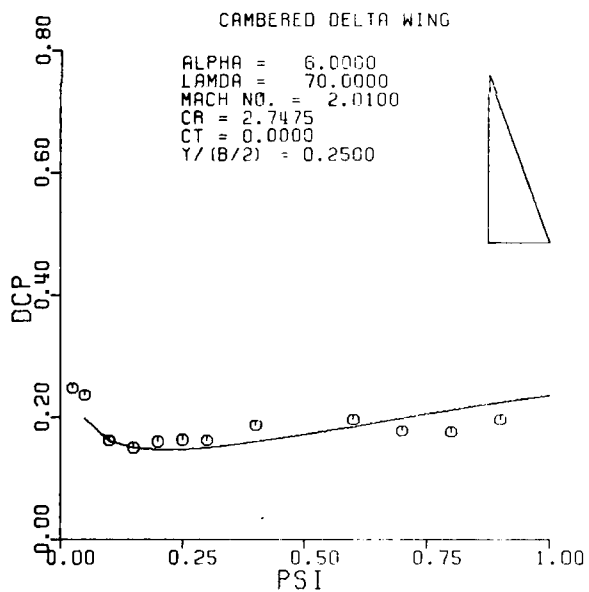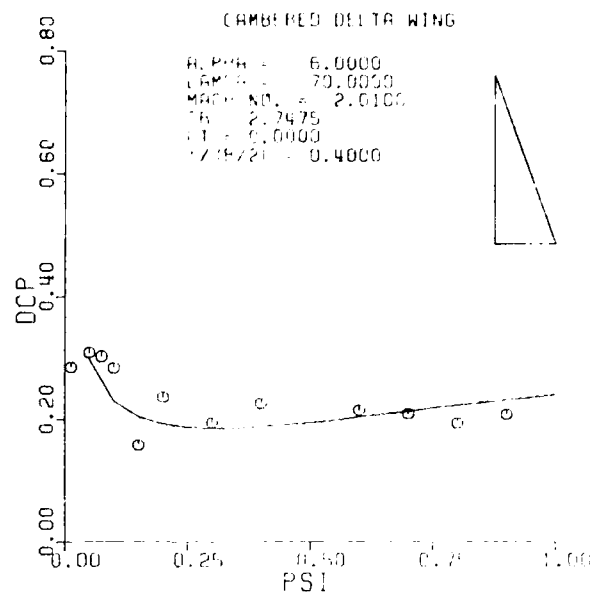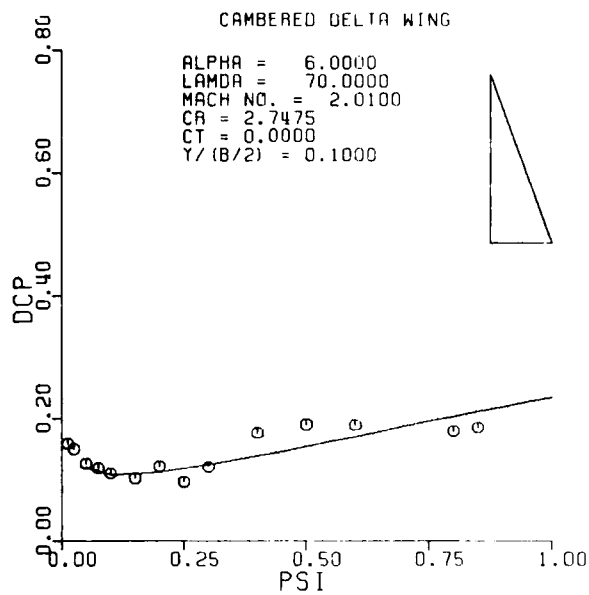
Figure 36. Pressure Distribution on a Cambered Delta Wing; M = 2.01, α = 6.0.

CAMBERED DELTA WING

ALPHA = 6.0000
LAMDA = 70.0000
MACH NO. = 2.0100
CR = 2.7475
CT = 0.0000
Y/(B/2) = 0.6000

CAMBERED DELTA WING

ALPHA = 6.0000
LAMDA = 70.0000
MACH NO. = 2.0100
CR = 2.7475
CT = 0.0000
Y/(B/2) = 0.8000

CAMBERED DELTA WING

ALPHA = 6.0000
LAMDA = 70.0000
MACH NO. = 2.0100
CR = 2.7475
CT = 0.0000
Y/(B/2) = 0.7000
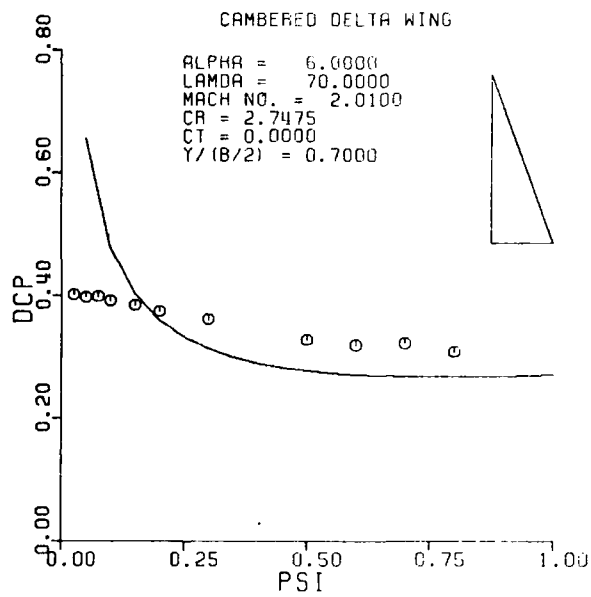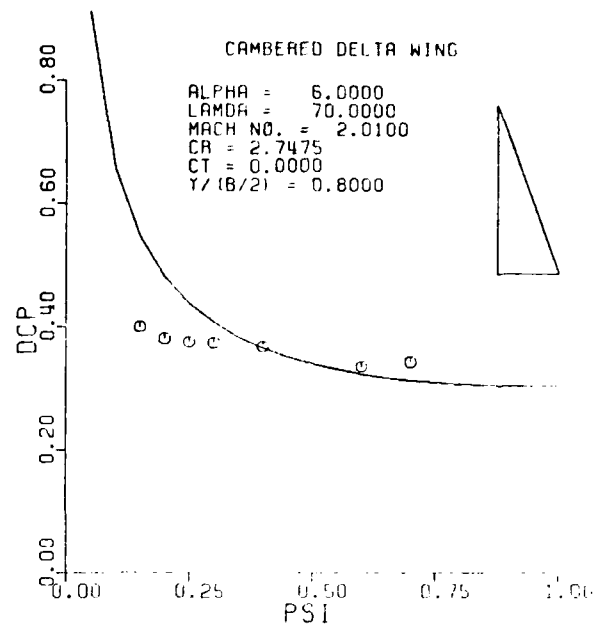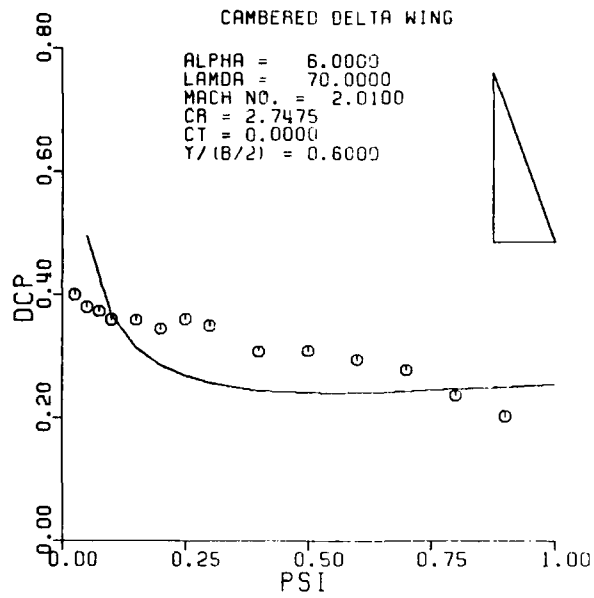
Figure 36.   Continued

Figure 37.   Sectional Normal Force and Pitching Moment for a
Cambered Delta Wing; M = 2.01, α = 6.0.
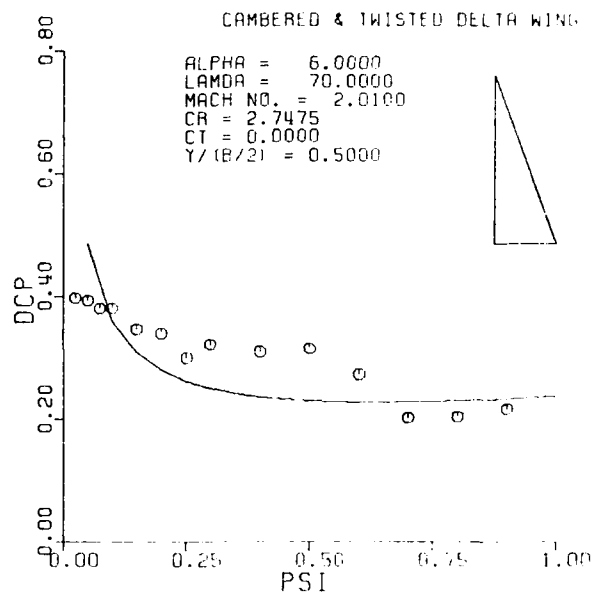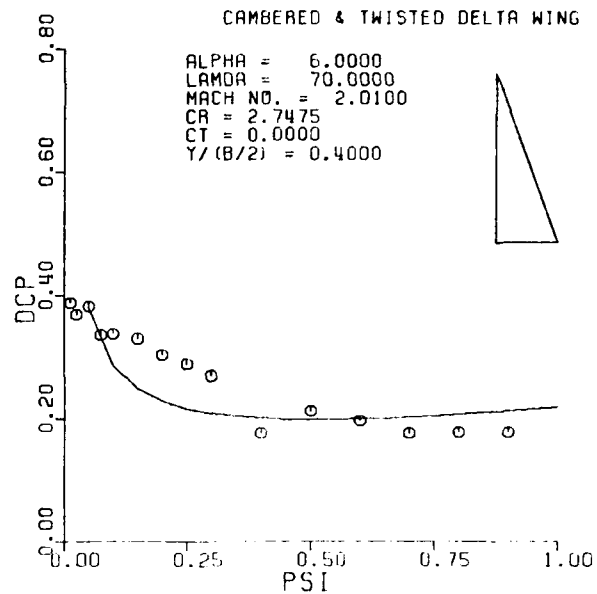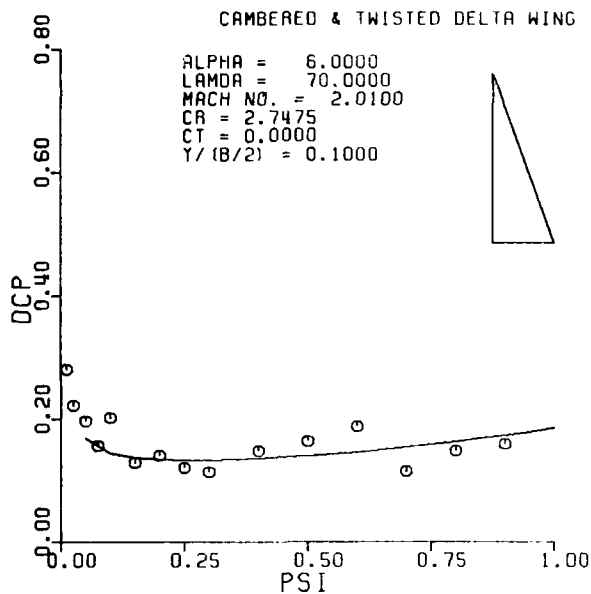
Figure 38. Pressure Distribution on a Cambered and Twisted Delta Wing;
M = 2.01, α = 6.0.

CAMBERED & TWISTED DELTA WING

ALPHA = 6.0000
LAMDA = 70.0000
MACH NO. = 2.0100
CR = 2.7475
CT = 0.0000
Y/(B/2) = 0.6000

CAMBERED & TWISTED DELTA WING

ALPHA = 6.0000
LAMDA = 70.0000
MACH NO. = 2.0100
CR = 2.7475
CT = 0.0000
Y/(B/2) = 0.8000

CAMBERED & TWISTED DELTA WING

ALPHA = 6.0000
LAMDA = 70.0000
MACH NO. = 2.0100
CR = 2.7475
CT = 0.0000
Y/(B/2) = 0.7000
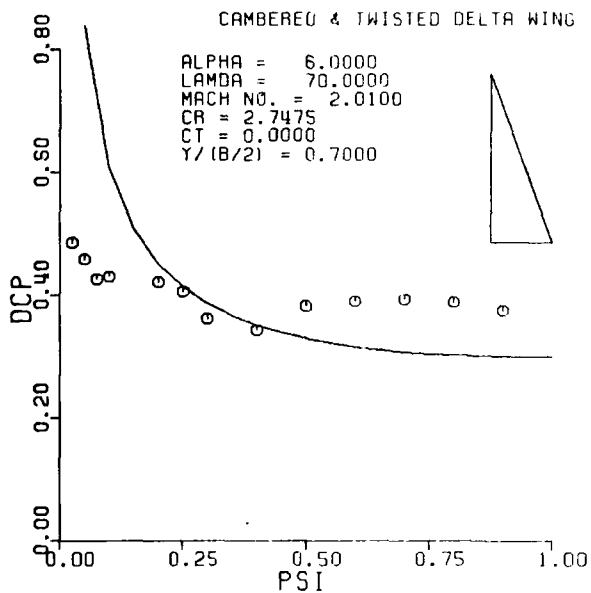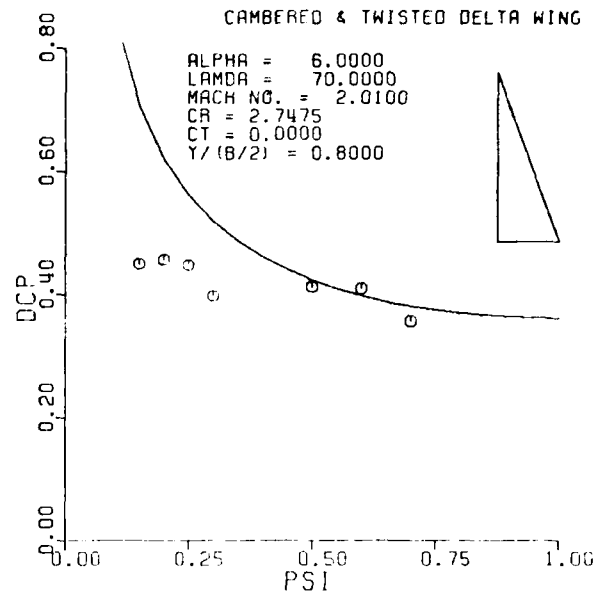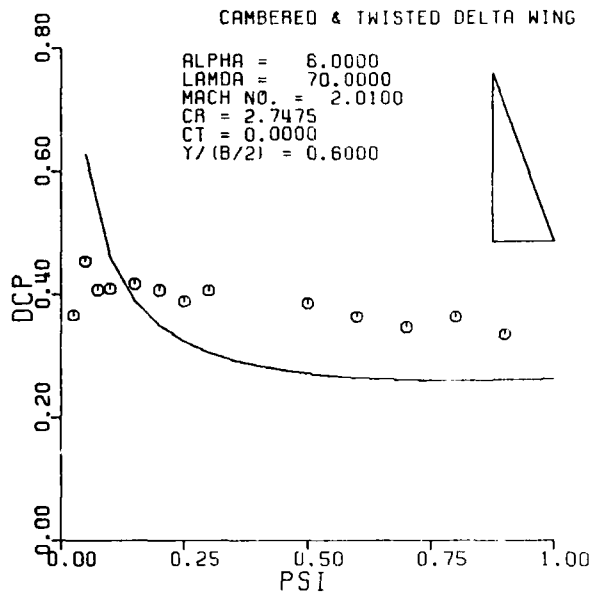
Figure 38.   Continued
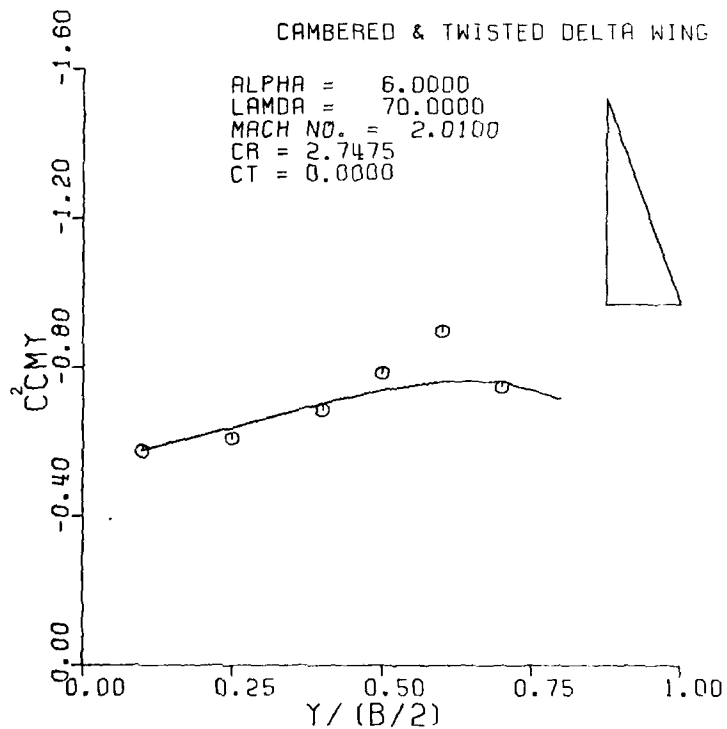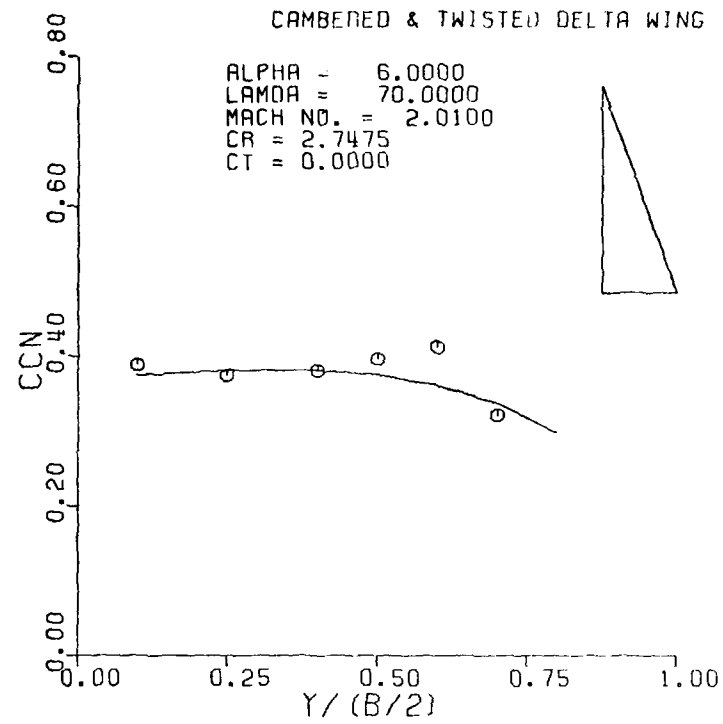
Figure 39. Sectional Normal Force and Pitching Moment for a Cambered and Twisted Wing; M = 2.01, α = 6.0.
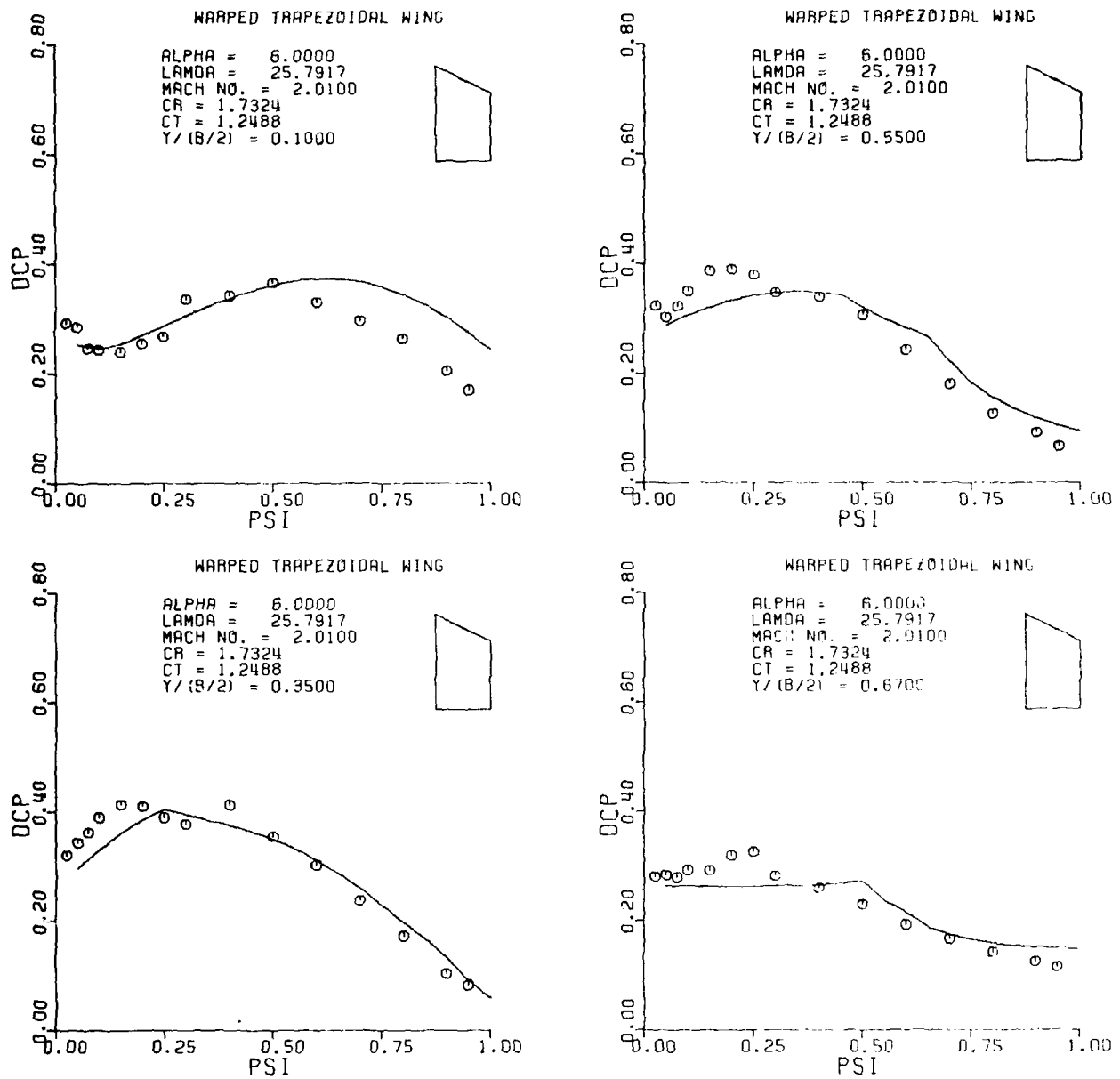
Figure 40. Pressure Distribution on a Warped Trapezoidal Wing; M = 2.01 α = 6.0.

WARPED TRAPEZOIDAL WING

ALPHA =   6.0000
LAMDA =   25.7917
MACH NO. =   2.0100
CR = 1.7324
CT = 1.2488
Y/(B/2) = 0.7700

WARPED TRAPEZOIDAL WING

ALPHA =   6.0000
LAMDA =   25.7917
MACH NO. =   2.0100
CR = 1.7324
CT = 1.2488
Y/(B/2) = 0.9700

WARPED TRAPEZOIDAL WING

ALPHA =   6.0000
LAMDA =   25.7917
MACH NO. =   2.0100
CR = 1.7324
CT = 1.2488
Y/(B/2) = 0.8700
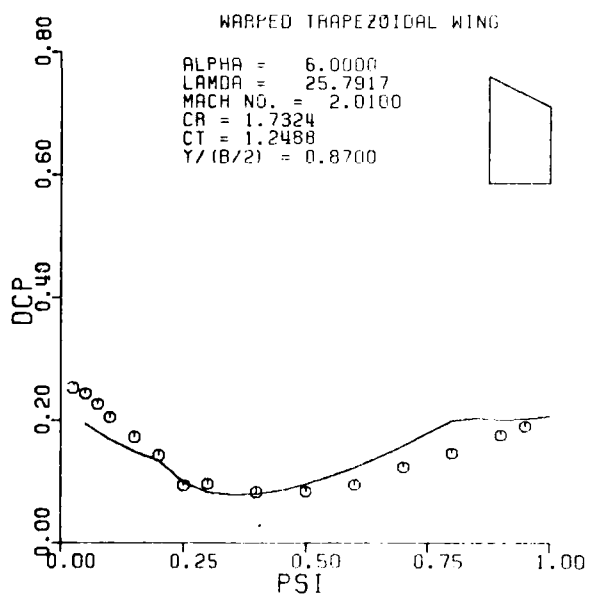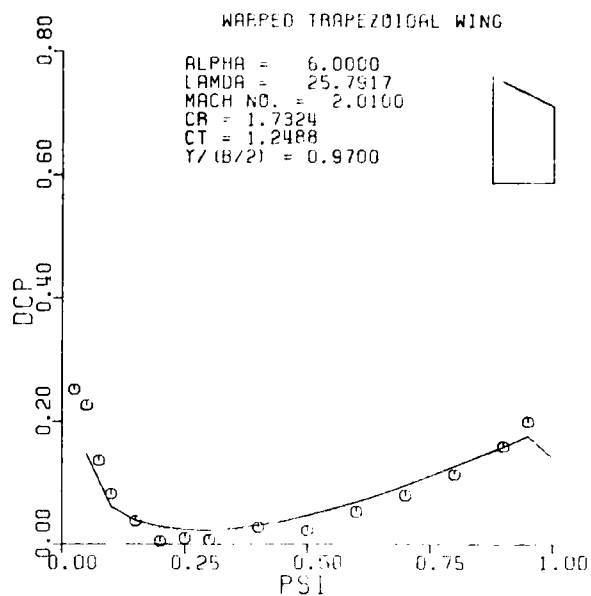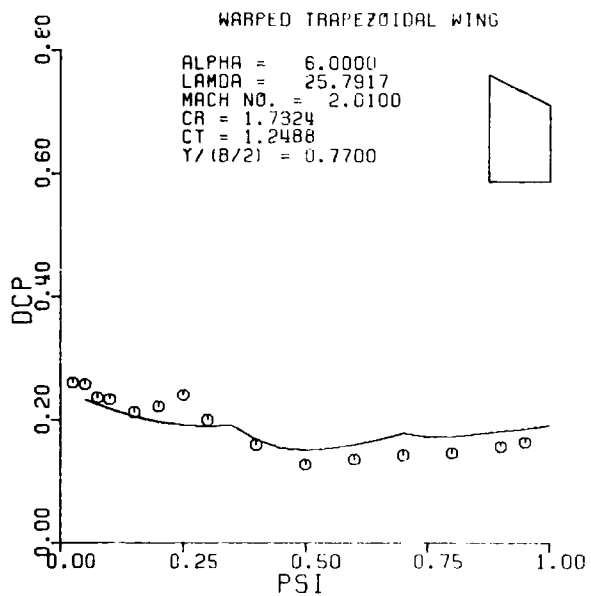
Figure 40.   Continued
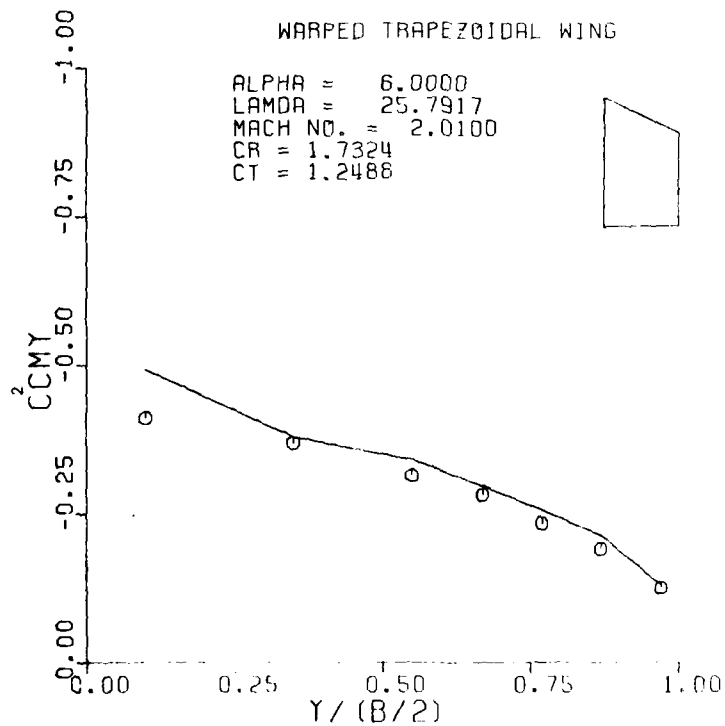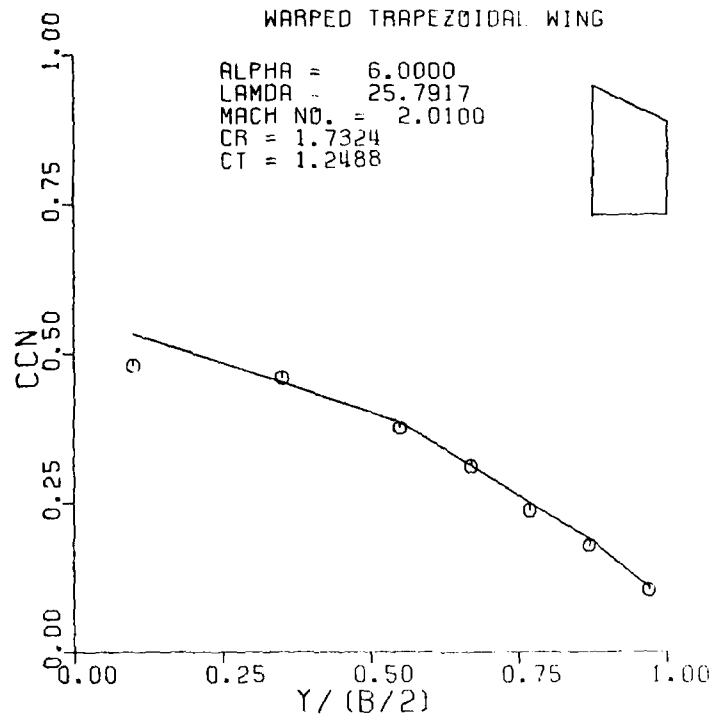
Figure 41.   Sectional Normal Force and Pitching Moment for a
             Warped Trapezoidal Wing; M = 2.01; α = 6.0.

deformed configurations at a Mach number of 2.01 and angle of attack of 6 degrees. A more complete summary of agreement between the theory and experimental data is presented in Appendix A.

For the cambered delta wing, agreement at the inboard stations is relatively good while outboard agreement is rather poor. However, note that in the regions where most of the wing loading occurs, the agreement is satisfactory. Additionally, the inclusion of the doublet paneling terms in the mathematical formulation provides the correct trends and an added degree of accuracy.

For the same planform shape, linear spanwise twist is added to the camber deformation such that the mean camber surface is now defined as

$$\theta_{i,j} = \tan^{-1}[0.140541(\xi-\xi\eta+\eta)\eta] \tag{101}$$

Results of this configuration are shown in Figs. 38 and 39 and in Appendix A. Similar results are obtained for these cases as was observed for the cambered (alone) case. Agreement is acceptable at the inboard stations but is questionable at the outboard stations.

In observing the experimental data for both the cambered alone and the cambered and twisted wings, the outboard stations ($\eta > .5$) appear to have a supersonic leading edge. Whereas the high leading edge sweep angle gives rise to a subsonic leading edge. In addition, at the $\eta = 0.5$ station, a weak shock appears to be located near $\xi = .4$ for M = 1.61 but is not present for M = 2.01 (see Appendix A). Since the theory does not account for the shocks, the disagreement in this region is not surprising.

The next wing subjected to the theoretical analysis was a "warped" trapezoidal wing (see Fig. 35). For both M = 1.61 and 2.01, the leading

edge is supersonic and multiple "fold over" regions occur because of the low aspect ratio of the fact that the wing is trapezoidally shaped. The equation governing the mean warped camber surface is

$$\theta_{i,j} = -\tan^{-1}[-0.033454\pi \sin(\frac{3\pi\eta}{2})\sin(\pi\xi)] \tag{102}$$

Results for this wing are presented in Figs. 40 and 41 and in Appendix A. Considering the wing deformation, the agreement is remarkably good over the entire wing for both Mach numbers. Note also that the addition of vorticity paneling to the ΔC_p distribution predicts the right trends and correctly accounts for local wing deformations in the upstream running Mach cones.

Elevon Loading

Very little experimental data exists for loading on an elevon immersed in the wake of a wing in supersonic flow. The only data found was Nielsen (Ref. 1) which included the blunt wing trailing edge as previously discussed. Figure 42 is a comparison of the normal force coefficient, C_N, and hinge moment, C_H, versus wing angle of attack for an elevon deflection angle of $-10°$. In this figure, the present theoretical results are compared to experimental data and to the theoretical results from Ref. 1. In the present theory, the blanking effect from the wing is included which seems to properly account for the normal force coefficient variation. It is noted also that compressibility or the Mach number effect, is also properly accounted for, thereby providing excellent agreement (at least for this case) between experimental data and theory.

The hinge moment for the elevon is also plotted and agreement here is not good except at very small angles of attack. Reasons for this discrepancy may be the result of one of the following problems in the analysis or perhaps combinations thereof: (1) It is known that viscous flow in this region could cause large changes in the pressure field as originally hypothesized in Ref. 1. However, because of the excellent agreement of the normal force coefficient data from a potential flow analysis and the schlieren photographs of this region, it is certainly not conclusive that viscous effects dominate the solution. (2) The downwash model as outlined in the theory section is inadequate in predicting the correct downwash velocities. As a matter of fact, if the downwash distribution is assumed to be constant across the elevon span

$\delta = -10°$, Gap = 0.0

△ M = 2.99
○ M = 2.20
□ M = 1.62

M = 2.99
M = 2.20
M = 1.62

M = 2.99 (Ref. 1)

M = 2.20 (Ref. 1)

M = 1.62 (Ref. 1)

CN

ALPHA (DEG)

$\delta = -10°$, Gap = 0.0

CH

M = 2.99 (Ref. 1)
M = 2.20 (Ref. 1)
M = 1.62 (Ref. 1)

M = 1.62
M = 2.20
M = 2.99

ALPHA (DEG)
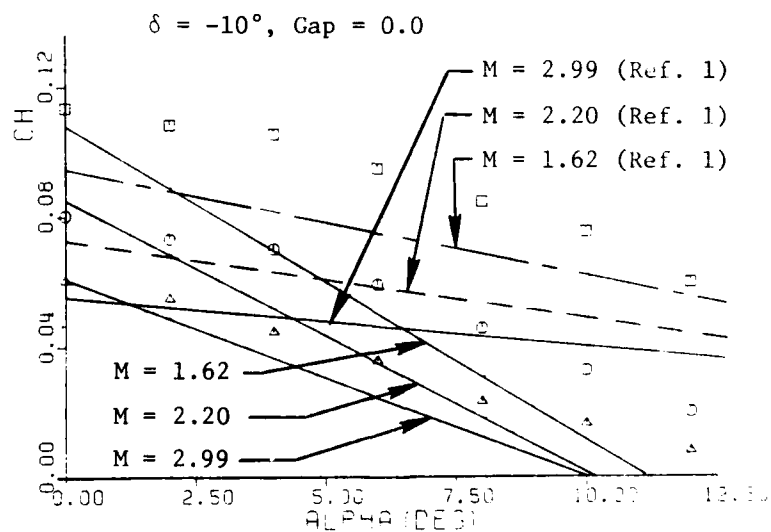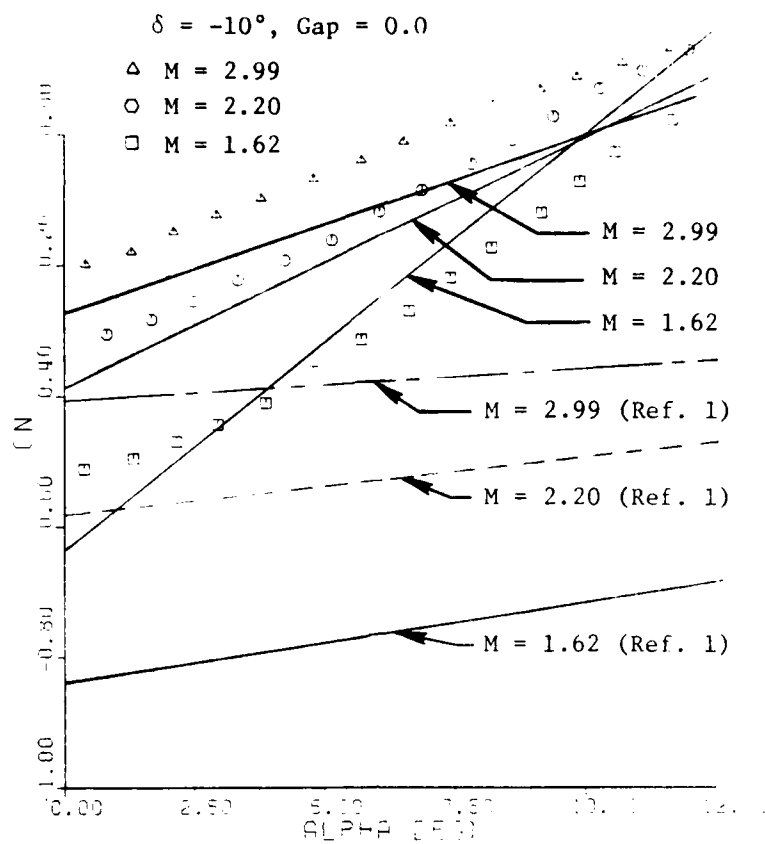
Fig. 42. Elevon Normal Force and Hinge Moment Coefficients
versus Wing Angle of Attack, $\delta = -10°$, Gap = 0.0.

and chord slightly better results are obtained. However, since the total normal force is predicted quite well, the chordwise <u>distribution</u> is apparently in error. From the schlieren photographs (Fig. 23) it appears that much more of the upper surface of the elevon may be blanked out than that predicted in the theory. If this were true, the normal force coefficients would decrease slightly and the moment coefficients would increase (leading edge up) which would give rise to an increase in the associated hinge moment. (3) The assumed location of the trailing vortices relative to the elevon is perhaps incorrect. (4) In analyzing the experimental data from Ref. 1, there is possibly a problem in interpretation and conversion to the reference areas and lengths used in the present theoretical analysis.

In conclusion, it is recognized that the flow field immediately behind the blunt wing trailing edge and elevon leading edge is not well understood. Detailed experiments to measure pressure and loads accompanied by schlieren photographs are required before an adequate model can be postulated.

Finally, Figure 43 is a plot of the theoretically predicted normal force and hinge moments for the elevon when a gap exists between the elevon and the wing. Similar results are obtained as for the "no gap" case but the influence of the gap is clearly identified and the present theory predicts the correct trends.
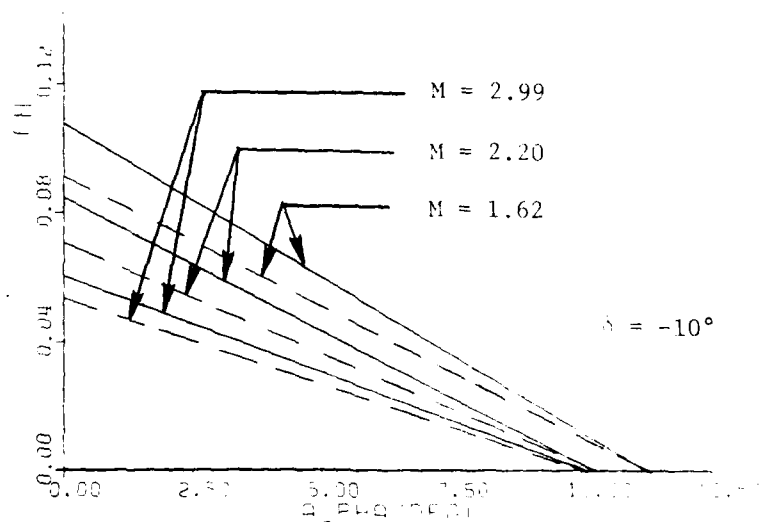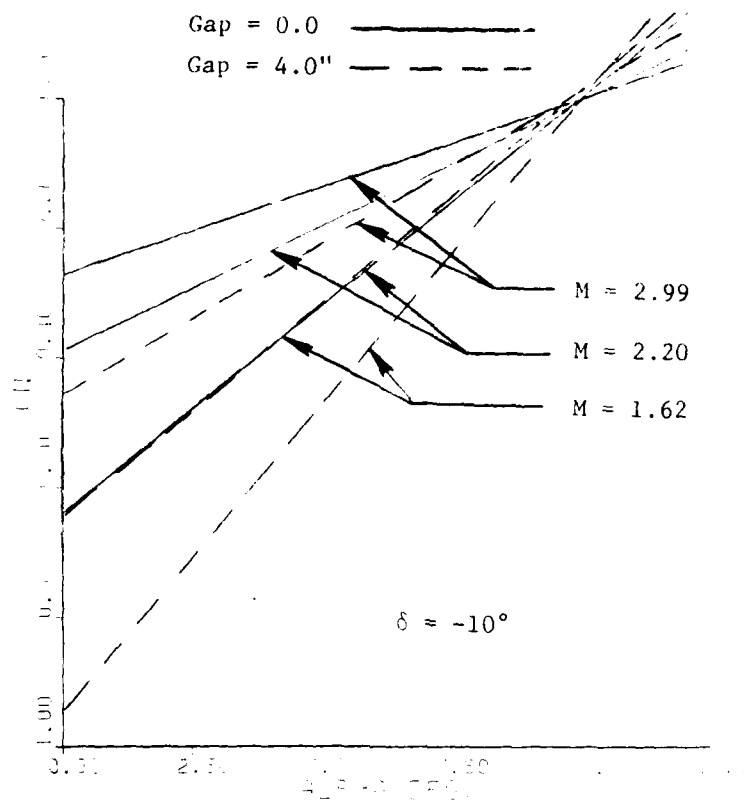
Fig. 43.   Theoretical Normal Force and Hinge Moment Coefficients
versus Wing Angle of Attack for Gap = 0.0 and 4.0",
δ = -10°.

VIII. REFERENCES

1. Selden, B. S., Goodwin, F. K., and Nielsen, J. N., "Analytical Investigation of Hinge Moments on Missile Trailing-Edge Control Surfaces," Final Report, U.S. Army Missile Command, September 1974.

2. Glauert, H., "A Theory of Thin Airfoils," British Aeronautical Research Committee, Rep. and Memo. 910, 1924.

3. Glauert, H., "Theoretical Relationships for an Airfoil with Hinged Flap," British Aeronautical Research Committee, Rep. and Memo., 1095, 1927.

4. Halsey, N. D., "Potential Flow Analysis of Multielement Airfoils Using Conformal Mapping," AIAA Paper No. 79-0271, Jan. 1979.

5. Halsey, N. D., "Potential Flow Analysis of Multiple Bodies Using Conformal Mapping," Master of Science Thesis, California State University, Long Beach, California, Dec. 1977.

6. Ashley, H., "Some Considerations Relative to the Prediction of Unsteady Air Loads on Interfering Surfaces," Symposium on Unsteady Aerodynamics for Aeroelastic Analyses of Interfering Surfaces, Part I, NATO AGARD-CP-80, April 1971.

7. Woodward, F. A., "Analysis and Design of Wing-Body Combinations at Subsonic and Supersonic Speeds," J. of Aircraft, Vol. 5, No. 6, Nov.-Dec. 1968, pp. 528-534.

8. Lan, C. E., "A Quasi-Vortex Lattice Method in Thin Wing Theory," J. of Aircraft, Vol. 11, No. 9, 1974, pp. 516-527.

9. DeJarnette, F. R., "Arrangement of Vortex Lattices on Subsonic Wings," Vortex-Lattice Utilization Workshop, NASA SP-405, NASA Langley Research Center, May 1976, pp. 301-323.

10. Cunningham, A. M., "Oscillatory Supersonic Kernel Function Method for Interfering Surfaces," AIAA Journal of Aircraft, November 1974. Vol. 11, No. 11.

11. Cunningham, A. M., "Unsteady Subsonic Collocation Method for Wings With and Without Control Surfaces," AIAA Journal of Aircraft, June 1972, Vol. 9, No. 6.

12. White, Richard B., And Landahl, Marten T., "Effect of Gaps on the Loading Distribution of Planar Lifting Surfaces," AIAA Journal, Vol. 6, No. 4, April 1968, pp. 626-631.

13. Landahl, M., "Pressure-Loading Functions for Oscillating Wings with Control Surfaces," AIAA Journal, Vol. 6, No. 2, February 1968, pp. 345-348.

14. Purvis, J. W., "Simplified Solution of the Compressible Subsonic Lifting Surface Problem," Master's Thesis, Aerospace Engineering Department, Auburn University, August 1975.

15. Burkhalter, J. E., and Purvis, J. W., "An Aerodynamic Analysis of Deformed Wings in Subsonic and Supersonic Flow," Final Report on U.S. Army Contract DAAG29-77-G-0069, Aerospace Engineering Department, Auburn University, December 1977.

16. Carlson, H. W., and Miller, D. S., "Numerical Methods for the Design and Analysis of Wings at Supersonic Speeds," NASA TN D-7713, 1974.

17. Vaughn, Milton E., Jr., "Pressure Distribution on an Ogee Wing in Supersonic Flow," Master of Science Thesis, Aerospace Engineering Department, Auburn University, Alabama, 1981.

18. Harmon, S. M., and Jeffreys, I., "Theoretical Lift and Damping in Roll of Thin Wings with Arbitrary Sweep and Taper at Supersonic Speeds - Supersonic Leading and Trailing Edges," NACA TN 2114, 1950.

19. Malvestuto, F. S., Margolis, K., and Ribner, H. S., "Theoretical Lift and Damping in Roll of Thin Sweptback Wings of Arbitrary Taper and Sweep at Supersonic Speeds - Subsonic Leading Edges and Supersonic Trailing Edges," NACA TN 1860, 1949.

20. Ashley, H., and Landahl, M., Aerodynamics of Wings and Bodies, Addison-Wesley, Reading, Mass., 1965.

21. Ashley, H., Widnall, S., and Landahl, M., "New Directions in Lifting Surface Theory," AIAA Journal, Vol. 3, No. 1, January 1965, pp. 3-16.

22. Pitts, W. C., Nielsen, J. H., and Kaattari, G. E., "Lift and Center of Pressure of Wing-Body-Tail combinations at Subsonic, Transonic, and Supersonic Speeds," NACA Report 1307, 1957.

23. Purvis, J. W., "Analytical Prediction of Vortex Lift," AIAA Paper 79-0363, 17th Aerospace Sciences Meeting, 1979.

24. Abernathy, J. M., "An Analysis of Gap Effects on Wing-Elevon Aerodynamic Characteristics," Master of Science Thesis, Aerospace Engineering Department, Auburn University, June 1980.

25. Tinling, Bruce E., and Dickson, Jerald K., "Tests of a Model Hori-
    zontal Tail of Aspect Ratio 4.5 in the Ames 12-Foot Pressure Wind
    Tunnel. II-Elevon Hinge Line Normal to the Plane of Symmetry,"
    NACA RM A9H11a, October 1949.

26. Abbott, Ira H., and Von Doenhoff, Albert E., Theory of Wing Sections,
    Dover Publications, Inc., New York, N. Y., 1959.

27. Jones, J. Lloyd, and Demele, Fred A., "Aerodynamic Study of a Wing-
    Fuselage Combination Employing a Wing Swept Back 63°. - Character-
    istics Throughout the Subsonic Speed Range with the Wing Cambered
    and Twisted for a Uniform Load at a Lift Coefficient of 0.25," NACA
    RM A9D25, August 1949.

28. Evvard, John C., "Use of Source Distributions for Evaluating
    Theoretical Aerodynamics of Thin Finite Wings at Supersonic Speeds,"
    NACA Report 915, June 1949.

29. Landrum, E. J., "A Tabulation of Wind-Tunnel Pressure Data and
    Section Aerodynamic Characteristics at Mach Numbers of 1.61 and
    2.01 for Two Trapezoidal and Three Delta Wings Having Different
    Surface Shapes," NADA TN D-1394, 1962.

30. Landrum, E. J., "A Tabulation of Wing-Tunnel Pressure Data and
    Section Aerodynamic Characteristics at Mach Numbers of 1.61 and
    2.01 for a Reflex Cambered Wing and a Cambered and Twisted Wing
    Having the Same Swept Planform," NADA TN D-1393, 1962.

APPENDIX A

TABLE A

Figure Number	Deformation Equation
A1–A28	No deformation
A29–A32	Cambered Delta Wing $\theta = -3.00825 + \tan^{-1}[\tan 6.0°(x - xy + y)]$
A33–A36	Cambered and Twisted Delta Wing $\theta = \tan^{-1}[(\tan 8.0°)(xy - xy^2 + y^2)]$
A37–A40	Warped Trapexoidal Wing $\theta = -\tan^{-1}[-0.033454 \ \pi \ \sin(\frac{3\pi y}{2}) \ \sin(\pi x)]$

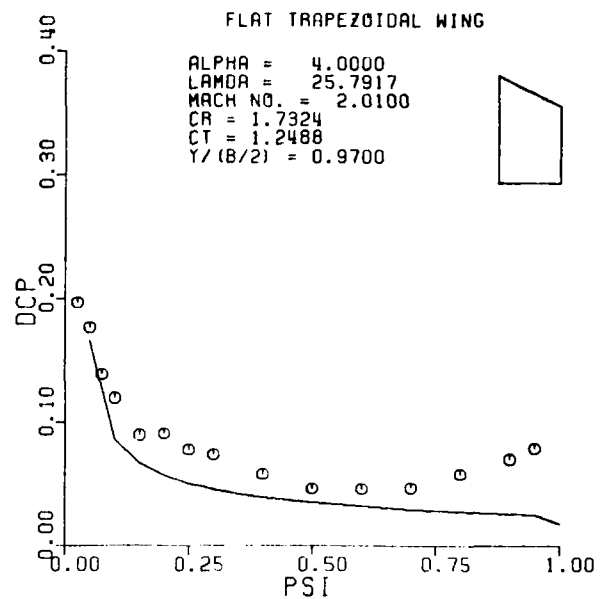Figure Al. Pressure Distribution on a Flat Trapezoidal Wing; M = 1.61,
α = 2.0.

113
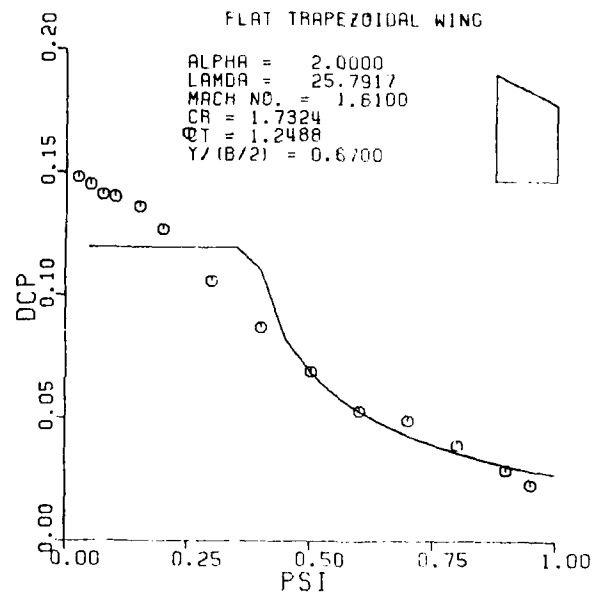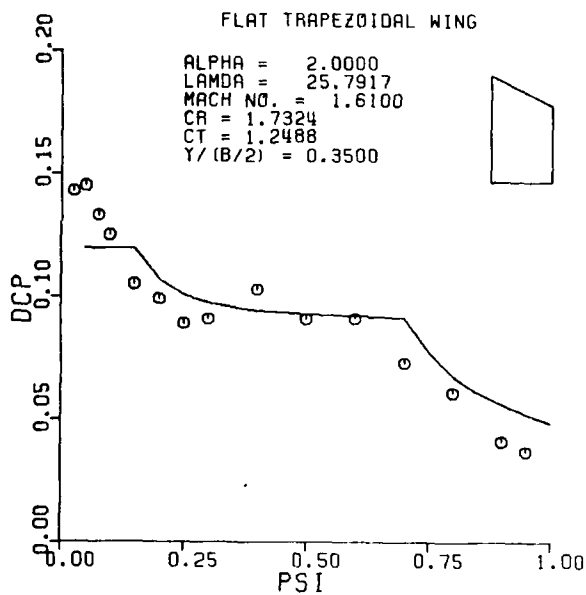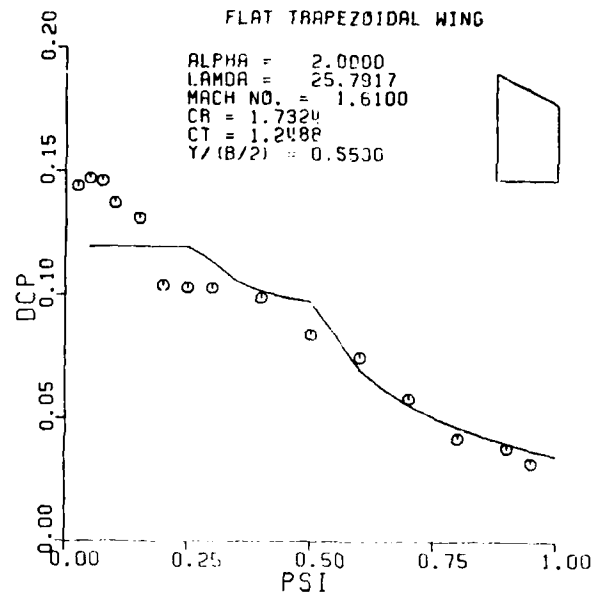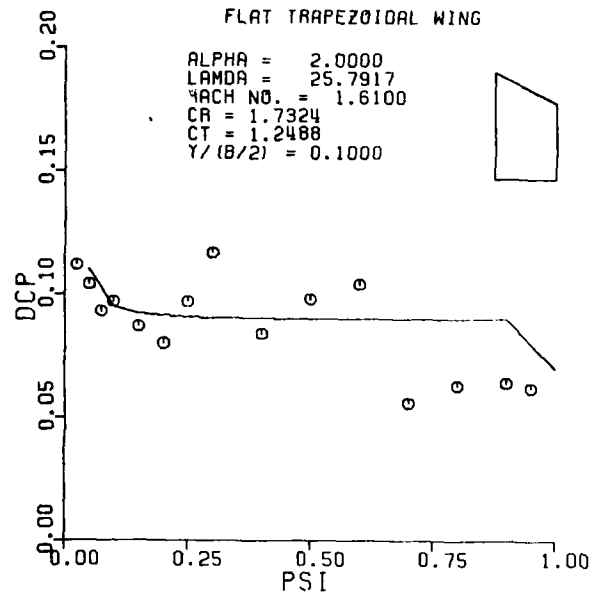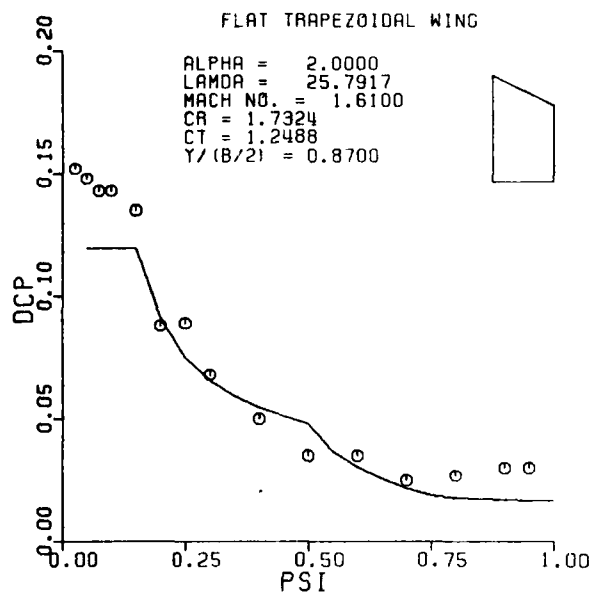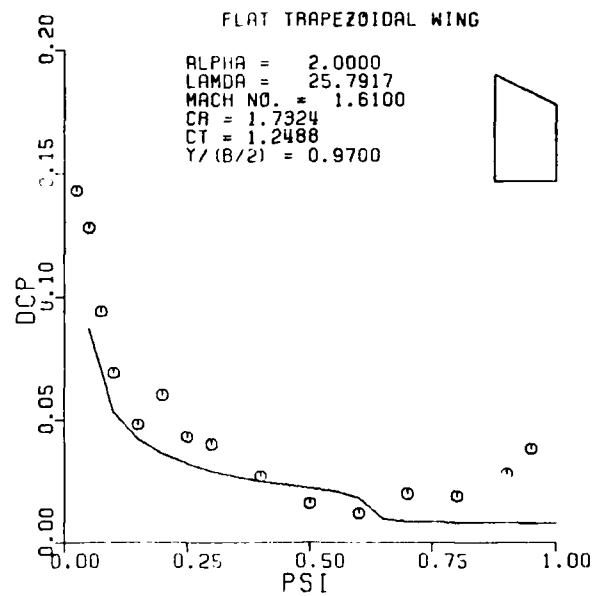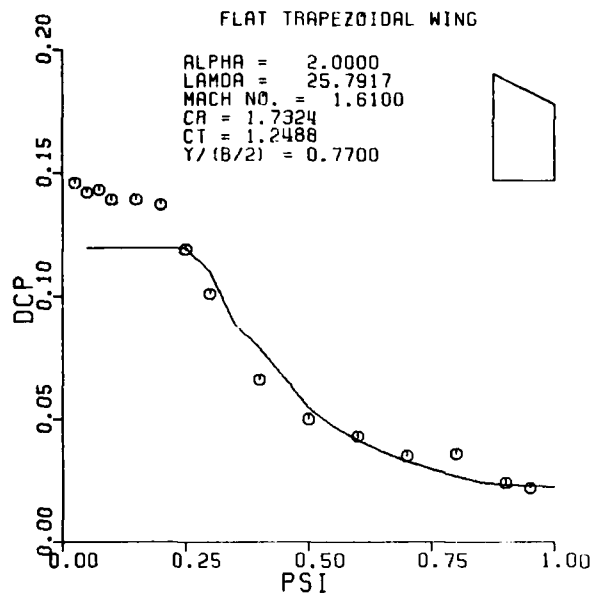
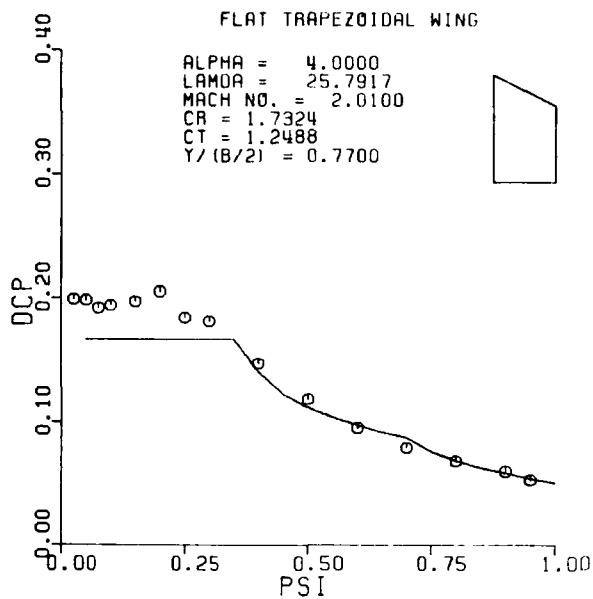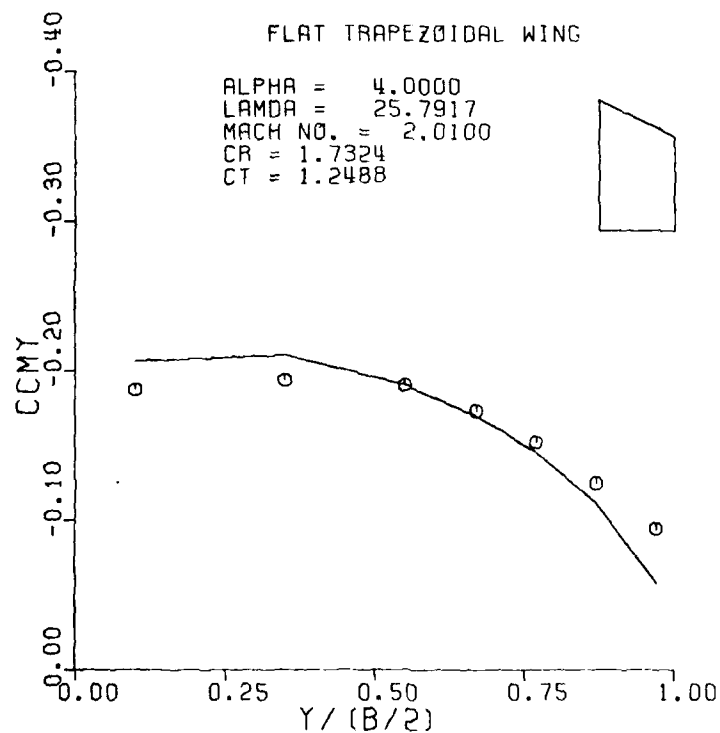Figure A1. Continued
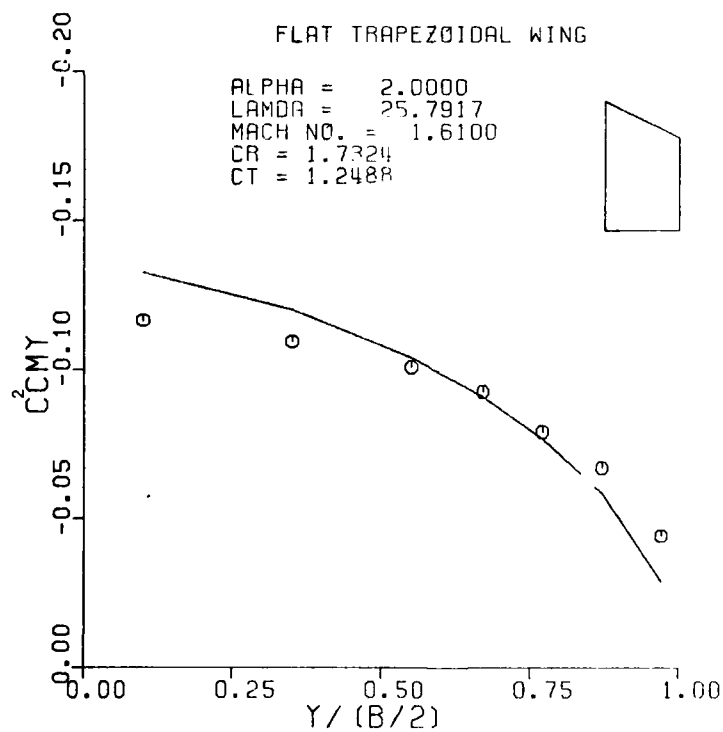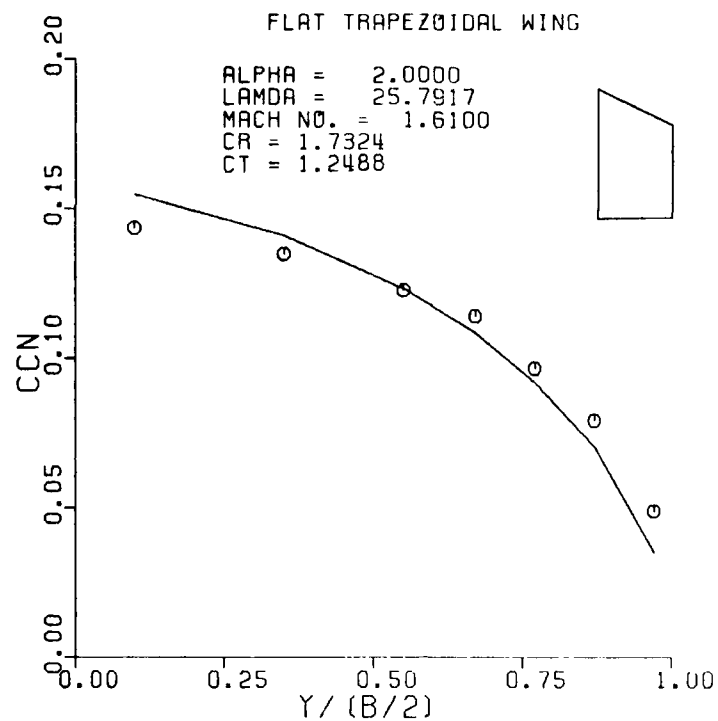
Figure A2.   Sectional Normal Force and Pitching Moment for a
Flat Trapezoidal Wing; M = 1.61, α = 2.0.

FLAT TRAPEZOIDAL WING

ALPHA = 2.0000
LAMDA = 25.7917
MACH NO. = 2.0100
CR = 1.7324
CT = 1.2488
Y/(B/2) = 0.1000

FLAT TRAPEZOIDAL WING

ALPHA = 2.0000
LAMDA = 25.7917
MACH NO. = 2.0100
CR = 1.7324
CT = 1.2488
Y/(B/2) = 0.5500

FLAT TRAPEZOIDAL WING

ALPHA = 2.0000
LAMDA = 25.7917
MACH NO. = 2.0100
CR = 1.7324
CT = 1.2488
Y/(B/2) = 0.3500

FLAT TRAPEZOIDAL WING

ALPHA = 2.0000
LAMDA = 25.7917
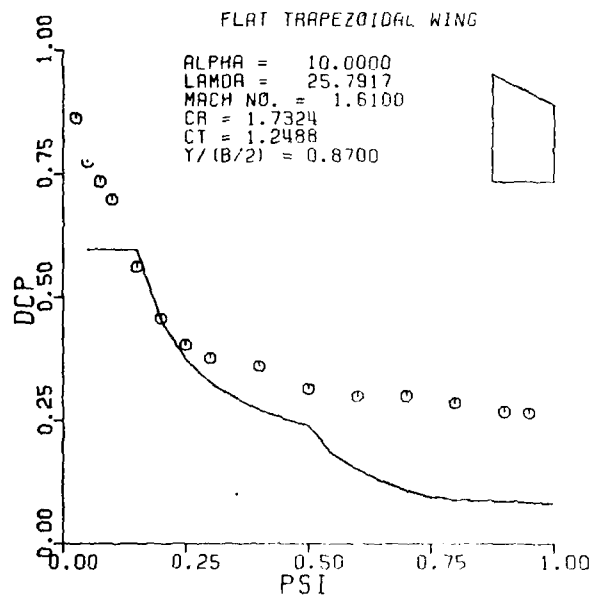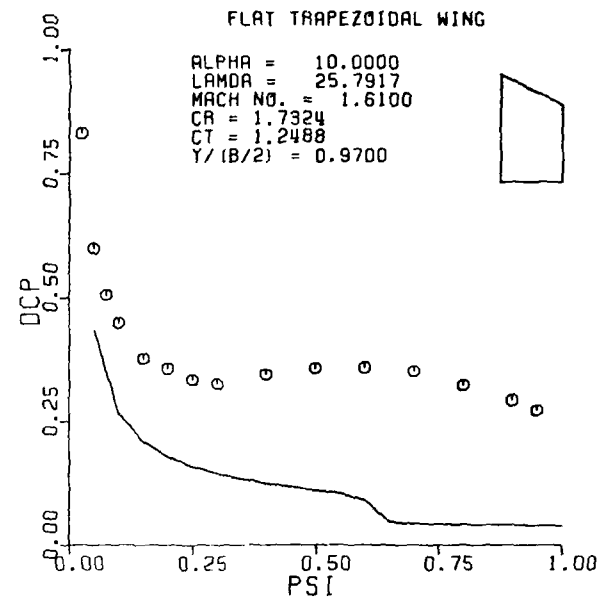MACH NO. = 2.0100
CR = 1.7324
CT = 1.2488
Y/(B/2) = 0.6700
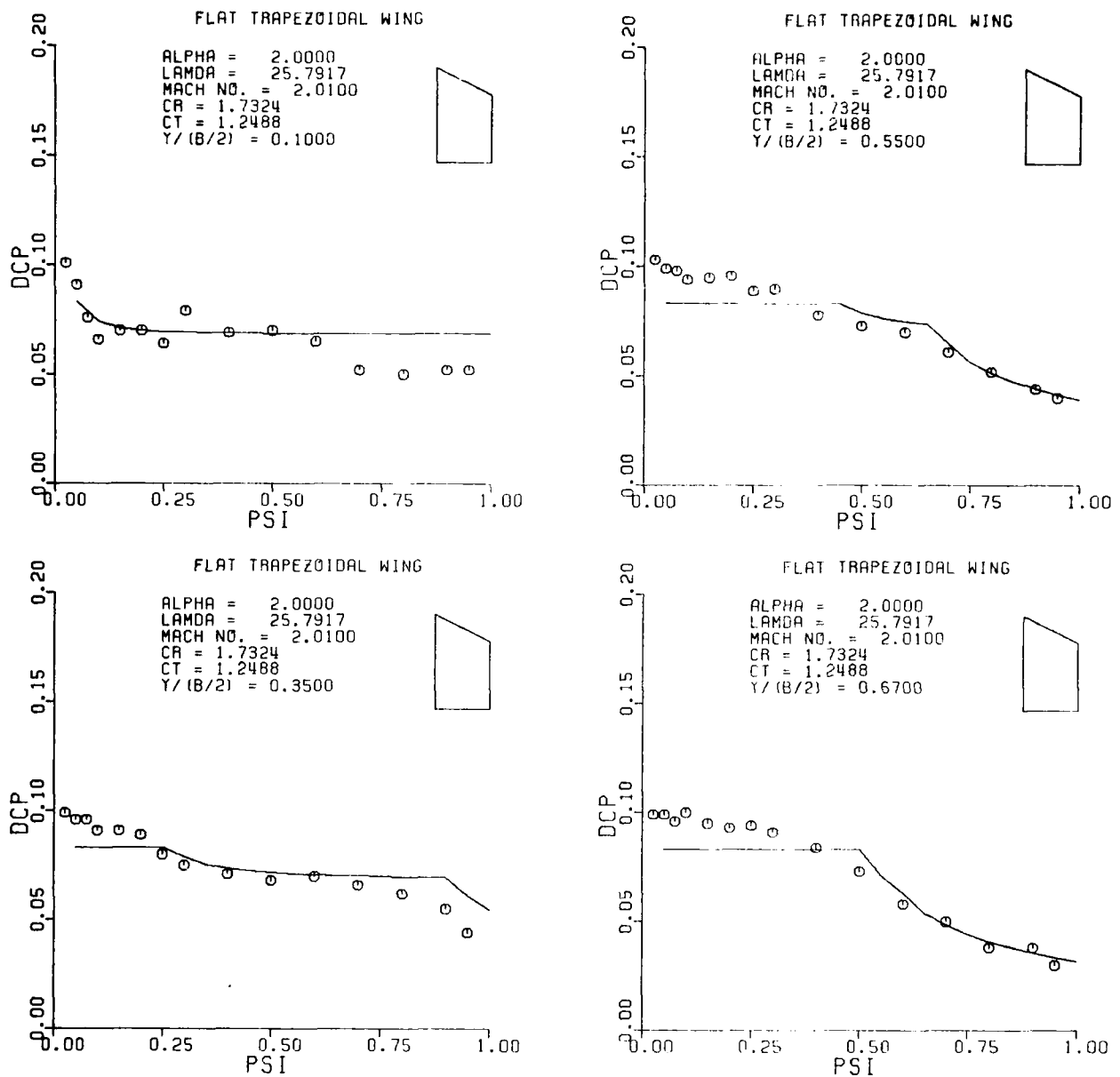
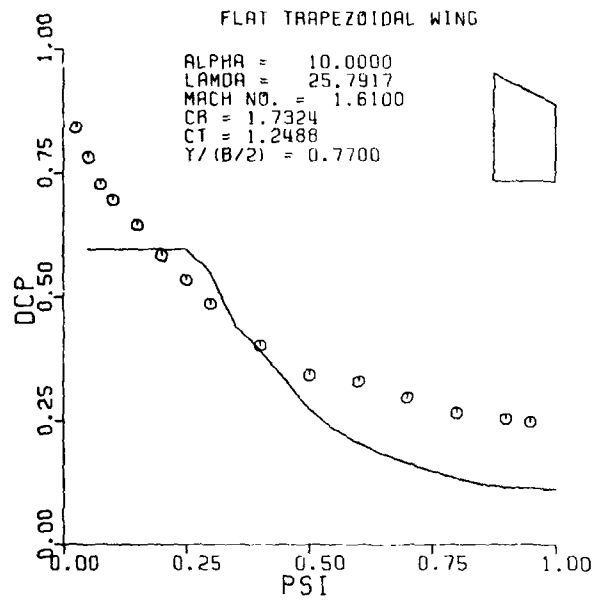Figure A3.   Pressure Distribution on a Flat Trapezoidal Wing; M = 2.01, α = 2.0.

FLAT TRAPEZOIDAL WING

ALPHA = 2.0000
LAMDA = 25.7917
MACH NO. = 2.0100
CR = 1.7324
CT = 1.2488
Y/(B/2) = 0.7700

FLAT TRAPEZOIDAL WING

ALPHA = 2.0000
LAMDA = 25.7917
MACH NO. = 2.0100
CR = 1.7324
CT = 1.2488
Y/(B/2) = 0.9700

FLAT TRAPEZOIDAL WING

ALPHA = 2.0000
LAMDA = 25.7917
MACH NO. = 2.0100
CR = 1.7324
CT = 1.2488
Y/(B/2) = 0.8700

Figure A3. Continued

FLAT TRAPEZOIDAL WING

ALPHA =   2.0000
LAMDA =   25.7917
MACH NO. = 2.0100
CR = 1.7324
CT = 1.2488

CCN

0.00   0.25   0.50   0.75   1.00
Y/(B/2)

FLAT TRAPEZOIDAL WING

ALPHA =   2.0000
LAMDA =   25.7917
MACH NO. = 2.0100
CR = 1.7324
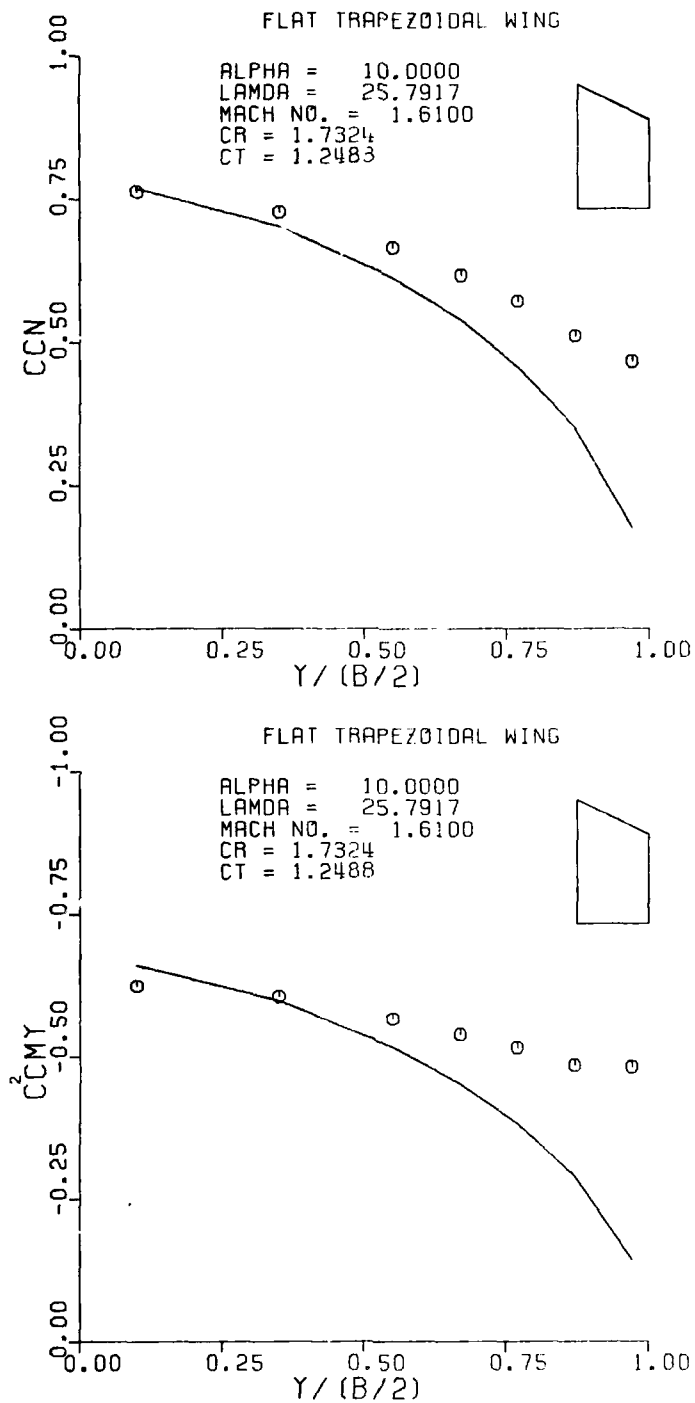CT = 1.2488

C^2CMY

0.00   0.25   0.50   0.75   1.00
Y/(B/2)

Figure A4.   Sectional Normal Force and Pitching Moment for a
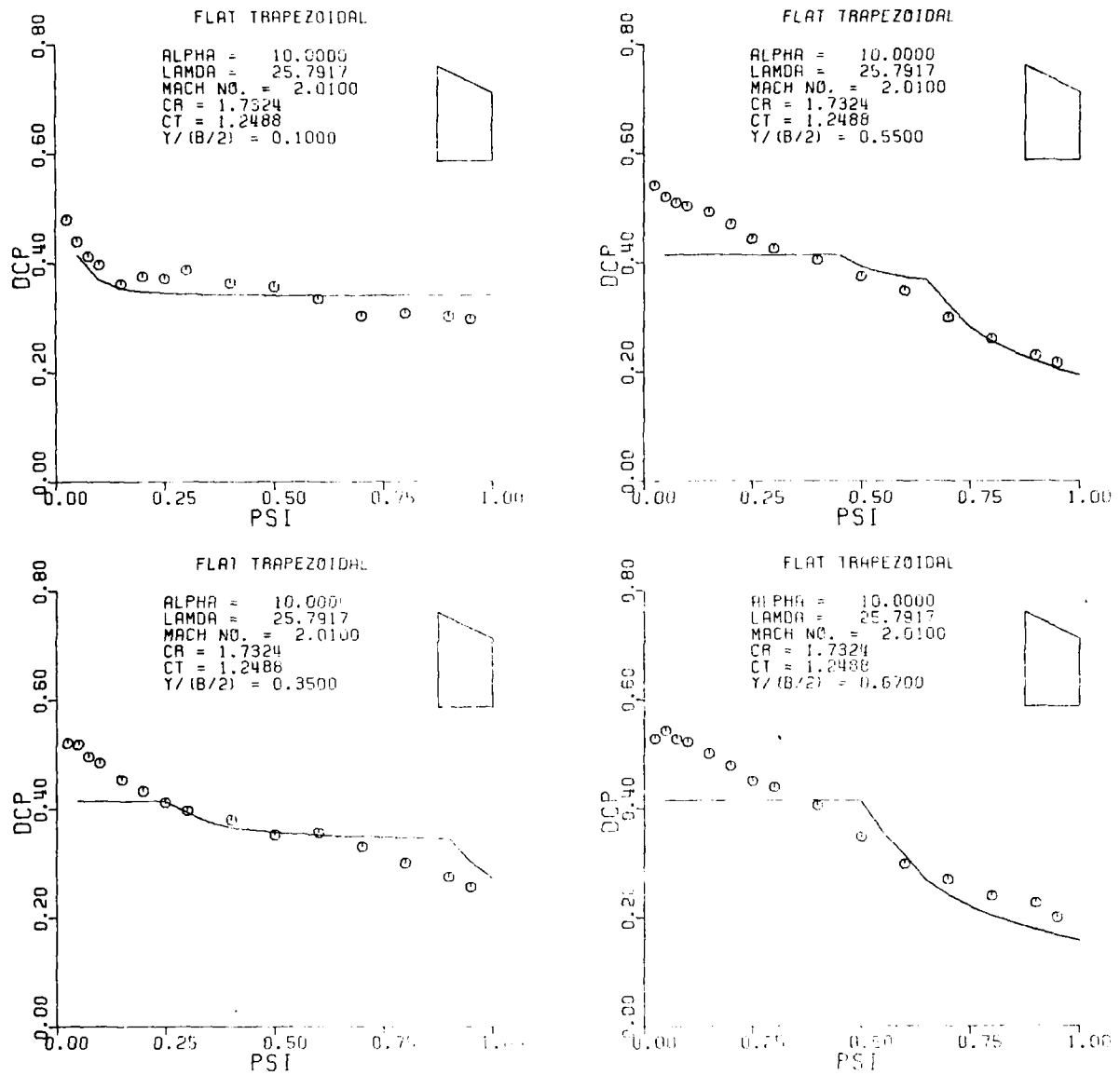Flat Trapezoidal Wing; M = 2.01, α = 2.0.
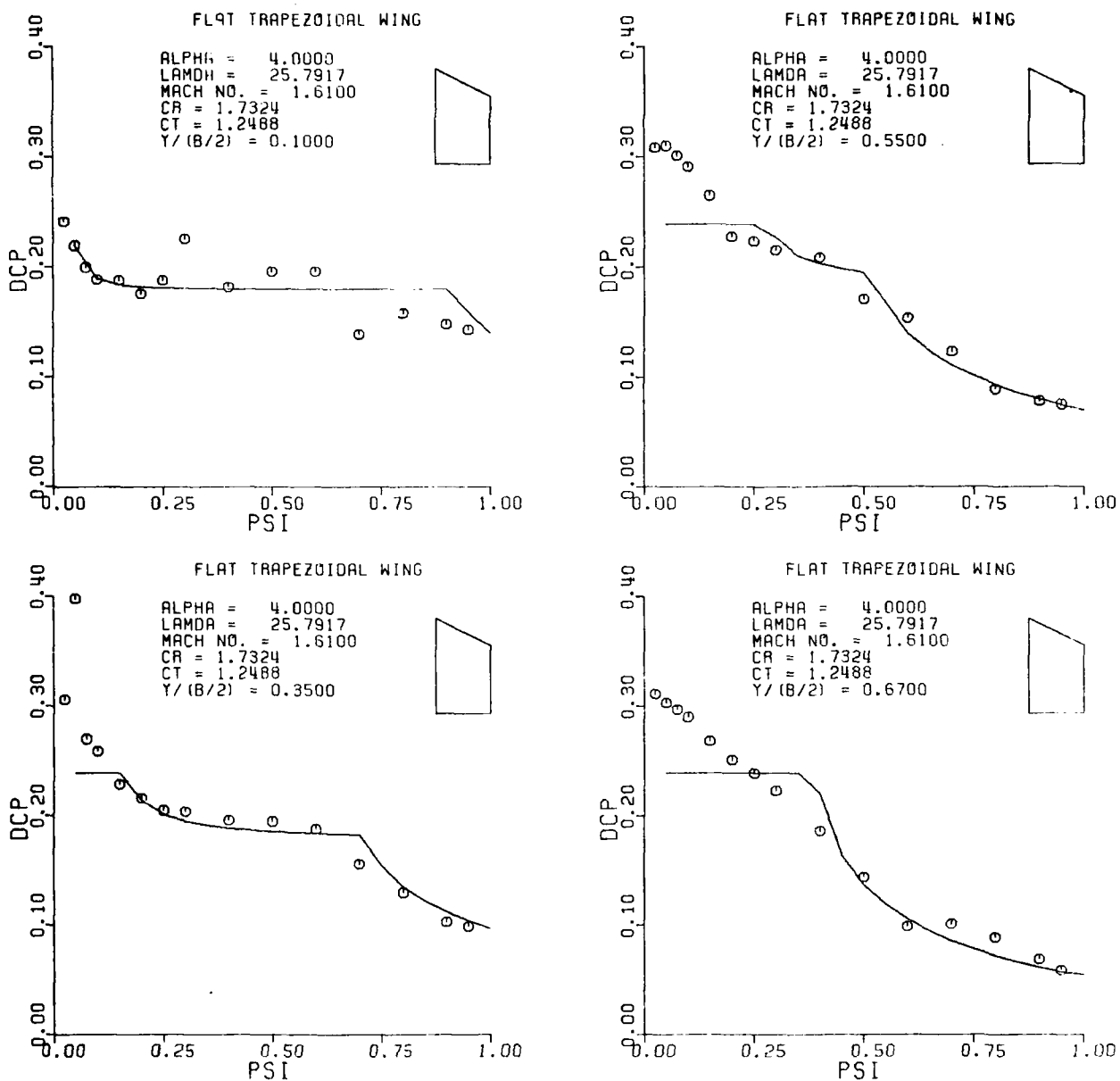
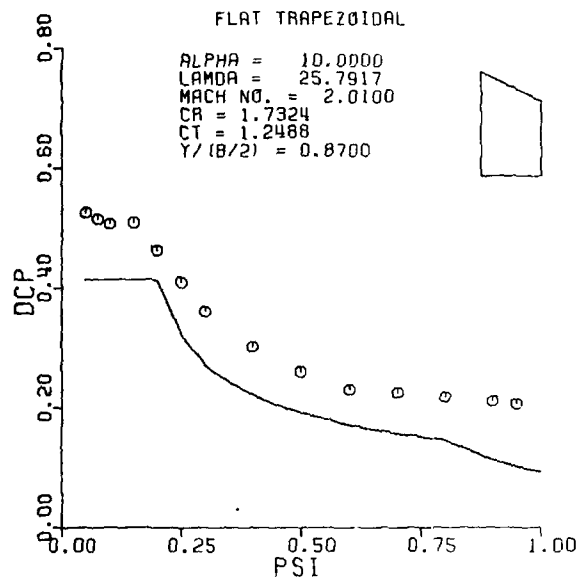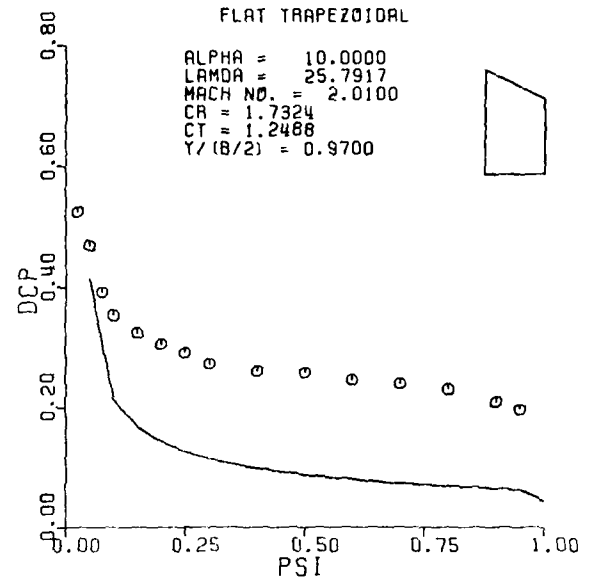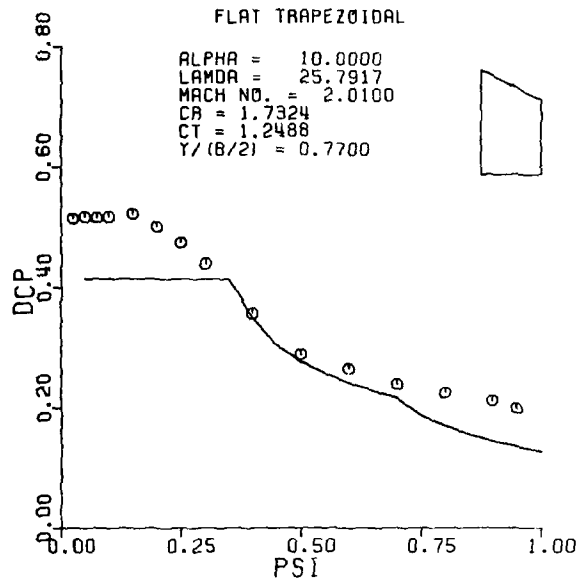Figure A5. Pressure Distribution on a Flat Trapezoidal Wing; M = 1.61, α = 4.0.

Figure A5.   Continued

FLAT TRAPEZOIDAL WING

ALPHA =   4.0000
LAMDA =   25.7917
MACH NO. = 1.6100
CR = 1.7324
CT = 1.2488

FLAT TRAPEZOIDAL WING

ALPHA =   4.0000
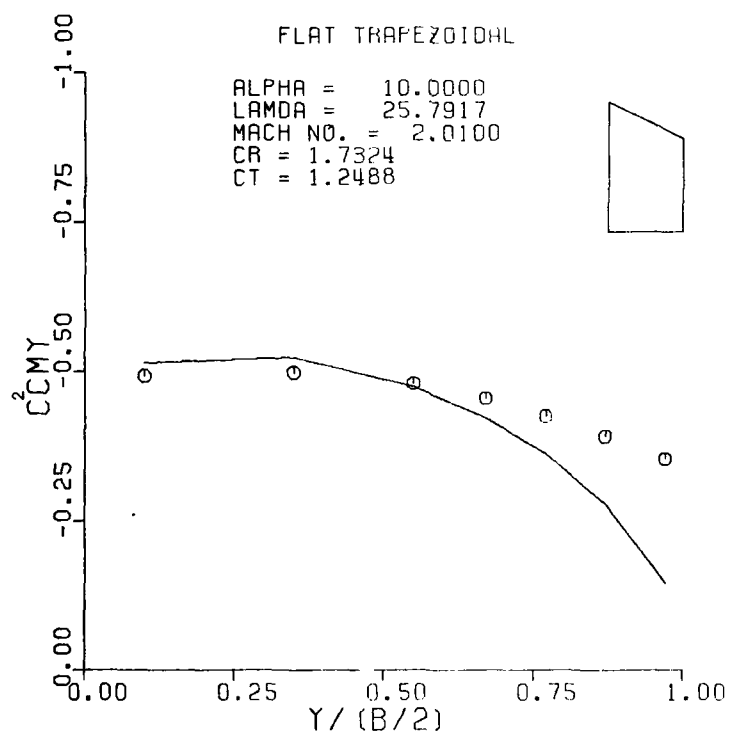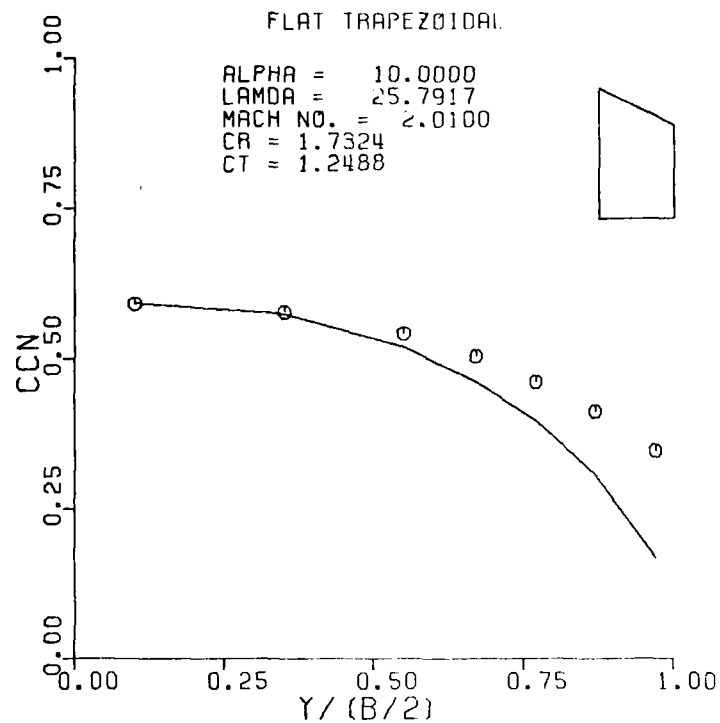LAMDA =   25.7917
MACH NO. = 1.6100
CR = 1.7324
CT = 1.2488
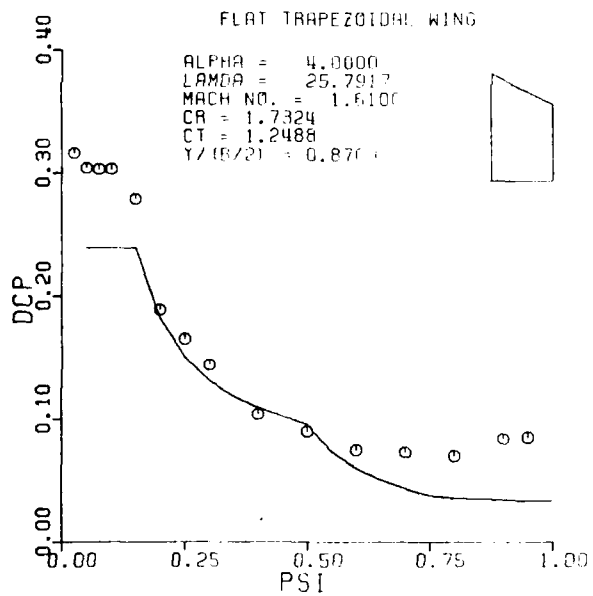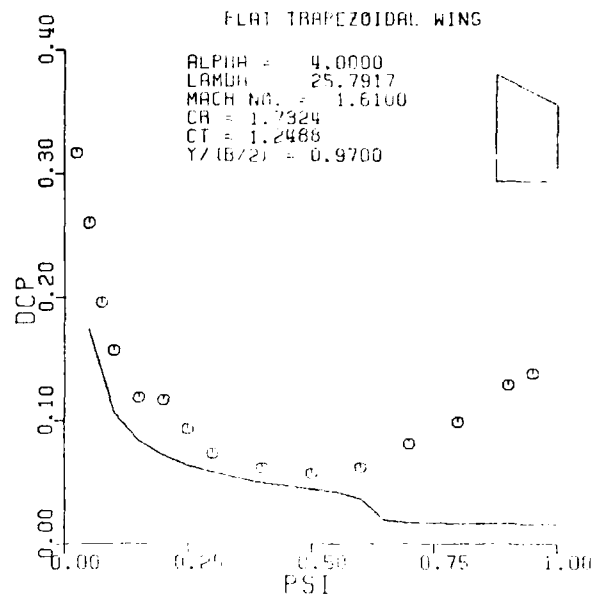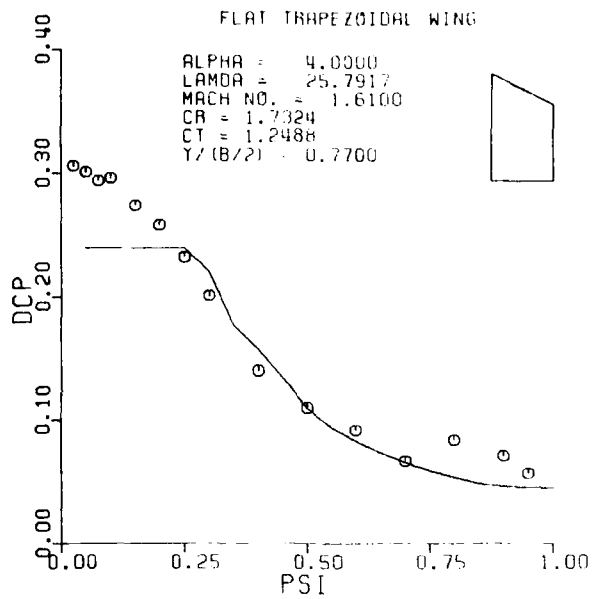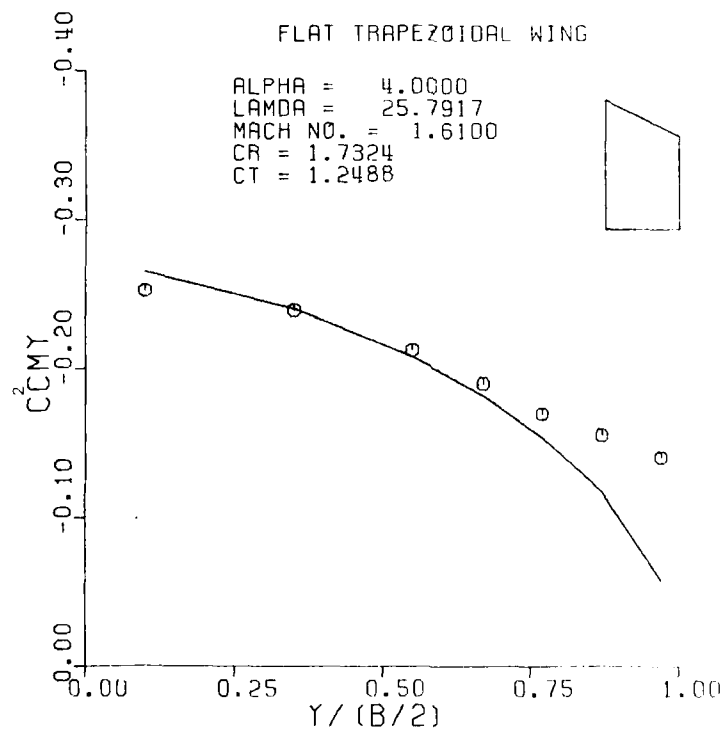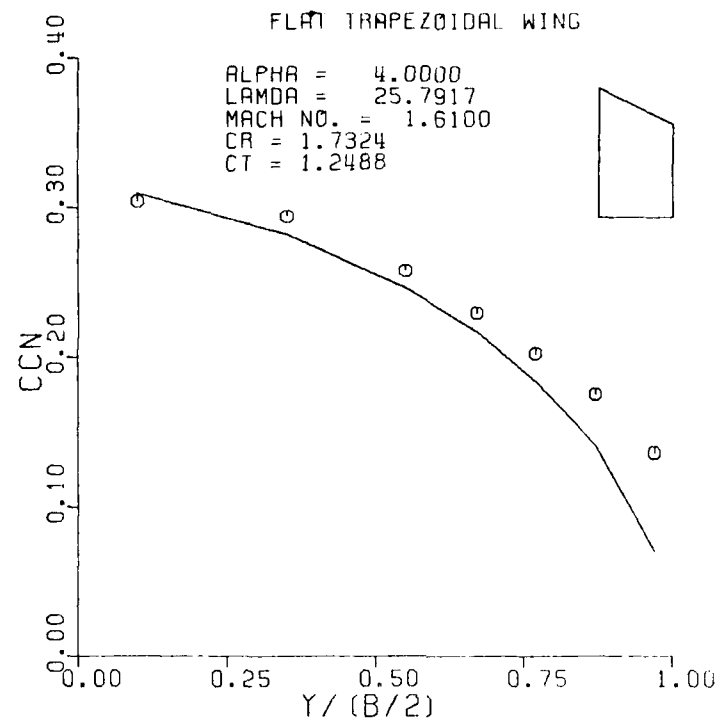
Figure A6. Sectional Normal Force and Pitching Moment for a Flat Trapezoidal Wing; M = 1.61, α = 4.0.
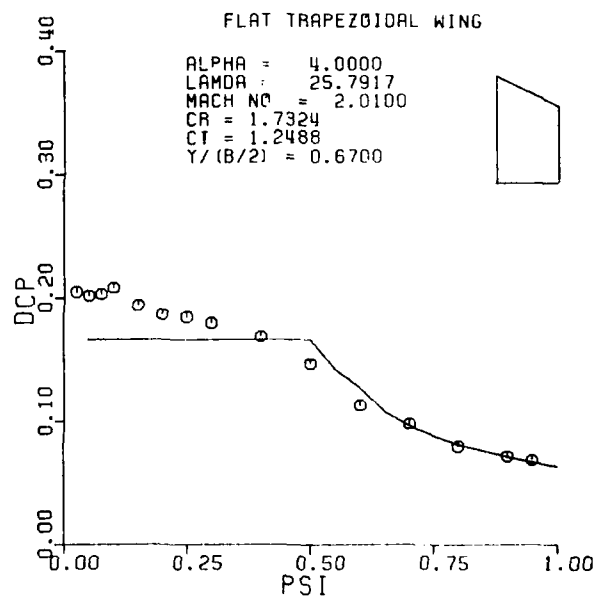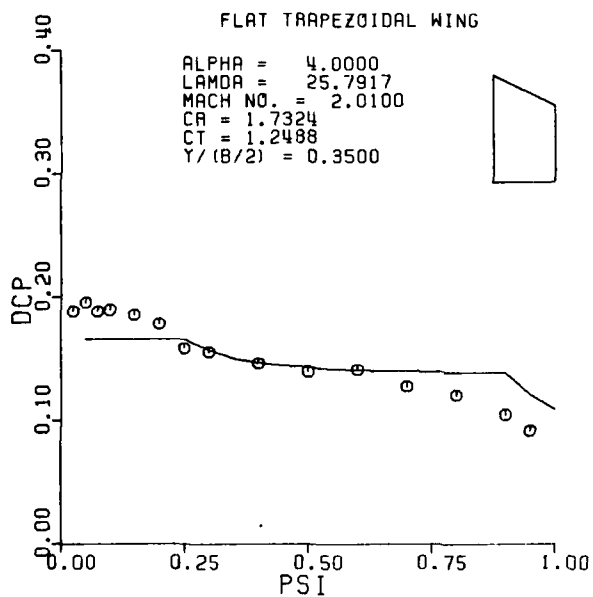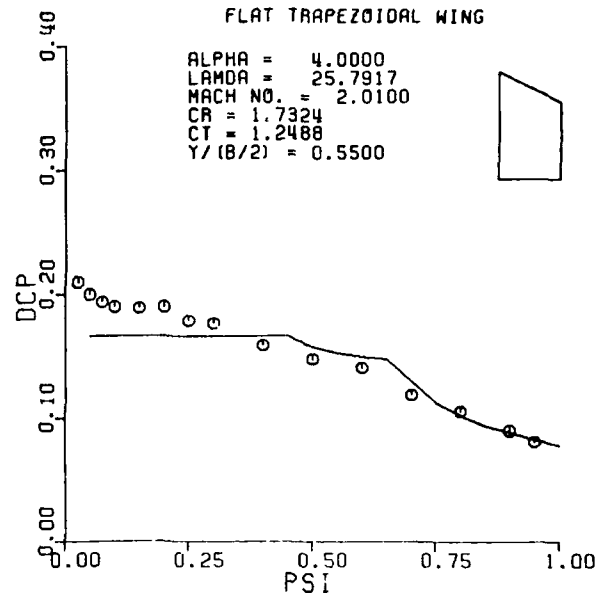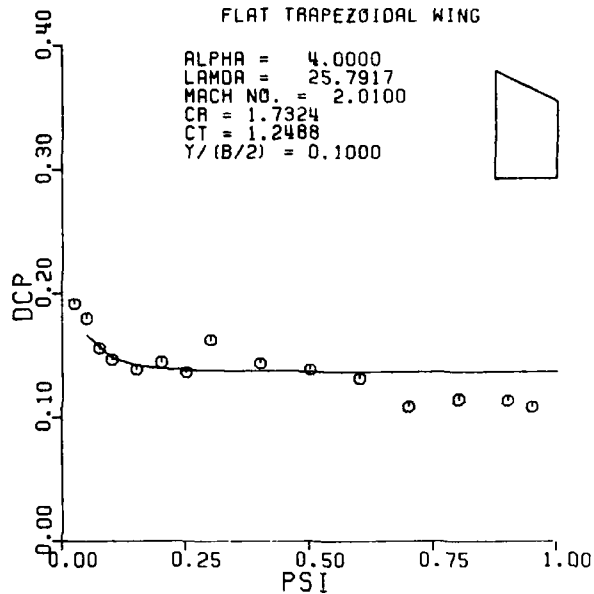
Figure A7. Pressure Distribution on a Flat Trapezoidal Wing; M = 2.01, α = 4.0.

FLAT TRAPEZOIDAL WING

ALPHA = 4.0000
LAMDA = 25.7917
MACH NO. = 2.0100
CR = 1.7324
CT = 1.2488
Y/(B/2) = 0.7700

FLAT TRAPEZOIDAL WING

ALPHA = 4.0000
LAMDA = 25.7917
MACH NO. = 2.0100
CR = 1.7324
CT = 1.2488
Y/(B/2) = 0.9700

FLAT TRAPEZOIDAL WING

ALPHA = 4.0000
LAMDA = 25.7917
MACH NO. = 2.0100
CR = 1.7324
CT = 1.2488
Y/(B/2) = 0.8700

Fig. A7.   Continued.

FLAT TRAPEZOIDAL WING

ALPHA =   4.0000
LAMDA =   25.7917
MACH NO. = 2.0100
CR = 1.7324
CT = 1.2488

FLAT TRAPEZOIDAL WING

ALPHA =   4.0000
LAMDA =   25.7917
MACH NO. = 2.0100
CR = 1.7324
CT = 1.2488

Figure A8.   Sectional Normal Force and Pitchimg Moment for a
Flat Trapezoidal Wing; M = 2.01, α = 4.0.
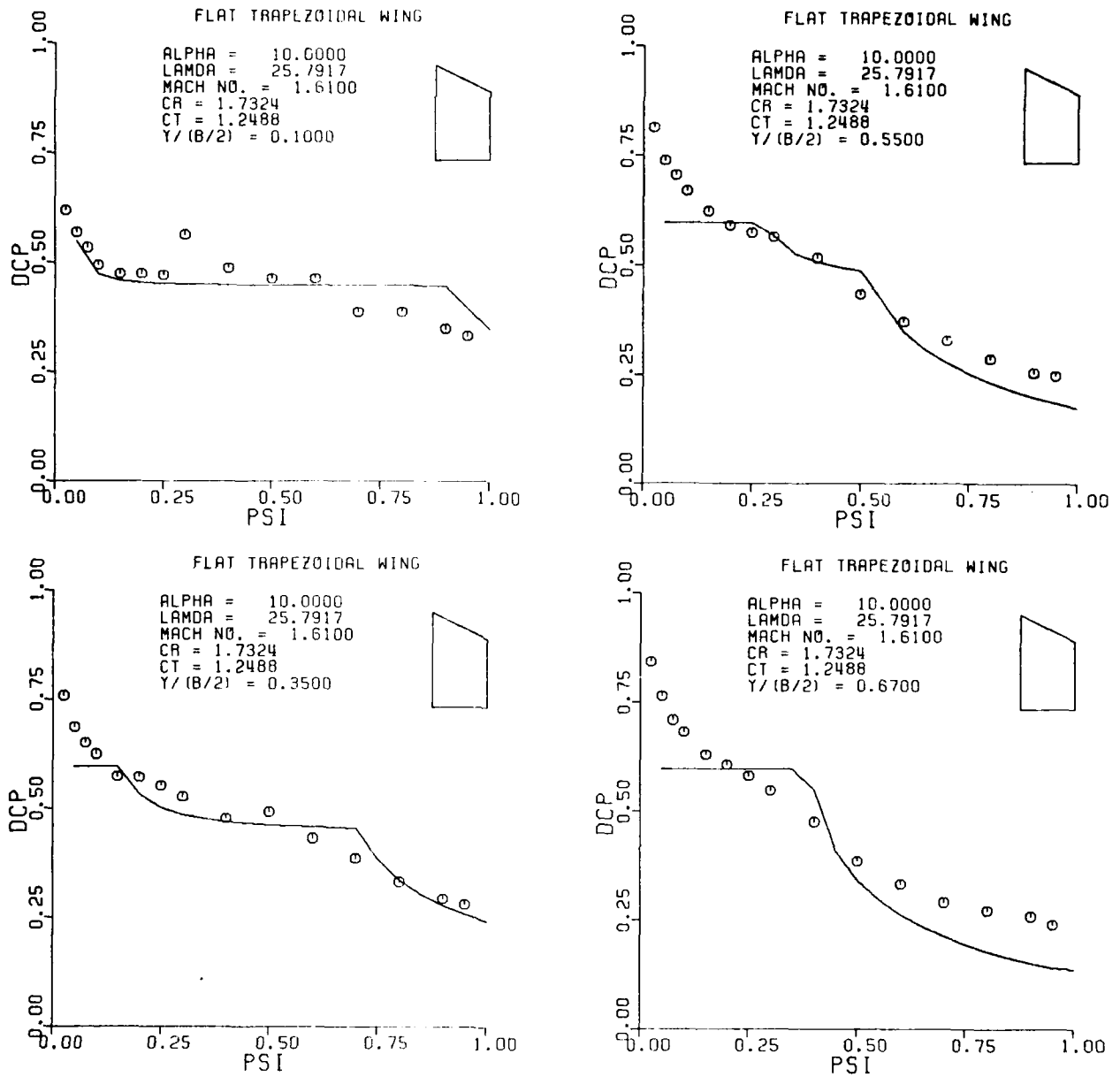
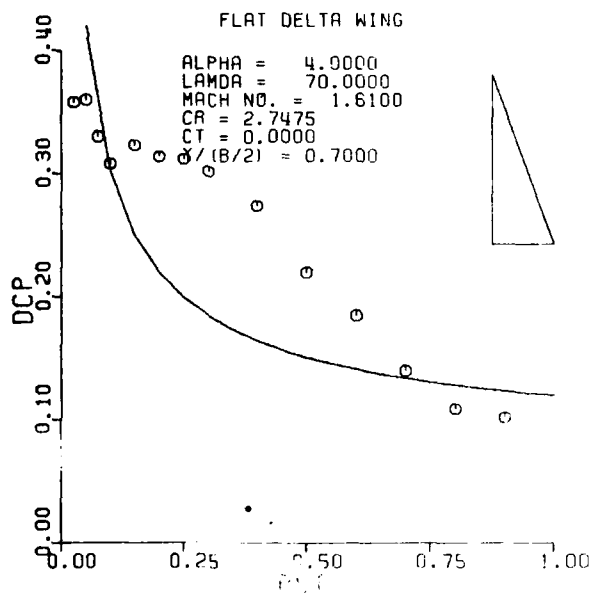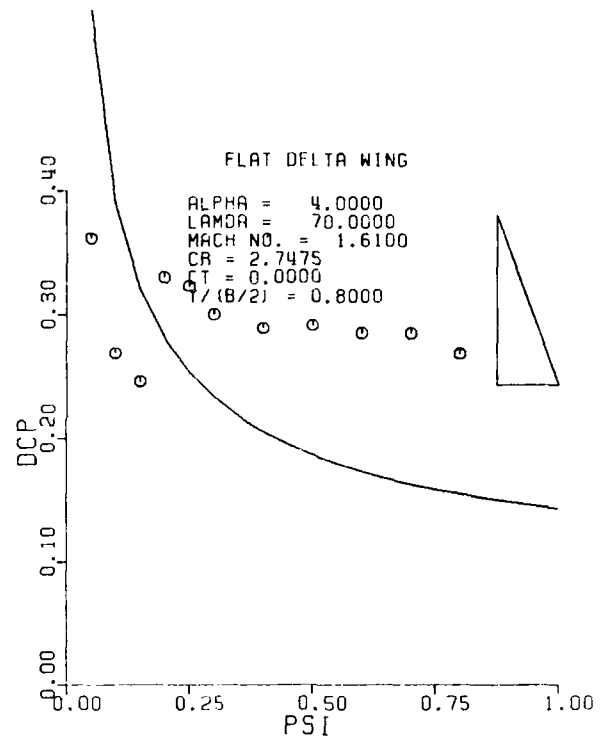Figure A9. Pressure Distribution on a Flat Trapezoidal Wing; M = 1.61, α = 10.0.

Figure A9. Continued

FLAT TRAPEZOIDAL WING

ALPHA =   10.0000
LAMDA =   25.7917
MACH NO. =   1.6100
CR = 1.7324
CT = 1.2483

FLAT TRAPEZOIDAL WING

ALPHA =   10.0000
LAMDA =   25.7917
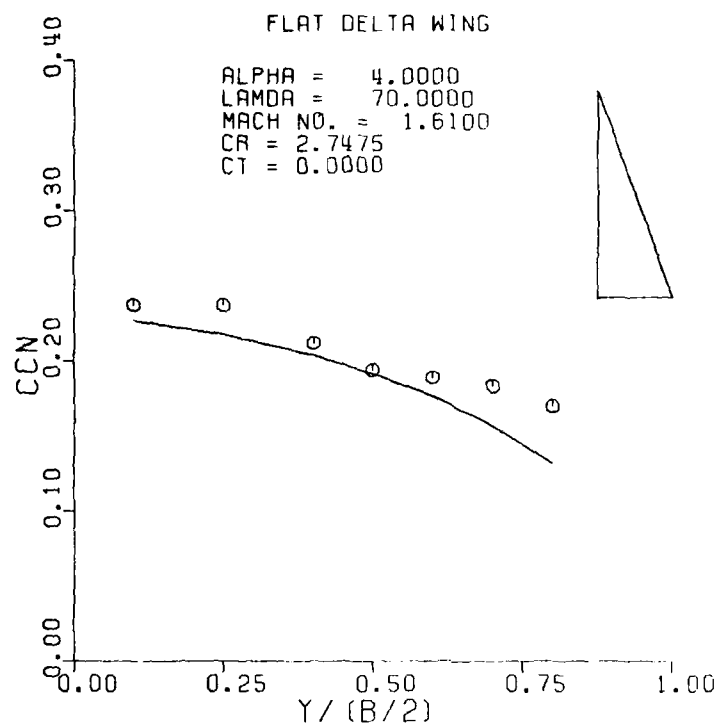MACH NO. =   1.6100
CR = 1.7324
CT = 1.2488

Figure A10.   Sectional Normal Force and Pitching Moment for a
              Flat Trapezoidal Wing; M = 1.61, α = 10.0.

Figure A11. Pressure Distribution on a Flat Trapezoidal Wing; M = 2.01, α = 10.0.

Figure A11.   Continued

FLAT TRAPEZOIDAL

ALPHA =   10.0000
LAMDA =   25.7917
MACH NO. = 2.0100
CR = 1.7324
CT = 1.2488

FLAT TRAPEZOIDAL

ALPHA =   10.0000
LAMDA =   25.7917
MACH NO. = 2.0100
CR = 1.7324
CT = 1.2488

Figure A12.   Sectional Normal Force and Pitching Moment for a
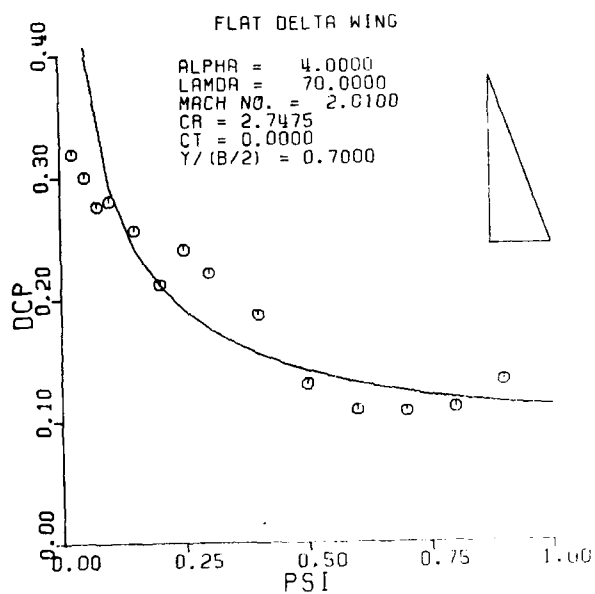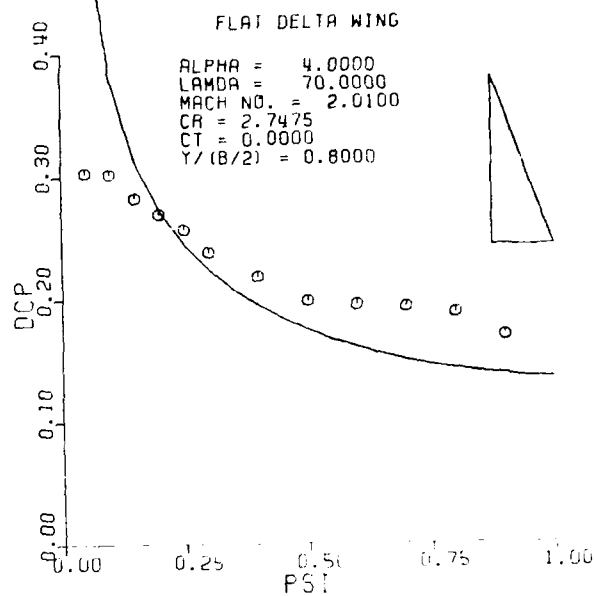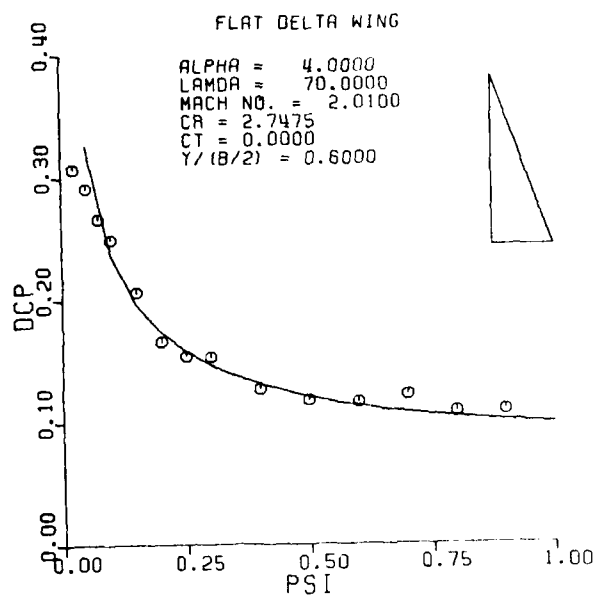Flat Trapezoidal Wing; $M = 2.01$, $\alpha = 10.0$.

130
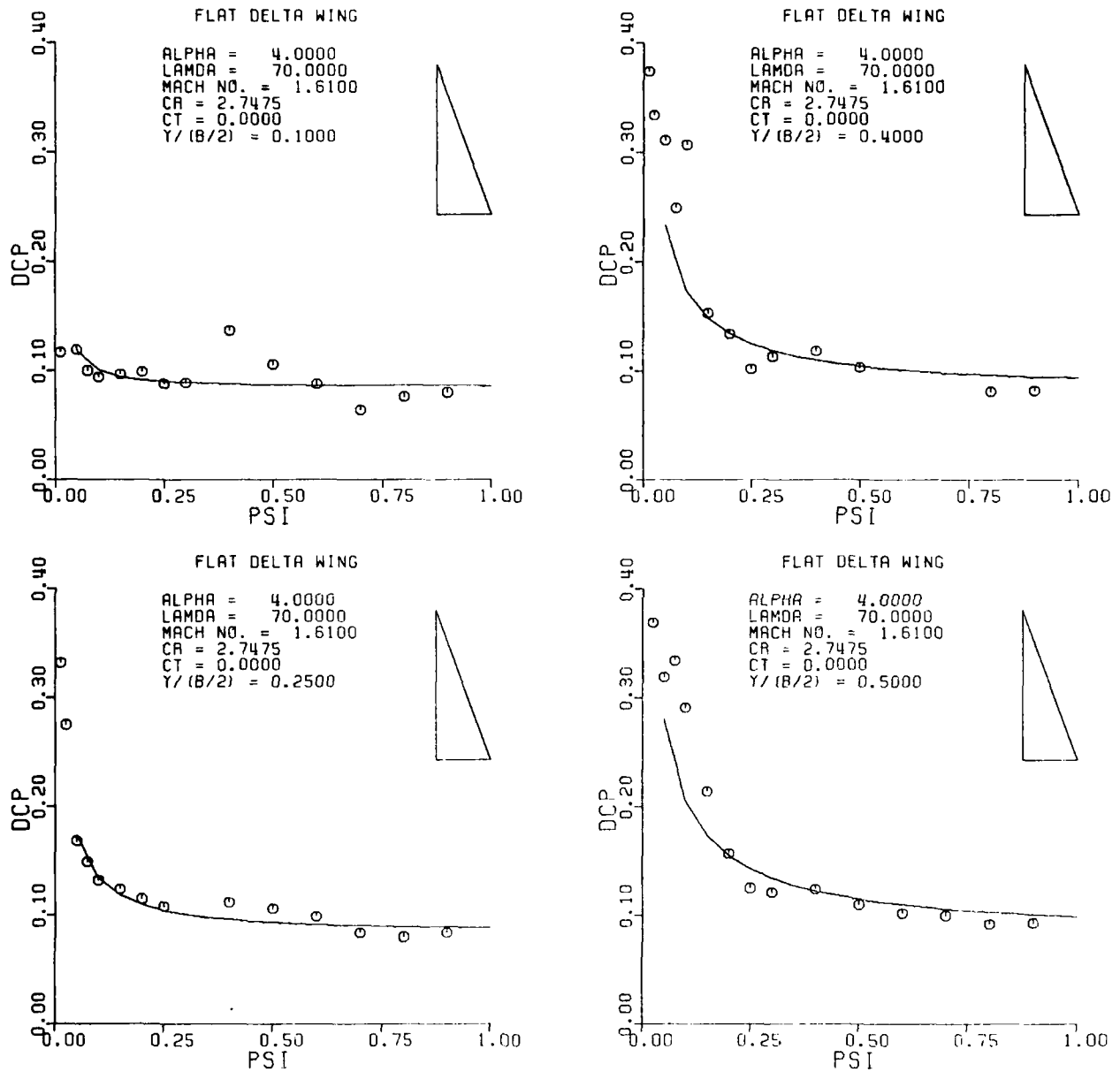
Figure A13. Pressure Distribution on a Flat Delta Wing; M = 1.61, α = 4.0.

FLAT DELTA WING

ALPHA   =   4.0000
LAMDA   = 70.0000
MACH NO. =   1.6100
CR = 2.7475
CT = 0.0000
Y/(B/2) = 0.6000

FLAT DELTA WING

ALPHA   =   4.0000
LAMDA   = 70.0000
MACH NO. =   1.6100
CR = 2.7475
CT = 0.0000
Y/(B/2) = 0.8000

FLAT DELTA WING

ALPHA   =   4.0000
LAMDA   = 70.0000
MACH NO. =   1.6100
CR = 2.7475
CT = 0.0000
Y/(B/2) = 0.7000

Figure A15. Continued

FLAT DELTA WING

ALPHA =   4.0000
LAMDA =   70.0000
MACH NO. = 1.6100
CR = 2.7475
CT = 0.0000

FLAT DELTA WING

ALPHA =   4.0000
LAMDA =   70.0000
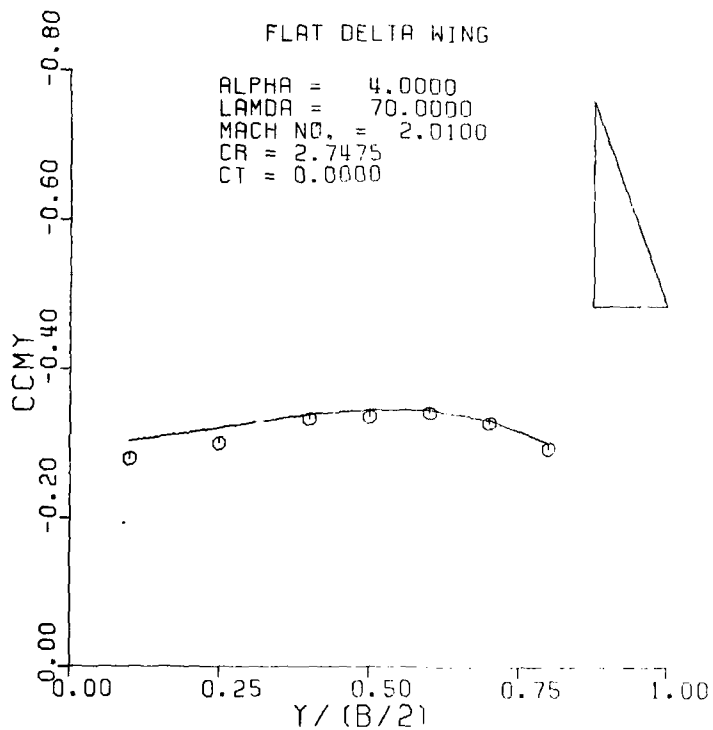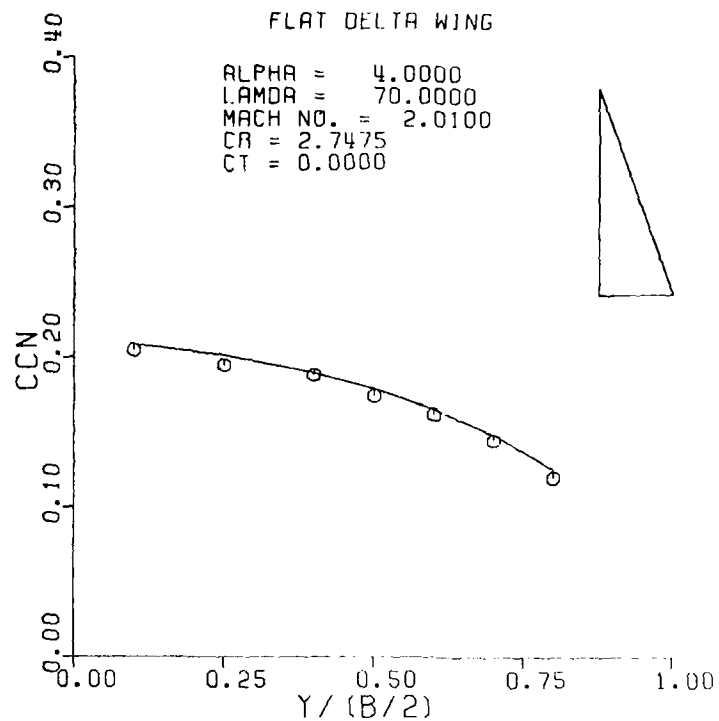MACH NO. = 1.6100
CR = 2.7475
CT = 0.0000
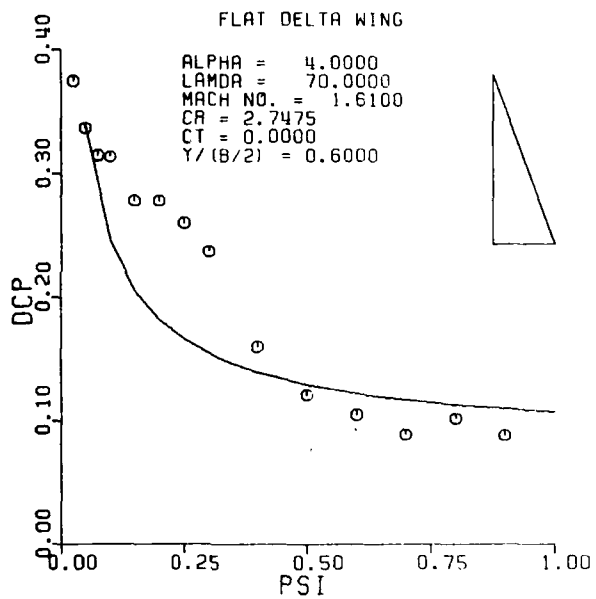
Figure A14.   Sectional Normal Force and Pitching Moment for a
Flat Delta Wing; $M = 1.61$, $\alpha = 4.0$.
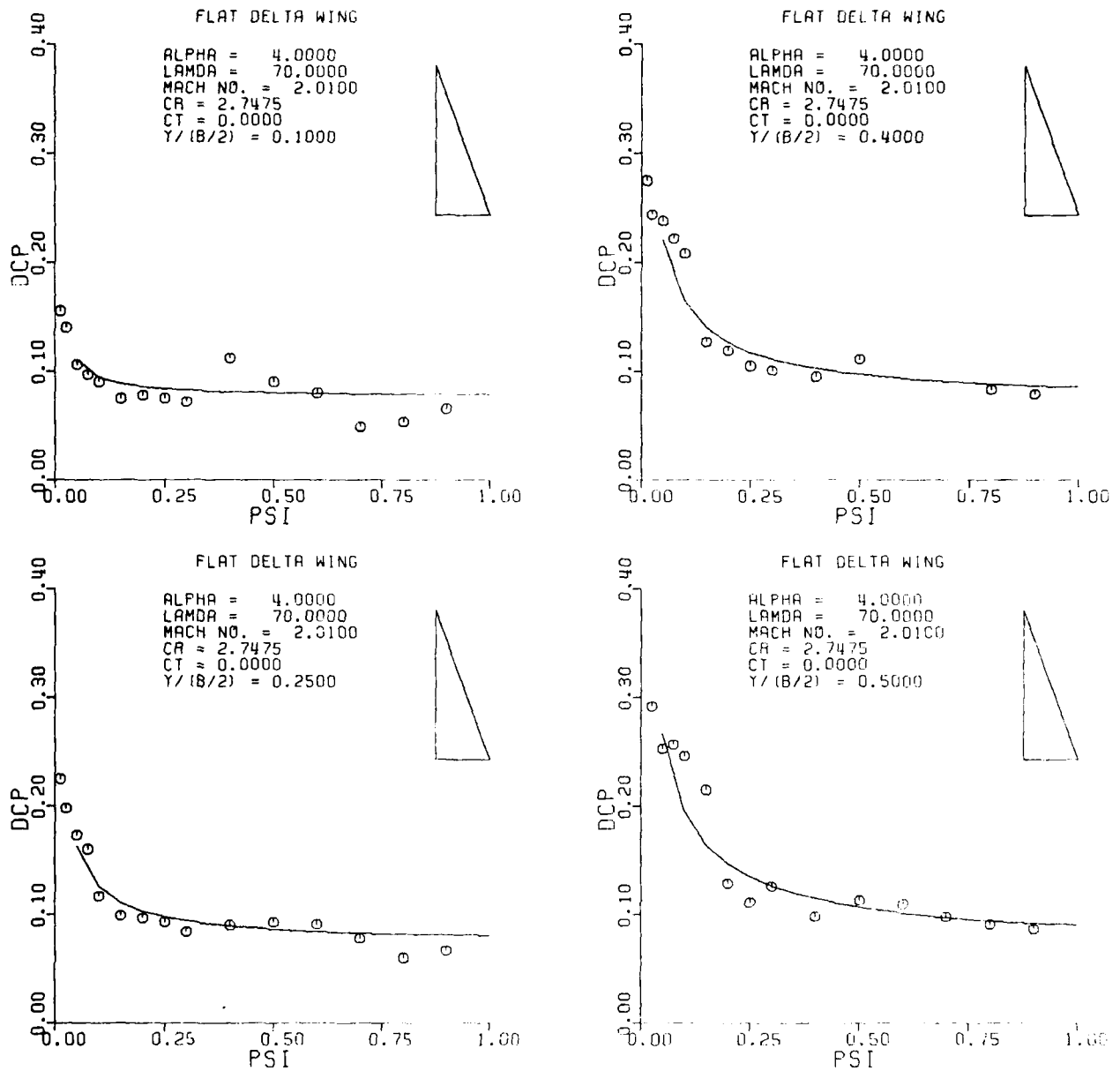
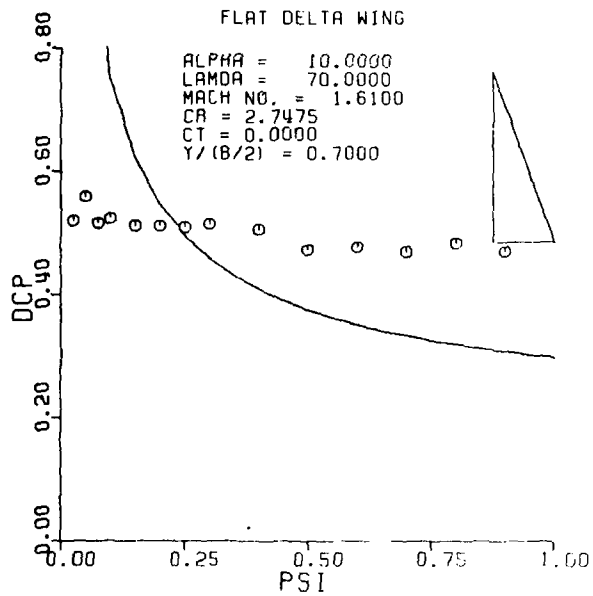Figure A15. Pressure Distribution on a Flat Delta Wing; M = 2.01, α = 4.0.

FLAT DELTA WING

ALPHA = 4.0000
LAMDA = 70.0000
MACH NO. = 2.0100
CR = 2.7475
CT = 0.0000
Y/(B/2) = 0.6000

FLAT DELTA WING

ALPHA = 4.0000
LAMDA = 70.0000
MACH NO. = 2.0100
CR = 2.7475
CT = 0.0000
Y/(B/2) = 0.8000

FLAT DELTA WING

ALPHA = 4.0000
LAMDA = 70.0000
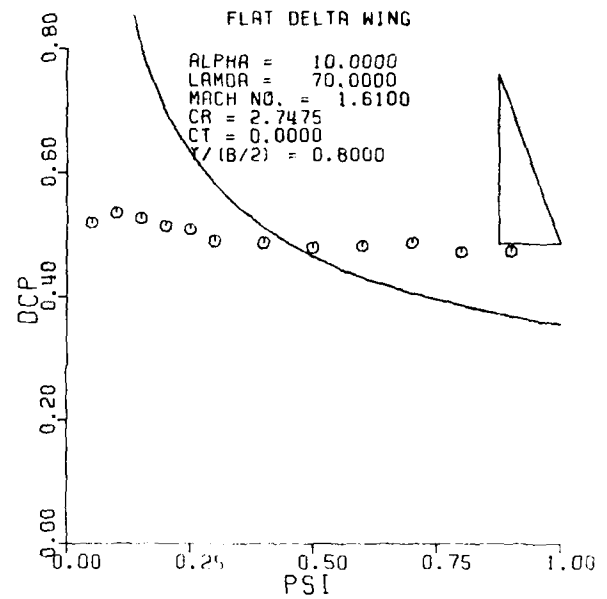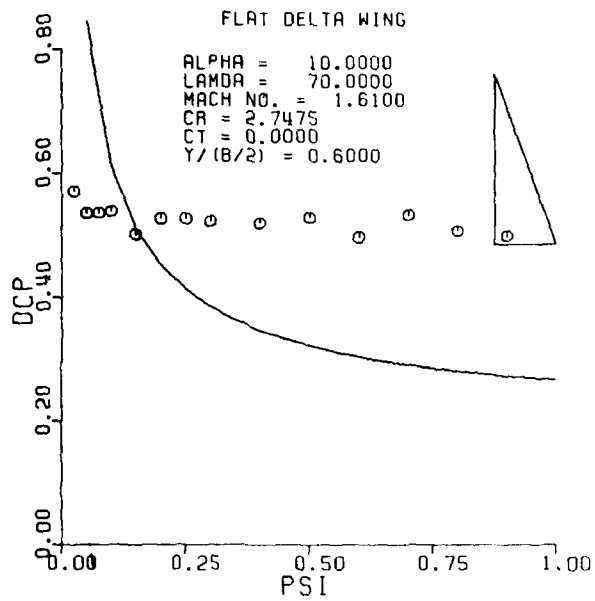MACH NO. = 2.0100
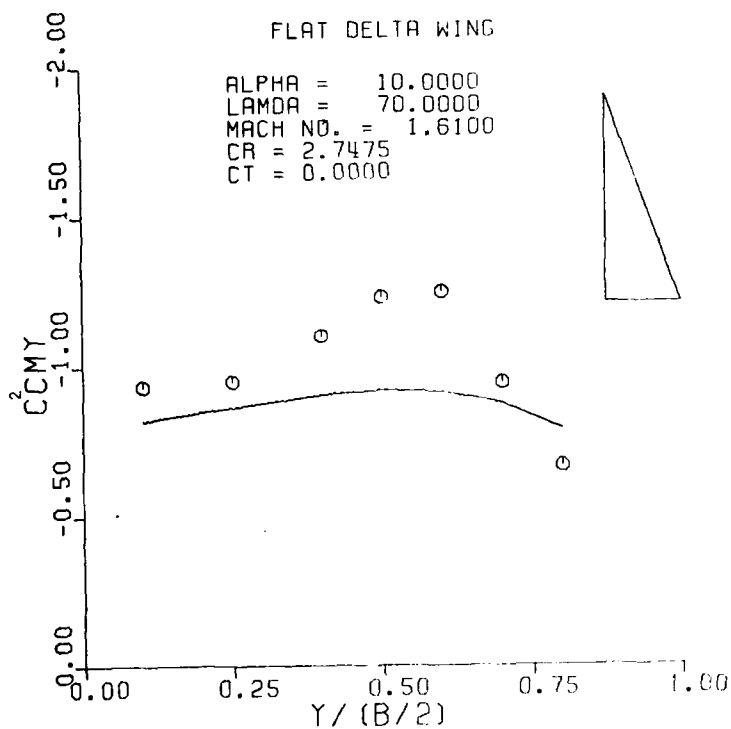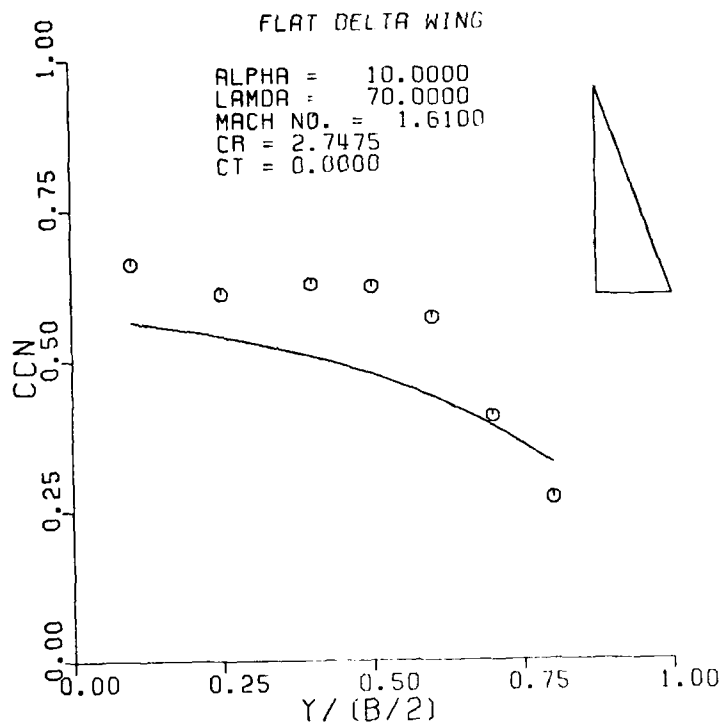CR = 2.7475
CT = 0.0000
Y/(B/2) = 0.7000

A15. Continued.

Figure A16. Sectional Normal Force and Pitching Moment for a
Flat Delta Wing; M = 2.01, α = 4.0.
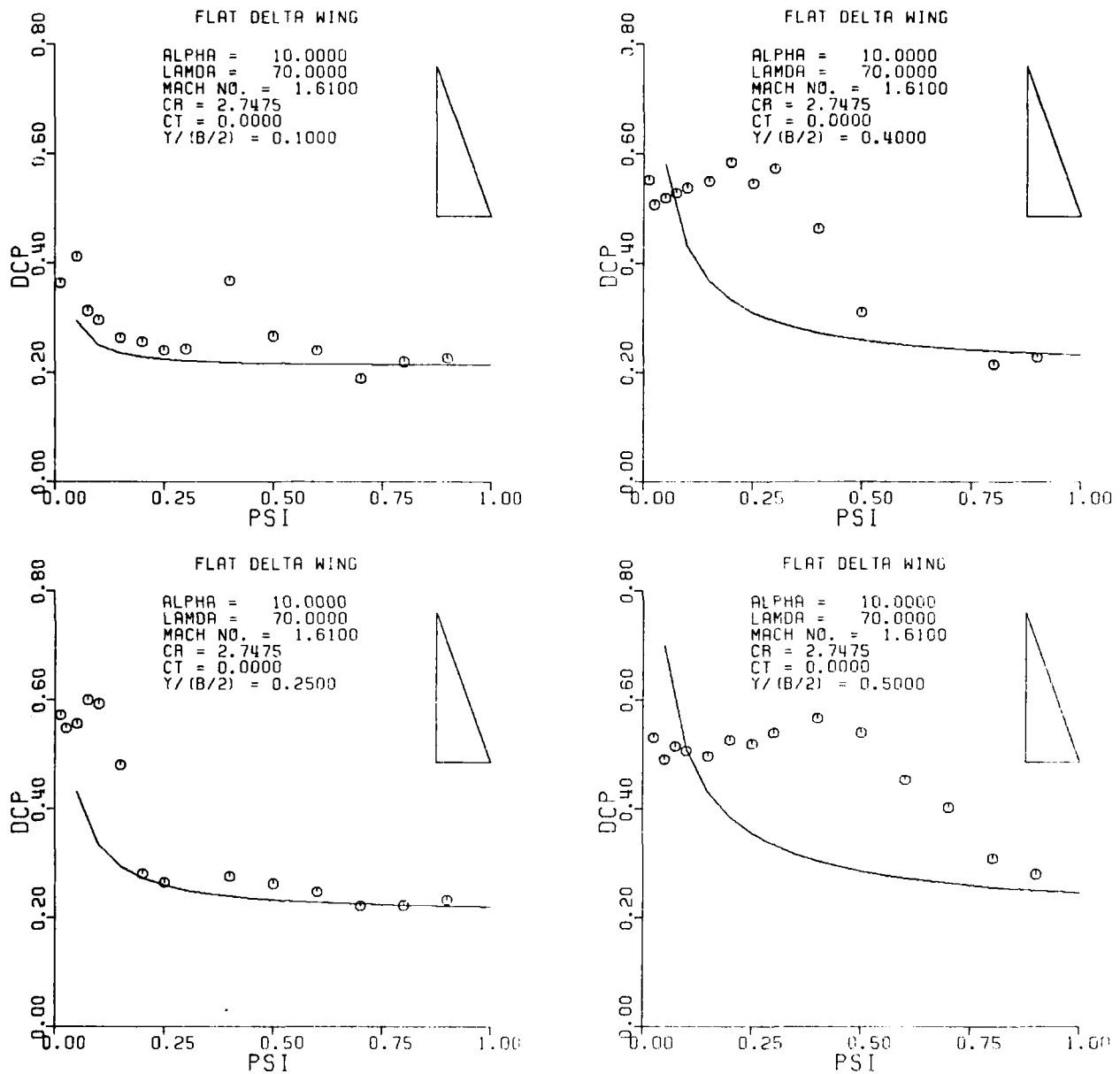
Figure A17.   Pressure Distribution on a Flat Delta Wing; M = 1.61, α = 10.0.

FLAT DELTA WING

ALPHA =   10.0000
LAMDA =   70.0000
MACH NO. =   1.6100
CR = 2.7475
CT = 0.0000
Y/(B/2) = 0.6000

FLAT DELTA WING

ALPHA =   10.0000
LAMDA =   70.0000
MACH NO. =   1.6100
CR = 2.7475
CT = 0.0000
Y/(B/2) = 0.8000

FLAT DELTA WING

ALPHA =   10.0000
LAMDA =   70.0000
MACH NO. =   1.6100
CR = 2.7475
CT = 0.0000
Y/(B/2) = 0.7000

Figure A17.   Continued

Figure A18. Sectional Normal Force and Pitching Moment for a
Flat Delta Wing; M = 1.61, α = 10.0.

FLAT DELTA WING

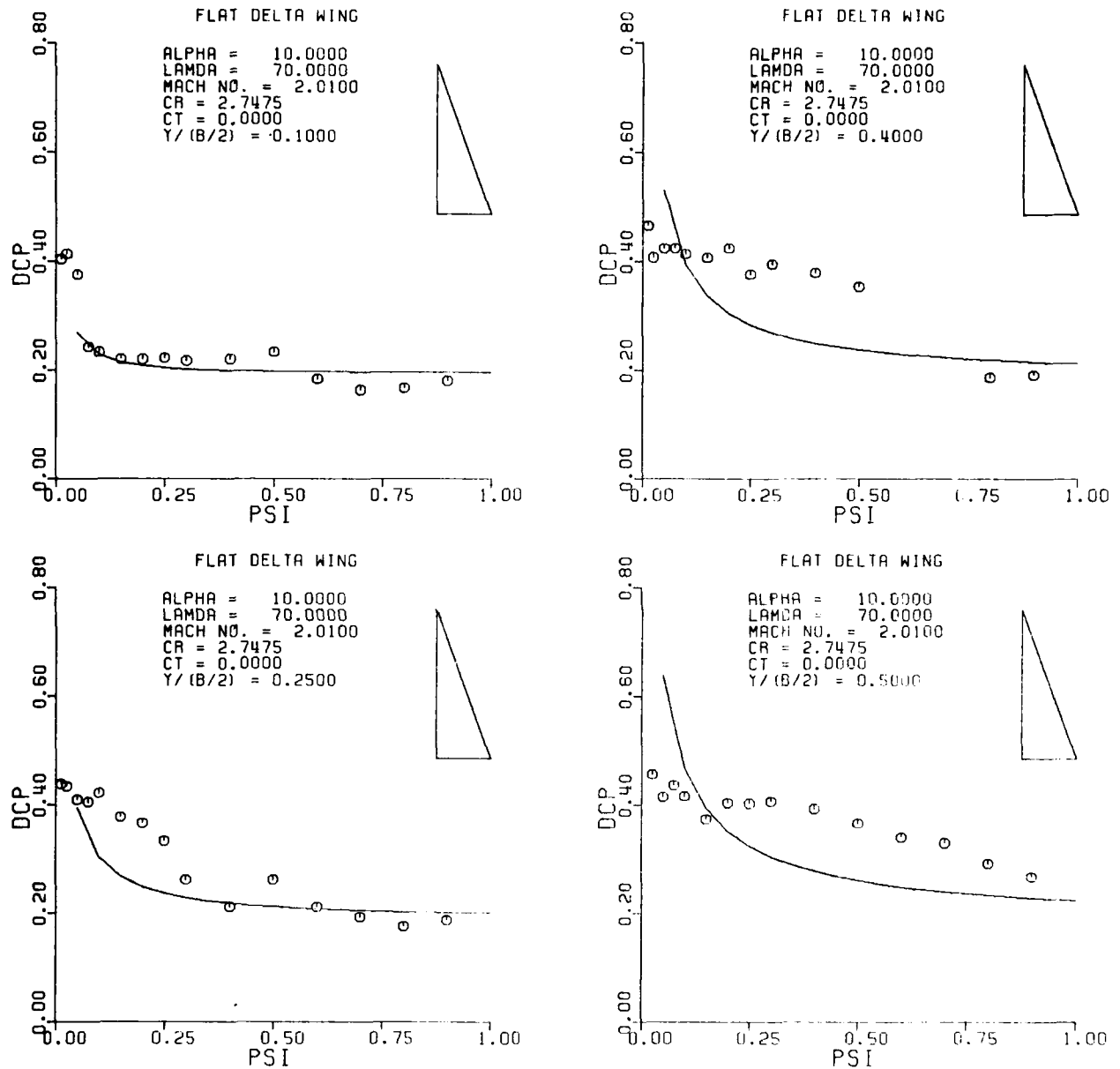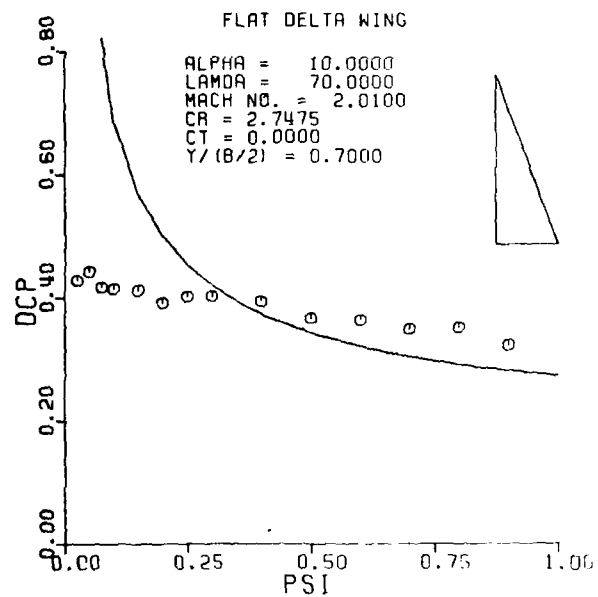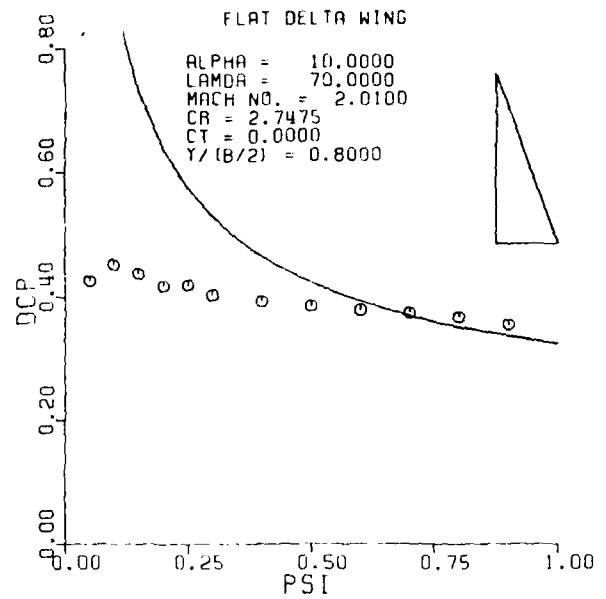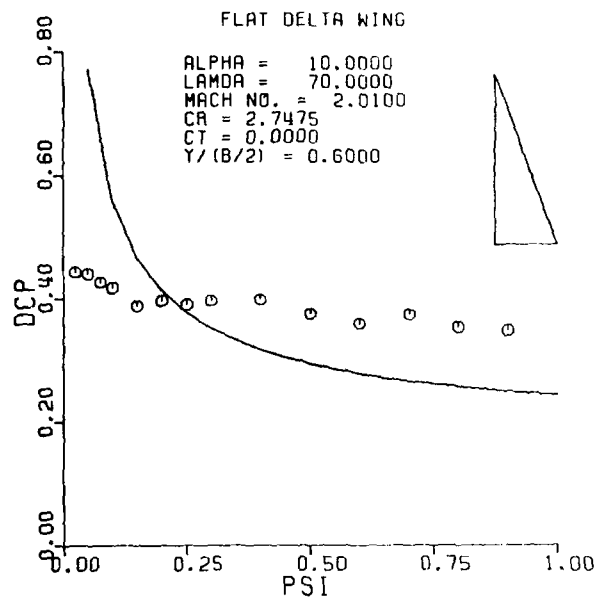ALPHA = 10.0000
LAMDA = 70.0000
MACH NO. = 2.0100
CR = 2.7475
CT = 0.0000
Y/(B/2) = 0.1000

FLAT DELTA WING

ALPHA = 10.0000
LAMDA = 70.0000
MACH NO. = 2.0100
CR = 2.7475
CT = 0.0000
Y/(B/2) = 0.4000

FLAT DELTA WING

ALPHA = 10.0000
LAMDA = 70.0000
MACH NO. = 2.0100
CR = 2.7475
CT = 0.0000
Y/(B/2) = 0.2500

FLAT DELTA WING

ALPHA = 10.0000
LAMDA = 70.0000
MACH NO. = 2.0100
CR = 2.7475
CT = 0.0000
Y/(B/2) = 0.5000

Figure A19. Pressure Distribution on a Flat Delta Wing; M = 2.01, α = 10.0.

Figure A19. Continued

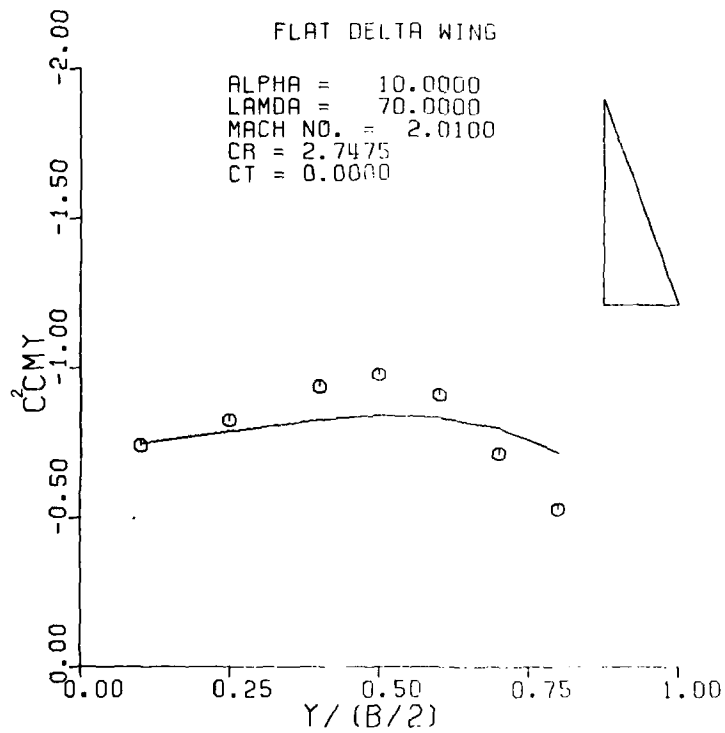FLAT DELTA WING

ALPHA =   10.0000
LAMDA =   70.0000
MACH NO. = 2.0100
CR = 2.7475
CT = 0.0000

CCN

Y/(B/2)

FLAT DELTA WING

ALPHA =   10.0000
LAMDA =   70.0000
MACH NO. = 2.0100
CR = 2.7475
CT = 0.0000

C^{2}CMY

Y/(B/2)
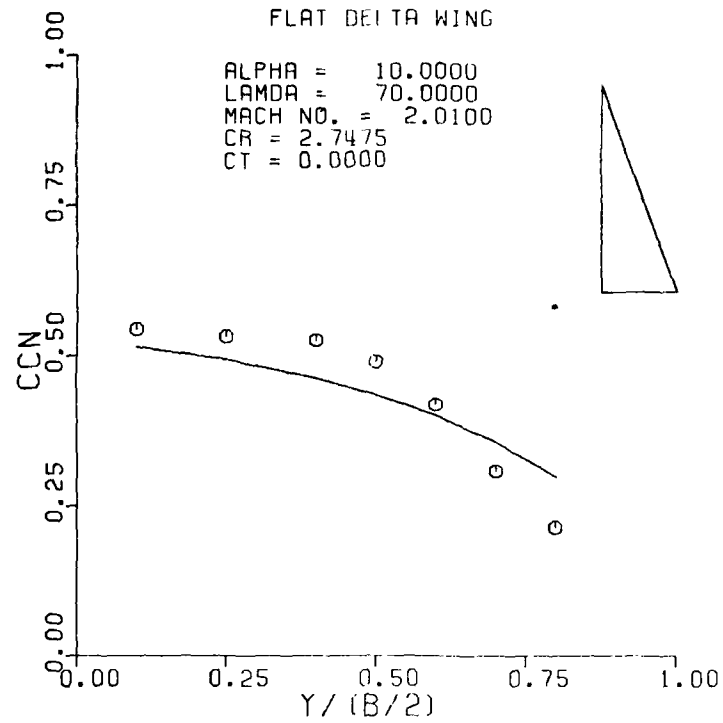
Figure A20.   Sectional Normal Force and Pitching Moment for a
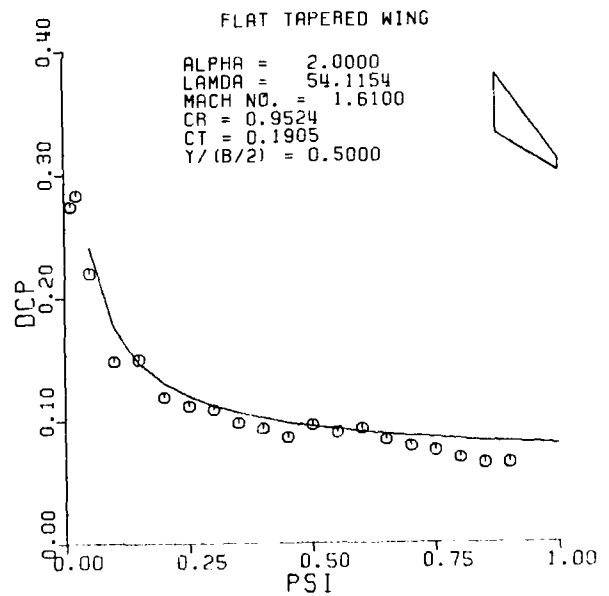Flat Delta Wing; M = 2.01, α = 10.0.

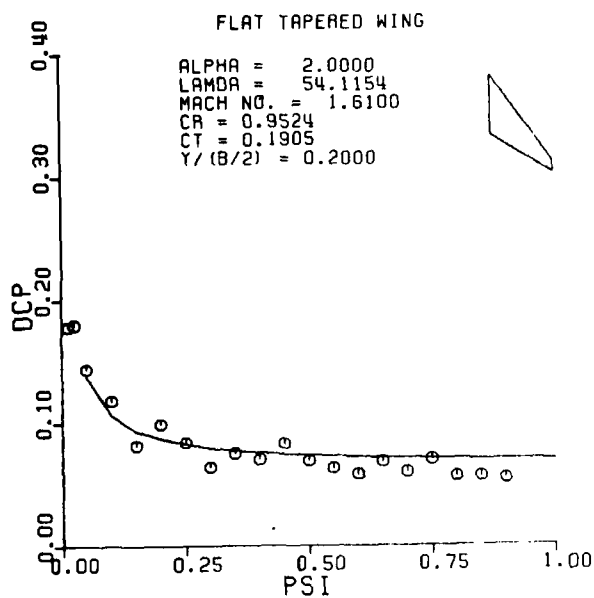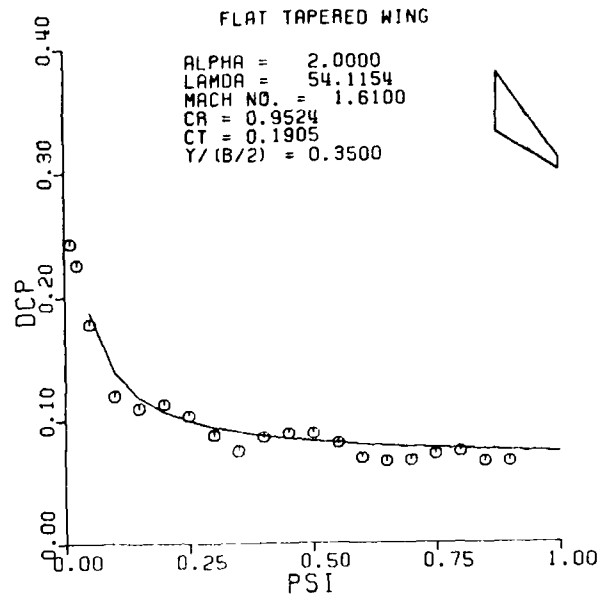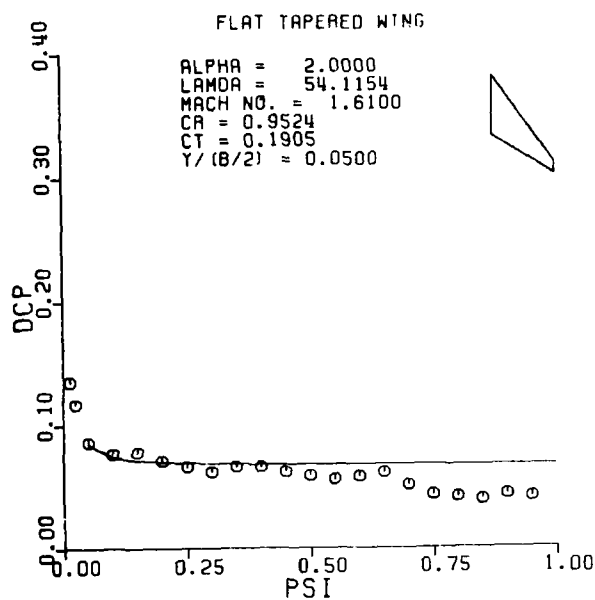**Figure A21.** Pressure Distribution on a Flat Tapered Wing; M = 1.61, α = 2.0.

FLAT TAPERED WING

ALPHA = 2.0000
LAMDA = 54.1154
MACH NO. = 1.6100
CR = 0.9524
CT = 0.1905
Y/(B/2) = 0.7000

FLAT TAPERED WING

ALPHA = 2.0000
LAMDA = 54.1154
MACH NO. = 1.6100
CR = 0.9524
CT = 0.1905
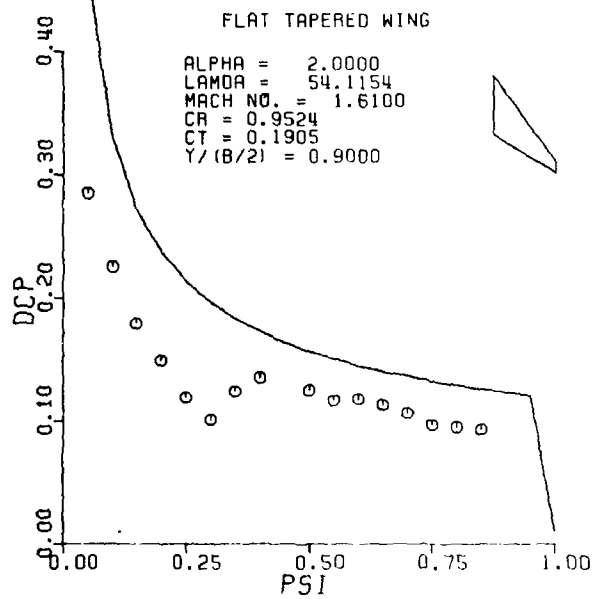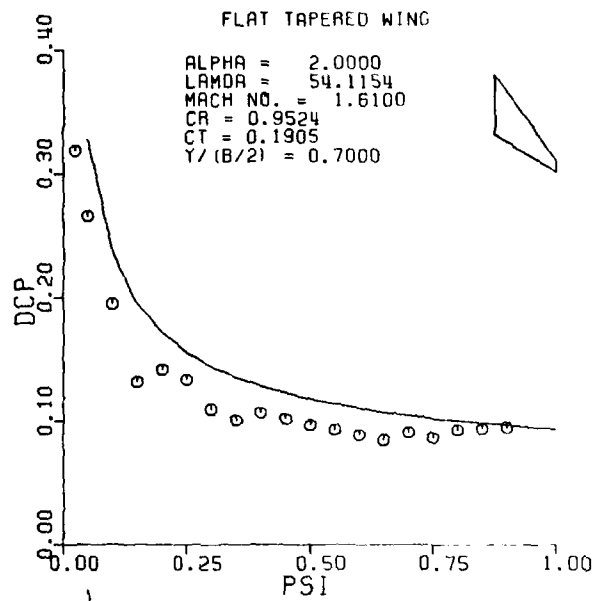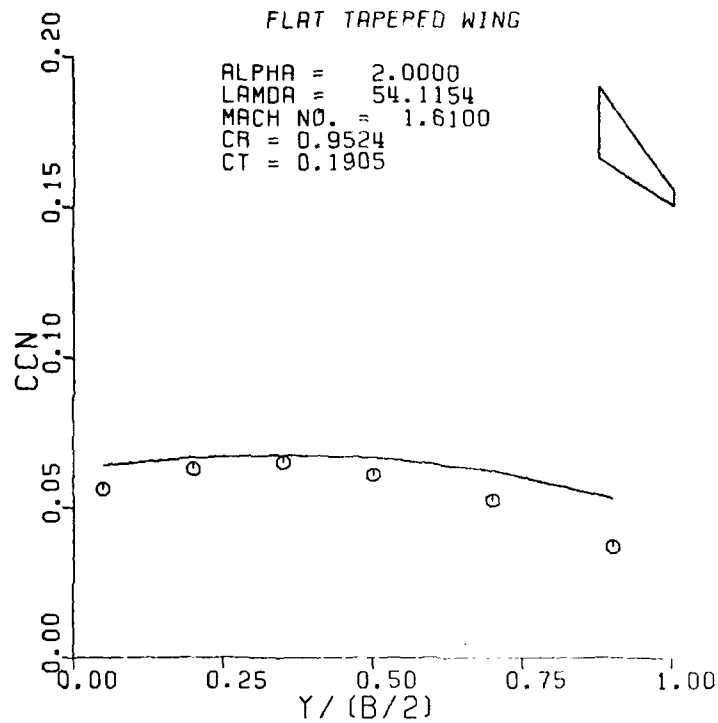Y/(B/2) = 0.9000

Figure A21.   Continued.

FLAT TAPEPED WING

ALPHA =   2.0000
LAMDA =   54.1154
MACH NO. = 1.6100
CR = 0.9524
CT = 0.1905

FLAT TAPERED WING

ALPHA =   2.0000
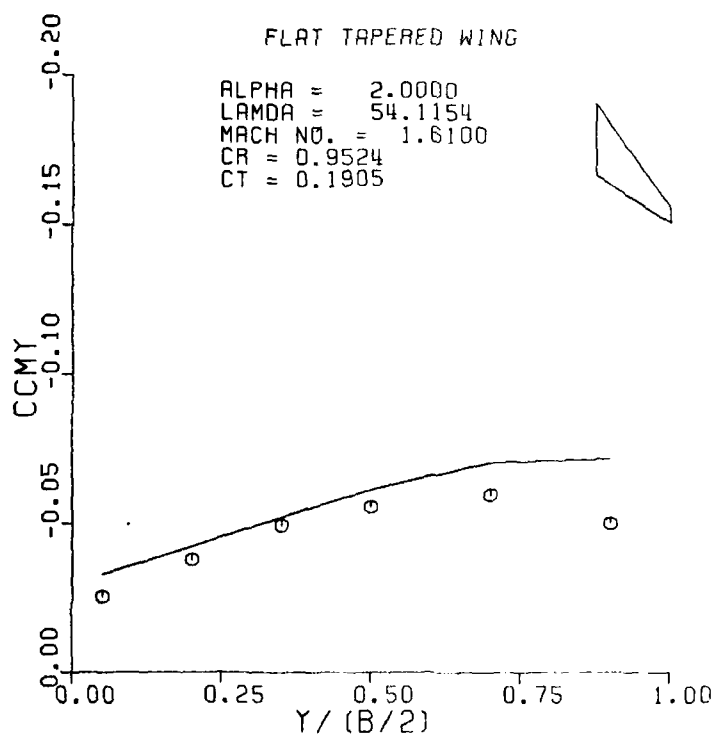LAMDA =   54.1154
MACH NO. = 1.6100
CR = 0.9524
CT = 0.1905

Figure A22. Sectional Normal Force and Pitching Moment for a
Flat Tapered Wing; M = 1.61, α = 2.0.

Figure A23. Pressure Distribution on a Flat Tapered Wing, M = 2.01, α = 2.0.

FLAT TAPERED WING

ALPHA = 2.0000
LAMDA = 54.1154
MACH NO. = 2.0100
CR = 0.9524
CT = 0.1905
Y/(B/2) = 0.7000

FLAT TAPERED WING

ALPHA = 2.0000
LAMDA = 54.1154
MACH NO. = 2.0100
CR = 0.9524
CT = 0.1905
Y/(B/2) = 0.9000

Figure A23.   Continued

Figure A24. Sectional Normal Force and Pitching Moment for
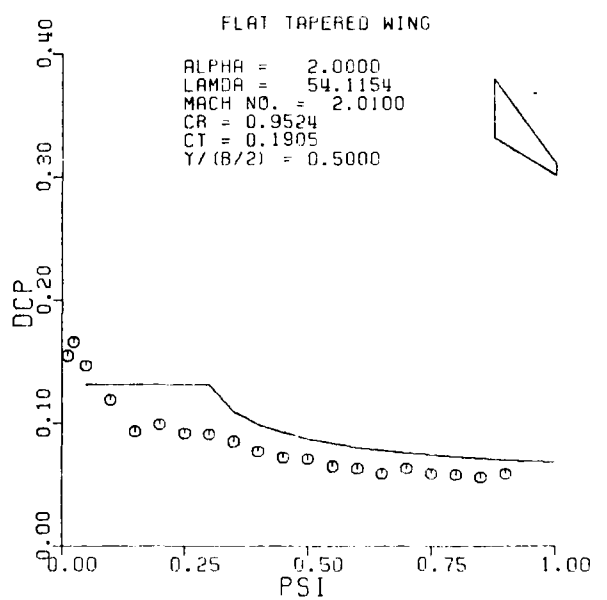a Flat Tapered Wing; M = 2.01, α = 2.0.
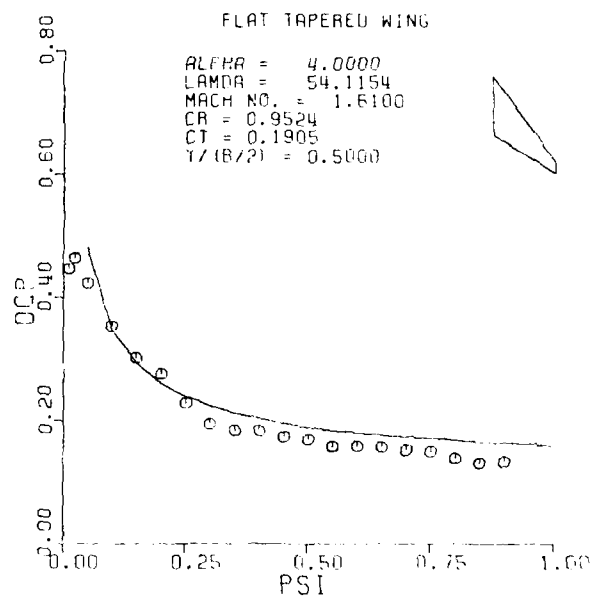
Figure A25.   Pressure Distribution on a Flat Tapered Wing; M = 1.61, α = 4.0.

FLAT TAPERED WING

ALPHA =   4.0000
LAMDA =   54.1154
MACH NO. =   1.6100
CR = 0.9524
CT = 0.1905
Y/(B/2) = 0.7000

FLAT TAPERED WING

ALPHA =   4.0000
LAMDA =   54.1154
MACH NO. =   1.6100
CR ≈ 0.9524
CT = 0.1905
Y/(B/2) = 0.9000

Figure A25.   Continued

FLAT TAPERED WING

ALPHA = 4.0000
LAMDA = 54.1154
MACH NO. = 1.6100
CR = 0.9524
CT = 0.1905

FLAT TAPERED WING

ALPHA = 4.0000
LAMDA = 54.1154
MACH NO. = 1.6100
CR = 0.9524
CT = 0.1905
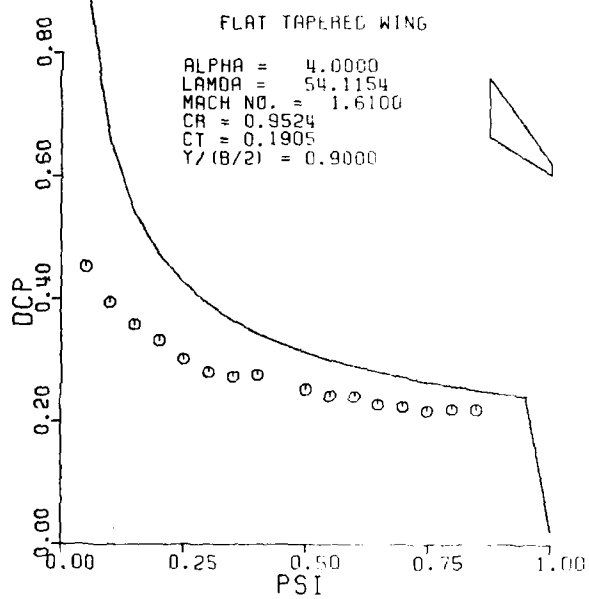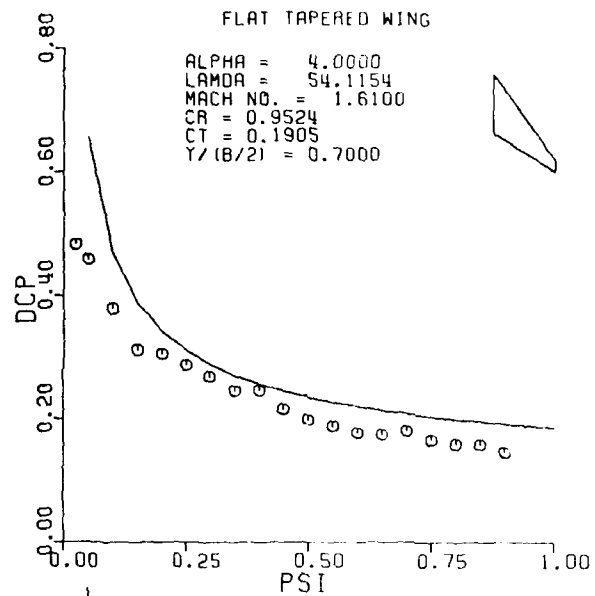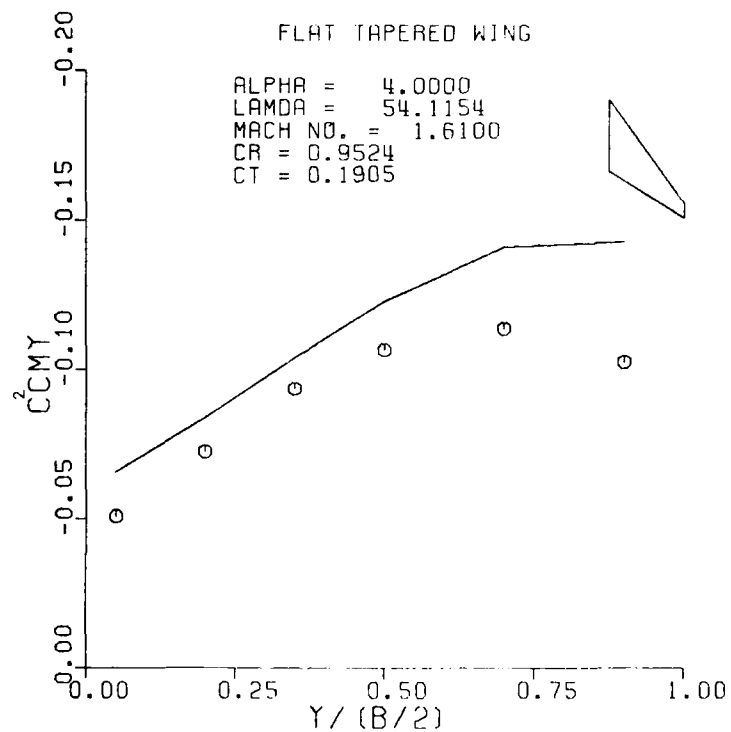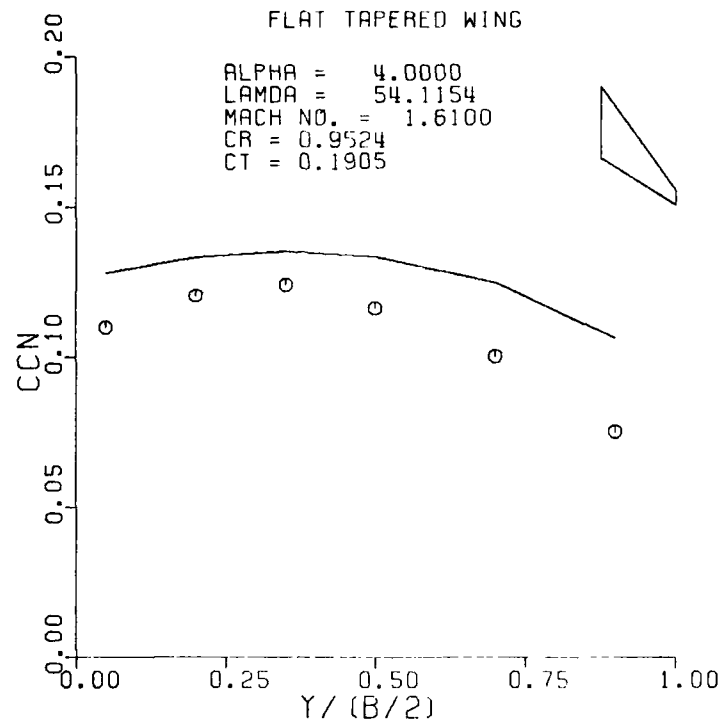
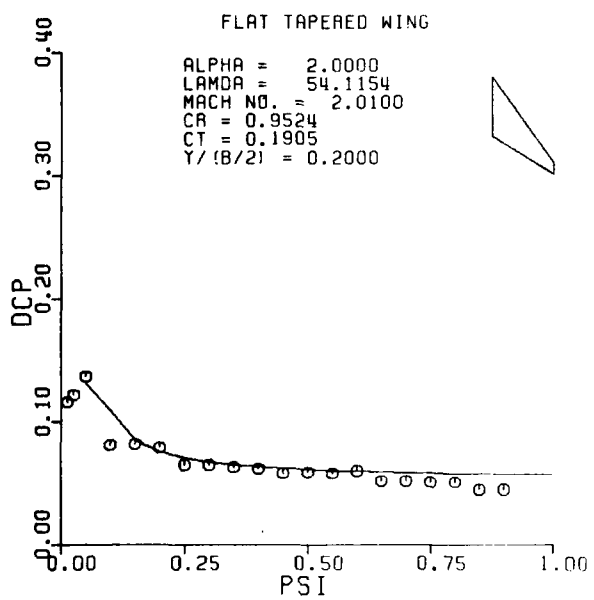Figure A26. Sectional Normal Force and Pitching Moment for a Flat Tapered Wing; M = 1.61, α = 4.0.
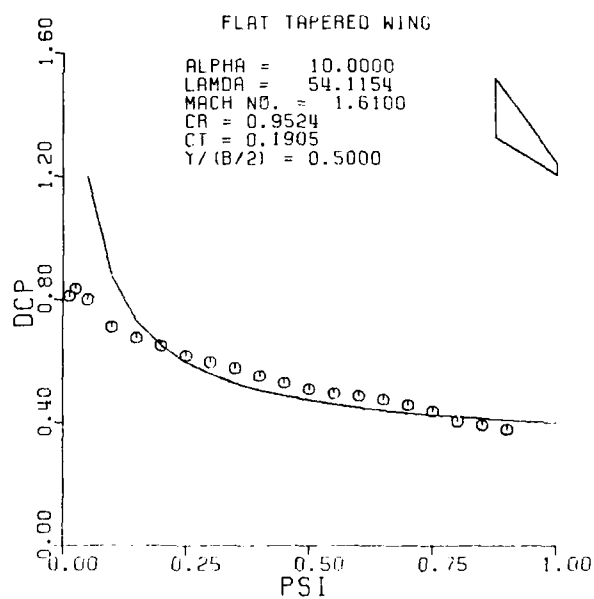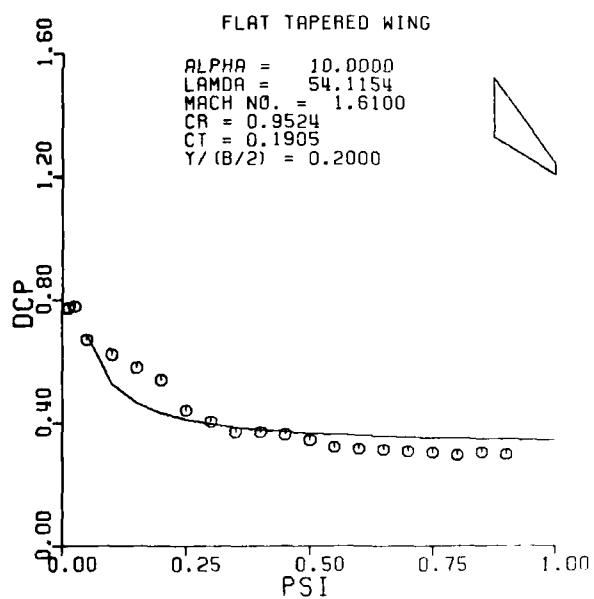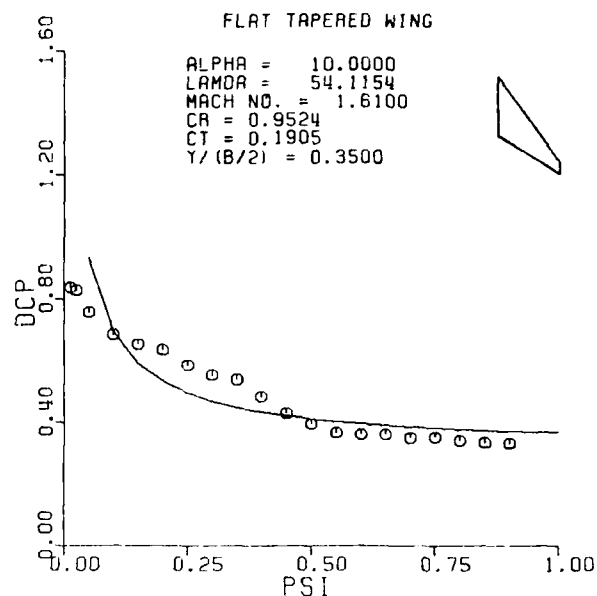
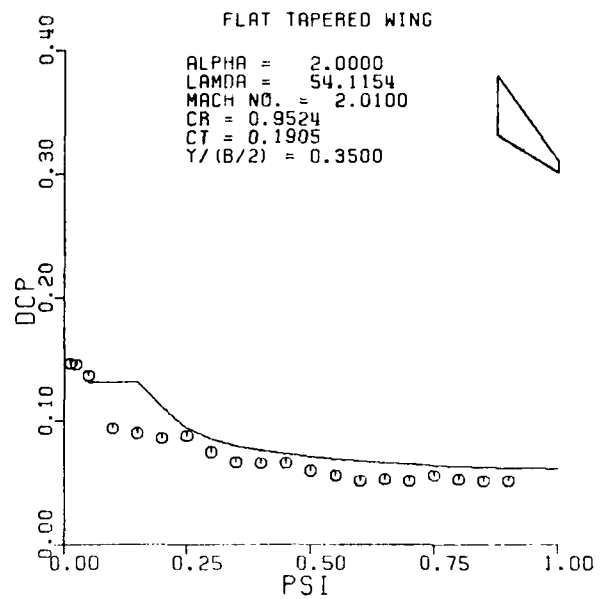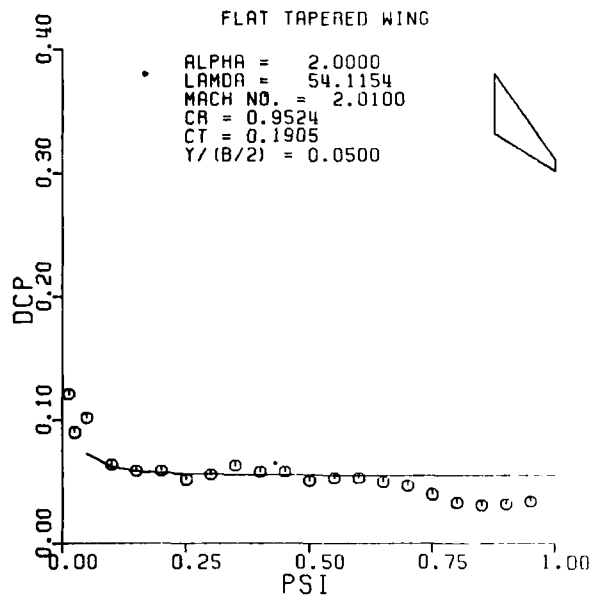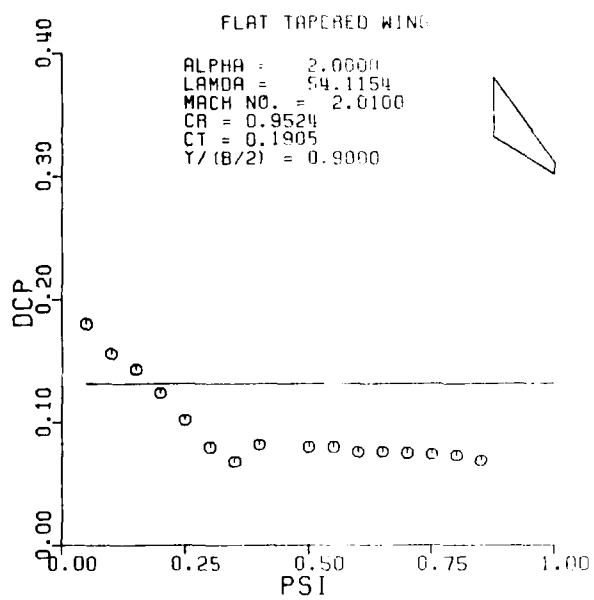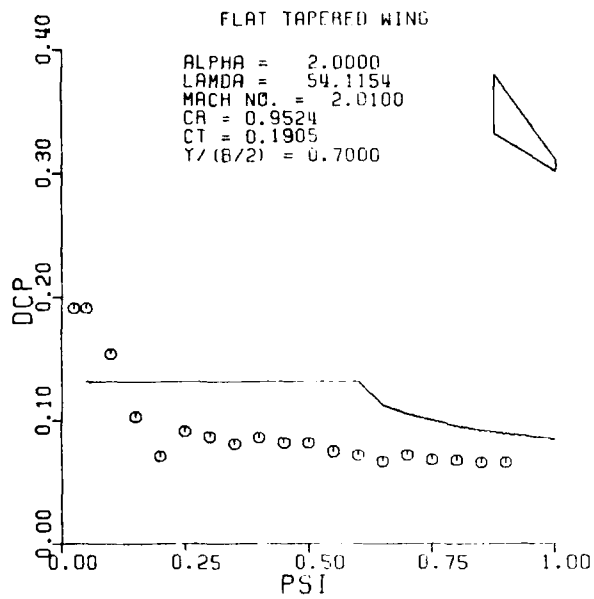**Figure A27.** Pressure Distribution on a Flat Tapered Wing; M = 1.61, α = 10.0.

FLAT TAPERED WING

ALPHA = 10.0000
LAMDA = 54.1154
MACH NO. = 1.6100
CR = 0.9524
CT = 0.1905
Y/(B/2) = 0.7000

FLAT TAPERED WING

ALPHA = 10.0000
LAMDA = 54.1154
MACH NO. = 1.6100
CR = 0.9524
CT = 0.1905
Y/(B/2) = 0.9000

Figure A27. Continued

FLAT TAPERED WING

ALPHA = 10.0000
LAMDA = 54.1154
MACH NO. = 1.6100
CR = 0.9524
CT = 0.1905

Y/(B/2)

FLAT TAPERED WING

ALPHA = 10.0000
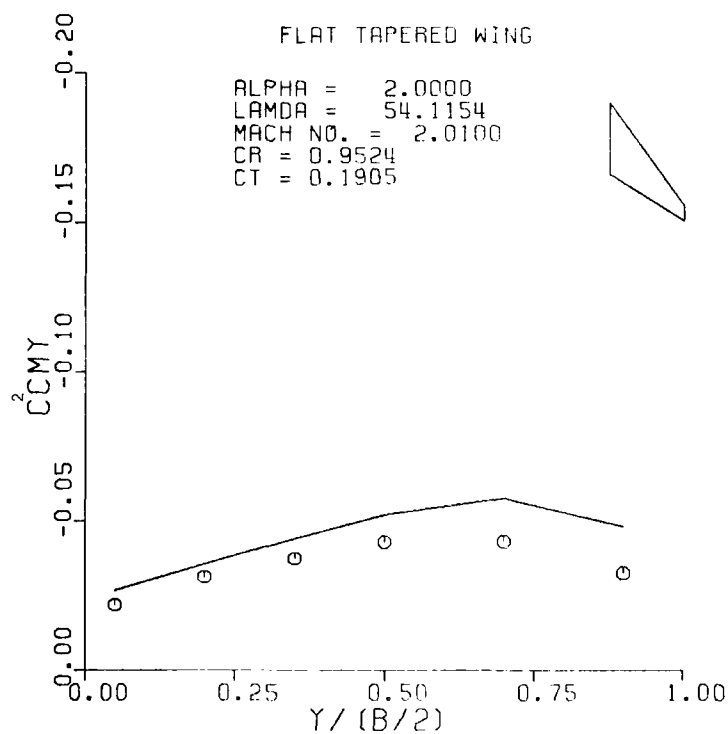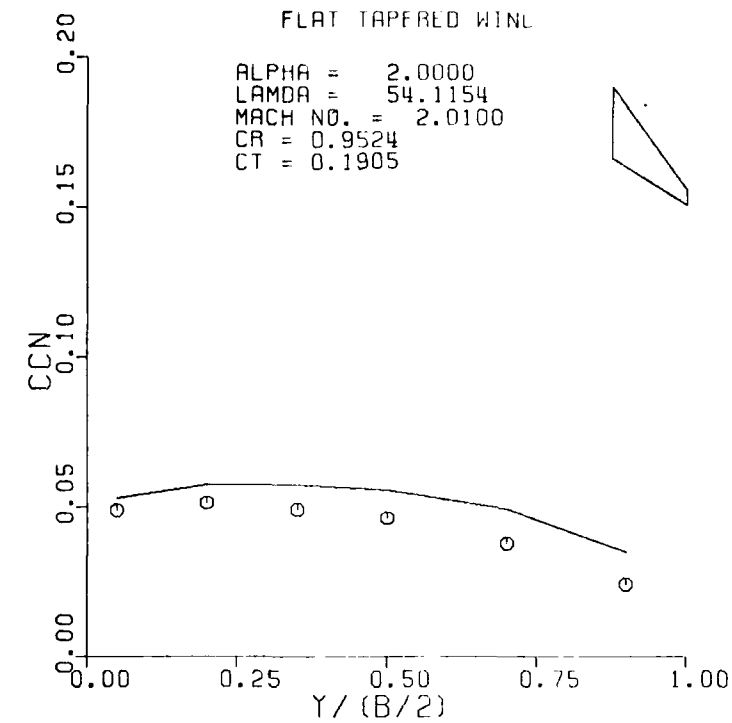LAMDA = 54.1154
MACH NO. = 1.6100
CR = 0.9524
CT = 0.1905

Y/(B/2)
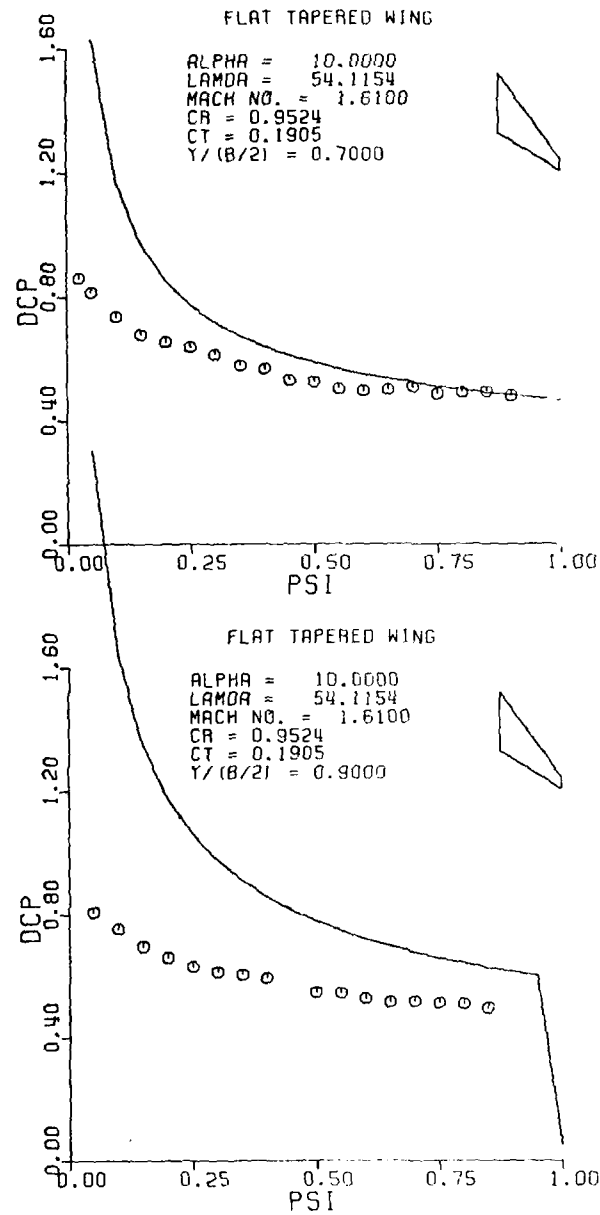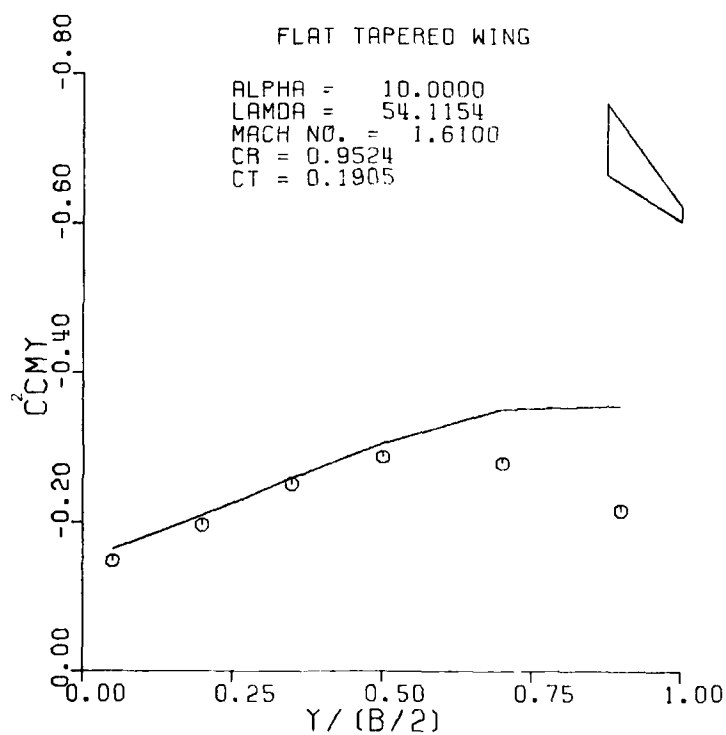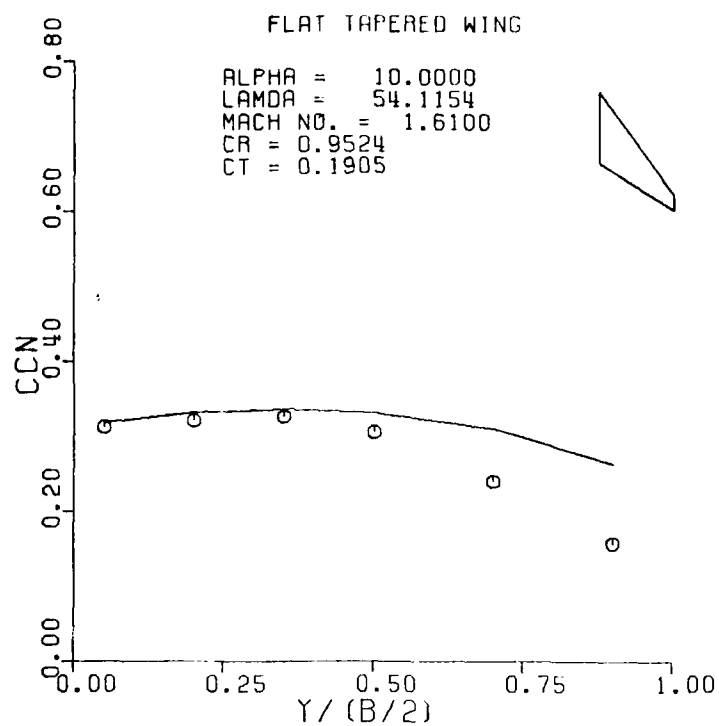
Figure A28.   Sectional Normal Force and Pitching Moment for a
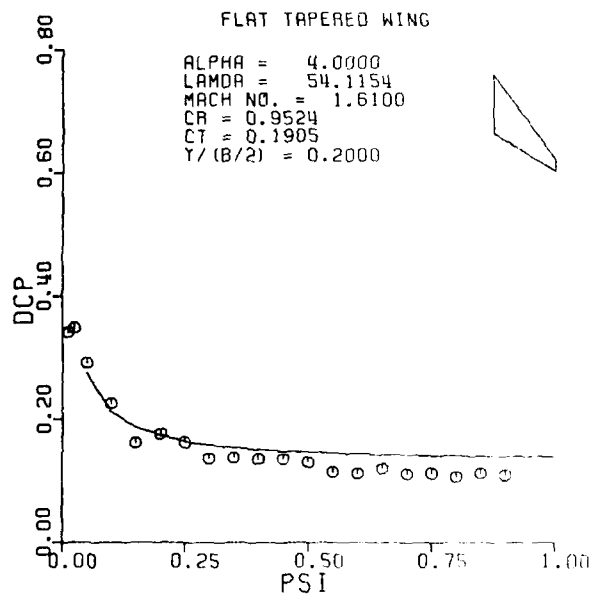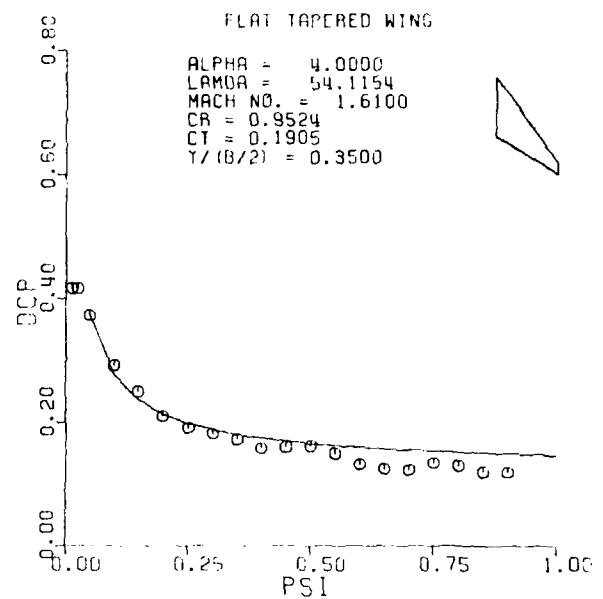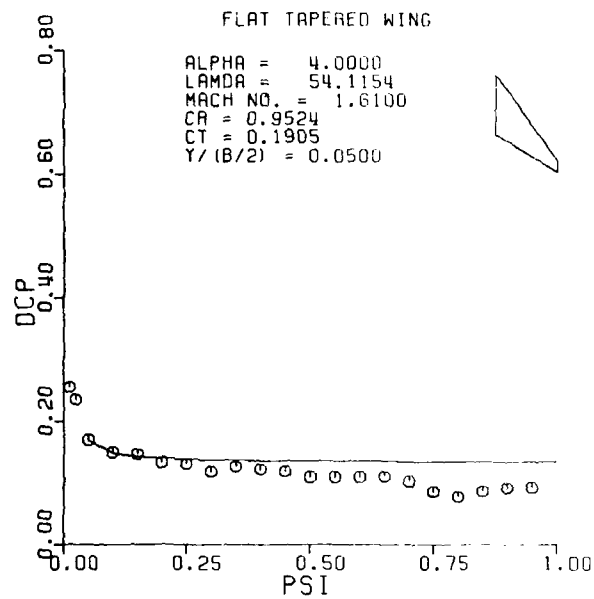Flat Tapered Wing; M = 1.61, α = 10.0.
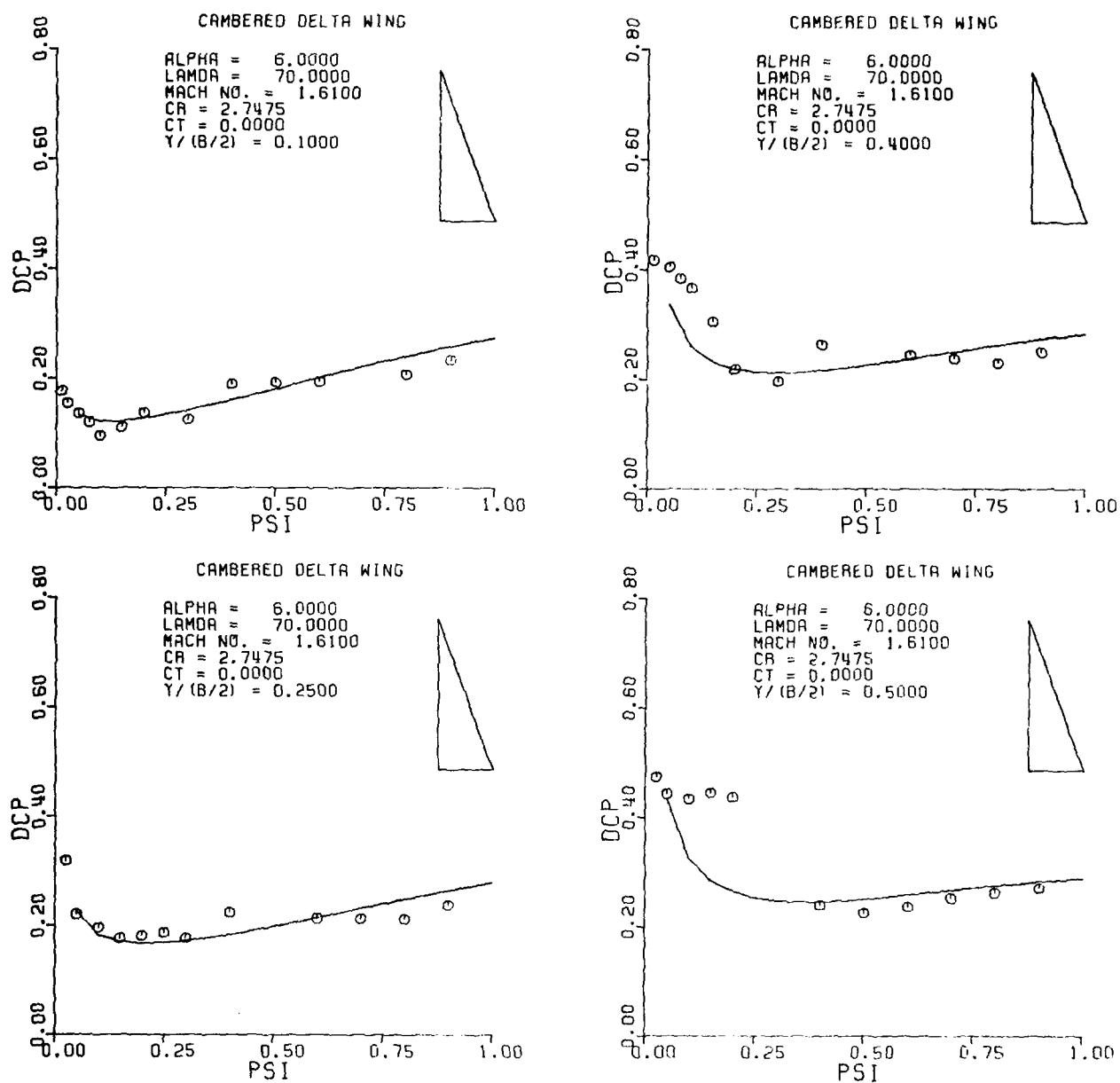
Figure A29. Pressure Distribution on a Cambered Delta Wing; $M = 1.61$, $\alpha = 6.0$.

Figure A29. Continued

CAMBERED DELTA WING

ALPHA = 6.0000
LAMDA = 70.0000
MACH NO. = 1.6100
CR = 2.7475
CT = 0.0000

CAMBERED DELTA WING

ALPHA = 6.0000
LAMDA = 70.0000
MACH NO. = 1.6100
CR = 2.7475
CT = 0.0000
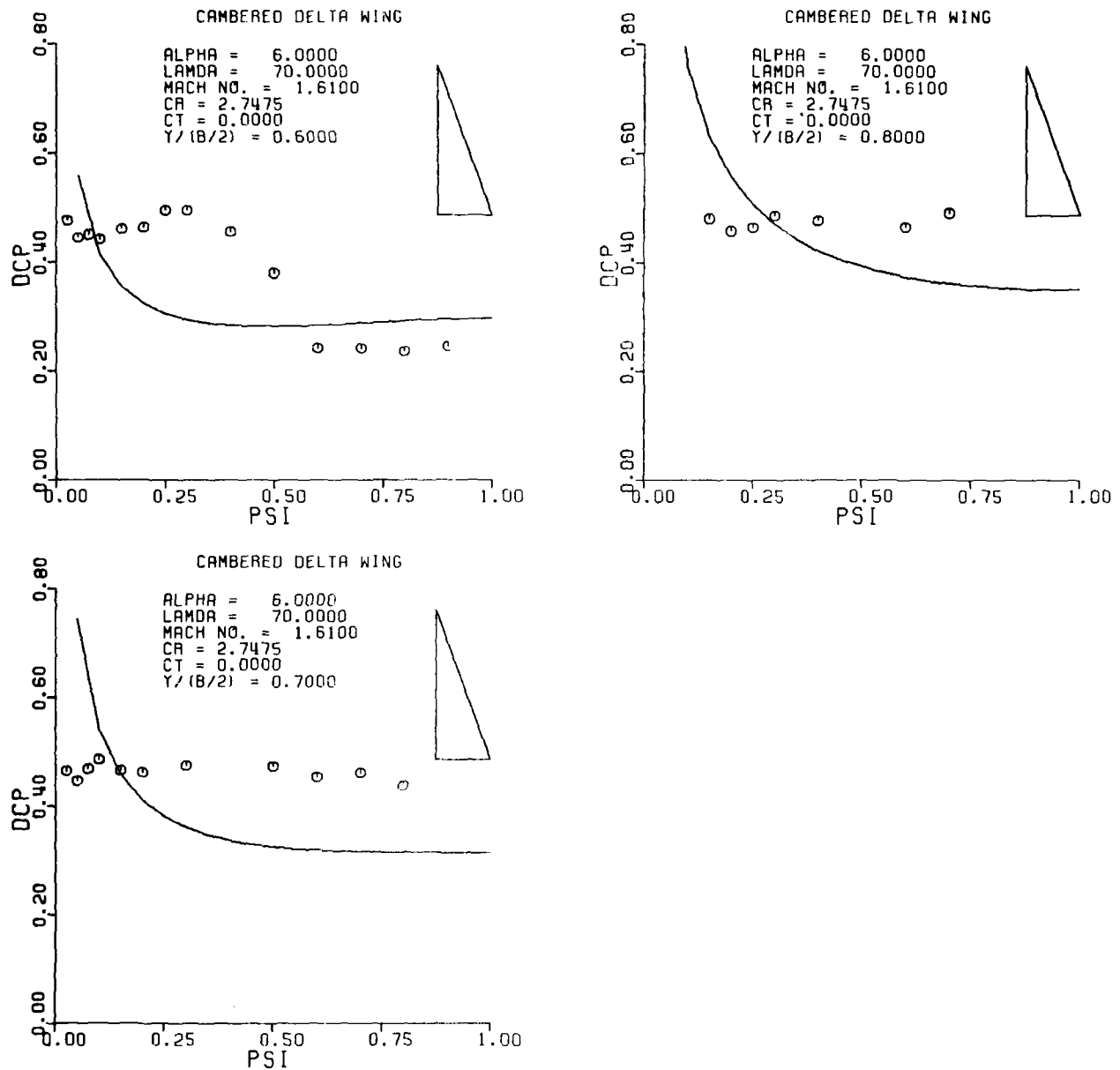
Figure A30.   Sectional Normal Force and Pitching Moment for a
Cambered Delta Wing; M = 1.61, α = 6.0.

157
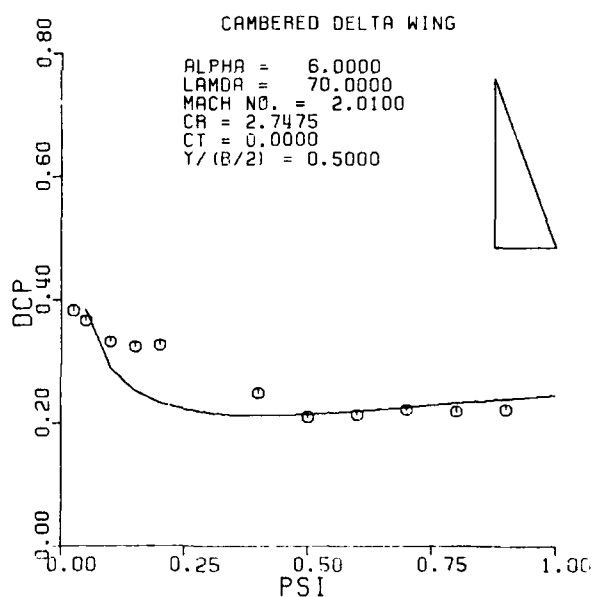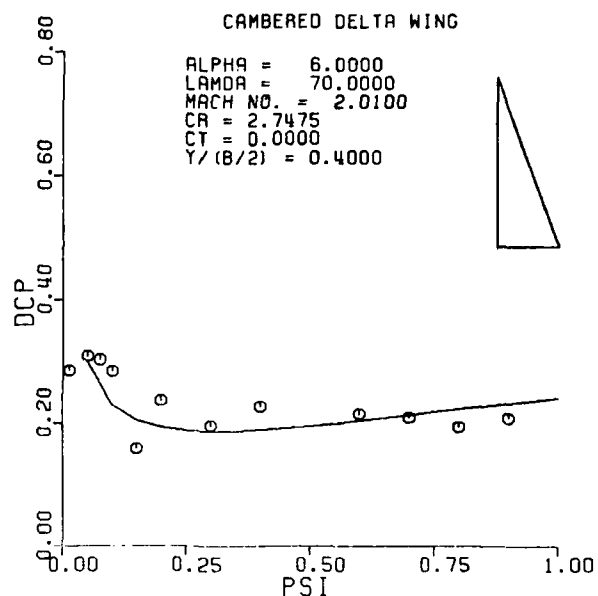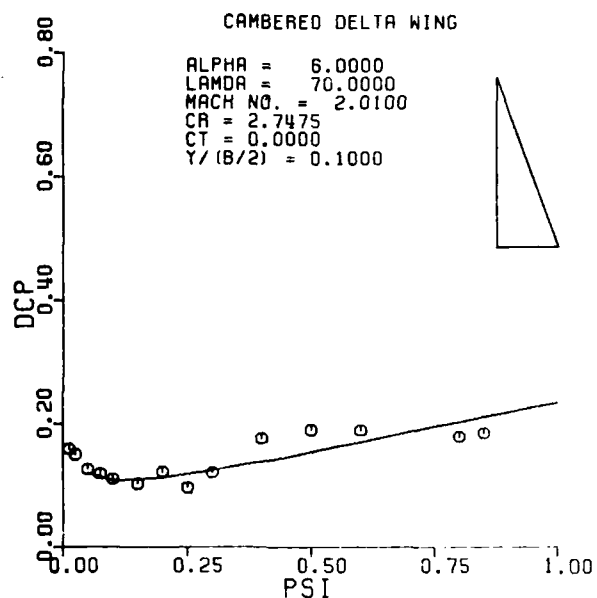
Figure A31. Pressure Distribution on a Cambered Delta Wing; M = 2.01, α = 6.0.

CAMBERED DELTA WING

ALPHA = 6.0000
LAMDA = 70.0000
MACH NO. = 2.0100
CR = 2.7475
CT = 0.0000
Y/(B/2) = 0.6000

CAMBERED DELTA WING

ALPHA = 6.0000
LAMDA = 70.0000
MACH NO. = 2.0100
CR = 2.7475
CT = 0.0000
Y/(B/2) = 0.8000

CAMBERED DELTA WING

ALPHA = 6.0000
LAMDA = 70.0000
MACH NO. = 2.0100
CR = 2.7475
CT = 0.0000
Y/(B/2) = 0.7000

Figure A31. Continued

CAMBERED DELTA WING

ALPHA =   6.0000
LAMDA =   70.0000
MACH NO. =   2.0100
CR = 2.7475
CT = 0.0000

CCN

Y/(B/2)

CAMBERED DELTA WING

ALPHA =   6.0000
LAMDA =   70.0000
MACH NO. =   2.0100
CR = 2.7475
CT = 0.0000

CCMY

Y/(B/2)

Figure A32. Sectional Normal Force and Pitching Moment for a
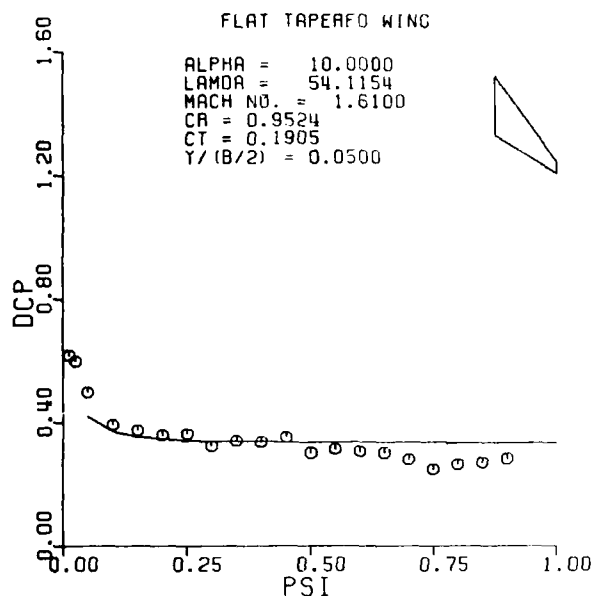Cambered Delta Wing; M = 2.01, α = 6.0.

160
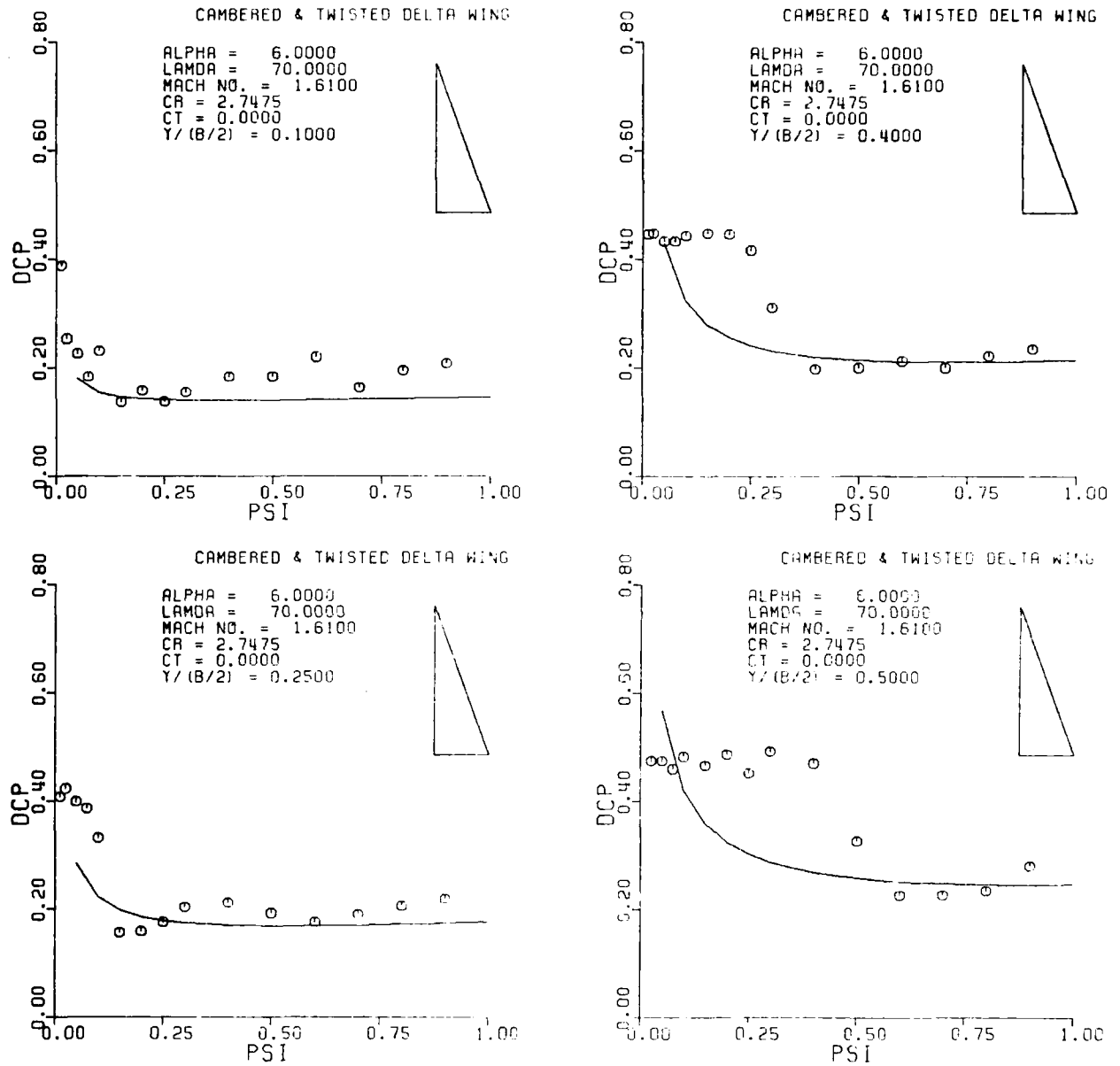
Figure A33. Pressure Distribution on a Cambered and Twisted Delta Wing; M = 1.61, α = 6.0.

CAMBERED & TWISTED DELTA WING

ALPHA = 6.0000
LAMDA = 70.0000
MACH NO. = 1.6100
CR = 2.7475
CT = 0.0000
Y/(B/2) = 0.6000

CAMBERED & TWISTED DELTA WING

ALPHA = 6.0000
LAMDA = 70.0000
MACH NO. = 1.6100
CR = 2.7475
CT = 0.0000
Y/(B/2) = 0.8000

CAMBERED & TWISTED DELTA WING

ALPHA = 6.0000
LAMDA = 70.0000
MACH NO. = 1.6100
CR = 2.7475
CT = 0.0000
Y/(B/2) = 0.7000

Figure A33.   Continued

CAMBERED & TWISTED DELTA WING

ALPHA = 6.0000
LAMDA = 70.0000
MACH NO. = 1.6100
CR = 2.7475
CT = 0.0000

CAMBERED & TWISTED DELTA WING

ALPHA = 6.0000
LAMDA = 70.0000
MACH NO. = 1.6100
CR = 2.7475
CT = 0.0000

Figure A34.   Sectional Normal Force and Pitching Moment for a
Cambered and Twisted Delta Wing; M = 1.61, α = 6.0.
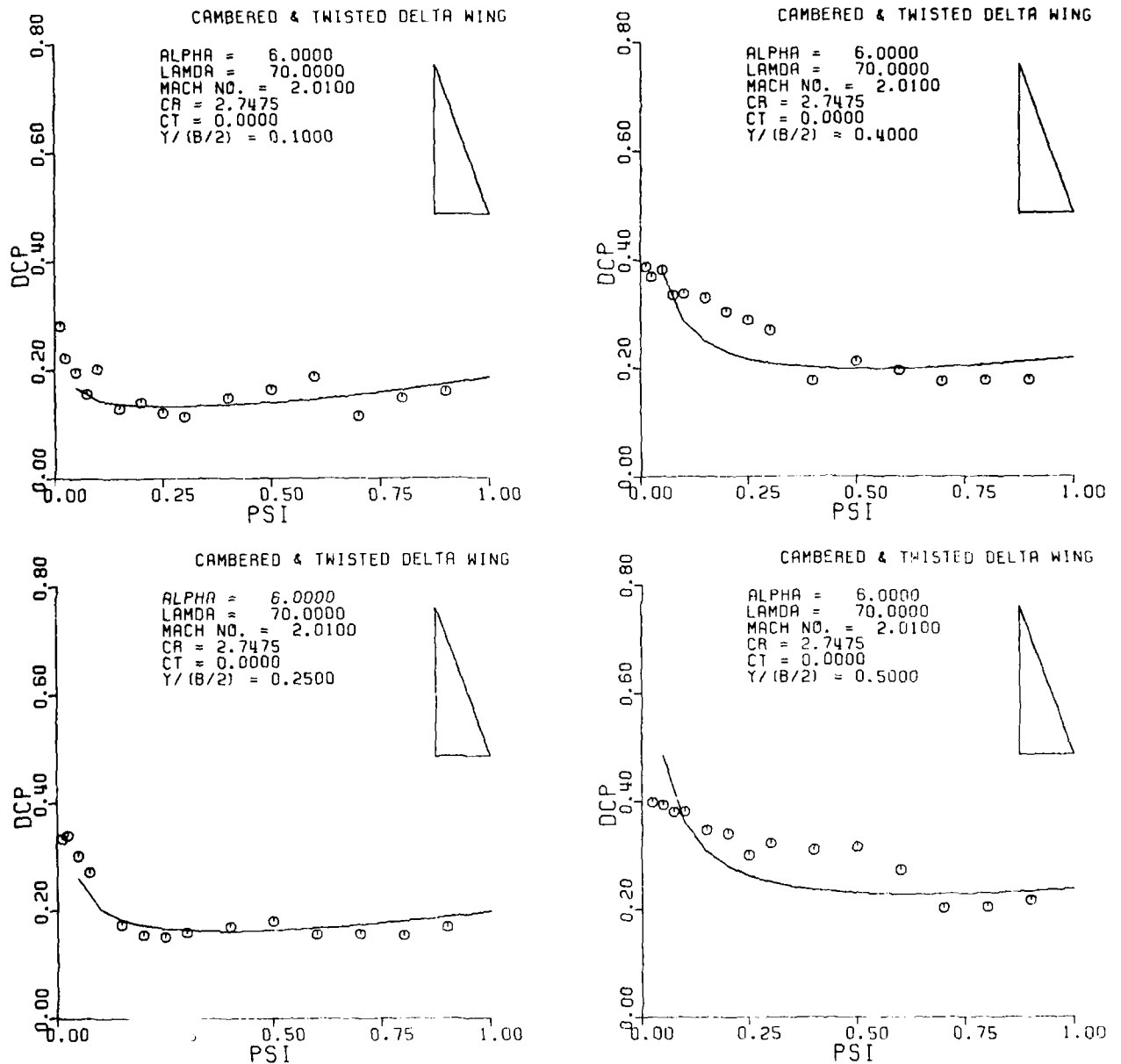
Figure A35. Pressure Distribution on a Cambered and Twisted Delta Wing;
M = 2.01, α = 6.0.

CAMBERED & TWISTED DELTA WING

ALPHA = 6.0000
LAMDA = 70.0000
MACH NO. = 2.0100
CR = 2.7475
CT = 0.0000
Y/(B/2) = 0.6000

CAMBERED & TWISTED DELTA WING

ALPHA = 6.0000
LAMDA = 70.0000
MACH NO. = 2.0100
CR = 2.7475
CT = 0.0000
Y/(B/2) = 0.8000

CAMBERED & TWISTED DELTA WING

ALPHA = 6.0000
LAMDA = 70.0000
MACH NO. = 2.0100
CR = 2.7475
CT = 0.0000
Y/(B/2) = 0.7000
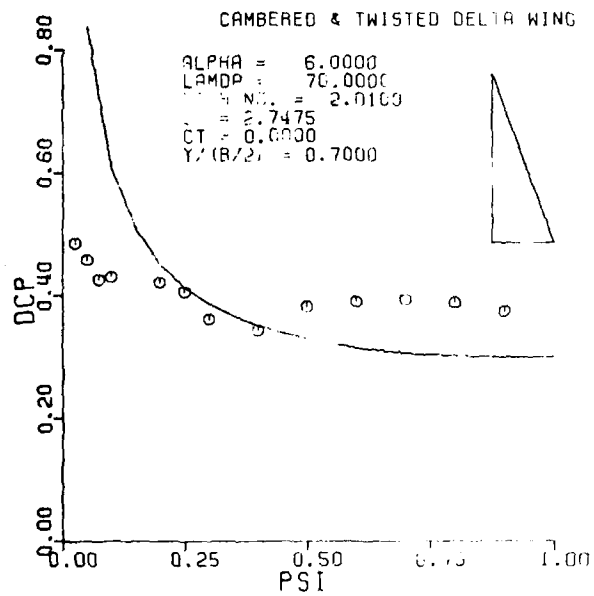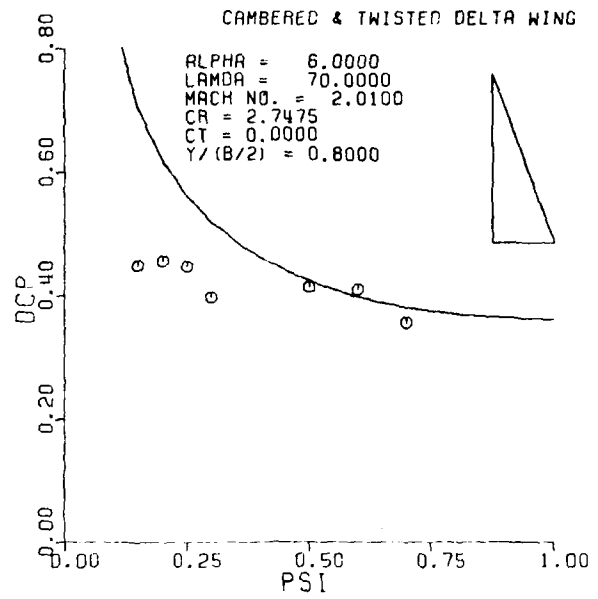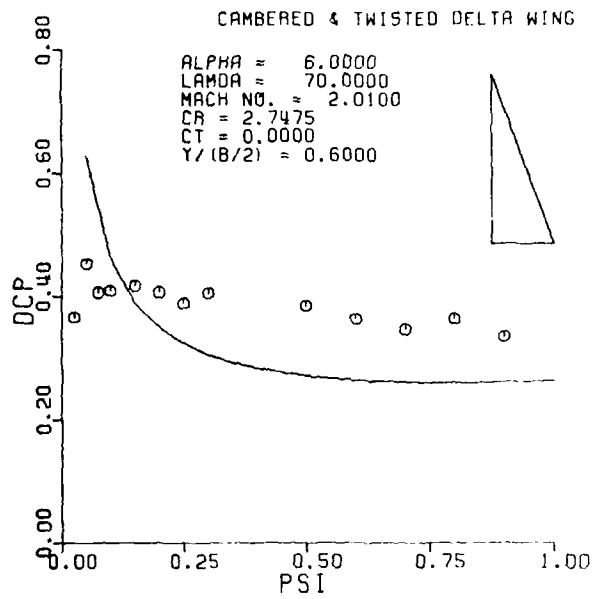
Figure A35.   Continued

CAMBERED & TWISTED DELTA WING

ALPHA =   6.0000
LAMDA =   70.0000
MACH NO. =   2.0100
CR = 2.7475
CT = 0.0000
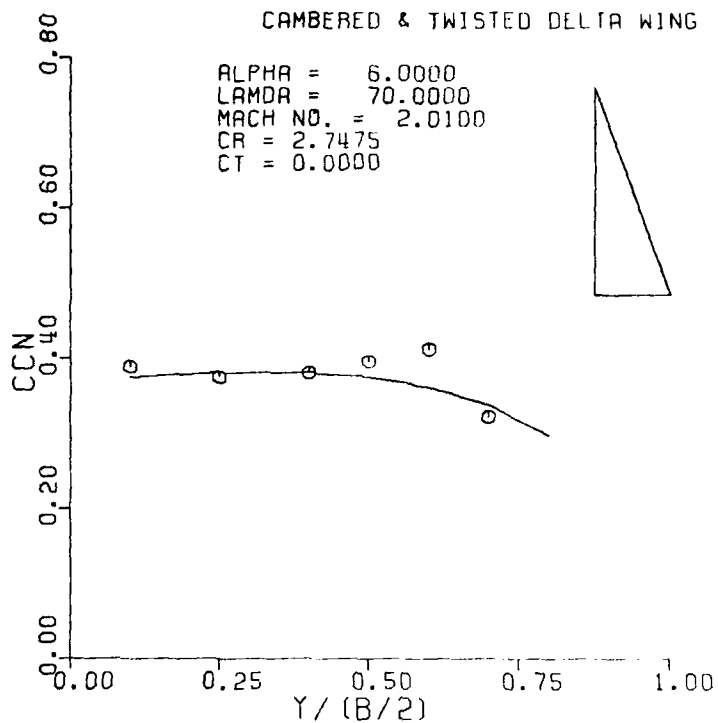
CAMBERED & TWISTED DELTA WING

ALPHA =   6.0000
LAMDA =   70.0000
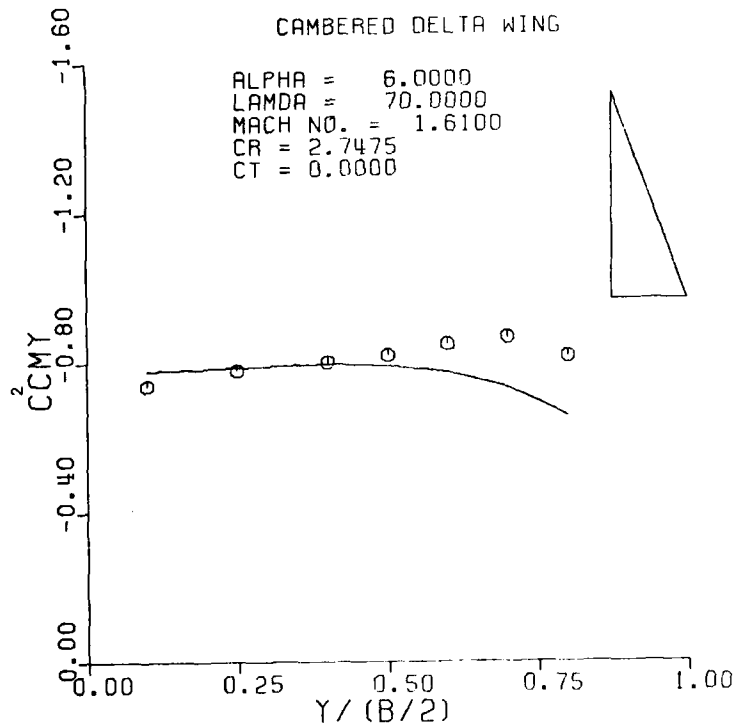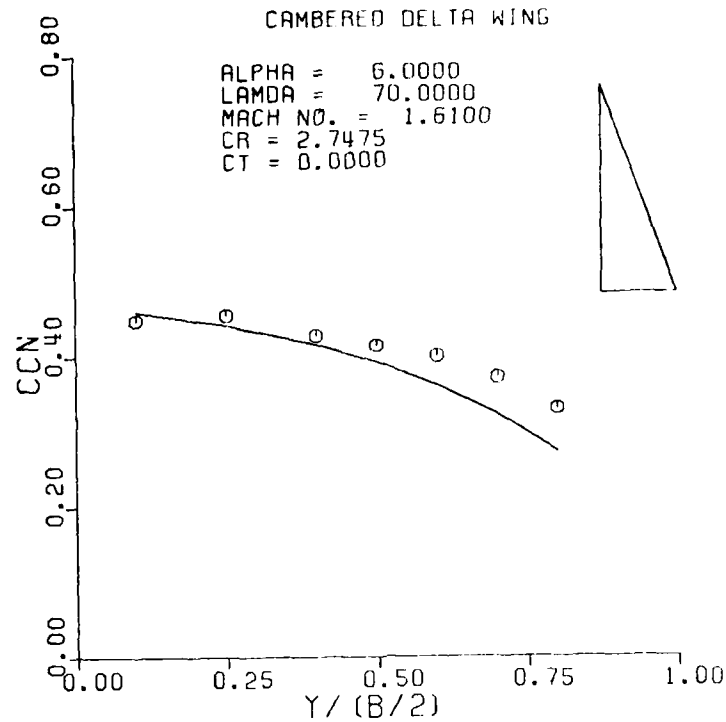MACH NO. =   2.0100
CR = 2.7475
CT = 0.0000
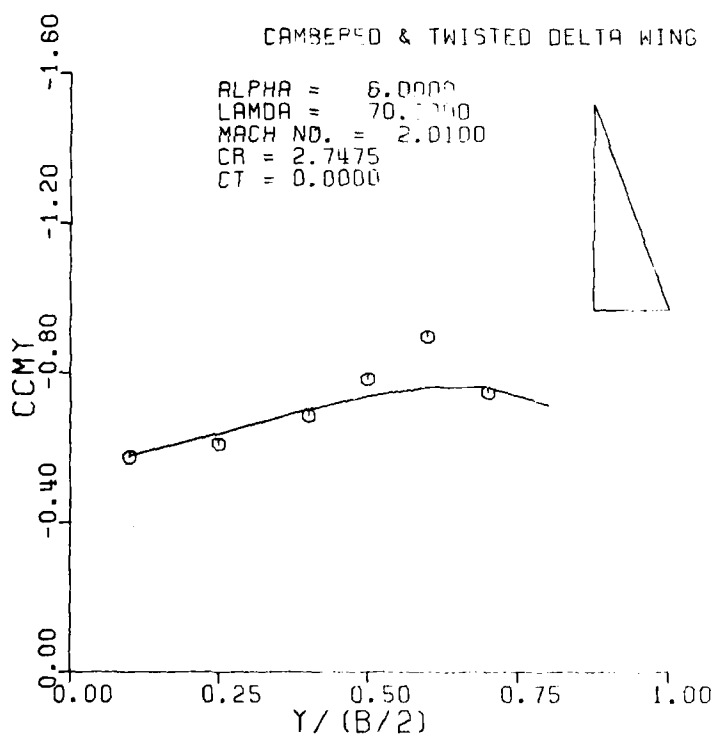
Figure A36. Sectional Normal Force and Pitching Moment for a
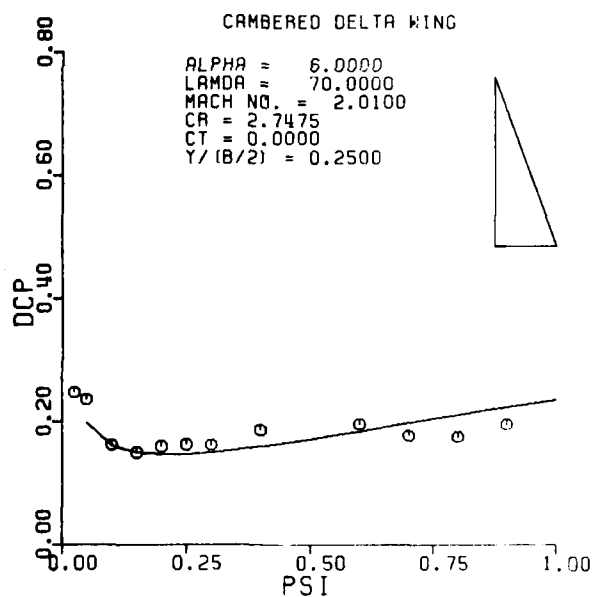Cambered and Twisted Delta Wing;   M = 2.01, α = 6.0.
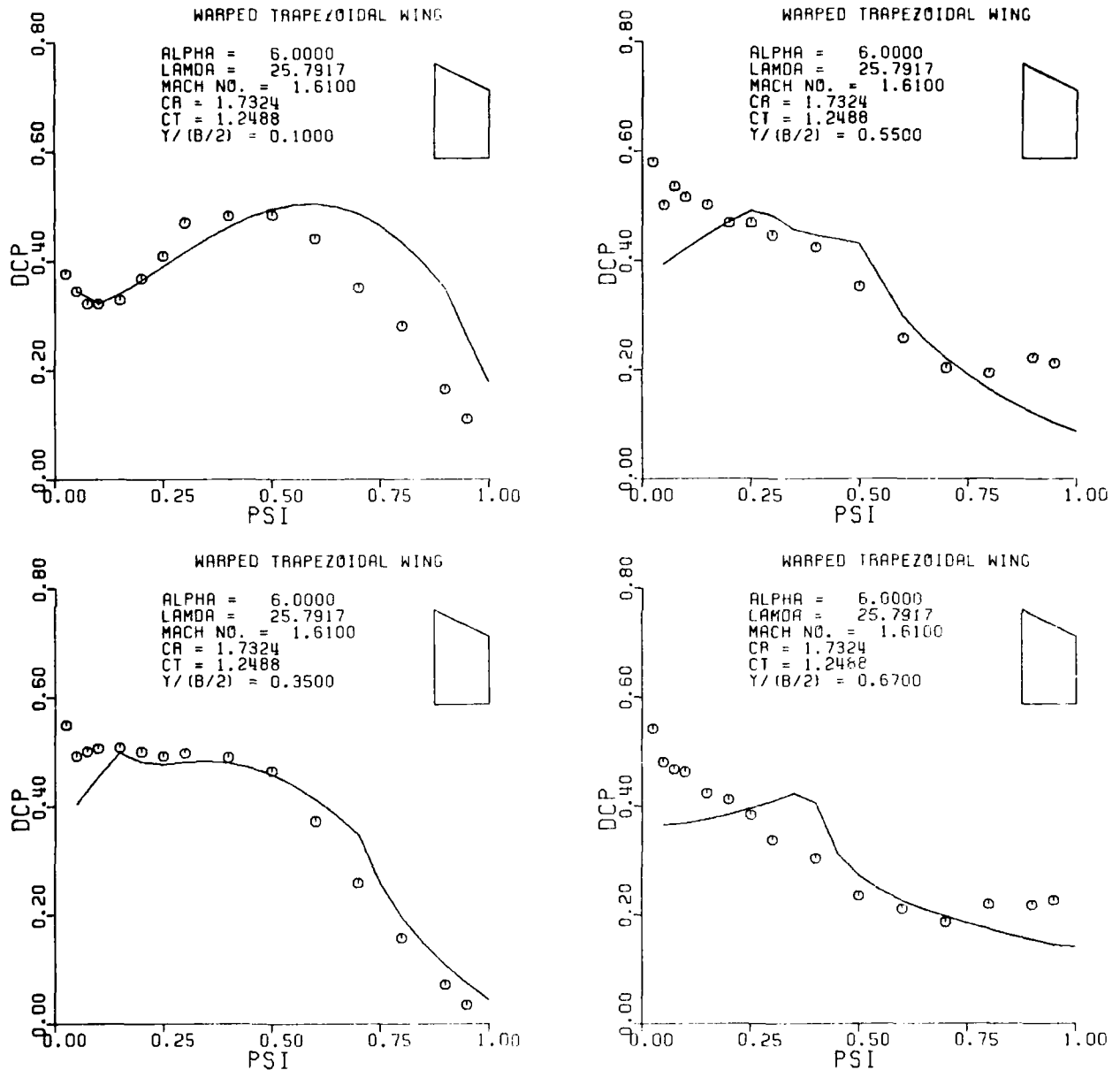
Figure A37. Pressure Distribution on a Warped Trapezoidal Wing; M = 1.61, α = 6.0.

WARPED TRAPEZOIDAL WING

ALPHA   =   6.0000
LAMDA   =   25.7917
MACH NO. =   1.6100
CR = 1.7324
CT = 1.2488
Y/(B/2) = 0.7700

WARPED TRAPEZOIDAL WING

ALPHA   =   6.0000
LAMDA   =   25.7917
MACH NO. =   1.6100
CR = 1.7324
CT = 1.2488
Y/(B/2) = 0.9700

WARPED TRAPEZOIDAL WING

ALPHA   =   6.0000
LAMDA   =   25.7917
MACH NO. =   1.6100
CR = 1.7324
CT = 1.2488
Y/(B/2) = 0.8700

Figure A37.   Continued

WARPED TRAPEZOIDAL WING

ALPHA = 6.0000
LAMDA = 25.7917
MACH NO. = 1.6100
CR = 1.7324
CT = 1.2488

CCN

Y/(B/2)

WARPED TRAPEZOIDAL WING

ALPHA = 6.0000
LAMDA = 25.7917
MACH NO. = 1.6100
CR = 1.7324
CT = 1.2488

C²CMY

Y/(B/2)

Figure A38. Sectional Normal Force and Pitching Moment for a
Warped Trapezoidal Wing; M = 1.61, α = 6.0.
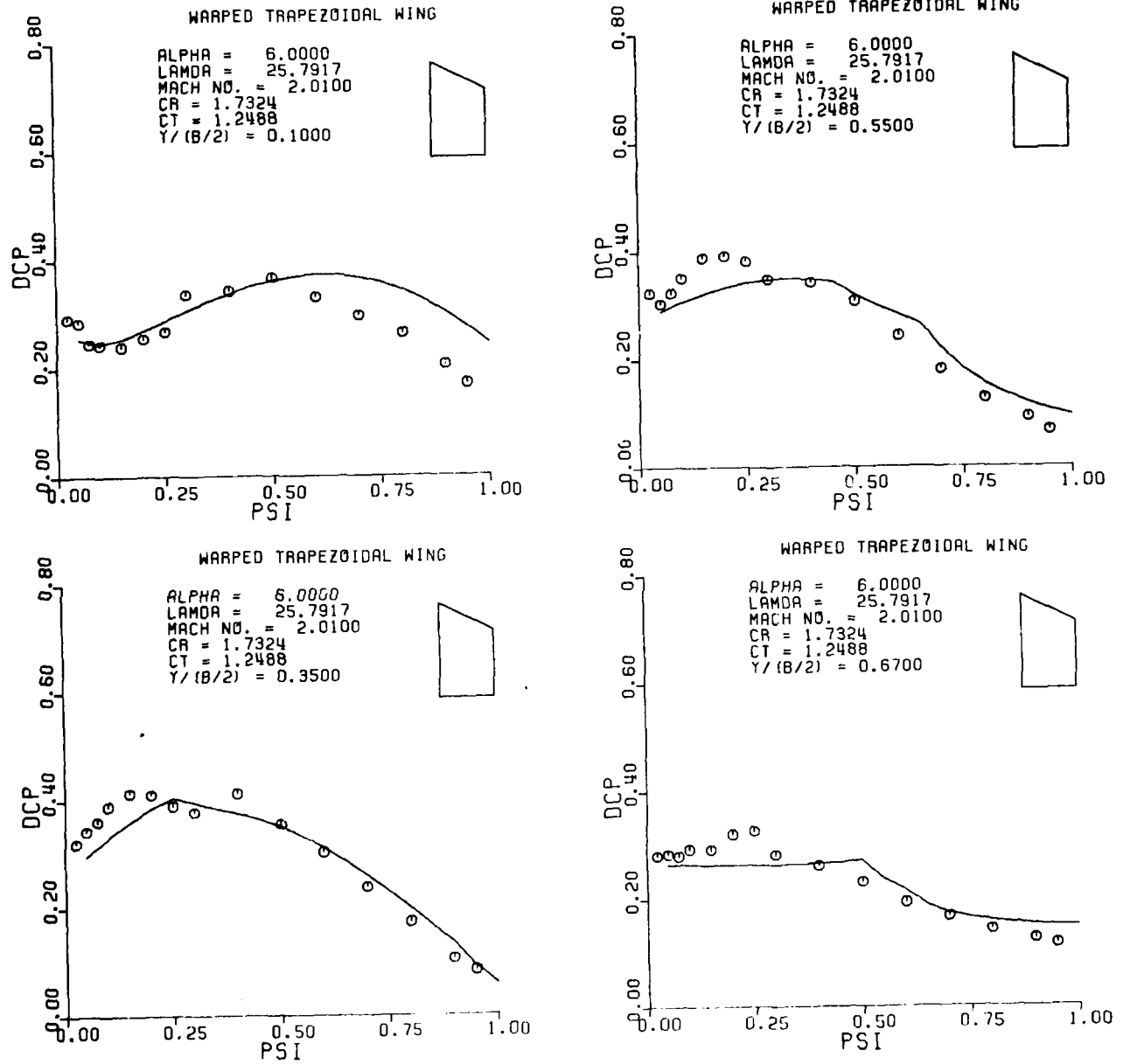
Figure A39. Pressure Distribution on a Warped Trapezoidal Wing; M = 2.01, α = 6.0.

WARPED TRAPEZOIDAL WING

ALPHA = 6.0000
LAMDA = 25.7917
MACH NO. = 2.0100
CR = 1.7324
CT = 1.2488
Y/(B/2) = 0.7700

WARPED TRAPEZOIDAL WING

ALPHA = 6.0000
LAMDA = 25.7917
MACH NO. = 2.0100
CR = 1.7324
CT = 1.2488
Y/(B/2) = 0.9700

WARPED TRAPEZOIDAL WING

ALPHA = 6.0000
LAMDA = 25.7917
MACH NO. = 2.0100
CR = 1.7324
CT = 1.2488
Y/(B/2) = 0.8700

Figure A39.   Continued

WARPED TRAPEZOIDAL WING

ALPHA = 6.0000
LAMDA = 25.7917
MACH NO. = 2.0100
CR = 1.7324
CT = 1.2488

WARPED TRAPEZOIDAL WING

ALPHA = 6.0000
LAMDA = 25.7917
MACH NO. = 2.0100
CR = 1.7324
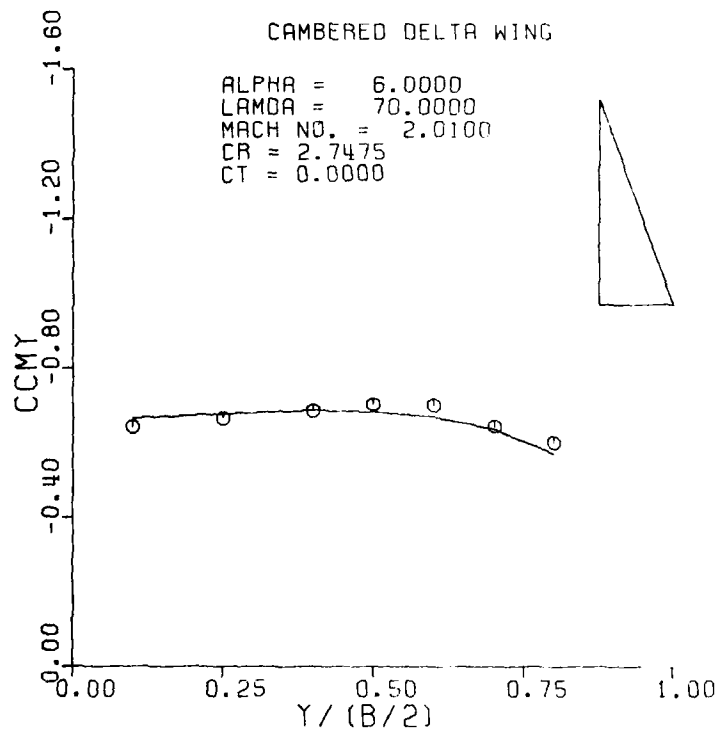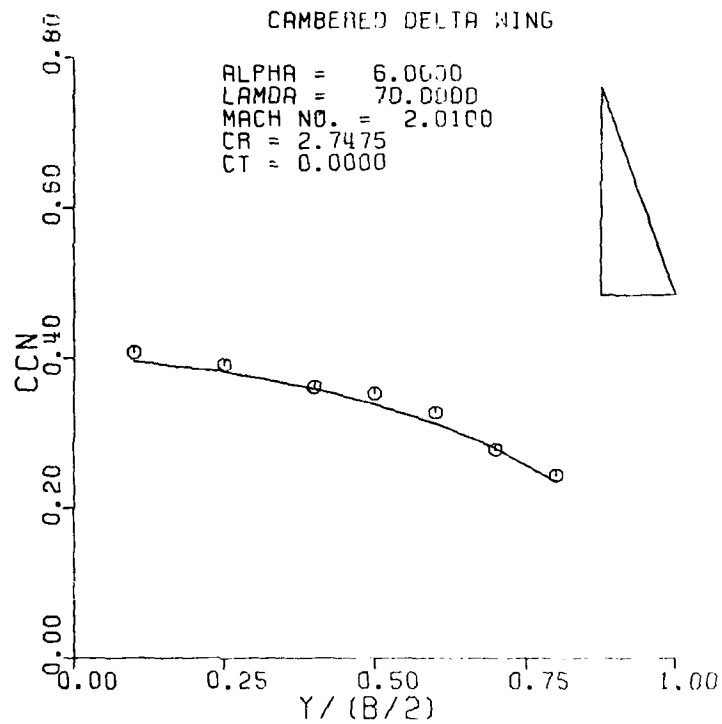CT = 1.2488

Figure A40. Sectional Normal Force and Pitching Moment for a
Warped Trapezoidal Wing; M = 2.01, α = 6.0.

APPENDIX B

SUBSONIC COMPUTER PROGRAM USERS GUIDE

I. General Description of the Main Program and Subroutines for
    the Subsonic Program

MAIN PROGRAM - This is the executive segment which primarily controls and

coordinates the various tasks performed by the subprograms. Other

functions performed by the main program include: (a) all input and the

majority of output; (b) non-dimensionalization; (c) calculation of the

boundary conditions (the "B" matrix); (d) computation of all total

characteristics, both exact results and numerical integrations (this

includes wing-elevon, fuselage, suction, and all combinations of these).

BLOCK DATA - This data gives coordinates of a non-planar mean line (XTB,ZTB)

as well as the slope (ZPTB) for use in calculating wing deformations.

The present data is for the deformed Hawk wing.

SUBROUTINE SURFIN - This routine computes the value of the surface integral

(the "A" matrix) by summing the effects of each grid panel at a control

point. It is called once for the wing and once for the elevon for each

control point.

SUBROUTINE SECLM - The sectional loading characteristics are calculated for

the wing or elevon in this subroutine. It is called after the pressure

loading coefficients are determined.

SUBROUTINE PRESUR - This subroutine is used, after the pressure loading

coefficients are determined, to calculate and print ΔC_p at NSPAN by

NCORD points on the lifting surfaces.

173

SUBROUTINE GEOM - This subroutine sets up the geometry of both the grid

panels and the control points, and then centers the control points

inside the grid element in which they appear. Basically, a cosine

distribution is used for both the grid elements and control points.

This routine is called once for the wing and once for the elevon.

SUBROUTINE INTV - This routine contains the actual equations of the sur-

face integral and, therefore, is utilized by SUBROUTINE SURFIN.

SUBROUTINE INVERT - Gauss elimination is used in this subroutine to

"invert" the A matrix and solve for the unknown leading coefficients,

B_{nm}'s.

SUBROUTINE HINGE - This contains the equations of the closed form solution

for the elevon hinge moment.

SUBROUTINE TLUP - This is a "table-lookup" routine which uses the data

given by the variables in BLOCK DATA to interpolate for wing mean line

slopes used in determining deformation angles. It is called by

FUNCTION WARP.

FUNCTION WARP - This function uses either the table-lookup or a function

definition to find wing/elevon deformation. It is called by both the

main program to determine deformation of control points (included in

the boundary conditions) and by SUBROUTINE SURFIN to determine deforma-

tion of grid panels.

II. INPUT DATA

A. Data Cards:

Card No.	Format	Variable List
1	18A4	WING
2	7F10.0	SPAN,CR,CT,LAMDA,SAREA,CBAR,MACH
3	F10.0,I5	ALPHA,KSTOP
4	10I5	NC,NS,NX,NY,NCF,NSF,NXF,NYF,NSPAN, NCORD
5	5F10.0	CRF,CTF,DELTA,ALTWMX,EPS
6	F10.0,I5,2F10.0	HNL,IDEF,AMP,DB
(Additional cards)	3F10.0	ALPHA,DELTA,ALTWMX

("Additional cards" allows more than one case of the given
geometry to be run with different boundary conditions.
There should be (KSTOP-1) additional cards.)

B. Variable definitions (all linear dimension units must be consistent)

WING - Alphanumeric problem description

SPAN - Total wing span

CR - Wing root chord

CT - Wing tip chord

LAMDA - Wing leading edge sweep angle

SAREA,CBAR - Reference area and reference length. If 0.0 is input,
the total area and mean aerodynamic chord will be
calculated and used.

MACH - Mach number

ALPHA - Angles of attack of wing, in degrees. Leading edge up
is positive.

KSTOP - Number of cases of different boundary conditions that are
to be run.

NC,NS - Number of chordwise and spanwise control points (respectively) on the wing (typically 4x4).

NX,NY - Number of chordwise and spanwise (respectively) grid panels on the wing (typically 45x45).

NCF,NSF - Chordwise and spanwise control points on the elevon (typically 3x4). NSF must be equal to NS.

NXF,NYF - Chordwise and spanwise grid panels on the elevon (typically 20x45). NYF must be equal to NY.

NSPAN,NCORD - Number of spanwise by chordwise points at which ΔC_p distribution is to be printed out.

CRF - Elevon root chord

CTF - Elevon tip chord

DELTA - Elevon deflection angle, in degrees. Trailing edge downward is positive.
ALTWAX - Maximum twist angle of the wing tip, in degrees. Leading edge down at the tip is positive.

EPS - Gap distance between wing and elevon.

HNL - Hinge line location from elevon leading edge.

IDEF - Deformation check. If IDEF=1, the Table-Lookup Routine is used. If IDEF=0, a function definition is used.

AMP - Amplitude of a function deformation.

DB - Diameter of fuselage.

III. OUTPUT DATA

Major Headings Are:

A. INPUT DATA - Dimensional imput as it was given on the data cards.

B. ACTUAL VALUES USED IN PROGRAM - Variables non-dimensionalized by b/2.

C. CONTROL POINTS - Location based on non-dimensionalization of local wing chord by b/2. Gap distance is not included in X0.

D. BOUNDARY CONDITIONS

   I – Control point number.

   B – Boundary condition matrix values.

   XO,YO – Control point location as above, except with **gap distance** included.

   ALTW – Local twist angle at the control point (degrees).

   TAU – Local deformation angle at the control point (degrees).

E. POLYNOMIAL COEFFICIENTS – B_{nm}'s of pressure loading function.

F. PRESSURE DISTRIBUTION

   ELEVON LEADING EDGE – Location in percent local chord (gap included)

   Y – Nondimensional spanwise location of the given pressure.

   X – Nondimensional chordwise location in percent local chord (gap included).

   XDIS – Chordwise location in terms of nondimensionalization by b/2.

   DCP – ΔC_p (pressure loading)

   C – Local chord length of the wing only.

G. SECTIONAL CHARACTERISTICS

   CLW – cc_ℓ of wing only.

   CMW – $c^2 c_m$ of wing only

   CLE – cc_ℓ of elevon only

   CMH – $c^2 c_m$ of elevon only

   CCL – cc_ℓ of total wing-elevon.

   CCM – $c^2 c_m$ of total wing-elevon

   XCP – Center of pressure in percent local chord behind the leading edge.

   Y – Nondimensional spanwise location of the sectional characteristics.

   C – Local wing chord nondimensionalized by b/2.

CF - Local elevon chord nondimensionalized by $b/2$.

CTDT - Total local wing-elevon chord (gap not included)

CDW - cc_{D_i} of wing only

CDE - cc_{D_i} of elevon only

CCD - cc_{D_i} of total wing-elevon

H. TOTAL FORCES AND MOMENTS

TOTAL LIFT, etc. - Characteristics of wing-elevon combination.

CORRECTED LIFT - Lift multiplied by $\sin \alpha$.

LIFT AND MOMENT DUE TO SUCTION - Contribution of suction only. Lift value is correct only when $\alpha > 0$. Both terms are incorrect for $\delta \neq 0$.

FUSELAGE LIFT AND MOMENT - Contribution of fuselage only.

WING-FUSELAGE... - Wing-elevon fuselage characteristics.

TOTAL CONFIGURATION...- Wing-elevon-fuselage-suction characteristics.

HINGE MOMENT ABOUT ELEVON HINGE LINE - Elevon hinge moment.

IV. NON-PLANAR CONFIGURATION OPTIONS

A. Wing Twist - Statement numbers 2310 and 4540 calculate wing twist with a linear distribution along the span (YO(J)). Other (spanwise) variations may be used by substituting the proper equation.

B. Deformations

1. Statement numbers 2200 and 5430 must be deleted if the elevon is to be deformed in addition to the wing.

2. The FUNCTION WARP routine supplies the deformation angles

a. If the input variable IDEF is 0, the equation for WARP given by statement number 9430 is used to compute deformations. The variable (also input) AMP may be used to modify this equation. The supplied equation must be for the slope ($dz/d\xi$) of the mean line. Different functions could be used at different spanwise locations if the variables YO(J) in statement number 2160 and YA in statement number 5450 are included in the argument list, and the appropriate modifications are made to FUNCTION WARP.

b. If IDEF $\geq$ 1, a table lookup routine is used to compute deformations based on a numerical table given by the variables in BLOCK DATA.

SUPERSONIC COMPUTER PROGRAM USERS GUIDE

I. General Description of the Main Program and Subroutines
    for the Supersonic Program

MAIN PROGRAM

This is the executive portion of the program and basically controls

the sequencing of the other subroutines. All data to be read into memory

is completed here as well as all nondimensionalization. Decisions are

made on the type of pressure solutions desired and appropriate transfer

of control is made. Geometry for the vorticity paneling for the wing

and elevon is completed. Wing pressure solutions are called and the

trailing legs vorticity strengths are computed. Most of the entire

elevon solution is complete in this program segment and appropriate

computational output is generated.

Subroutine BLOCK DATA

This subroutine establishes the spanwise locations at which the

chordwise pressure distribution si computed. If one wishes to alter these

locations, it must be done in this subroutine.

Subroutine DAUGHN

This subroutine calculates the downwash of any arbitrary location on

the elevon due to the trailing vortices on the wing. This routine is

called after the wing loading and trailing vorticity strength is estab-

lished.

179

Subroutine EXACT

This subroutine calculates the pressure distributions on the wing or elevon using planar three-dimensional supersonic flow theory. This subroutine calls the load coefficient subroutine where sectional forces and moments are calculated.

Subroutine LODCOF

This subroutine takes the ΔC_p arrays and integrates the chordwise distribution using Simpson's Rule. It integrates the spanwise distributions using trapezoidal integrations.

Subroutine DOWN

This subroutine calculates a numerical value for the downwash on the wing only at some (x,y) location. It is used primarily to check boundary condition agreement.

Subroutine SURF

This subroutine computes the surface integral over the forecone from the field point (x,y) by summing the contribution from each subpanel. In doing so it loads the "A" matrix to be inverted later for the unknown polynomial coefficients, B_L.

Function CW

This function evaluates a cosine function which is used frequently in the program.

Subroutine INTV

This subroutine evaluates the results of the downwash integral over a subpanel.

Subroutine INVERT

This subroutine is a matrix "inversion" routine which actually uses a Gaussian reduction to find the unknown coefficients, B_L.

Function PRESS

This function evaluates the appropriate expression to find the ΔC_p at a point using supersonic three-dimensional theory.

Subroutine ELLIP

This subroutine numerically evaluates an elliptic integral used in Function Press.

Subroutine THA

This subroutine establishes the deformation equations of the deformed wings and returns the local wing slope relative to the wing chord line.

Subroutine SUM

This subroutine performs a summation step used often in Subroutine SURF.

Subroutine ETHA

This subroutine is identical to subroutine THA except the deformation equations define local slopes on the elevon surface.

II. Input Data

    A. Data Cards:

Card No.	Format	Variable List
1	8I5	IDOWN, IWGEX,IWGVP,IELEX,IELVP, IPRINT, IWGDF, IELDF
2	6I5,2F10.0	NC,NS,NX,NY,NCORD,NSPAN,VAG,DB
3	12A4	CONFIG
4	4F10.0	SPAN,CR,CT,LAMDA
5	4F10.0	SWING,CBRW,MACH,ALPHA
6	4I5,F10.0	LVON,NCE,NXE,NCRE,CRE
7	5F10.0	CTE,GAP,DELTA,XH,SIV
8	2F10.0	THIK,THTED

Additional configurations can be run by adding sets of cards

4 through 8. After the last set to be run, SPAN should be

read in as 0.0.

B. Variable Definition (all linear dimension units must be consistent)

IF (IDOWN = 1) a subroutine is called in which the downwash is computed at all pressure computed points on the wing.

IF (IWGEX = 1) uses exact solution for wing.

IF (IWGVP = 1) uses vortex paneling also for wing solution.

IF (IELEX = 1) uses exact solution for elevon.

IF (IELVP = 1) uses vortex paneling also for solution of elevon.

IF (IPRINT = 1) a more extensive printout is produced at intermediate computation points.

IF (IWGDF = 1) the wing has deformation as specified in function THA. Otherwise wing deformation is zero (planar).

IF (IELDF = 1) the elevon has deformation as specified in function ETHA. Otherwise elevon deformation is zero (planar).

NC is the number of chordwise control points for the wing.

NS is the number of spanwise control points for the wing.

NX is the number of grid points in the chordwise direction.

NY is the number of gridpoints in the spanwise direction.

NCORD is the number of chordwise points at which the pressure is computed for the wing.

NSPAN is the number of spanwise points at which the pressure is computed for the wing.

VAG is the angle in degrees that the vortices leave the wing reference plane.

DB is the dimensional body diameter.

CONFIG is the alphanumeric configuration description.

SPAN is the dimensional total wing span.

CR is the exposed wing root chord.

CT is the wing tip chord.

LAMDA is the wing leading edge sweep angle in degrees.

SWING is the dimensional reference area. If 0.0 is read in, the program will compute and use the wing area as the reference area.

CBRW is the dimensional reference length. If 0.0 is read in, the program will compute and use the mean aerodynamic chord as the reference length.

MACH is the freestream Mach number.

ALPHA is the angle of attack of the wing alone in degrees.

IF(LVON = 0) the elevon is omitted from all computations and the wing alone case is analyzed.

NCE is the number of control point locations on the elevon in the chordwise direction.

NXE is the number of subelements on the elevon in the chordwise direction.

NCRE is the number of points in the chordwise direction on the elevon at which pressure is to be computed.

CRE is the elevon root chord.

CTE is the elevon tip chord.

GAP is the gap distance between the wing TE and the elevon LE.

DELTA is the elevon deflection angle in degrees relative to wing trailing edge down is positive.

XH is the dimensional distance from the Y axis to the elevon hinge line.

SIV is the nondimensional chordwise location at which the wing trailing vortices are started.

THIK is the dimensional wing TE thickness.

THTED is the (positive) wing surface slope at the trailing edge in degrees.

III. Output Data

Major Headings Are:

A. Input Data - Dimensional or nondimensional data as it was given on the data cards.

B. Actual Values used in Program - Variables after non-dimensionalization by b/2.

C. Pressure Distribution -

D. Sectional Properties as Follows:

YA	(X_{LE})	CA	CCL	CCMY	XAC	XCPA
(η)	(x_{LE})	(c)	(cc_ℓ)	$(c^2 c_{m_y})$	(ξ_{ac})	(X_{ac})

E. Total load coefficients from "exact" theory

CN - Total normal force coefficient for wing only.

CLT - Total load coefficient.

CMTY - Total moment coefficient.

YBAR - Spanwise location for mean aerodynamic chord.

SIAC - Chordwise location for aerodynamic center.

CMC4 - Moment coefficient about the quarter chord.

CD-CDMIN - Induced drag.

SAREA - Reference area.

CBAR - Reference length.

F. [For deformed wings, the following is also output]

1. (a) Control point location; XO, YO, local chord; CA,

The x location of the last row of control points is re-located at trailing edge of wing and new locations are printed out.

(b) XO and YO are the nondimensional control point locations on the wing.

(c) Deform angle is the local deformation angle.

(d) B is the boundary condition (right-hand side side of equation 57).

2. (a) x and y are the dimensional location of the control points.

(b) B is the boundary condition (reference equation 59)

(c) WW is a dummy variable representing part of boundary condition term.

(d) BOD DBLET UPWSH is the body doublet upwash.

3. (a) Polynomial coefficients are the coefficients which describe ΔC_P loading distribution on the wing (Reference equation 54).

4. (a) Pressure distribution for wing using doublet paneling. The left-hand column, PSI, are the nondimensional chord-wise locations; the top row are the nondimensional spanwise locations at which the pressure is computed.

5. (a) The next output is the sectional coefficients for the deformed wings (reference section D, above).

(b) Next is the total coefficients for the deformed wings (reference section E, above).

G. 1. XG and YG are the x and y locations of the starting point of the trailing vortices on the wing.

2. GMA are the strengths of the trailing vortices.

H. Pressure distribution for elevon using exact functions (reference section 4(a)).

I. This section contains the sectional properties for the elevon (reference section D).

J. Total force coefficients for the elevon (reference section E).

K. Conversion to Neilsen's Data.